January 2016

Lateral Load Behavior and Capacity of Structures Composed of Steel-Plate Composite (SC) Walls

Peter N. Booth
Purdue University

Graduate School Form
30 Updated 12/26/2015

PURDUE UNIVERSITY
GRADUATE SCHOOL
Thesis/Dissertation Acceptance

This is to certify that the thesis/dissertation prepared

By Peter N. Booth

Entitled

LATERAL LOAD BEHAVIOR AND CAPACITY OF STRUCTURES COMPOSED OF STEEL-PLATE COMPOSITE (SC) WALLS

For the degree of Doctor of Philosophy

Is approved by the final examining committee:

Amit H. Varma
Chair

Arun Prakash

Robert J. Connor

Vikas Tomar

To the best of my knowledge and as understood by the student in the Thesis/Dissertation Agreement, Publication Delay, and Certification Disclaimer (Graduate School Form 32), this thesis/dissertation adheres to the provisions of Purdue University's "Policy of Integrity in Research" and the use of copyright material.

Approved by Major Professor(s): Amit H. Varma

Approved by: Dulcy M. Abraham 8/5/2016

Head of the Departmental Graduate Program Date

LATERAL LOAD BEHAVIOR AND CAPACITY OF STRUCTURES COMPOSED OF STEEL-PLATE COMPOSITE (SC) WALLS

A Dissertation

Submitted to the Faculty

of

Purdue University

by

Peter N. Booth

In Partial Fulfillment of the

Requirements for the Degree

of

Doctor of Philosophy

December 2016

Purdue University

West Lafayette, Indiana

ACKNOWLEDGEMENTS

My time at Purdue University has been rewarding both personally and professionally. I would like to thank my advisor, Professor Amit Varma for giving me the exciting opportunity to be part of such a great research team. It has been a genuine pleasure to work with such a great and talented group of people and to experience the process of growth and discovery that has occurred over the years through the study of the age old building materials steel and concrete, combined in new and innovative ways.

TABLE OF CONTENTS

Page

Page

Page

LIST OF TABLES

LIST OF FIGURES

Figure Page

Figure Page

Figure Page

LIST OF SYMBOLS

A_{cv}	Concrete area for shear strength calculation
A_{stud}	Cross-section area of headed stud anchor
b_w	Beam width
d_{max}	Maximum aggregate size
D	Outside diameter of circular core-wall structure
E'_c	Effective concrete compression stiffness
E_c	Concrete modulus of elasticity (secant)
E_{ci}	Concrete modulus of elasticity (tangent)
E_s	Steel modulus of elasticity
E_{co}	Constant (21,500 MPa) used in Equation 3.1
f'_c	Concrete compressive strength
f_{ck}	Characteristic concrete strength, equal to $f_{ck} = f_{cm} - \Delta f$
f_{cko}	Constant used in Equation 3.2
f_{cm}	Concrete mean compressive strength
f_{cmo}	Constant (10 MPa) used in Equation 3.1
$f_{ctko,m}$	Constant used in Equation 3.2
$f_{ctko,m}$	Constant used in Equation 3.2
f_{ctm}	Concrete mean tensile strength

f_{cy} Concrete compression stress at yield of steel faceplates

f_u Steel tensile strength

$f_{u,stud}$ Tensile strength of headed stud anchor

f_y Steel yield strength

G_s Steel shear modulus

G_c Uncracked concrete shear modulus

G_f Fracture energy

G_{Fo} Base fracture energy

h Clear height of shear wall or structure

H Lateral load applied to structure

K_s Steel shear stiffness

K_{sc} Composite shear stiffness

K_{xy}^{cr} Composite cracked concrete shear stiffness

K_{xy}^{uncr} Composite uncracked concrete shear stiffness

l Length of structure in direction of applied load

l_{CL} Centerline length of SC wall

l_w Length of shear wall considered in direction of shear force

m Steel strain hardening plateau factor

M Bending moment

M_{calc} Calculated moment strength

M_{FE} Section moment from FE analysis

M_{OTM} Overturning moment

M_p	Plastic moment strength
M_r	Required section moment strength
n	Steel stress-strain curve hardening exponent
P	Axial force
P_r	Required axial strength
Q	Headed stud anchor shear force
Q_u	Ultimate strength of headed stud anchor (Ollgaard et al. [63])
Q_{nv}	Ultimate strength of headed stud anchor (AISC 360-10 [65])
R_y	Steel expected strength factor
s	Stud spacing
S	Resultant unit force
S_{base}	Unit base shear
S_{xy}^{cr}	Resultant composite concrete cracking strength
S_{xy}^{y}	Resultant composite yield strength
t_p	Thickness of steel faceplate
t_{sc}	Wall thickness
V_c	Concrete shear strength contribution
V_n	Nominal shear strength
$V_{n\text{-}psw}$	Calculated shear strength of PSW structure
V_s	Steel shear strength contribution
V_u	In-plane shear ultimate strength
V_y	In-plane shear yield strength

w	crack opening width
w_c	Crack opening width at $\sigma_{ct} = 0$
w_1	Crack opening width at $\sigma_{ct} = 00.15\ f_{ctm}$
α_c	Shear wall aspect ratio factor used in Equation 4.1
β	Concrete compression softening factor
β_1	Effective concrete compression depth factor (ACI 349-06, 10.2.7.3)
δ	Horizontal displacement measured at load point
Δ	Interfacial slip at headed stud anchor location
Δf_c	Incremental concrete stress
ΔT	Temperature change
ΔS	Incremental resultant unit shear strength
ΔV	Incremental concrete shear strength
ε_{ct}	Concrete tensile strain
ε_{sh}	Uniaxial steel strain-hardening strain
ε_u	Uniaxial steel ultimate strain
ε_y	Uniaxial steel yield strain
γ	Shear strain
κ	Correction factor for composite shear yield strength
ν_c	Concrete Poisson's ratio
ν_s	Steel Poisson's ratio
ρ	Reinforcement ratio

$\overline{\rho}$	Normalized reinforcement ratio
ρ_t	Transverse shear wall reinforcement ratio
σ_u	Steel ultimate stress
σ_y	Steel yield stress
σ^c	Concrete infill stress
σ^s	Steel faceplate stress

ABSTRACT

Booth, Peter N. Ph.D., Purdue University, December 2016. Lateral Load Behavior and Capacity of Structures Consisting of SC Walls. Major Professor: Amit H. Varma.

The structural behavior and design of steel-plate composite (SC) nuclear power plant structures has been an active research area in recent years. The use of SC construction in new power plants is part of a trend in the industry towards more economical construction through increased use of modularization and prefabrication. Power plant structures are constructed with numerous structural walls that make up the external shield building, internal shield walls, and additional walls within the containment internal structure. Thorough understanding of the structural behavior of these walls and systems of connected walls is important since they are typically designed as the primary lateral force resisting system of the power plant. The objective of this research is to provide insight into the structural behavior from the perspective of the overall structural system. Prior research has studied the mechanical behavior of SC structural members (beams, shear walls, bearing walls, connections, etc.) in detail. This research aims to apply the information currently known about the fundamental behavior of SC structural members to the analysis of complete SC structural systems. Since full-scale testing of complete SC structures is impractical and expensive, this study uses a benchmarked finite element modeling approach to analyze and study the behavior of whole structures.

The research focuses on the lateral load behavior and capacity of SC structures configured in geometric shapes commonly used in safety-related nuclear power plant structures. Key parameters are studied including the structure aspect ratio (h/l), in-plane shear strength of SC walls, effect of wall openings and very thick walls on lateral behavior, and the cross-sectional shape of core-wall structures. The analytical study begins with the development of a finite element modeling approach where a series of previous experimental SC component tests are selected, modeled, and benchmarked. The analytical modeling then uses the benchmarked modeling parameters for the development of analytical models of complete structures. The benchmarking focuses primarily on validation of the constitutive models, steel-concrete composite interaction behavior, and the dynamic explicit analysis. The finite element models account for the complexities of mechanical behavior including steel yielding, steel faceplate buckling, force-slip behavior of stud anchors, concrete cracking, tension softening, shear retention, and concrete failure. Findings from the analytical study are finally used for the development of a unified lateral load design strength methodology for SC structures.

CHAPTER 1. INTRODUCTION

1.1 Background

A number of recently built nuclear power plants are constructed with modular steel-plate composite (SC) walls. Depending on the specific design, the containment internal structure, the shield building, or other wall and floor systems are constructed with SC modules. Two prominent examples of power plants using modular SC construction are the Westinghouse AP1000 [1] and the Mitsubishi Nuclear Energy Systems US-APWR. SC construction is used to expedite construction and improving quality. This is primarily achieved with prefabrication of structural modules in specifically designed assembly buildings. After the modules are fabricated they are erected and assembled in place thus resulting in shortened construction critical paths. Modular SC construction is also the subject of current research for use in lateral load resisting core-wall structures for multi-story building structures.

SC walls are composed of two parallel steel plates on the surfaces of the walls with concrete filled in the middle as shown in Figure 1.1. The steel plates are connected to each other with transverse steel members (tie-bars) such as angles, channels, or rods that brace the steel plates so that a given structural module can resist construction loads associated with concrete placement and transportation. The transverse tie-bars then remain in place, embedded in the concrete infill where they provide the function of transverse shear

reinforcement in the completed wall, similar to the shear reinforcement in a reinforced concrete beam. The steel and concrete are also mechanically connected with headed stud anchors that are welded to the interior faces of the steel plates and develop composite action.

SC walls can be constructed in a number of basic configurations. For the interior shield walls of power plants, they are typically very thick and massive in order to provide sufficient strength and also to provide radiation shielding. These walls, such as the primary shield walls (PSW) in the US-APWR power plant design, can be on the order of 12 ft thick. Very thick shield walls can also have more than two steel plate layers, with additional parallel and transverse steel plates embedded in the concrete infill to provide additional strength. In contrast, most other SC walls used for containment internal structures are on the order of 12 to 60 in. thick depending on application. SC wall reinforcement ratios ($\rho = 2t_p/t_{sc}$) are typically in the range of 1.5% to 5.0%.

1.2 Motivation

In the past, most power plant containment internal structures were built with reinforced concrete. In the US, these structures are designed with building codes such as ACI 349-06 [2] and ASCE 43-05 [3]. The recent introduction of SC construction in US power plant designs generated the need for additional design codes that specifically address the design of SC walls in safety-related structures. This led to the recent development of AISC N690s1-15 Appendix N9 [4] that provides design provisions for SC walls and structures. The development of this code was based on a combination of experimental and analytical research of SC structures primarily conducted in Japan, South Korea, the US, the UK, and

China, combined with guidance from current structural steel, reinforced concrete, and composite structure design codes. For example, the out-of-plane shear and flexural behavior of SC walls are similar in many ways to reinforced concrete beams where the steel plates of an SC wall provide a similar function as the longitudinal rebar reinforcement of a typical reinforced concrete beam and the transverse tie members act as vertical shear reinforcement. Similarly, the steel plates of an SC shear wall provide similar function as typical reinforced concrete shear wall reinforcement. These similarities resulted in design provisions in the new SC codes that are roughly equivalent to provisions in existing reinforced concrete codes. The SC codes also draw on structural steel design provisions reinterpreted for SC structures such as the slenderness ratios of steel plates to resist local compression buckling and the design and detailing of headed stud anchors for composite response.

To date, most of the experimental research of SC structures has focused on the structural response at the member level. Although a number of prominent reduced-scale experimental tests of whole structures have been conducted in Japan such as a test of a $1/6^{th}$ scale PSW by Shodo et al. [5] and a 10^{th} scale test of a containment internal structure by Akiyama et al. [7]. These two experimental tests (and supporting analytical work) provided findings that were primarily limited to these specific structures since they were exceedingly geometrically complex and unique.

The purpose of this research is to use analytical methods to study the global structural behavior of SC structural systems and core-wall structures and to present findings that can

be used for the development of future code provisions. The analytical work uses a benchmarked nonlinear inelastic finite element modeling approach with the commercial finite element computer program Abaqus/Explicit [6].

1.2.1 Research goal

The goal of this work is to provide practical findings on the mechanical behavior of SC structures. Results from the findings are used to develop simplified methods for prediction of the lateral load-deformation response and ultimate strength of safety-related PSW structures and core-wall structures. The goal is to also provide general conclusions on the behavior and performance of specific geometric parameters on the global structural response of SC structures.

1.2.2 Research objectives

The objectives are divided into the following list of tasks:

1. Development of a nonlinear inelastic finite element modeling approach using Abaqus/Explicit that is benchmarked and validated with results from a series of previous experimental tests of SC structures and components.
2. Use the finite element modeling approach to model and simulate the lateral load-deformation response of a specific PSW design.
3. Determine recommendations based on the results of the PSW simulation for prediction of the shear and flexural strength of the structure.
4. Development of a mechanics based method for prediction of the ultimate in-plane shear strength of SC walls connected to boundary elements and comparison of this

method to experimental results in the literature and finite element simulations of SC shear wall panels.

5. Conduct lateral load push-over simulations on a series of finite element models of SC core-wall structures. Study the influence of key parameters on global behavior primarily including: overall structure aspect ratio, wall cross-section reinforcement ratio, and structure plan shape.
6. Development of a comprehensive method for prediction of the ultimate strength of a core-wall structure constructed with SC walls.

1.2.3 Research scope and method

The focus of this research is on the analytical modeling of structures that are made up of multiple connected SC walls. The approach first includes the development of a finite element modeling approach that is benchmarked with the results of experimental tests of SC structural members. This is followed by the benchmarking and analysis of a reduced scale physical test of a PSW structure. This analysis is then studied and used to develop a design methodology for geometrically complex SC PSW structures. The analysis of the PSW structure serves as a case study and provides additional validation of the finite element modeling approach. In this analysis, only quasi-static lateral loads are considered that simulate seismic loads. In general, power plant structures are subjected to a wide range of additional load cases including most significantly, accident thermal. Additionally, shield buildings are designed in some cases to resist internal accident pressures, localized external projectile loads stemming potentially from missiles, airplanes, tornado wind loads, etc. The effect of these loads are beyond the scope of this work.

Additional results from experimental tests in the literature and finite element modeling of shear wall tests are then used to develop design equations for prediction of the in-plane shear strength of SC walls with boundary elements. The results of this are then used to develop a general method for prediction of the ultimate lateral strength of SC core-wall structures. The analytical core-wall models are designed to be as generic as possible and representative of what would likely used in practice. Parameters (such as structure height, and reinforcement ratio) are then considered so that their influence on the global response can be determined. Structural and geometric details of the core-wall models are selected to be similar to that of safety-related SC walls.

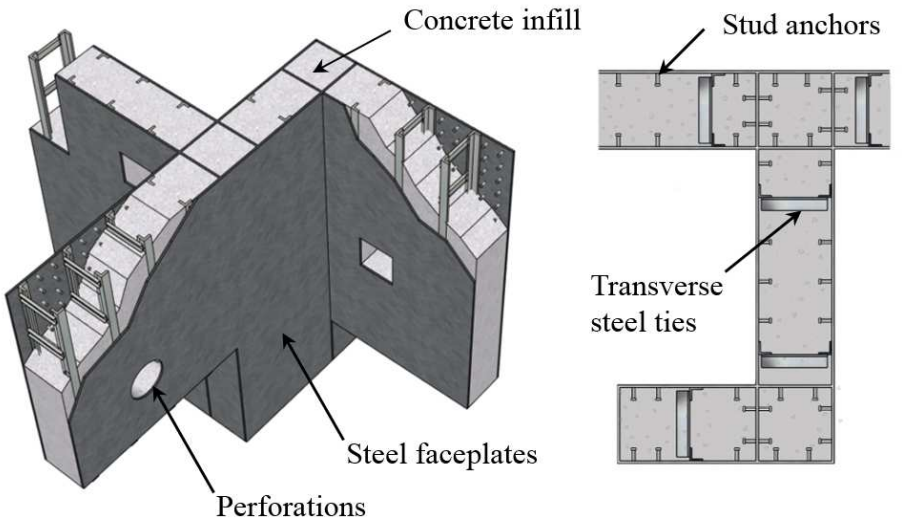

(a) Typical SC wall detailing (b) SC wall cross-section

Figure 1.1 Typical SC wall detailing and properties

CHAPTER 2. LITERATURE REVIEW

Steel plate-composite construction has been considered as an alternative to reinforced concrete since the 1980s. The most common applications have included nuclear power plant shield buildings and containment internal structures, rapidly deployable blast-resistant barriers, ice-resisting arctic offshore structures, tunnel structures, and more recently lateral force resisting building core-wall structures.

Significant early experimental and analytical research of SC structures for nuclear power plants occurred in Japan and was primarily conducted by Akiyama et al. (1989) [7], Akiyama (1991) [8], Fukumoto et al. [9], Takeuchi et al. [10], and Kato et al. [11]. This was followed by more recent research in South Korea also studying the feasibility of SC construction for nuclear power plant structures [12] that resulted in the development of a South Korean design code for SC structures, KEPIC-SNG 2010 [13]. The study of arctic offshore structures constructed with SC walls was undertaken in various countries by Narayan et al. [14], Ohno et al. [15], Adams et al. [16], Matsuishi et al. [17] and O'Flynn and MacGregor [18]. In the UK, a series of research studies were conducted on the use of SC structures for tunnels by a group of industry consultants in collaboration with Wright et al. [19]. Also, in the UK a proprietary product, Bi-Steel, was developed for use in a wide range of applications from blast-resistant barriers, prefabricated shear walls, and building

core-wall structures [20][21]. The development of a US design code for safety-related nuclear power plant SC structures (AISC N690s1-15 [4]) and also a Japanese code, JEAC-4618 [22] occurred more recently.

2.1 Previous research on structural behavior of SC walls

The experimental and analytical study of the behavior of SC structural members has been the subject of extensive previous research. This section summarizes a number of the more notable research programs.

2.1.1 Axial strength of SC walls

The axial response of SC sections has been the subject of extensive previous research in Japan by Akiyama et al. [8], Usami et al. [23], Kanchi [24] and more recently by Varma et al. [25] in the US. Akiyama conducted experimental compression tests on SC sections and reported detailed results on the stiffness and strength behavior of the specimens. Since the steel faceplates were not connected to each other with transverse tie-bars, the faceplates ultimately buckled and partially delaminated from the SC specimens at ultimate load. A method for predicting the ultimate strength was proposed based on the squash-load model where the compressive strength of the section is assumed proportional to the cross-sectional areas of steel and concrete and also the respective compressive strengths. The Varma et al. study provided similar findings and additionally studied the effects of accident thermal loads on compressive strength.

2.1.2 Out-of-plane shear and flexural response of SC walls

The out-of-plane flexure response of SC walls has been studied by a number of researchers including Wright et al. [19], Takeuchi et. al [26], Hong et. al [27], Chu et al. [28], and more recently, Sener et al. [29]. These studies included experimental out-of-plane one-way flexure tests of SC beams that were proportioned and detailed such that the ultimate capacity would be governed by flexural failure. Sener et al. [29] summarized the results of all of the previous experiments and compiled a database of 54 beam tests. Design equations for calculating the flexural strengths from the Korean code KEPIC-SNG [13], the Japanese code JEAC-4618 [22], and a method based on provisions from ACI 349-06 [2] were compared with the experimental results. All of the beams showed tension-controlled flexural failure with failure initiated by yielding of the tension steel faceplate. The flexural strengths calculated using the design equations predicted the strengths of the beam tests with reasonable accuracy and were in some cases slightly conservative.

The out-of-plane shear behavior of SC beams has also been studied experimentally and analytically primarily in Japan by Ozaki et al. [30], in South Korea by Hong et al. [27], and in the US by Varma et al. [31] and more recently, by Sener and Varma [32]. These works, among others led to the development of shear strength code equations in the Japanese code (JEAC-4618), the South Korean code (KEPIC-SNG), and the US code for safety-related SC structures (AISC N690s1-15).

2.1.3 In-plane shear response of SC walls

Research studying the in-plane shear response of SC walls can be divided into three basic categories: (1) combined in-plane shear in-plane flexure of SC wall piers (shear walls without boundary elements), (2) membrane shear panel tests, and (3) combined in-plane shear in-plane flexure of walls with boundary elements (such as flanged shear walls or walls with structural steel boundary elements).

2.1.3.1 Pier walls

Research focusing on the in-plane lateral response of SC pier walls (wall segments without vertical boundary elements or flange walls) has been conducted by Akiyama et al. [33] and more recently been studied by Epackachi et al. [34]. The Epackachi research program included experimental tests on pier walls with varying parameters (aspect ratio (h/l_w), steel reinforcement ratio (ρ), etc.) and also included detailed finite element analyses of the walls. The experimental study resulted in the following conclusions: (i) the walls sustained damage as a result of cyclic loading including spalling and crushing of the concrete at the base of the wall on the compression face, (ii) local buckling of the steel faceplates at the base of the wall, (iii) ultimate failure of the walls initiated by fracture of the steel faceplates in tension, and (iv) high ductility during post-peak load cycles.

2.1.3.2 Shear panels

Experimental and analytical research of SC shear panels has been conducted by Takeda et al. [35] and followed up with additional analysis by Ozaki et al. [36]. Also, experimental

tests of shear panels with and without ribs was conducted by Hong et al. [27], and more recently Danay developed an analytical method for modeling the stiffness response of panels subjected to combined shear and axial loading [37].

The experimental tests were conducted in a test setup that subjected the shear panels to a near state of pure shear. The shear loads were applied to steel headed stud anchors that were embedded in the concrete infill around the perimeter of the panels. A number of the tests also included the application of in-plane axial force along one axis of the panel in addition to the applied shear. Steel reinforcing plates were attached around the perimeters of the specimens and through-bolted in order to prevent the concrete from splitting at the edges.

Takeda et al. [35] conducted a series of seven physical tests of SC shear panels. The structural responses of the SC panels followed a progression of concrete cracking of the infill, yielding of the steel faceplates, and finally an increased load carrying capacity until peak load was achieved. The analytical work by Takeda et al. developed a method for calculating the shear stiffness for increasing force levels associated with the following phases: (1) uncracked concrete state, (2) cracked concrete, (3) and after the point of yielding of the steel faceplates. The corresponding shear forces at these transitions were also calculated (i.e. concrete cracking, faceplate yielding, and ultimate shear strength). The first loading phase, prior to concrete cracking was modeled with a plane stress composite shell model, with elastic isotropic constitutive models for steel and concrete. Strain compatibility and equilibrium were enforced at the interfaces of the steel and concrete infill.

After the initiation of concrete cracking, a concrete constitutive model developed by Kupfer et al. [38] was used and initiation of steel faceplate yield was defined by von Mises yield.

Ozaki et al. [36] subsequently conducted additional panel tests, finite element analysis and development of design equations. Nine panels were tested with and without partitioning webs and six more panels were tested with square holes in the center of the panels. Loadings were also applied that included combinations of shear and axial forces. Conclusions from this study included the following: (i) the yield strength of the panel was approximately proportional to the thickness of the steel faceplates, (ii) the concrete cracking strength was influenced by the application of axial force, (iii) the addition of axial force had a negligible effect on the ultimate strength of the panels, (iv) the derived equations using the truss analogy were in good agreement with the experimental results, (v) the strengths of the panels with openings can be predicted with a design approach based on reinforced concrete principles, and (vi) the inclusion of partitioning webs had a negligible effect on the ultimate strength of the panels. Results from the Ozaki et al. study were adopted in the Japanese SC design code, JEAC-4618 [22].

Hong et al. [39] tested a total of seven SC shear panels: four with ribs (small steel H-sections spaced equally and welded to the inner surfaces of the steel faceplates), and three specimens without ribs. All of the specimens showed a predictable progression of mechanical response with (i) cracking of the concrete infill, followed by (ii) yielding of the steel faceplates, and finally (iii) diagonal compression failure of the concrete infill.

Hong et al. also developed an analytical approach for calculating the shear force-shear strain response of SC wall elements subjected to pure shear. Up to the point of yielding of the steel faceplates, this approach was similar to previous studies but with additional equations taking into account the effect of the steel reinforcing ribs. The method used conventional composite shell theory with plane stress isotropic constitutive models for concrete and steel and steel-concrete strain compatibility and equilibrium. After yield, reserve shear strength was attributed to arch action of the concrete infill and peak strength a function of the ultimate effective concrete compressive strength, taken as $0.85f'_c$. After steel yield, the state of stress in the steel faceplate can change but must remain on the yield surface as the applied shear is increased. The state of stress in the steel faceplates associated with the minimum concrete compressive stress was then determined so that a lower bound prediction of the shear strength of the shear panel could be determined.

More recently, Danay [37] developed a comprehensive analytical method for predicting the stiffness of SC panels (prior to yielding of the steel faceplates) subjected to the following combinations of in-plane forces: bi-axial compression, bi-axial tension, bi-axial tension-compression, and in-plane pure shear. Like Takeda et al. and Ozaki et al., Danay used composite shell theory to model the pre-cracked response of the SC panel. After the occurrence of initial cracking, a smeared shear spring model was used for the headed stud anchor and composite response of the system. A constitutive model was developed for the composite response of the panels that considered the variation of stresses in the steel and concrete across crack planes. The experimental tests by Ozaki et al. [36] were modeled with this approach and results also compared to JEAG-4618 and the Ozaki equations. For

the pure shear case, all three approaches resulted in very similar shear force-shear strain curves for the uncracked and cracked portions of the panel response.

2.1.3.3 Flanged shear walls

Physical testing and research of SC flanged shear walls has primarily been conducted in Japan by Sasaki et al. [40], Suzuki et al. [41], Takeuchi et al. [42], and subsequently Ozaki et al. [43]. Six SC flanged shear wall tests were also conducted by Korean researchers Hong et al. [39] and in the US one SC flanged shear wall test was conducted by Varma et al. [44].

These tests were conducted on free-standing flanged shear wall assemblies that were connected to reinforced concrete foundations with either baseplates or the walls embedded into the foundations. Similarly, the tops of the flanged wall specimens were embedded within upper reinforced concrete loading blocks. Cyclic lateral loads were applied with hydraulic actuators connected directly to the upper loading blocks such that the test specimens were subjected to a simultaneous combination of in-plane shear and over-turning moment. A number of the tests also included the application of vertical axial (compression) loads.

The Sasaki et al. [40] research included a series of seven flanged shear wall tests with the primary control variables being the structure aspect ratio h/l_w, reinforcement ratio ρ, and wall thickness, t_{sc}. The wall thicknesses ranged from 4.53 in. thick to 13.58 in. thick and aspect ratios from 0.99 to 1.75. Thick steel plates were attached to the ends of the flanges

so that the wall specimens would undergo shear failure in the web walls prior to flexural failure of the whole system. In particular, the steel plates were sized such that the predicted shear strengths of the web walls would be reached after first flexural yielding of the steel flange plates but before full flexural failure of the whole wall system. All of the walls showed similar progressions of failure and damage: concrete tension cracking in the tension flange, yielding of the web wall steel faceplates, and finally buckling of the faceplates. All of the wall specimens were pushed with displacement-controlled lateral load after the point of peak strength until rotations ranging from 1/25 to 1/40 were achieved.

An analytical model was developed by Suzuki et al. [41] for predicting the ultimate lateral strength of SC flanged shear walls. The method uses a truss analogy approach where the lateral strength of the web wall is equal to the sum of the strengths of the steel faceplate in diagonal tension and the strength of the concrete infill in diagonal compression. The ultimate strength is also a function of the angles of principle steel tension and concrete compression and the strengths of the flange walls and flange-web connections are assumed to be greater than the strength of the web wall. A simplified design approach was also proposed that assumes principle stress angles of 45 degrees for the principle tension and compression directions in the steel and concrete, respectively. This method demonstrated good agreement with the peak lateral strengths from the experiments.

Ozaki et al. [43] conducted physical tests on SC flanged shear walls. The test series included five tests that were designed to be shear-critical, and five additional tests with varying parameters intended to induce flexural failure, strength of anchorage connections,

and response of a flanged shear wall with an opening in the web wall. The tests resulted in a number of key findings including: (i) cracking of the concrete in the web wall and cracking of the concrete in the flanges similar to the response of a reinforced concrete structure, (ii) yielding of the web wall steel faceplates proportional to the thicknesses of the steel faceplates, and (iii) the flexural moment associated with first yield can be calculated using elastic cracked section properties and slender beam theory, and (iv) the flexural strength of the flanged wall system can be calculated with reasonable accuracy using standard concrete flexural strength design equations.

A series of six SC flanged shear walls were also tested by Hong et al. [27]. Four with the previously described steel H-section ribs on the internal faces of the steel faceplates and two additional tests with SC walls without ribs. The specimens were proportioned with two different reinforcement ratios (2.78% and 5.22%) and three aspect ratios were also considered: 0.71, 0.79, 0.87. The tests included specimens that were designed to either be flexure critical or shear critical. The results were consistent with those from previous tests and included predictable progressions of structural behavior including: (i) concrete cracking, (ii) steel faceplate yield, and finally, (iii) diagonal compression failure of the concrete in the web walls, or flexural yielding of the steel in the flanges for the flexure-critical test specimens.

2.1.4 Flexural response of SC structures and composite sections

The study of the out-of-plane flexural response of SC sections (described in Section 2.1.1) has been the subject of extensive previous analytical and experimental research. In contrast,

research on the in-plane flexural response or the flexural response of whole SC structures (specifically lateral force resisting core-wall systems, multiple connected shear walls, or SC pier walls) is relatively limited primarily since physical testing of whole structures (full scale or reduced scale) is impractical and expensive. A recent test of an SC shear wall (T-shaped) was conducted by Ramesh [45]. Nie et al. [46] conducted a series of tests of flanged SC shear walls with aspect ratios (h/l_w) ranging from 1.0 to 2.0. Nie et al. also conducted a comprehensive series of shear wall tests with SC wall panels and varied detailing including internal transverse steel stiffeners and concrete filled tube boundary elements on select specimens. The tests also used high strength concrete and rebar within the walls for additional strength. The study included analytical modeling of the stiffness degradation due to cyclic damage and a detailed moment-curvature analysis using a fiber model approach. A study on the behavior of SC pier walls conducted by Epackachi et al. [34] included analytical modeling (moment-curvature) with and without consideration of flexure-shear interaction. The Nie, Ramesh, and Epackachi studies all included modeling of the flexural response of SC walls with fiber model analyses that assumed steel-concrete strain compatibility, bending strain magnitudes proportional to the distance from the neutral axis, negligible shear deformation, and nonlinear constitutive models for steel and concrete.

2.2 Previous research of SC structural systems

As stated previously, the experimental study of whole SC structures is limited due to the high cost of experimental testing of whole structures. Over the years, a number of prominent experimental and analytical tests of reinforced concrete containment internal

structures and shield buildings have been conducted primarily to determine the response of these structures to extreme loads i.e., impact, earthquake, overpressure, or accident thermal loads. Pressure tests were conducted on prestressed concrete containment vessels at Sandia National Laboratory as part of a containment integrity research project. This program included pressure testing of a $1/6^{th}$ scale containment structure in 1987 and a $1/4^{th}$ scale test of a prestressed concrete containment structure in 1997 [47]. Physical tests of structures subjected to seismic loads have also been conducted such as a shake table test of a reinforced concrete containment vessel as part of an experimental and analytical research program [48].

Two prominent physical tests of SC structures were conducted in Japan in the 1980s. These tests were part of a joint effort between Mitsubishi Heavy Industries Ltd., the Japan Atomic Power Co., and Obayashi Corp. and conducted by Shodo et al. [5]. This study included the physical testing of a $1/6^{th}$ scale PSW structure. The second study by Akiyama et al. [7] (including researchers from the University of Tokyo and Mitsubishi Heavy Industries Ltd. included the physical testing of a comprehensive $1/10^{th}$ scale model of the complete containment internal structure made with SC walls. Both of these tests included lateral cyclic loading applied to the specimens up to the point of ultimate failure. The progression of local failure (steel plate buckling, weld fracture, concrete cracking, etc.) were monitored closely during the tests. Detailed finite element models were also developed and benchmarked with the tests so that additional information about the structural responses could be determined.

2.3 Summary

Abaqus/Explicit is used for all of the finite element modeling in this work. Modeling assumptions and parameters are developed with detailed benchmarking of physical tests of SC structures. Experimental tests are selected that emphasize aspects of the mechanical behavior of SC structures that are relevant to the subsequent modeling of complete SC structures. Tests are selected that focus on the out-of-plane flexural stiffness and strength of SC walls, in-plane shear and flexure of shear walls, push-out tests that isolate the composite force-slip response of SC walls, and two experimental tests of reduced-scale SC safety-related structures that combine all of the mechanical behaviors. Inelastic steel and concrete constitutive models are used in order to fully capture the behavior of SC structures including yielding and buckling of the steel faceplates, cracking, tension softening, and shear retention of the concrete, and the nonlinear shear force-slip behavior of the stud anchors. All of the modeling assumptions developed in the benchmarking models are identical to those used in the subsequent modeling of SC structures.

CHAPTER 3. ANALYTICAL MODELING AND BENCHMARKING

This chapter describes the development of the analytical modeling approach used in all subsequent chapters. The following topics are covered: (i) an overview of the modeling of structures with the finite element method, (ii) a description of the finite element analysis approach used, (iii) a detailed description of the modeling properties and parameters (with emphasis on the steel and concrete constitutive models, the steel-concrete composite interaction modeling, and the explicit analysis method) and (iv), verification and benchmarking of select experimental tests of SC structures and structural members.

Detailed three-dimensional (3-D) finite element modeling of nuclear power plant structures has historically been a common part of the design process of new power plants and also for the evaluation and assessment of existing power plants. This is in contrast to the structural design of conventional building structures that is primarily based on linear elastic (frame analysis or shear wall models) structural analysis methods. The reason for this difference is primarily due to the additional engineering resources that are available in the nuclear engineering industry, stringent levels of quality control, peer review of analytical methods and calculations, and also the result of the design of nuclear power plants that are often best modeled as solids or shells due to their complex geometry and monolithic construction.

A number of commercial finite element software packages are used for analysis of power plant structures. For dynamic analyses, lumped mass-spring-dashpot models have been historically used for the determination of frequencies, mode shapes and structural responses of the power plants and components. With this approach, analysis models typically group shear wall responses into springs with corresponding equivalent stiffness and damping properties, and the mass of components are combined into point masses at story levels [49]. Software packages such as SAP2000 [51] along with numerous others are especially conducive to this type of modeling. Dynamic analysis of the soil-structure interaction response is conducted with computer programs such as SASSI (System for Analysis of Soil Structure Interaction), that is capable of modeling below-grade flexible foundation structures and uses an equivalent linear finite element analysis method [50]. For the detailed 3-D modeling of containment structures, shield buildings, etc., a number of general purpose finite element packages are used including LSDYNA [52], ANSYS [53], GTSTRUDAL [54], and Abaqus CAE [6]. For this research, Abaqus CAE was used due to its wide range of modeling capabilities, extensive library of inelastic constitutive models, and prior successful history as an analysis tool for the modeling of SC structures.

3.1 Finite element modeling approach

The finite element computer program Abaqus CAE (Explicit) [6] (versions 6.12 and 6.13) were used for all of the analytical modeling work. This program provides a comprehensive set of advanced modeling tools (constitutive models, interaction properties, element types, etc.) that address the modeling requirements in a wide range of industries.

3.1.1 Concrete constitutive model

3.1.1.1 Overview of Abaqus concrete constitutive models

Abaqus CAE includes three built-in constitutive models that can be used for concrete modeling: (1) the smeared crack model, (2) the concrete damaged plasticity model, and (3), the brittle cracking model. All three models have unique characteristics that make them suitable for specific applications. The smeared crack concrete model is used for modeling plain concrete or reinforced concrete structures and uses Abaqus/Standard (implicit integration). An elastic-plastic model with strain hardening for modeling of the compression behavior is used. The yield surface is based on the first and second stress invariants (pressure dependent) and uses the associated flow rule with isotropic hardening. For the concrete tension and cracking response, the model uses a damaged elasticity approach where the post-cracking elastic stiffness is reduced according to the brittle fracture concept from Hillerborg et al. [55]. The cracking response is averaged over the element and executed with stress and stiffness calculations at the integration points. In this model, the post-cracked behavior is written in terms of the fracture energy, G_f, required to generate a unit area of crack surface. Shear retention across crack planes is modeled with a shear retention model that linearly reduces the shear stiffness to zero stiffness as the crack approaches a defined crack opening displacement value. Since this approach does not model elastic damage in compression, its usefulness is restricted to conditions involving only monotonic loading. One of the shortcomings of the use of isotropic hardening and associated flow rule is that it has been shown to over-predict inelastic volume strain.

The concrete damaged plasticity (CDP) model can be used with the implicit or explicit solver and can be used to model the general response of plain or reinforced concrete structures. The key feature of this model is the incorporation of compression and tension damage variables that reduce the elastic stiffness and thus allow for the simulation of cyclic loading and consequent material damage. The elastic modulus of the material is multiplied by a scalar degradation variable that is in turn, a function of compression and tension damage variables and the given stress state. A pressure dependent yield function with non-associated flow rule is used based on a derivation by Lubliner et al. [56] with modifications made by Lee and Fenves [57]. One of the key shortcomings of constitutive models with isotropic damage is that the reduction in stiffness in one direction subjected to a large extension may unrealistically reduce stiffness in transverse directions [58].

The brittle cracking concrete model is used with Abaqus/Explicit and also incorporates the previously described cracking model based on the fracture energy approach. In addition, the model includes orthotropic non-rotating, orthogonal crack planes. The model simplifies the compression response with a linear elastic isotropic model in order to improve the overall stability of the analysis for cases involving a high degree of nonlinear and inelastic response. The cracking response is initiated by Mode I fracture using a maximum stress (Rankine) criterion and followed by a tension softening curve and a corresponding user-defined exponential or linear shear retention relationship. This constitutive model is selected for the analytical modeling in subsequent chapters since it includes orthotropic modeling of cracked states and shear retention. Details of the brittle cracking model are described in more detail in the following sub-sections.

3.1.1.2 Elastic material properties

The concrete constitutive model assumes a linear elastic isotropic response for stresses less than the tension cracking stress limit. The elastic constants used are based on recommendations from the 2010 CEB-FIP Model Code [60]. This code includes recommendations on research and best practices for design and analysis of concrete structures and represents a synthesis of state-of-the-art scientific and technical research. It is intended to be both a stand-alone guide and a source document for the development of international and national building codes. CEB-FIP provides detailed recommendations for defining concrete material properties for finite element modeling. The Model Code recommends that a bilinear pre-cracked tension response is implemented where the elastic stiffness is slightly reduced when the tensile stress reaches 90% of the cracking stress. For the brittle cracking model, the tensile response is simplified and assumed to be linear as shown in Figure 3.1 (a) up to the point of cracking. The modulus of elasticity (at 28-day strength), E_{ci}, is derived from the experimentally measured concrete cylinder compressive strength and defined in Equation 3.1 (with SI units). E_{ci} is defined as the initial tangent modulus (taken at the origin point of the stress-strain curve) and is intended for use with concrete constitutive models that simulate nonlinear compression response.

$$E_{ci} = E_{co}\left[\left(f_{ck} + \Delta f\right)/ f_{cmo}\right]^{1/3} \qquad \text{Equation 3.1}$$

For the concrete constitutive models that assume linear elastic behavior for stresses below the cracking threshold, the secant elastic modulus defined in ACI 349-06 is used, where the elastic modulus, E_c, is defined as $57{,}000\sqrt{f'_c}$ with psi units (and f'_c also specified with psi units). This definition of modulus is approximately equal to the secant line extending

from the origin to the point on the stress-strain curve approximately equal to 45% of the ultimate strength [59]. CEB-FIP recommends a value for Poisson's ratio between 0.10 and 0.20 for concrete stress levels below approximately half of the characteristic strength, f_{ck}. In this work, a commonly used value of 0.17 is used. The density of plain concrete is taken as 145 lb./ft^3.

3.1.1.3 Cracking response: tension softening and shear retention

As described previously, the Abaqus/Explicit brittle cracking model focuses on simulation of the tension cracking and shear retention response of concrete. The tensile cracking response is modeled with initiation of cracking at the integration point defined independently for the three orthogonal directions (non-rotating) when the tension stress reaches the cracking stress according to a maximum stress (Rankine) failure criterion. Numerically, the post-cracking response is then calculated in terms of damaged elasticity for the direction subjected to cracking. CEB-FIP defines the mean concrete tensile strength, f_{ctm}, in terms of the characteristic compressive strength, f_{ck}, if experimental tension test data is not available. The relationship is shown in Equation 3.2:

$$f_{ctm} = f_{ctko,m}\left(\frac{f_{ck}}{f_{cko}}\right)^{2/3} \qquad \text{Equation 3.2}$$

In the equation, f_{cko} is a constant equal to 10 MPa and $f_{ctko,m}$ is equal to 1.40 MPa. To account for initial concrete shrinkage cracking commonly found in SC structures, the calculated mean tension cracking stress, f_{ctm}, is divided by two when implemented in the finite element model.

The post-cracking tension softening response is based on the fracture energy, G_f. The fracture energy is assumed to be a material property and defined as the energy released upon creation of a unit area of crack surface. CEB-FIP provides a means for estimating the fracture energy calculated in terms of the mean concrete compressive strength, f_{cm}:

$$G_f = G_{Fo}\left(f_{cm}/f_{cmo}\right)^{0.7} \qquad \text{Equation 3.3}$$

Where G_{Fo} is defined as the base fracture energy and defined in terms of maximum aggregate size, d_{max}. The correlation between G_{Fo} and d_{max} is listed in Table 3.1 for three typical aggregate sizes.

The post-cracking tension softening response is then assumed to follow a bilinear tensile stress-cracking opening displacement response with the fracture energy equal to the area under the bilinear stress-displacement curve as shown in Figure 3.1(b). The initial linear softening leg extends from the peak tensile stress, f_{ctm}, to $0.15f_{ctm}$ at a crack opening displacement of w_1. After a crack width of w_1 is reached, the response is linear until zero tension stress at a crack width of w_c.

The Abaqus brittle cracking constitutive model uses a power law shear retention formulation developed by Rots and Blaauwendraad [61] where the elastic shear modulus is reduced as a function of the tension stress-crack opening relationship. This model simulates the retention of shear stiffness across cracked surfaces (Mode II and III) resulting from shear friction or aggregate interlock and assumes full elastic shear stiffness prior to crack initiation decreasing to zero stiffness when the crack width reaches the limit of w_c. The power law formulation allows for different shear retention responses ranging from linear to exponential. For simplicity, a linear model is used in this analysis (Figure 3.1 (c)).

3.1.1.4 Element types and meshing

The concrete elements are modeled with solid linear stress-displacement 8-node brick elements with reduced integration (single integration point) and hourglass control (C3D8R). Abaqus CAE includes mesh generation capability that includes various options and approaches for mesh generation. In this work, automated meshing is used where characteristic element sizes can be specified. For the benchmarking analysis models, an attempt was made to maintain similar element sizes throughout the different models, although some variability could not be entirely avoided. Elements were kept within a size range of 1 in. to 3 in. depending on the overall size of the analysis model. For the subsequent analytical modeling, an element size of 3 in. was used. The sizing of concrete elements must be maintained within reasonable limits and take into account typical crack spacing that occurs in SC walls.

The previously described tension softening model based on fracture energy G_f, is used to determine the stiffness response of the element and is most commonly specified on the assumption that a maximum of a single crack can form in each orthogonal direction within an element. This then results in the stress-strain response becoming sensitive to mesh size since the simulation of cracking is averaged out over the length of the element. If too large of an element size is specified such that realistically multiple parallel cracks could form within a single element in a given direction, then the tension softening stiffness would become unrealistically low. Also, if elements are sized such that they are shorter than the typical fracture process zone (band of micro cracks ahead of the crack front), then the thickness of the fracture process zone could potentially be less than what has been

physically measured in experiments. These considerations require care in selection of concrete element sizes, consistent element sizing across models, and verification of results with physical experiments in order to ensure reasonable modeling assumptions.

3.1.2 Steel constitutive model

The steel constitutive model used for the finite element modeling of the SC wall faceplates is shown in Figure 3.2(a) and includes the initial linear elastic response with the proportional limit defined by σ_y and ε_y, followed by the yield plateau, and strain hardening leg. The elastic properties (elastic modulus, E_s, and Poisson's ratio, ν_s) are taken from AISC 360-10 [65] with E_s equal to 29,000 ksi and ν_s equal to 0.3. The idealized stress-strain relationship is based on equations by Varma [62] and includes a horizontal yield plateau bounded by the yield strain ε_y, and strain initiating strain hardening ε_{sh}, with the length of the plateau equal to ε_y multiplied by a factor, m. The strain hardening segment is defined in Equation 3.4:

$$\sigma = \sigma_u - \left(\sigma_u - \sigma_y\right) \cdot \left(\frac{\varepsilon_u - \varepsilon}{\varepsilon_u - \varepsilon_{sh}} \right)^n \qquad \text{Equation 3.4}$$

Where the ultimate stress, σ_u, and ultimate strain, ε_u, are governed by the exponent, n, that typically takes values between 3 and 6. This uniaxial stress-strain relationship is converted to a true stress-true plastic strain relationship used in the finite element analyses so that large-deformation response can be simulated. The steel model includes a linear elastic isotropic response, von Mises yield surface, associated flow rule, and isotropic hardening. Also, a simplified steel model (with a bilinear stress-strain relationship) is used for the

analytical models for the cyclic analysis that requires kinematic hardening. In this model, the post-yield response is replaced with a linear hardening leg as shown in Figure 3.2(b).

3.1.2.1 Element types and meshing

The steel faceplates are modeled with first-order stress-displacement 4-node shell elements with reduced integration (S4R). The element formulation accounts for finite membrane strains, large rotations, and is effective for the simulation of elastic and inelastic buckling. The elements are assumed to be thin and include the Kirchhoff constraint with shell normals remaining perpendicular the tangent plane at any given point.

3.1.3 Headed stud anchor model

In SC walls, the steel faceplates are mechanically connected to the concrete infill with headed stud anchors (shear studs) and tie-bars (typically steel channels, rods, or angles) that are welded to the the steel plates. In actual SC wall designs, a number of different tie-bar details may be used. One common detailing option includes steel angles that are welded to the interior surfaces of the steel plates (almost acting as reinforcing ribs spaced at regular intervals along the inner surfaces of the steel plates). Then the tie-bars are attached to the ribs with welds. This type of detail only works with sufficiently thick walls that permit welding access to the inside of the structural modules. Another tie-bar detail includes deformed bars that extend through holes in the steel plates that are then welded on the exterior surfaces of the walls (a variation of this includes threaded rods extending through

holes in the steel plates connected with nuts on both sides of the steel plates). These details have the advantage of being constructible with thinner walls.

The connectors and transverse tie-bars are then embedded in the concrete infill thus resulting in a composite section. The composite response of the section is primarily governed by the slip at the steel-concrete interface and is a function of factors such as the headed stud anchor size, stud spacing, and material properties of the studs and concrete. The ultimate strength of a given headed stud anchor may be limited by the quality of the weld, the strength of the stud subjected to combinations of bending and tension, the direct bearing strength of the concrete against the stud, or if the concrete is unconfined, concrete cracking or breakout.

There are a number of approaches for analytical modeling of the SC wall composite behavior. Detailed methods can be employed where headed stud anchors are modeled in 3-D with solid elements and embedded in the concrete, or more efficient and simplified approaches where the composite response is lumped into connector elements that tie nodes on the surfaces of the concrete solid elements with nodes that make up the steel shell elements. The simplified method was developed and described in Zhang et al. [64]. In the detailed approach, the aim is to replicate the interfacial force-slip response by modeling in detail the shear studs and the contact between the steel faceplates and shear studs and the concrete infill. If the modeling is detailed enough, then the global force-slip behavior will be simulated including with contributions coming from: the bending and tension response of the shear stud, local concrete bearing and cracking of the concrete, and friction between

the steel plate and the concrete. This approach leads to challenges since it is difficult to accurately model all of these contributing properties that all combine to produce the global response. This method also comes at a significant computational cost. The simplified approach is advantageous in that the global force-slip response can be directly defined by the user and simply lumps together all of the complex properties into a single force-slip definition. The force-slip relationship is then taken directly from the results of experimental push-out tests. This approach is used for all of the finite element modeling in this work in order to reduce the computational cost of the very large models. The force-slip behavior of the headed stud anchor is specified with a user-defined elastic and plastic response. The force-slip curve is based on work by Ollgaard et al. [63] and defined in Equation 3.5 and Equation 3.6:

$$Q = Q_u \left(1 - e^{-18\Delta}\right)^{2/5} \qquad \text{Equation 3.5}$$

$$Q_u = 0.5 \cdot A_{sa} \cdot \sqrt{f'_c \cdot E_c} \qquad \text{Equation 3.6}$$

Ollgaard fit the results of experimental push-out tests in order to calculate, Q_u, the shear strength of a single shear stud. The experimental study included tests with 3/4 in., and 5/8 in. stud diameters. The Ollgaard study concluded that the strengths were proportional to the square root of the concrete compressive strength, f'_c, multiplied by the concrete elastic modulus, E_c. The tensile strength of the shear stud was found to not have significant influence on strength. In contrast, AISC 360-10 Equation 3.7 puts a limit on stud strength based on the tensile strength of the stud. This applies if the condition is such that the concrete is subjected to substantial confinement thus forcing direct failure of the stud.

$$Q_{nv} = f_u \cdot A_{sa}$$ Equation 3.7

The stud strength is defined in terms of the tensile strength of the stud and assumes that structural detailing is such that limit states such as concrete breakout or pullout do not govern ultimate strength. This strength equation is adopted by AISC N690s1-15 since SC headed stud anchors with SC walls are not typically vulnerable to concrete breakout. The stud strength is then taken as the lesser of Equation 3.6 and Equation 3.7.

The force-slip relationship is defined in Equation 3.5, where Q is the shear force (kips), and Δ is the interfacial slip. Figure 3.3 shows the calculated shear force-slip curve for 3/4 in. studs and typical stud and concrete material properties.

3.1.4 Analysis approach

Abaqus/Explicit is used for all of the finite element modeling since simulation of large-deformations (such as local buckling of steel faceplates) inelastic material response (primarily concrete cracking), steel yielding, and contact must be modeled. All of the analyses are conducted with quasi-static loading with very high numbers of analysis steps. The solver uses explicit central difference integration. Since element masses are lumped, the mass matrix is diagonal resulting in inversion being equivalent to division. Therefore, the accelerations at successive steps can be solved quickly and a higher number of increments can be used. The time incrementation is fully automated with initial estimates of the stable time increment based on the element with the shortest dilatational wave travel time defined as the shortest length of the element divided by the dilatational wave speed.

The resulting stable time increment is reduced further by a factor to ensure that the initial time increment is conservative. The time increment must be sufficiently small to ensure that unrealistic accelerations or compounding displacement oscillations do not occur during the analysis. Semi-automatic mass scaling is also used in order to shorten analysis times. The mass of all elements are scaled equally if the stable time increment for an element drops below the specified limit of one microsecond. This would result in a maximum of 1,000,000 time increments for an analysis duration of 1 second. The Abaqus Theory Manual recommends that for quasi-static explicit analyses when semi-automatic mass scaling is used, the ratio of kinetic energy to total internal energy (or external work) is less than 10%. These ratios are listed in Table 3.7 for the analytical models used for benchmarking. In the table the ratio is defined as the highest ratio occurring for all of the time steps in a given analysis.

3.2 Benchmarking analysis

The finite element modeling details described in the previous sections are verified with benchmarking of a series of physical experiments of SC structural members. The purpose of the benchmarking is to verify the modeling assumptions with emphasis on the concrete response (simulation of fracture, cracking, and failure), the behavior of the headed stud anchors and composite behavior, and to verify that the explicit analysis is providing consistent and reasonable results. The selection of physical tests is based on particular aspects of mechanical response of SC walls that commonly occur in SC structures. Most of the tests emphasize particular aspects of behavior such as out-of-plane flexure and shear, in-plane flexure and shear, composite force-slip, etc. All of the elements of mechanical

response are then assumed to be present in the analysis of complete SC structures to a greater or lesser extent. A summary of the physical tests used for benchmarking are listed in Table 3.2.

3.2.1 Out-of-plane flexure

Three experimental out-of-plane flexure tests are benchmarked. The experimental tests were originally conducted in order to study the flexural stiffnesses and strengths of SC walls subjected to out-of-plane loads. The tests were conducted on beams with structural details typical of safety-related SC walls with two steel faceplates, concrete infill, welded transverse steel tie-bars that connect the faceplates to each other, and headed stud anchors welded on the interior faces of the steel faceplates.

3.2.1.1 Description of experimental tests

The three beam tests were all subjected to one-way bending and four-point loading configurations similar to the test-setup shown in Figure 3.4(a) (roller supports at both ends and two vertical loads applied with hydraulic actuators to the top surfaces of the beams at approximate third-points along the beam lengths). The beams were designed as SC wall cross-sections with widths approximately equal to the beam thicknesses (approximately square in cross-section). The beams were therefore oriented such that the steel faceplates were situated along the top and bottom faces of the beams, and the side walls of the beam were exposed concrete infill.

Details of the first two tests are described in detail in Booth et al. [66]. These two tests (OOP-1 and OOP-2) included combinations of thermal and mechanical loadings. The primary objective of these tests was to determine the flexural behavior of the beams to the application of mechanical loading with and without the application of heating. The loading sequence was designed to replicate accident thermal loads – a condition that is considered in the design of safety-related SC containment internal structure walls. The sequence began with application of a mechanical load (25 kips per actuator) intended to be similar in magnitude to the predicted equivalent fluid pressure that would occur during an accident thermal event. This load was then maintained at a constant constant value of 25 kips while the top steel faceplates were heated. For OOP-1, the steel faceplate in the mid-span was heated (64 in. of beam length between the two actuators) as shown in Figure 3.4(b), and for OOP-2 heating was applied to the top steel faceplate to a length of 32 in. on either side of one of the two load points (Figure 3.4(c)). After a given amount of time, the mechanical loads were then increased to approximately 90 kips. Dimensional and material properties of test specimens OOP-1 and OOP-2 are listed in Table 3.2.

The third experimental beam test (OOP-3) was only subjected to mechanical loading that was monotonically increased until the beam ultimately failed in flexure (initiated by flexural tension yielding of the bottom steel faceplate). Details of this beam test are reported in Varma et al. [67]. Dimensional and material properties of the beam are listed in Table 3.3.

3.2.1.2 Analytical results

The three beam tests were analyzed with 3-D finite element models. The meshing and part instances used for OOP-1 and OOP-2 are shown in Figure 3.5. The models included shell elements for the steel faceplates and tie-bars, solid part instances for the loading plates and end assemblies, and all of the shear studs discretely modeled with connector elements. The analyses replicated the loading sequences (for OOP-1 and OOP-2, initial mechanical loading, followed by heating of the top steel faceplate, and final monotonic load to approximately 90 kips). In the analysis, a constant coefficient of thermal expansion for steel of $6.5 \cdot 10^{-6}$ (1/°F) was assigned to the steel shell elements. The heating load was simulated by changing the temperature of the steel with a ΔT equal to 200°F for OOP-1 and 220°F for OOP-2 during the heating phases. For simplicity, only the temperature of the steel faceplate was changed, and not the underlying concrete infill adjacent to the faceplates.

The experimental and analytical load-displacement results for OOP-1 and OOP-2 are plotted in Figure 3.6(a) and Figure 3.6(b), respectively. The applied force plotted represents the force per actuator (therefore the total force applied to the top of the beam is twice this value). The three loading phases are clearly shown in the plots: (1) the initial ambient loading to 25 kips, (2) the heating phase at constant mechanical load of 25 kips, and (3) the final monotonic mechanical load. The plotted vertical deflection was measured at the beam mid-span. During the initial loading phase, the beams deflected down, during the heating phase, thermal expansion of the top steel faceplate force the beam to bend upwards, followed by the final loads where the beams were forced back down into positive curvature.

The analysis shows very good agreement with the experimental results (the lengths of the thermal deflections agree and the load-deflection stiffness compare well for the final loading legs). For the initial loadings, the analysis predicts substantially higher flexural stiffness partially due to the fact that the concrete infill in both OOP-1 and OOP-2 were substantially pre-cracked as a result of the physical test specimens being shipped by truck after the concrete had been placed in the specimens. The pre-cracked concrete was not accounted for in the analytical models. The analytical and experimental flexural stiffness are listed Table 3.7 for comparison. The stiffness values listed represent the ratio of force and displacement values taken at the ends of the segments that are shown (in pink) in the two plots.

The deflected shapes of OOP-1 and OOP-2 are shown in Figure 3.7 and Figure 3.8 (scaled in the vertical direction by a factor of 100 for the purpose of illustration). The contours represent the maximum principal concrete strains. The effects of heating are clearly shown, where the vertical upward deflection of OOP-1 heated in the mid-span, is centered symmetrically about the centerline of the beam, and the vertical deflection of OOP-2 is centered on the left loading point.

The load-displacement response of OOP-3 is plotted in Figure 3.10(a) and the initial portion of the same curve is plotted in Figure 3.10(b) for the purpose of comparing initial stiffnesses (the stiffness are also listed in Table 3.7). In the plot the stiffness line segment (shown with the solid black line) denotes the portion of the load-displacement response where the stiffness is compared. In Figure 3.10(b) comparisons of initial stiffness are

shown with the pre and post concrete cracking stiffness from the analysis (occurring at approximately 15 kips) are slightly higher and slightly lower, respectively than the experimental stiffness. Maximum principal concrete strain contours and deflected shapes (with a scale factor of 20) of OOP-3 are rendered in Figure 3.9. The three figures represent increasing applied load levels of 31, 129, and 228 kips, respectively.

3.2.2 Push-out tests

3.2.2.1 Description of experimental tests

Push-out tests conducted by Ollgaard et al. [63] studied the composite behavior of headed stud anchors embedded in lightweight and normal weight concrete. The test program included 48 push-out tests that applied shear parallel to the orientation of the steel-concrete interface. Figure 3.11(a) shows details of the Ollgaard pushout test specimens that were configured with 4 headed stud anchors on each side of the wide flange beam. The main control variables in the tests were stud diameter (5/8 in. and 3/4 in.), number of headed stud anchors and concrete aggregate properties. The specimens had either 2 or 4 shear studs welded to each flange (4 or 8 per test setup) of a 28 in. long segment of a W8x40 beam. The headed stud anchors were embedded in reinforced concrete block that were cast against each flange of the W8x40. The concrete blocks were reinforced with rebar that served to confine the concrete in the immediate vicinity of the embedded shear studs. A majority of the tests were conducted when the age of the concrete reached 28 days. Three specimens were tested for each of the 16 configurations. Two of each specimen type were loaded up to a force level that was considered equivalent to a service level load, then unloaded and

reloaded to ultimate. The third specimen of each group was loaded monotonically to ultimate failure. All of the tests showed substantial inelastic deformation of the connections prior to failure. The strength limit states were either governed by shearing of the headed stud anchors at the welded connection to the steel beams or breakout failure of the concrete surrounding the shear studs. The empirical equations defining ultimate shear stud strength and force-slip relationship previously described in Equation 3.5 and Equation 3.6 were the result of this work.

3.2.2.2 Analytical results

Two finite element analyses of pushout tests were analyzed: one with 4 headed stud anchors (PO-1) and one with 8 headed stud anchors (PO-2). Figure 3.11(c) shows the part instances and meshing that were used for both analyses. The steel wide flange segment was modeled with shell elements and the concrete blocks with solid elements. For simplicity, the concrete reinforcement was omitted. A monotonically increasing vertical point load was applied to the top of the steel section at a reference point that controlled a rigid body region assigned to the nodes on the upper edge of the steel beam. The bases of the concrete blocks were fixed against translation in the vertical direction.

Results from the two analyses are plotted in Figure 3.12(a) and Figure 3.12(b). For the two cases, the force is equal to the total applied load subjected to the pushout specimen divided by the number of headed stud anchors. Therefore, for PO-1, the load equals the applied load divided by 4 and PO-2 equals the applied load divided by 8. The slip values are equal

to the vertical component of slip between the two nodes that are linked with the connector elements. The experimental shear force-slip curve from Ollgaard et al. is also plotted using 0.75 in. diameter studs and normal weight concrete. As shown, the analytical results show good agreement with reasonable predictions of initial stiffness and peak strength (listed in Table 3.7). In the two analyses, the concrete did not reach cracking stress levels nor did the steel yield. All of the behavior was the result of elastic deformation of the concrete and steel part instances and deformation of the connector elements representing the headed stud anchors. Therefore, the emphasis of these two analyses is limited to confirmation that the stud modeling assumptions are reasonable.

3.2.3 In-plane pier wall tests

Three experimental tests of SC wall piers were benchmarked. The tests were conducted in 2013 and 2014 at the Bowen Laboratory at Purdue University. Details of the three tests are described in Kurt et al. [68]. The purpose of the tests was twofold: to study the overall response of the shear wall panels subjected to cyclic loads, and to evaluate the performance of the base connection design.

3.2.3.1 Description of experimental tests

The tests were configured as free-standing piers of SC walls without boundary elements (such as flange walls, steel end plates, steel sections are internal rebar reinforcement). The wall aspect ratio (free height of wall divided by length parallel to the loading direction, h/l_w) was the primary variable in the tests. The aspect ratio for the first test (WP-0.60) was

0.60, the second test (WP-0.75), 0.75, and the third wall (WP-1.00) was constructed with an aspect ratio of 1.00. The wall aspect ratios were selected such that the response and ultimate strengths of the walls were governed by a combination of in-plane flexure and in-plane shear. In particular, the effect of in-plane shear on the in-plane flexural strength was of primary interest. Consequently, walls with aspect ratios of 1.00 and less were tested. The three tests were designed and constructed at a reduced scale (approximately 1/3rd) so that the ultimate strengths would not exceed the capacity of the available laboratory equipment. The steel faceplates were mechanically connected to the interior concrete with headed stud anchors and the faceplates were connected to each other and braced with threaded rods that were bolted through holes that were drilled through the faceplates. The bottom edges of both faceplates were welded to a thick (1.375 in.) steel baseplate that was, in turn, anchored to the reinforced concrete base with vertical rebar. The rebars were threaded on the top ends and attached to threaded couplers that were welded to the underside of the steel baseplate. The overall connections of the pier walls to the reinforced concrete bases were designed using over-strength criteria such that the strengths of the connections would exceed the strengths of the connected SC pier walls. The tests therefore presented findings on both the overstrength performance of the connections and also the strength and post-peak ductility response of the pier walls.

The lateral loads were applied to the top of the SC pier walls such that the walls would be subjected to combined in-plane shear and in-plane flexure. The loading protocol included a series of load cycles (with full load reversal during each cycle) that were applied until the wall reached ultimate failure.

For the three tests (PW-0.60, PW-0.75, and PW-1.00), it was observed that the applied lateral loads produced a biaxial stress state in the steel faceplates with significant vertical bending stresses apparent at both ends of the walls. The loading also produced diagonal compression in the concrete infill. As the applied loads were increased and the wall piers approached peak strength, concrete cracked and spalled at the ends of the walls (at the base) and the steel plates buckled outward at the base of the walls at the ends that were subjected to compression. At the ends of the wall subjected to tension, the steel plates yielded in the vertical direction. For the 0.60 and 0.75 aspect ratio tests, ultimate failure was precipitated by substantial damage and spalling of the concrete on the exposed ends of the wall combined with yielding of the steel plates at both ends of the wall. For the 1.0 aspect ratio wall, the ultimate strength of the wall was governed more by flexural over-turning forces. The steel plates yielded in tension and eventually fractured just above the connection weld.

3.2.3.2 Analytical modeling and results

The three pier wall tests were analytically modeled. Modeling parameters are summarized in Table 3.6. Since the SC pier walls were constructed at reduced scale (approximately 1/3rd), a smaller mesh size was required in comparison to previous models. For the concrete infill a mesh size of 2 in. x 2 in. x 2 in. was used and for the steel faceplates, a mesh of 1 in. x 1 in. was used. Details of the meshing and part instances are shown in Figure 3.14. The baseplates were also modeled with shell elements and the vertical anchor rods that tie the baseplates to the reinforced concrete bases were modeled with truss elements.

Frictionless contact was assigned between the steel faceplates and the concrete infill so that the corrected buckling mode and response of the steel faceplate could be simulated.

The force-displacement results of the three analyses are plotted in Figure 3.15, Figure 3.16, and Figure 3.17, respectively. The applied load in the plots are defined as the total lateral point load applied to the top of the SC wall pier and the displacement is also taken at the top of the wall at the same point. Overall, the load-displacement curves show good agreement with the experimental responses with very slightly higher initial stiffnesses predicted by the analyses and very close comparisons of peak strength. The ratios of peak strength (analytical strength over experimental strength are listed in Table 3.7 and equal to 1.09 for PW-1.00, 1.00 for PW-0.75, and 0.96 for PW-0.60. Figure 3.18 shows the stress contour output for the steel faceplate (von Mises) and the concrete infill (maximum principal concrete stress) for PW-1.00. The contours are shown for three applied force levels: 154 kips (Figure 3.18(a)), 509 kips (Figure 3.18(b), and 527 kips (Figure 3.18(c)). The figures show the progression of von Mises stress for increasing loads primarily along the tension side of the wall and along the base. The maximum principal concrete strains are shown initially as flexural tension cracks that transition into diagonal tension shear cracks at the higher force levels. The near peak load Figure 3.18(c) shows extensive concrete flexural tension cracking, diagonal cracking and failure of concrete at the compression toe (at the lower right corner). Similar results are presented for PW-0.75 and PW-0.60 in Figure 3.19 and Figure 3.20, respectively where flexural tension cracking initiates at low forces and then transitions into diagonal concrete cracking combined with steel yielding along the base of the walls.

3.2.4 In-plane flanged wall tests

A series of six SC shear walls with flanges were modeled analytically and benchmarked. The experimental tests used for the benchmarking were conducted by Sasaki at al. [40] and were briefly described in the Chapter 2 Literature Review.

3.2.4.1 Description of experimental tests

Figure 3.21(a) and (b) show plan and elevation views of the test setup used for the flange wall tests. As described previously, the tests were conducted on free-standing flanged SC shear walls that were connected to reinforced concrete bases and embedded at the top within concrete loading blocks. As shown in the figure, hydraulic actuators applied lateral loads to the tops of the walls. The experimental tests included 7 specimens: 6 with applied lateral loads and a seventh with combined horizontal and vertical loads. For the benchmarking analysis, only the 6 tests without vertical loading were modeled and analyzed.

3.2.4.2 Analytical modeling and results

Figure 3.22 shows typical part instances and meshing for test for the flange wall models (test H10T15 is shown in the figure). The concrete base and top blocks were modeled with solid elements and assigned a linear elastic isotropic material model with the concrete stiffness, E_c, for simplicity. Concrete infill within the shear wall and the two flange walls were modeled with solid elements and assigned the previously described brittle cracking constitutive model. Details of the material properties are listed in Table 3.5 and Table 3.6.

The lateral load-story drift displacement responses for the six analyses are plotted in Figure 3.23, Figure 3.24, and Figure 3.25. The load-displacement results from the six experiments are also plotted for comparison and represent backbone curves from the cyclic tests. Overall, the six analyses show good agreement in terms of initial stiffness, inelastic response, and peak strength. The ratios of peak strengths (analysis divided by experiment) are listed in Table 3.7.

3.3 Summary

The finite element benchmarking process included the compilation of a series of physical tests of SC structures with a wide range of mechanical behaviors characteristic of the behavior that would be evident in a complete SC structure. Emphasis was placed on out-of-plane flexure, in-plane shear and flexure, and composite (force-slip) behavior. A modeling approach is described using Abaqus/Explicit and includes the use of constitutive models for steel, concrete, and the composite force-slip response. The explicit analysis approach was selected so that the highly inelastic (concrete cracking) and nonlinear (large deformation) and contact response could be analyzed. The analytical results were qualitatively compared with the experimental results and show reasonable agreement consistently across the series of benchmarking tests. The ratios of peak strengths are listed in Table 3.7 with an overall mean of 1.00 and a standard deviation of 0.06.

Table 3.1 Base values of fracture energy G_{Fo}
(CEB-FIP Model Code 2010 [60])

d_{max} (mm)	G_{Fo} (Nmm/mm^2)
8	0.025
16	0.030
32	0.058

Table 3.2 Summary of benchmarking tests

ID	Test Type	Loading
OOP-1	Out-of-plane flexure	Mechanical loading with heated mid-span
OOP-2	Out-of-plane flexure	Mechanical loading with heated centered on load point
OOP-3	Out-of-plane flexure	Mechanical load to ultimate failure
PO-1	Pushout	Composite pushout test (4 studs)
PO-2	Pushout	Composite pushout test (8 studs)
PW-0.60	Pier wall	In-plane shear-flexure (h/l_w = 0.60)
PW-0.75	Pier wall	In-plane shear-flexure (h/l_w = 0.75)
PW-1.00	Pier wall	In-plane shear-flexure (h/l_w = 1.00)
H07T10	Flanged wall	In-plane shear-flexure (h/l_w = 0.99)
H010T05	Flanged wall	In-plane shear-flexure (h/l_w = 1.24)
H010T10	Flanged wall	In-plane shear-flexure (h/l_w = 1.24)
H10T10V	Flanged wall	In-plane shear-flexure (h/l_w = 1.24)
H10T15	Flanged wall	In-plane shear-flexure (h/l_w = 1.24)
H15T10	Flanged wall	In-plane shear-flexure (h/l_w = 1.75)

Table 3.3 Out-of-plane beam specimen details

ID	Beam span (in)	Shear span (in)	b_w (in)	t_{sc} (in)	t_p (in)	ρ (%)	f'_c (psi)	f_y (ksi)
OOP-1	264	96	30	31	1/2	3.2	5,000*	50*
OOP-2	216	72	30	30.6	5/16	2.0	5,000*	50*
OOP-3	105	48	30	30	1/2	3.3	8,200	48.7

* Specified strength

Table 3.4 SC pier wall specimen details

ID	h (in)	l_w (in)	t_p (in)	t_{sc} (in)	f'_c (psi)	f_y (ksi)	Stud dia. (in)
PW-0.60	36	60	0.1875	12	4,982	55.7	0.375
PW-0.75	45	60	0.1875	12	4,000*	55.7	0.375
PW-1.00	60	60	0.1875	12	4,000*	55.7	0.375

* Specified strength

Table 3.5 SC flanged wall specimen details

ID	h (in)	l_w (in)	t_p (in)	t_{sc} (in)	f'_c (psi)	f_y (ksi)	Stud dia. (in)
H07T10	49.2	63.4	0.091	4.53	4308	41	0.354
H010T05		63.4	0.091	9.06	4308	41	0.354
H010T10		63.4	0.091	9.06	4743	41	0.354
H10T10V		63.4	0.091	9.06	4743	41	0.354
H10T15		63.4	0.091	13.58	4308	41	0.354
H15T10		63.4	0.091	9.06	4743	41	0.354

* Specified strength

Table 3.6 Benchmarking analysis modeling properties

ID	Steel mesh size (in)	Conc. mesh size (in)	E_c (ksi)	f_{ctm} (ksi)	w_c (in)	Q_u (kips)
OOP-1	5	3	4,031	0.386	0.0102	20.4
OOP-2	5	3	4,031	0.386	0.0102	20.4
OOP-3	5	3	5,162	0.579	0.0074	20.4
PO-1	1	2	3,694	0.331	0.0115	20.4
PO-2	1	2	3,694	0.331	0.0115	20.4
PW-0.60	1	2	4,023	0.385	0.0102	7.2
PW-0.75	1	2	3,605	0.316	0.012	7.2
PW-1.00	1	2	3,605	0.316	0.012	7.2
H07T10	1.5	1.5	3,002	0.339	0.011	6.4
H010T05	1.5	1.5	3,002	0.339	0.011	6.4
H010T10	1.5	1.5	3,394	0.369	0.011	6.4
H10T10V	1.5	1.5	3,394	0.369	0.011	6.4
H10T15	1.5	1.5	3,002	0.339	0.011	6.4
H15T10	1.5	1.5	3,394	0.369	0.011	6.4

Table 3.7 Summary of experimental and analytical results

	Stiffness comparisons			Peak strengths			Energy
	FE (kip/in)	Exp. (kip/in)	$\frac{FE}{Exp.}$	FE (kips)	Exp. (kips)	$\frac{FE}{Exp.}$	$\frac{Kinetic}{Total}$ %
OOP-1	556	417	1.33	-	-	-	2.31
OOP-2	433	355	1.22	-	-	-	2.17
OOP-3	371	452	0.78	238	250	0.95	7.39
PO-1	1923	1613	1.19	28.3	29.1	0.97	1.23
PO-2	1754	1613	1.09	28.3	29.1	0.97	0.71
PW-0.60	2298	2110	1.09	692.6	719.6	0.96	4.29
PW-0.75	4846	3921	1.24	618.6	618.0	1.00	3.15
PW-1.00	6288	3330	1.89	535.3	489.3	1.09	5.93
H07T10	7688	6001	1.28	1091	1166	0.94	2.95
H010T05	3498	3106	1.13	652	620	1.11	3.88
H010T10	5430	3958	1.37	1148	1039	1.06	2.60
H10T10V	6076	4638	1.31	1149	1229	1.05	0.82
H10T15	7418	5492	1.35	1679	1725	0.97	1.79
H15T10	2564	2378	1.08	1046	990	0.94	4.44

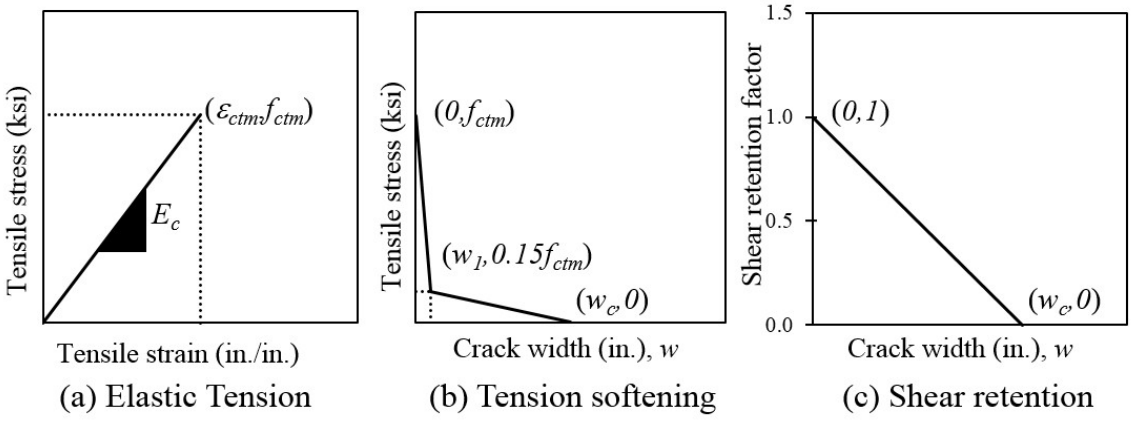

Figure 3.1 Concrete Uniaxial stress-strain and stress-crack opening relationships

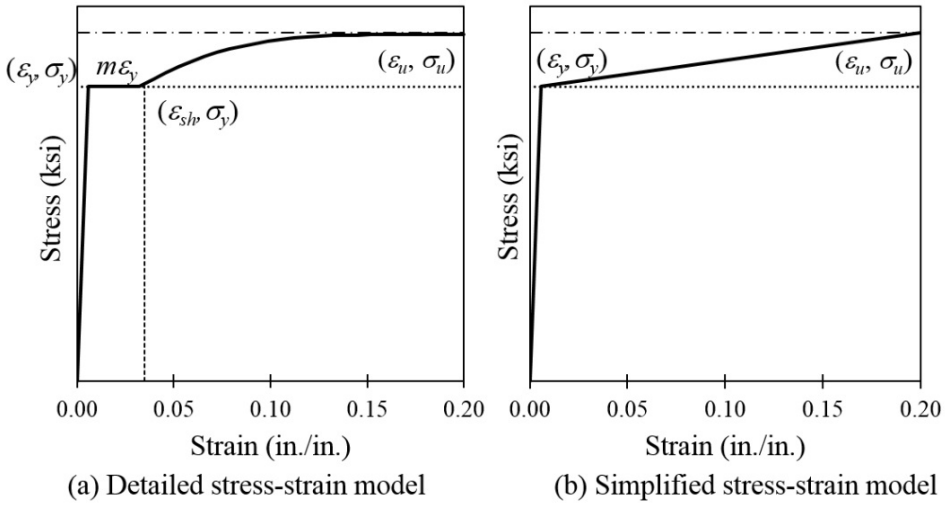

Figure 3.2 Idealized uniaxial steel stress-strain relationships

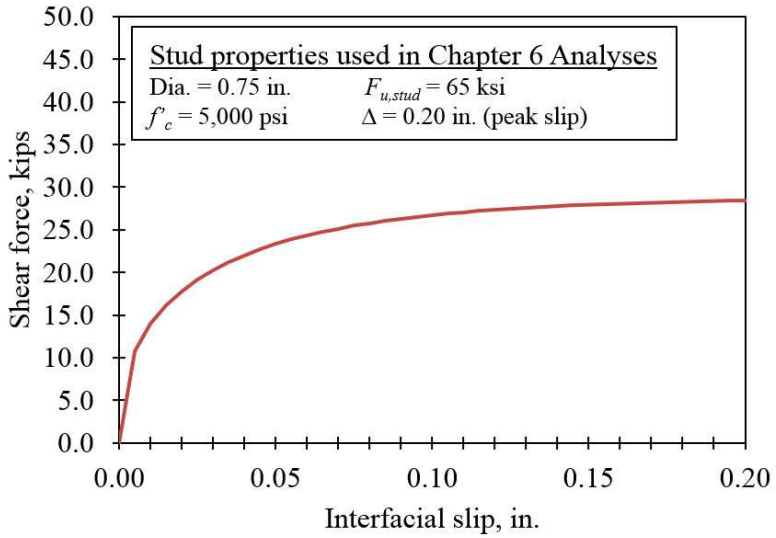

Figure 3.3 Typical Ollgaard et al. [63] headed stud anchor shear force-slip curves

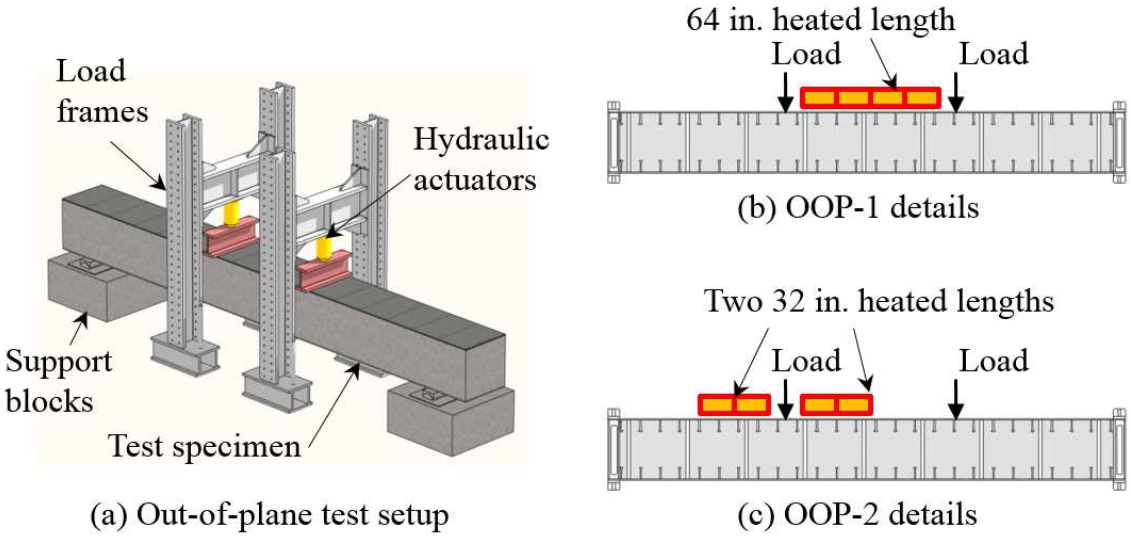

Figure 3.4 Test setup and loading configurations for OOP-1 and OOP-2

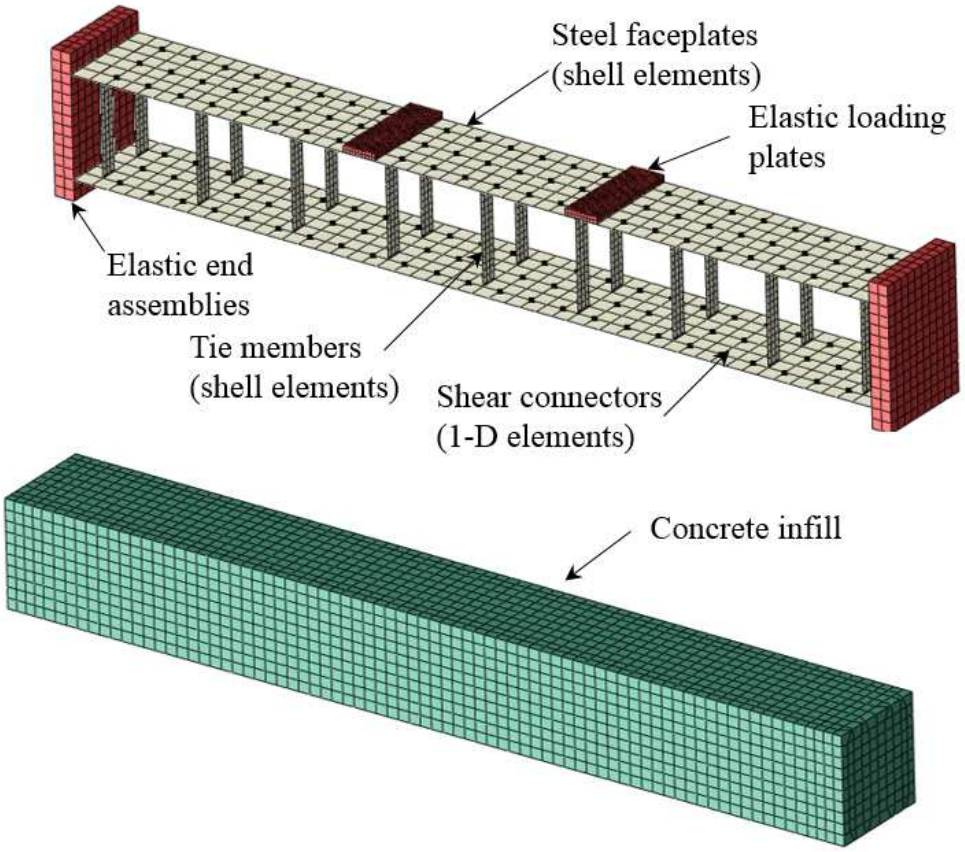

Figure 3.5 OOP-1 and OOP-2 part instances and meshing

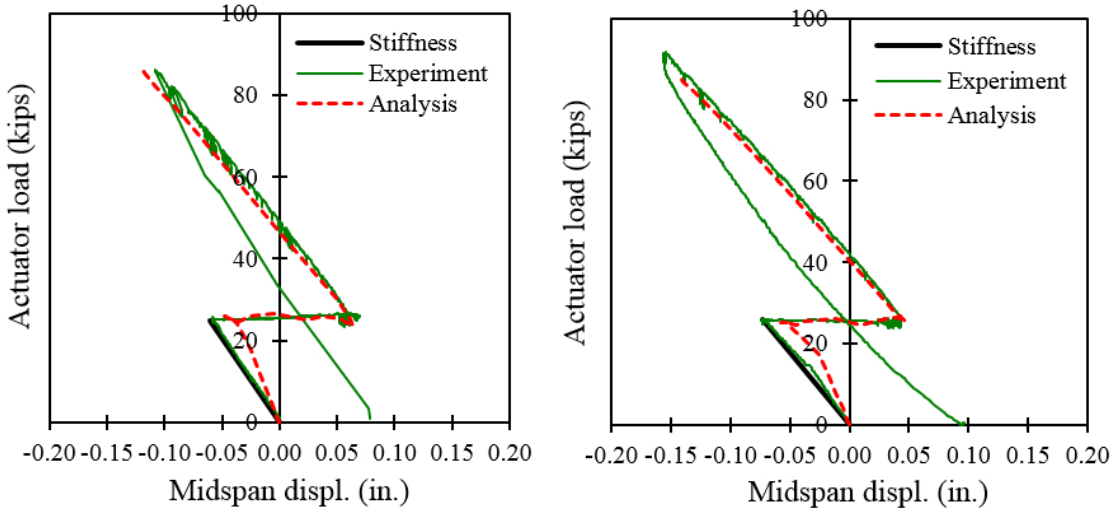

(a) OOP-1 Load-displacement (b) OOP-2 Load-displacement

Figure 3.6 OOP-1 and OOP-2 load-displacement results

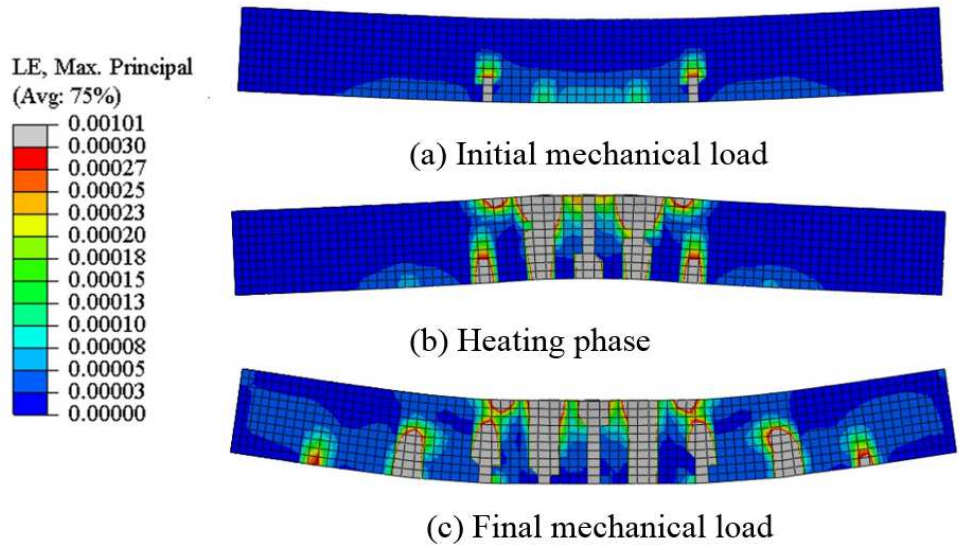

Figure 3.7 OOP-1 maximum principal concrete strains

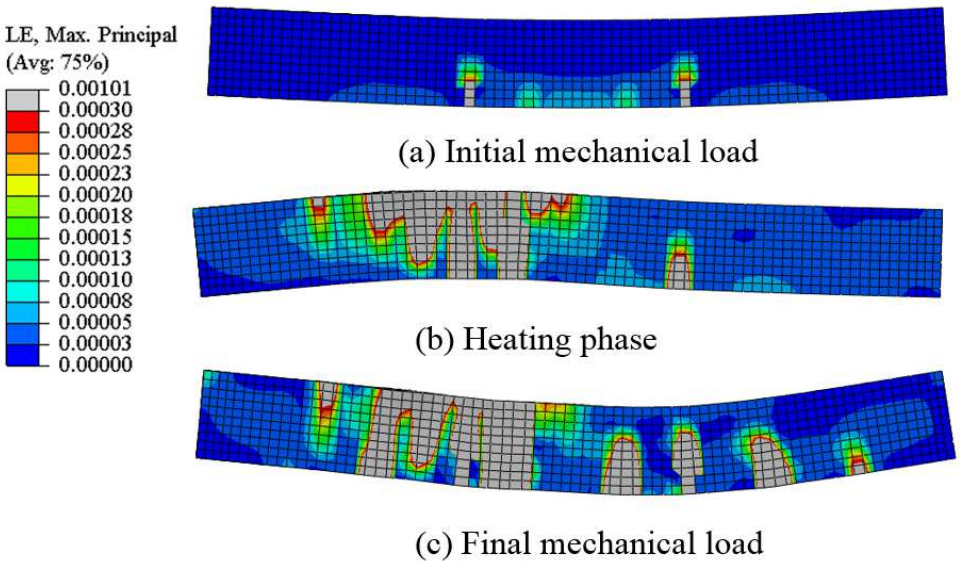

Figure 3.8 OOP-2 maximum principal concrete strains

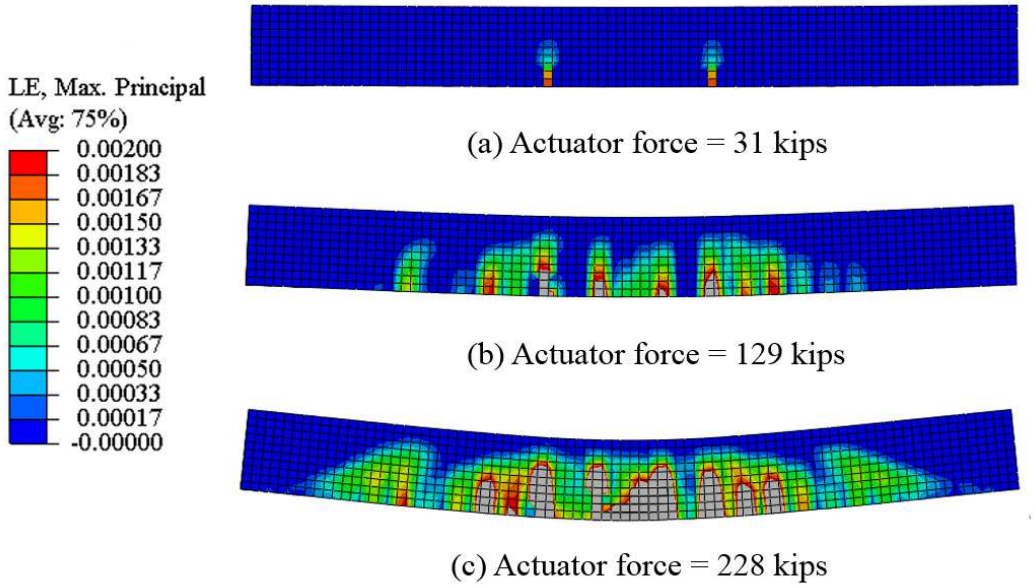

Figure 3.9 OOP-3 maximum principal concrete strains

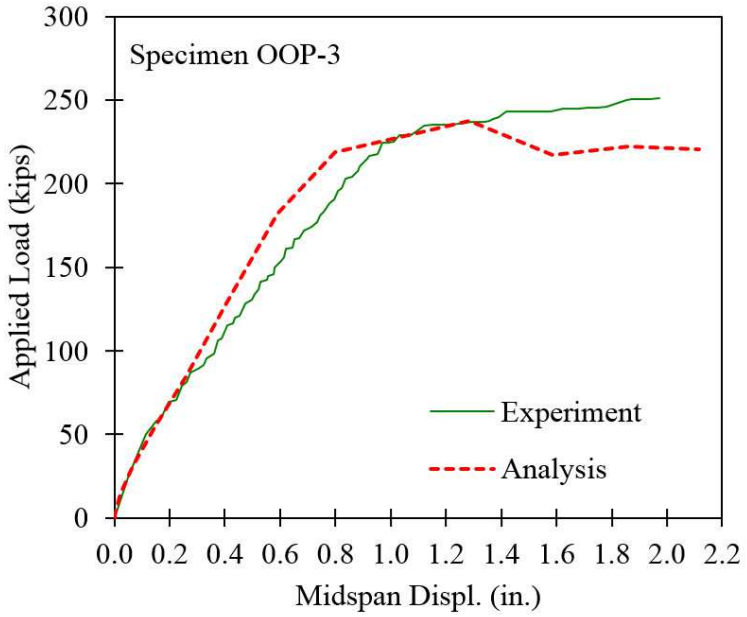

Figure 3.10 OOP-3 load-displacement results

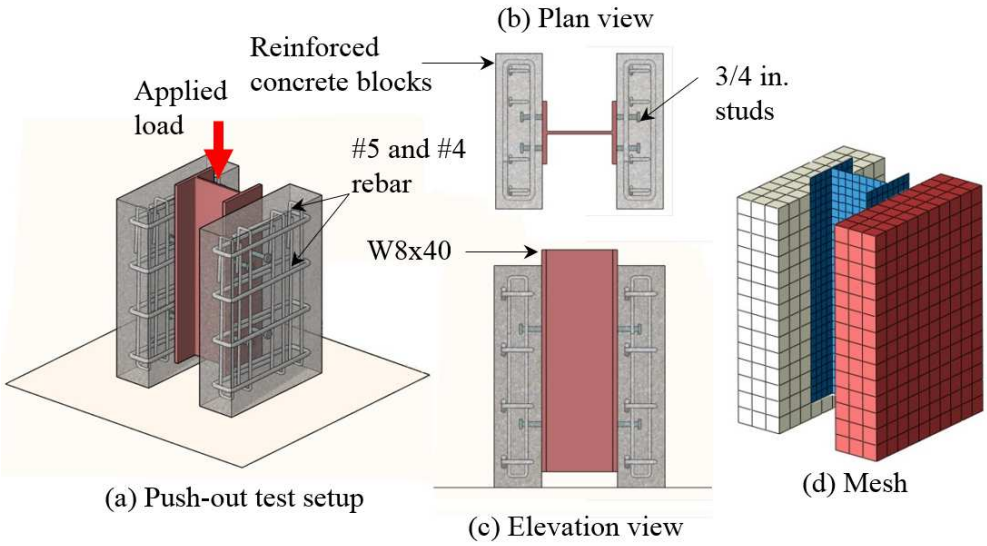

Figure 3.11 Details of Ollgaard et al. pushout tests

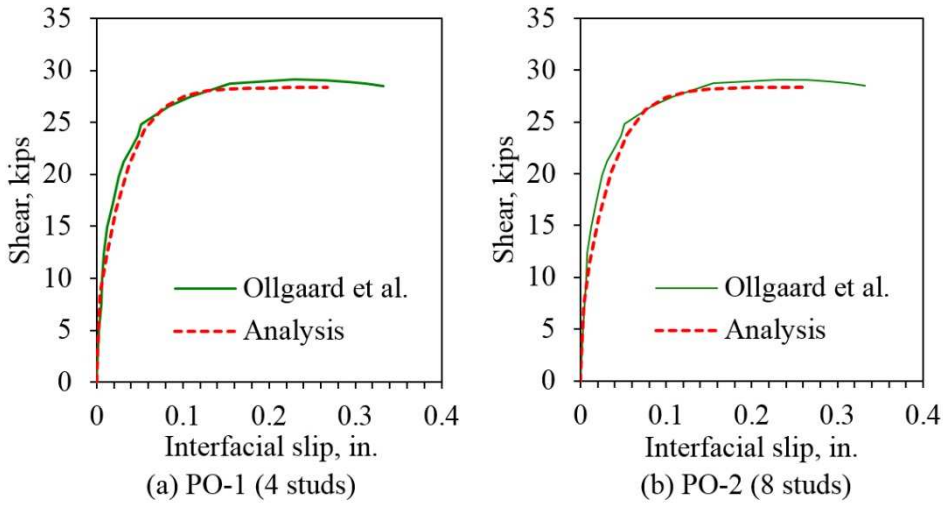

Figure 3.12 Pushout force-slip results

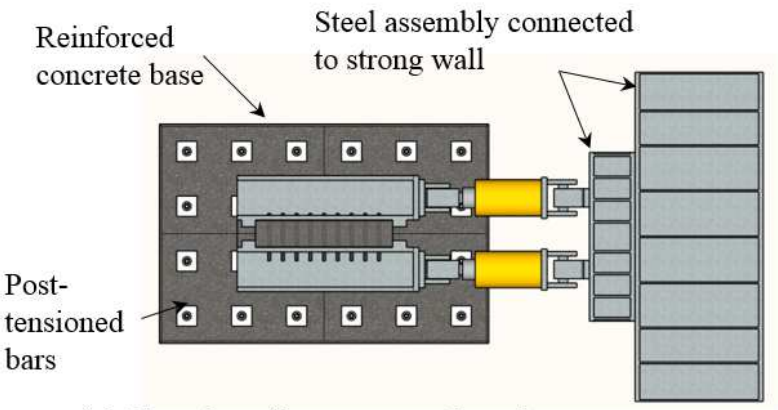

(a) Plan view of test setup and specimen

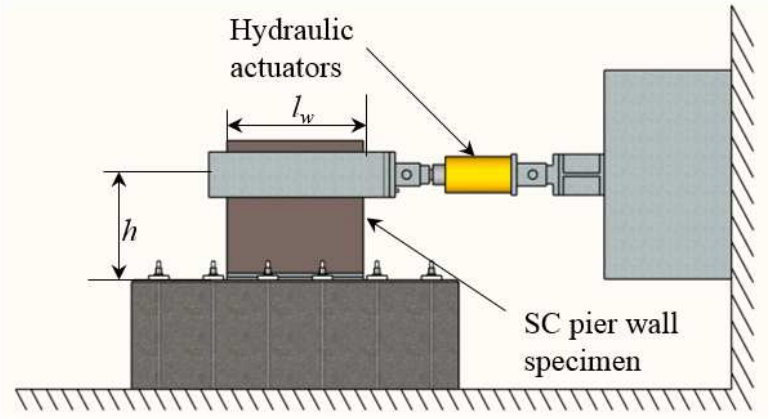

(b) Elevation view of test setup and specimen

Figure 3.13 Plan and elevation views of typical test setup used for in-plane pier tests

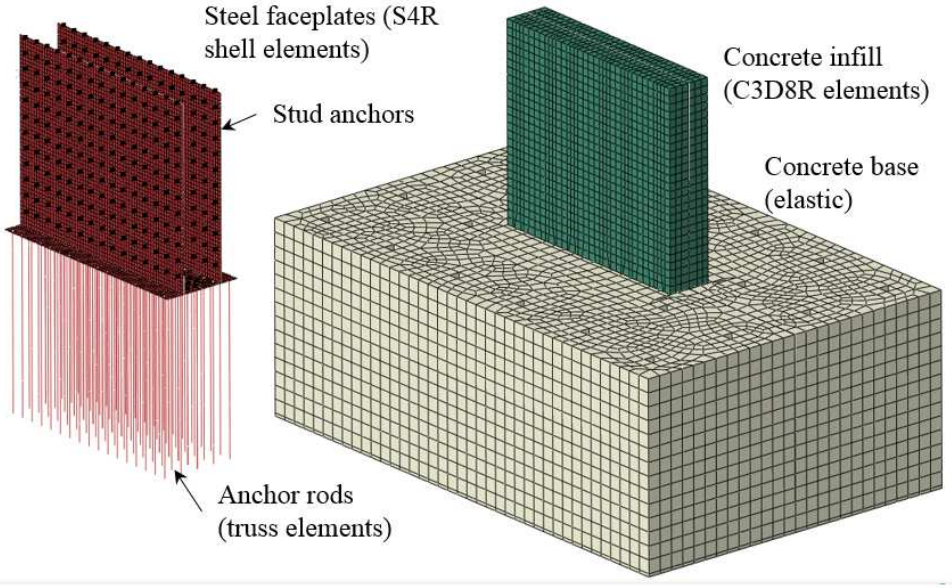

Figure 3.14 Meshing and part instances for finite element benchmarking model

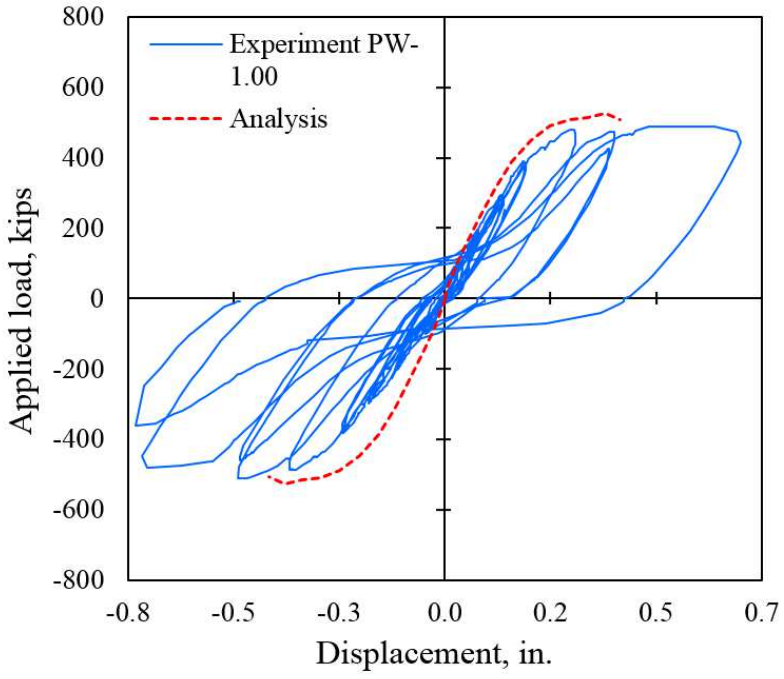

Figure 3.15 Force-displacement curves for PW-1.00

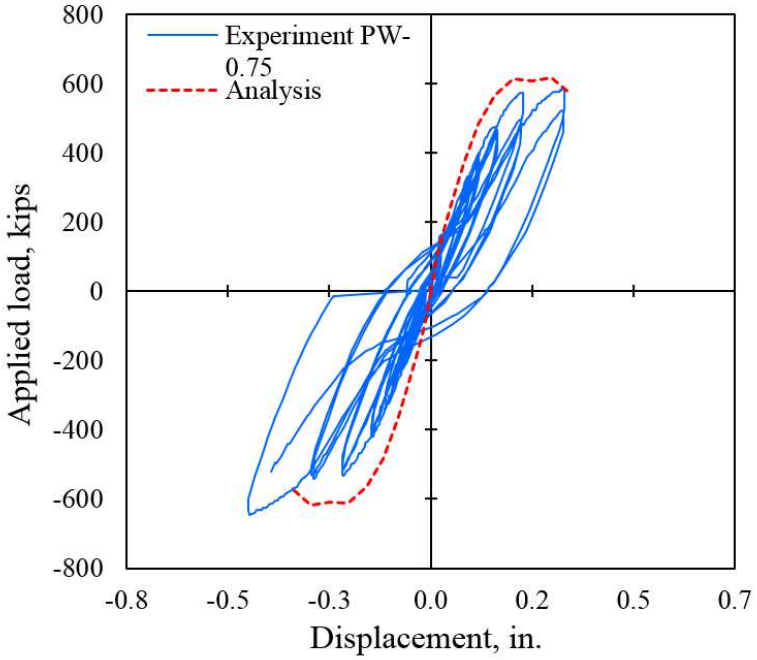

Figure 3.16 Force-displacement curves for PW-0.75

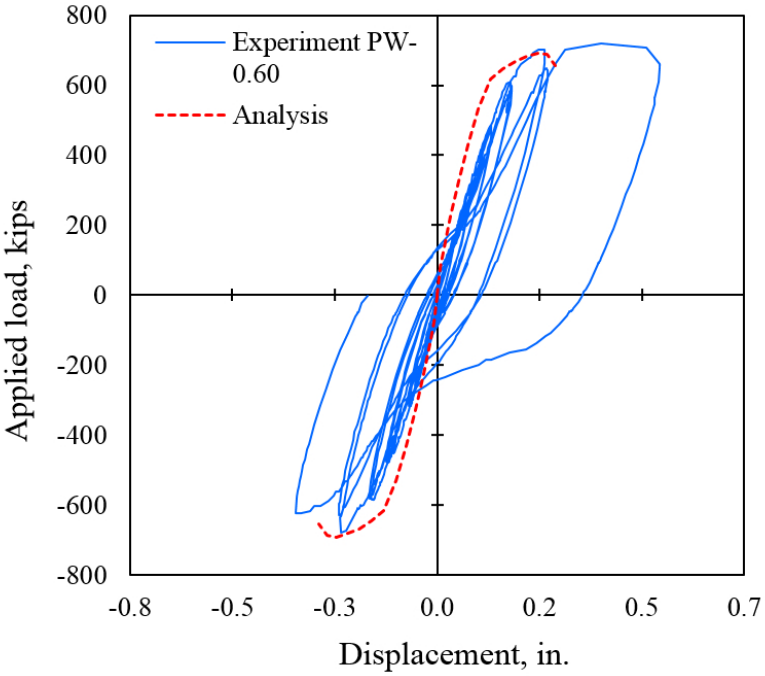

Figure 3.17 Force-displacement curves for PW-0.60

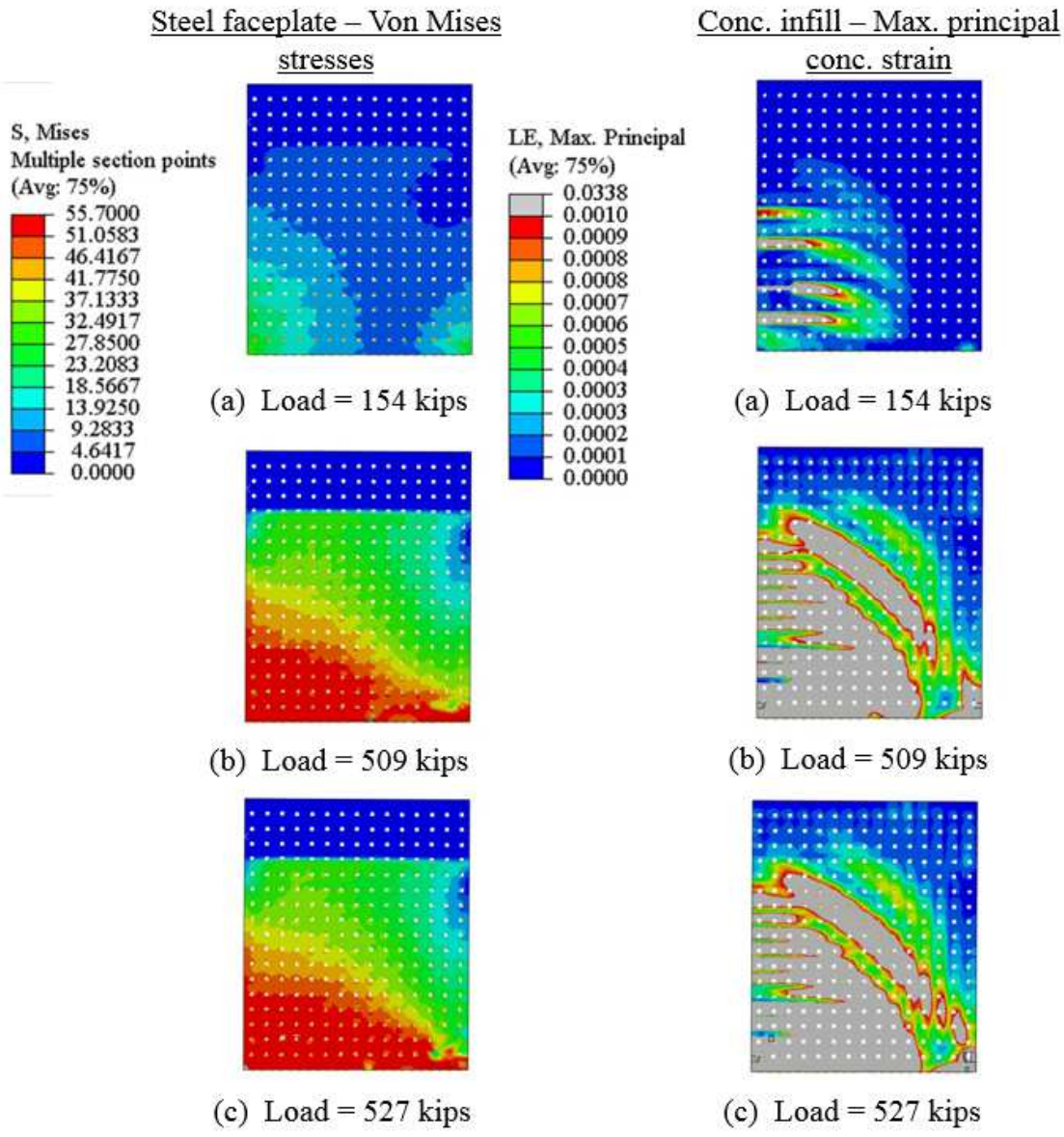

Figure 3.18 PW-1.00 von Mises stress contours and max. principal conc. strains

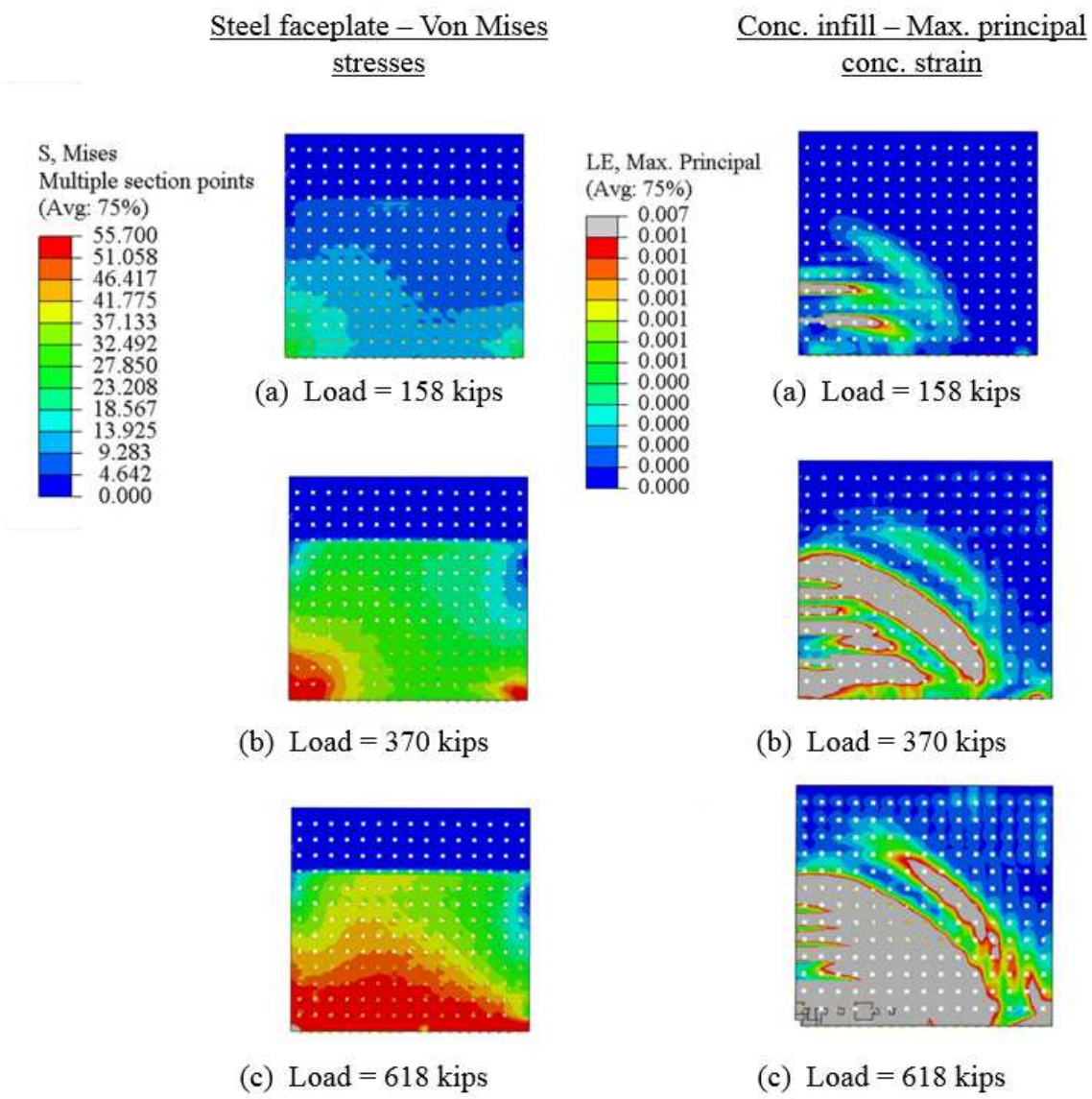

Figure 3.19 PW-0.75 von Mises stress contours and max. principal conc. strains

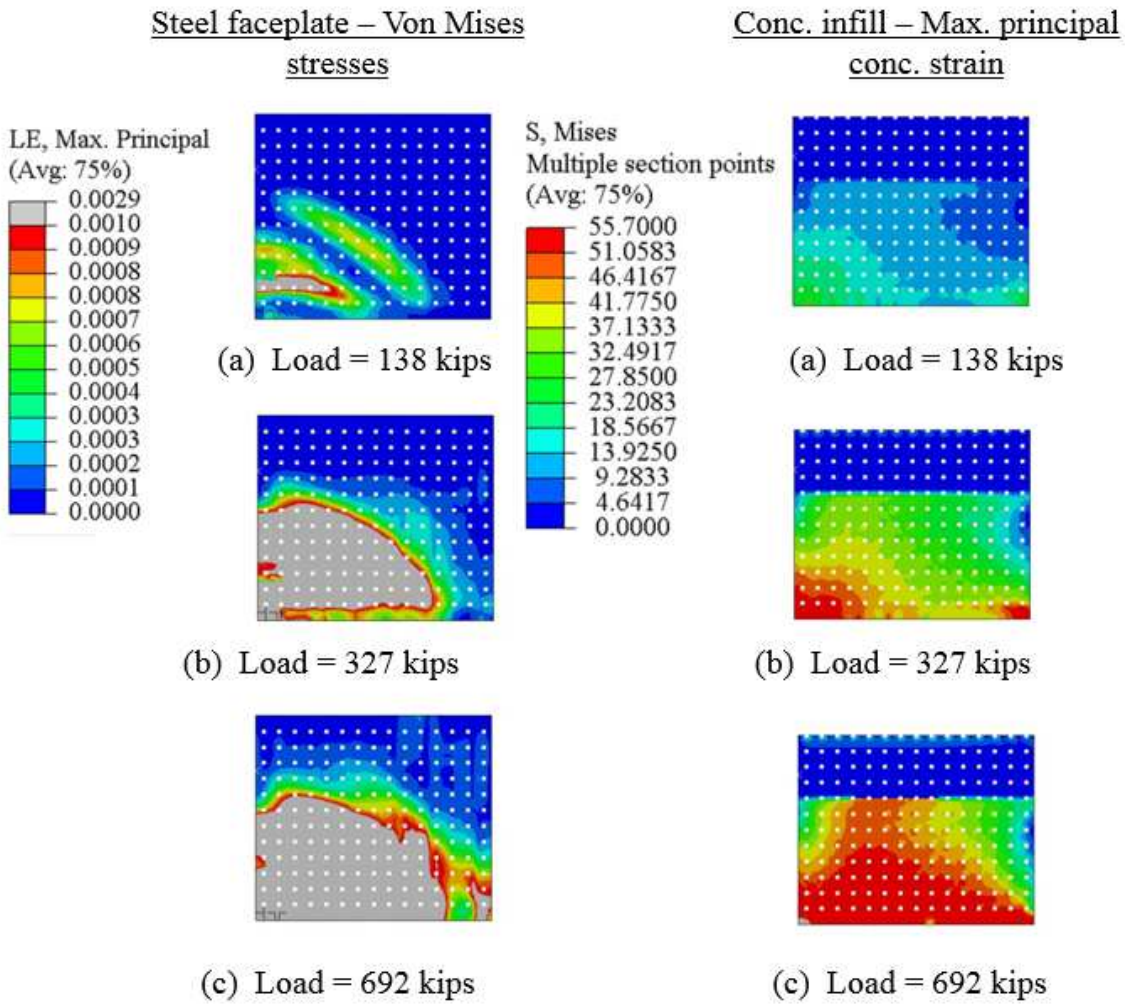

Figure 3.20 PW-0.60 von Mises stress contours and max. principal conc. strains

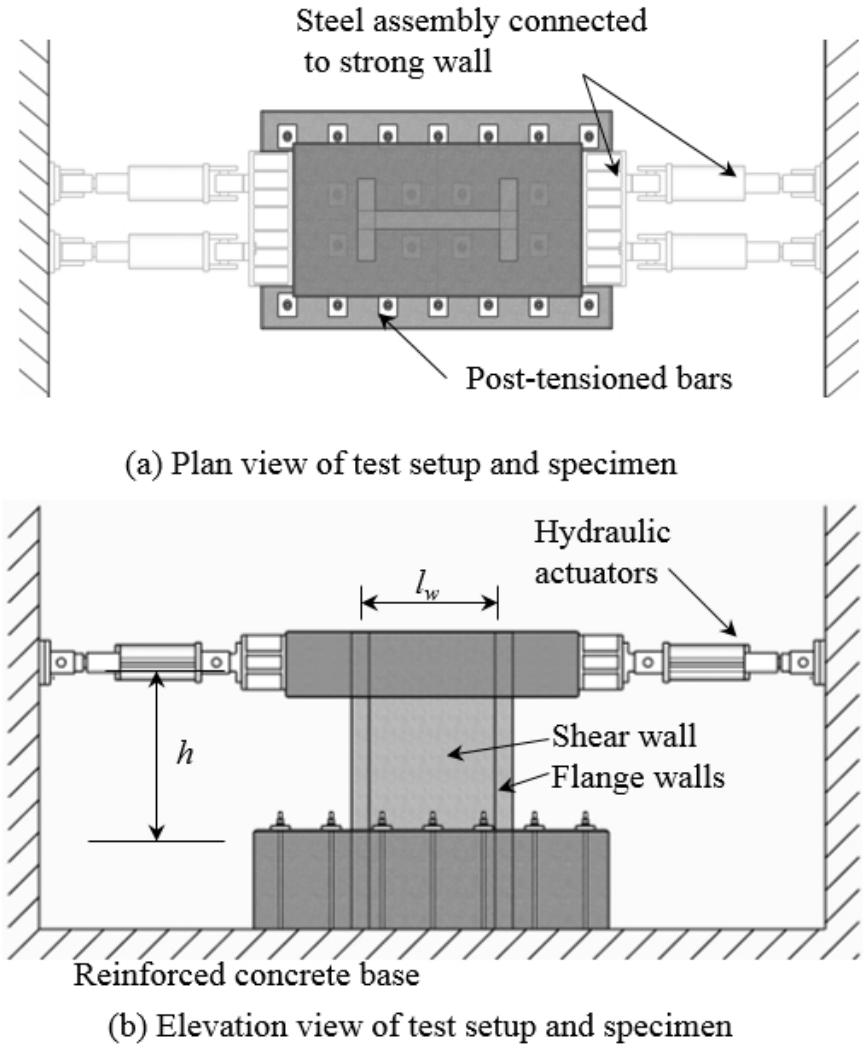

Figure 3.21 Plan and elevation views of SC flanged wall tests

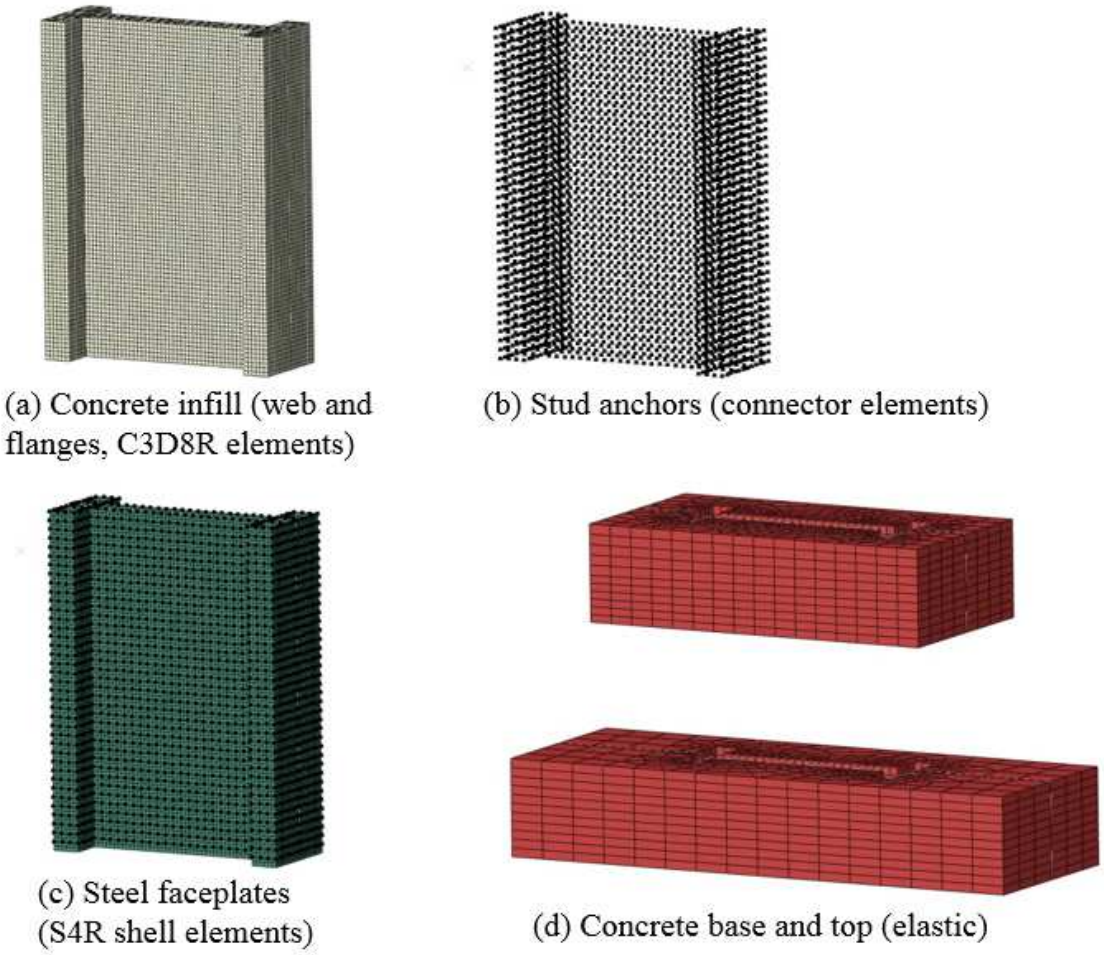

Figure 3.22 Meshing and part instances for SC flanged wall benchmarking analyses

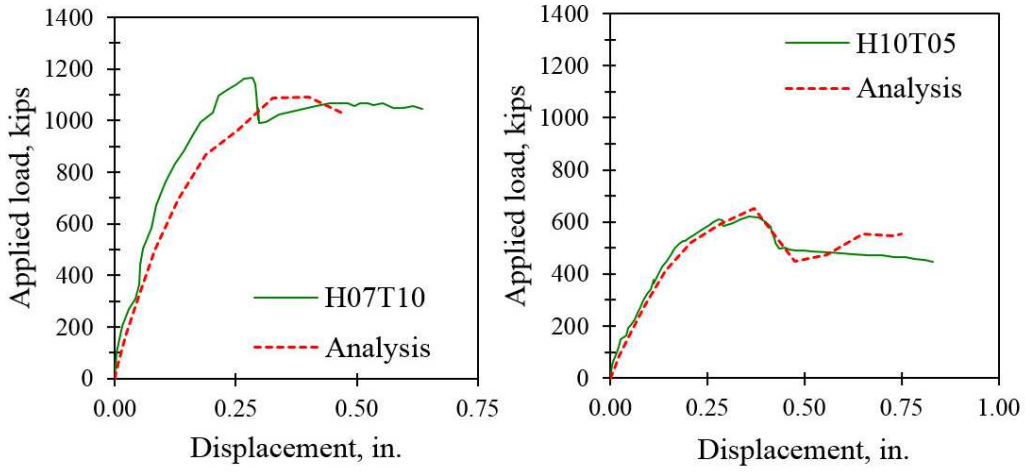

Figure 3.23 Load displacement results for H07T10 and H10T05

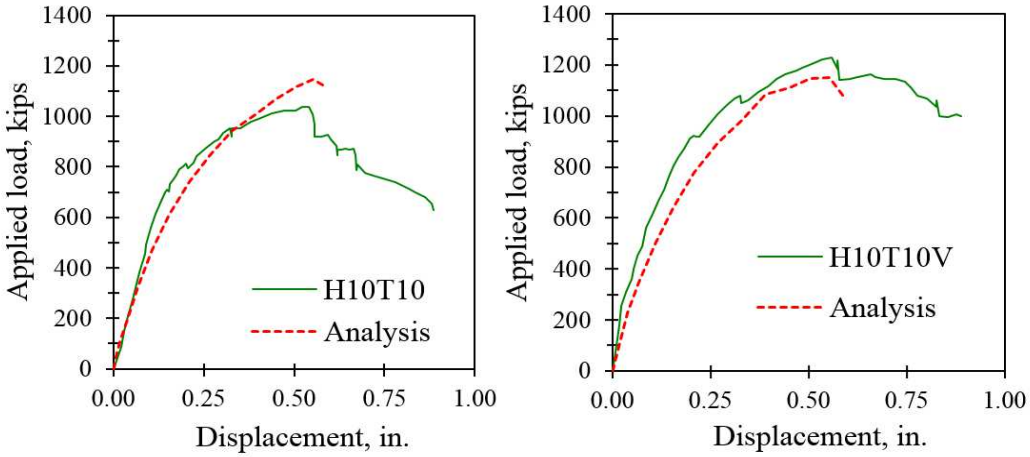

Figure 3.24 Load displacement results for H10T10 and H10T10V

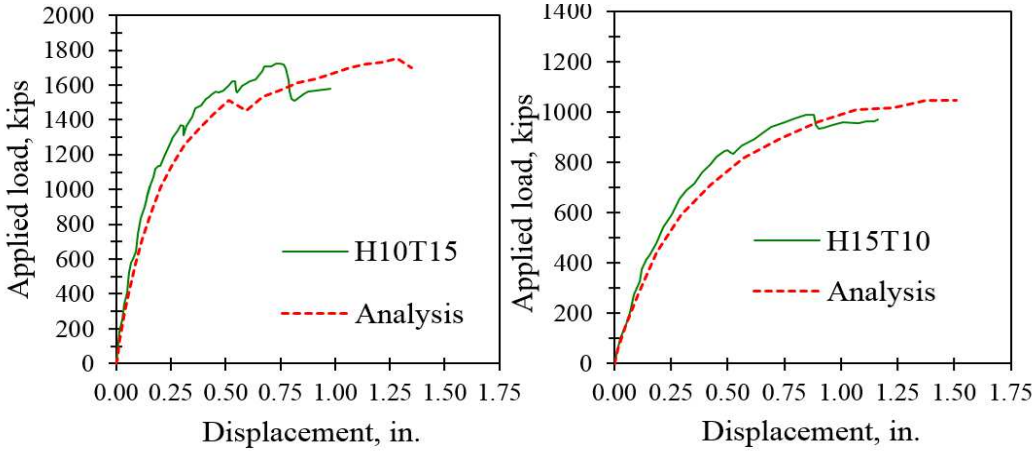

Figure 3.25 Load displacement results for H10T15 and H105T10

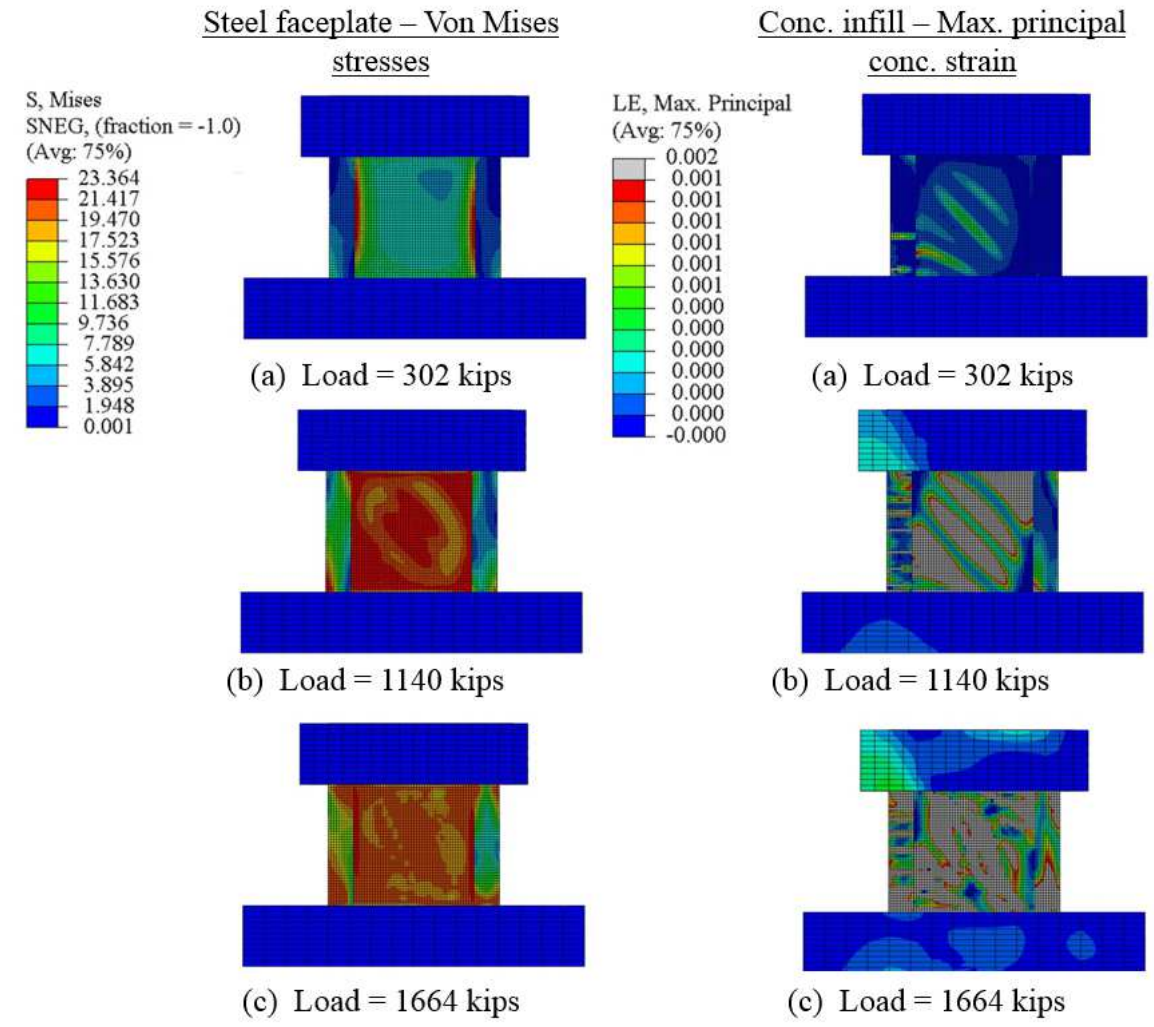

Figure 3.26 H10T15 von Mises stress contours and Max. principal conc. strains

CHAPTER 4. ANALYSIS OF A PRIMARY SHIELD WALL STRUCTURE

This chapter presents the results of an analytical study of a nuclear power plant PSW structure constructed with SC walls. The results of an experimental test of a $1/6^{th}$ scale model of a PSW are used to further benchmark the finite element modeling approach described in the previous chapter. Additionally, the results of the analysis and experimental test are used to develop a design methodology for prediction of the lateral strength of the PSW structure and structures that are similarly configured. A detailed 3-D finite element model is developed so that the detailed lateral load behavior can be studied. The results from the analysis include the full lateral load-deformation response and the progression of mechanical states for increasing load levels including concrete cracking, steel plate yielding and buckling, and development of concrete diagonal compression action within the walls. These results are then compared to results and observations reported from the physical test. The results from the finite element analysis are then used to supplement the findings from the physical test since the analytical results provide additional information that could not be directly determined from the experimental results such as the internal mechanical state of the concrete infill including cracking and compression failure. The analytical results are also post-processed to determine the forces and moments acting on internal cross-sections within the individual wall segments. The findings are then used to develop a simplified method for calculating the design lateral load capacity based on

existing code provisions for reinforced concrete in ACI 349-06 [2]. Also, to complete the design approach, a simplified linear elastic finite element (LEFE) modeling approach is developed and tested that is intended to serve as a more conventional design tool for the determination of design section forces and moments. The results of this approach and application to the PSW structure are then discussed.

4.1 Introduction and background

As briefly described in Chapter 2, physical tests of a 1/6th scale PSW and a 1/10th scale test of a complete containment internal structure were conducted in the 1980s in Japan. These tests were conducted by a joint research program between three agencies: The Japan Atomic Power Co., Obayashi Corp., and Mitsubishi Heavy Industries. Details of the 1/6th scale experiment and supporting analysis were presented in a technical paper presented at the annual meeting of the Architectural Institute of Japan in 2003 by Shodo et al. [5] and the results of the 1/10th scale containment internal structure were presented by Akiyama et al. at the International Association for Structural Mechanics in Reactor Technology Conference (SMiRT-10) in 1989 [7]. At the time of the original experimental tests, the use of SC construction for shield wall structures and other containment internal structures was new and unprecedented. Research on the physical behavior and performance of SC walls and structural members had already been conducted but testing of whole structures was deemed necessary in order to confirm satisfactory performance.

The tested 1/6th scale PSW structure was based on the design of an existing pressurized water reactor (PWR) plant design developed by Mitsubishi Heavy Industries and includes

similarities with subsequent designs for third generation power plants such as the US-APWR [69]. The test specimen and setup are shown in Figure 4.1. The base of the PSW was embedded into a reinforced concrete block that was connected to the laboratory strong floor with post-tensioned bars. This resulted in a fixed base condition where lateral load applied to the top of the specimen resulted in horizontal shear and overturning forces within the PSW that were largest at the connection to the reinforced concrete base. The lateral force, *H*, was applied with hydraulic actuators that were connected to the top concrete loading block, as shown in Figure 4.1. The reinforced concrete base used for the experiment was approximately 20 ft long and the height to the top of the concrete loading block was approximately 12 ft.

In general, the PSW structure resists gravity and lateral loads and provides support for the reactor vessel and mechanical, instrumentation, and hydraulic systems within the power plant. The walls of the PSW are connected together such that they form a closed circle (or polygon) thus isolating and providing radiation shielding between the reactor vessel and the surrounding power plant. All of these critical power plant systems must be supported and connected to the structure and designed to withstand structural loads associated with normal operating and accident conditions. US design codes require that the PSW remains essentially elastic when subjected to external environmental loads (such as earthquake demands) and also demonstrate satisfactory performance in the presence of internal accident thermal loads [70]. The geometry and layout of PSW structures are typically complex with polygonal configurations in plan and numerous perforations and openings in the walls so that plant systems can pass through and connect to other areas of the power

plant. For the PSW structure considered in this work, the openings are sufficiently large and frequent such that they have a significant influence on the overall structural behavior of the PSW.

PSW structures are typically very large and massive. In this case, the SC walls that make up the PSW are on the order of 12 ft thick (in the actual full-scale design). The walls extend from the reinforced concrete basemat up to the elevation of the reactor vessel and extend above to connect to other walls within the containment internal structure. Up to the elevation of the reactor vessel the PSW walls have three layers of steel plates. Two steel faceplates (as is typical for conventional SC walls) and an additional steel plate embedded within the wall in the approximate center. In this design, transverse steel web plates are also embedded in the wall and continuously welded at all edges to the steel faceplates and the interior steel plate. The structural wall is therefore partitioned into individual cells (oriented vertically) that are filled with concrete. This configuration, while quite complex, provides excellent strength to the PSW structure as a whole. The structure has four large openings that extend the full height of the $1/6^{th}$ scale PSW structure. The openings are located in the North-East, South-East, South-West, and North-West corners of the structure and effectively divide the PSW into four individual wall segments. In the actual power plant design, the purpose of the four openings is to provide passages from the reactor vessel cavity to other areas of the plant for the nuclear instrumentation systems. The four wall segments include two on the East and West sides, and one each on the North and South sides, as shown in the figure. Figure 4.2(b) shows a plan view cross-section with the four individual wall segments and the three layers of steel plates and web plates. In the figure,

the middle steel plates are shown in red, and the circular opening in the middle is the reactor vessel cavity. Also, the outer and inner steel faceplates are shown with green and blue lines, respectively. Figure 4.2(a) shows an isometric view of the PSW with concrete omitted for clarity. The typical steel plate thickness for the faceplates and internal embedded plates was 0.1 in., except for the steel plates along the four openings that were equal to 0.17 in. thick (shown in green in Figure 4.2(a)). Also, all of the internal steel surfaces (in contact with concrete infill) were covered with welded headed stud anchors. The spacing of the stud anchors was assumed to be uniform on all internal surfaces.

4.1.1 Experimental 1/6th scale test

The results from the experimental test included measured properties (such as applied force, H, and lateral displacement measured at the loading point, δ) and also numerous qualitative descriptions of the progression of localized failure and damage. The test specimen was subjected to quasi-static cyclic, displacement-controlled loading with load reversals in the negative direction equal to the peak load of each cycle. The loading was applied in the East-West direction. A total of 9 cycles were conducted at progressively increasing load levels until the PSW reached its peak strength. For the first three loading cycles the PSW specimen was subjected to a peak lateral displacement of 0.2 in., followed by subsequent cycles with increasing levels of lateral drift (applied in pairs of cycles of equal displacement) until ultimate failure was achieved during the ninth cycle. The applied lateral loading resulted in combinations of shear, flexure, and axial forces in the four wall segments. The end segments were subjected to axial compression and tension due to the overturning moment. The overturning moment resulted in flexural tension concrete cracking in the end

segments on the tension side of the PSW and at higher force levels, yielding of the steel faceplates. The shear force caused concrete cracking and steel yielding at the base of the middle wall segments and stress concentrations at the corners of the four openings eventually led to localized failure including fracture of the welds and buckling of the steel plates in those areas. The weld fractures were observed at the weld connecting the outer steel faceplates to the web plates that line the openings. The reported observations from Shodo et al. [5] of mechanical behavior from the experiment are listed in Table 4.1 as milestones associated with the listed force levels. The mechanical states listed are a result of global response (such as flexural response due to overturning forces) and also localized behavior such as the failure and damage that occurred at the corners of the four openings. A number of the milestones are duplicated if the behavior was observed in both the positive, West to East (a-direction) or negative, East to West (b-direction) loading directions.

4.2 Finite element analysis of the PSW structure

The finite element analysis consisted of two models: a comprehensive nonlinear inelastic model using the modeling approach developed in Chapter 3, and a simplified linear elastic model intended to be representative of what would be developed for design calculations.

For all of the analyses, the lateral loading was applied to the structure in the East-West direction. For the detailed nonlinear model, two analyses were conducted with different loading protocols: a quasi-static monotonic load up to the point of peak strength and loaded until the structure reached failure, and a second analysis replicating the first three load cycles of the experimental test. Hereafter, the East and West segments are referred as the

end segments and the North and South segments are referred as the middle segments. Since the PSW structure is mirror symmetric about a horizontal line passing through the center of the reactor vessel cavity, the application of lateral load in the East-West direction would result in essentially identical mechanical response in the two middle (North and South) wall segments. Also, it is assumed that the loading is monotonically applied in the West to East direction such that the West wall segment is subjected to vertical tension (in addition to shear and flexure) and conversely, the East wall segment is subjected to vertical compression in order to resist overturning forces. In summary (for the monotonic analysis), the middle wall segments were subjected to shear and flexure, the West wall segment shear, flexure, and axial tension, and the East wall segment was subjected to shear, flexure, and axial compression. Also, the West wall segment is slightly larger than the East wall segment thus slightly altering the response if the loading were applied in the East to West direction.

For the nonlinear and linear elastic models, all of the geometric properties of the PSW were modeled individually with solid elements (C3D8R) for the concrete infill, concrete base block and top loading block, and shell elements (S4R) used for the modeling of the steel faceplates and internal (middle) steel plates and transverse web plates. The part instances (concrete infill, top and bottom concrete blocks, steel plates, and stud connectors) and meshing are shown in Figure 4.3. The composite interaction between the steel and concrete was modeled with with the force-slip model described in Chapter 3 based on the model by Ollgaard et al. [63] assigned to connector elements. Details of the analytical model are listed in Table 4.2. The measured average concrete compressive strength, f'_c, was 4,728

psi, and the average measured yield strength of the steel plates, σ_y, was equal to 67.3 ksi and the ultimate steel strength, σ_u, was assumed equal to 80 ksi. The steel yield and ultimate strengths were assumed to apply uniformly to all of the steel in the model. The uniaxial stress-strain curves for steel are shown in Figure 4.4(b), were the dotted green stress-strain relationship is used in the cyclic analysis and the red line relationship is used in the monotonic analysis (kinematic hardening is used for the cyclic analysis and isotropic hardening is used for the monotonic analysis). The concrete tension softening (stress-displacement) relationship is plotted in Figure 4.4(a).

4.2.1 Analytical results

Figure 4.5(a) shows the lateral load-displacement response from the monotonic analysis, and the envelope of load-displacement response from the experiment. Figure 4.5(a) indicates that the analytical load-displacement response compares favorably with the experimental response including the initial stiffness, post-cracking (or secant) stiffness, and the peak strength the PSW test structure. The analysis results indicate similar (but conservative) post-peak behavior and deformation capacity as the experiment. The peak strength in the analysis (4,500 kips) was achieved at an approximate displacement of 0.63 in., and failure occurred at an approximate displacement of 1.6 in. The test structure had a peak strength of 4,676 kips and slightly more deformation capacity with a displacement of approximately 2 in. at failure.

Figure 4.5(b) show the lateral load-displacement response from the cyclic analysis, and those from the first three cycles of the experiment. The comparison in Figure 4.5(b)

indicates that the analytical load-displacement cycles compare favorably with the experimental response, particularly during the loading phases of the cycles. The analytical load-displacement responses unload linearly, whereas the experimental load-displacement responses unload nonlinearly and have some pinching, thus dissipating slightly more energy. The cyclic analysis results are relevant for their load-displacement characteristics, but not useful for subsequent discussion, which will focus on the structural behavior, progression of yielding and damage, and failure mode of the PSW test structure as predicted by the monotonic (pushover) analysis.

4.2.1.1 Yielding progression of steel plates

The results from the monotonic analysis were post-processed further to evaluate the progression of yielding in the steel plates of the PSW structure. Figure 4.6 shows the von Mises stress contours for the exterior steel faceplates. It includes the stress contour plots for applied lateral loads of 1,000, 2,000, 3,000, 4,000 kips. In the contour plots, the red regions define the highest stress interval such that the average stress in the interval is equal to the yield stress of 67.3 ksi. Therefore, the red regions indicate yielding of the steel plates. Yielding occurred in the exterior steel plate at the corners of the openings (due to stress concentration) and in the middle segment around 3,000 kips of lateral loading. Extensive yielding of the exterior steel plate occurred for 4,000 kips of lateral loading.

Similarly, Figure 4.7 and Figure 4.8 show von Mises stress contours for the middle and interior steel plates. These figures also include the stress contour plate for applied lateral

loads of 1,000, 2,000, 3,000, and 4,000 kips. The red contours once again indicate yielding of the steel plate. Figure 4.7 and Figure 4.8 indicate that yielding occurred in the middle and interior steel plates at the corners of the openings (due to stress concentrations) around 3,000 kips of lateral loading. Extensive yielding of the middle and interior steel plates occurred for 4,000 kips of lateral loading.

Thus, extensive yielding occurred in all three (exterior, middle, and interior) steel plates for 4,000 kips of lateral loading. All three steel plates contributed to the lateral load resistance of the PSW test structure, and yielded extensively before the peak strength was reached at 4,500 kips. This is a significant behavioral insight that was not evident from the experimental results alone. The apparent yielding (and stress concentration) at the corners of the openings also indicates that the four openings have a significant effect on the local response of the structure.

4.2.1.2 Concrete compression struts

Additional post-processing indicated that the wall segments show structural behavior that is similar to typical reinforced concrete squat shear walls (where squat shear walls are defined as walls having an aspect ratio (h/l_w) of less than approximately 1.0) where the overturning moment causes flexural cracking on the tension side, and the shear force causes additional diagonal cracking and compression struts in the concrete infill.

Figure 4.9 shows the minimum principal stresses in the end wall segments (East and West) for lateral load levels of 1,000, 3,000, and 4,000 kips. The figure shows a cross-section of the PSW structure that cuts vertically through the end wall segments. It includes the vector plots of the minimum principal stresses in the concrete infill of the end wall segments. For the applied lateral load of 1,000 kips, diagonal compression struts begin to form in the two end wall segments. The overturning moments the base of the PSW structure causes vertical tension in the West end wall segment and vertical compression in the East end wall segment. This causes flexural tension cracking in the West end wall segment, and the diagonal compression action is more pronounced in the East end wall segment (on the compression side), as shown in Figure 4.9(a). Figure 4.9(b) and (c) show the compression struts in the end wall segments for lateral loads of 3,000 and 4,000 kips, respectively. The compression struts carry higher stresses with increasing lateral load.

Figure 4.10 shows the minimum principal stresses in the middle wall segment for lateral load levels of 1,000, 3,000, and 4,000 kips. The figure shows a section of the PSW structure that cuts vertically through the middle segment. It includes vector plots of the minimum principal stresses in the concrete infill of the middle (South) segment, which was representative of the stresses in both middle segments. As shown in Figure 4.10, lateral loading causes diagonal compression struts to form in the concrete infill of the middle wall segments. These diagonal compression stresses are spread over a wide band and extend from the upper corners on the tension side of the wall segments to the lower corners of the compression sides. For the applied lateral load of 1,000 kips, the diagonal compression stresses in the middle segment (shown in Figure 4.10(a)) are slightly higher than the

diagonal compression stresses in the end segments (shown in Figure 4.9(a)). The peak concrete compression stress in the middle wall segment was about 1,000 psi for an applied lateral load of 1,000 kips. However, as the lateral load increased to 3,000 kips, the diagonal compression struts begin to degrade as concrete cracking increased as the lateral load increased to 4,000 kips, the concrete infill in the middle wall segment had degraded, but the compression struts in the end wall segments were sustained, as shown in Figure 4.9(b) and (c).

4.2.1.3 Strength limit states and failure

The progression of steel plate yielding and concrete diagonal compression provide insight into the behavior and failure modes of the PSW structure. Lateral loading caused an overturning moment and shear at the base of the structure. The overturning moment caused vertical tension and compression in the wall segments, which were resisted by the steel plates and concrete infill, respectively. As the lateral load was increased, flexural yielding of the steel plates occurred in the West wall segment (subjected to tension from the overturning moment).

The shear force was resisted by all the wall segments (middle and end wall segments) by the formation of diagonal compression struts in the concrete and steel plate yielding. As the lateral load was increased, all three steel plates developed yielding at the corners near the opening, and the compression struts in the middle wall segments started degrading. As the lateral load reached 4,000 kips, all the steel plates had yielded extensively, and the

compression struts in the middle segments had degraded. The compression struts in the end wall segments sustained up to the peak strength. The overall failure of the PSW structure was due to the in-plane shear failure of the middle wall segments followed by in-plane shear failure of the end wall segments.

Four of the major milestones from the experimental results are compared with the analytical results in Table 4.3 and Figure 4.11. The milestones (A, B, C, and D) correspond to the experimentally observed milestones: 2(a, b), 5(a, b), 7(a, b) and 10(a) respectively in Table 4.1. From the analysis, flexural tension cracking (Event A) occurred in the West wall segment at a lateral load of approximately 750 kips. Flexural yielding of the exterior steel late (Event B) occurred in the West wall segment at a lateral load of approximately 2,500 kips. Shear yielding of the exterior steel plate (Event C) in the middle wall segment occurred at a lateral load of approximately 3,000 kips. The peak strength (Event D) was achieved in the analysis at a lateral load of 4,500 kips. Overall, the analytical behavior shows reasonable agreement with the major milestones from the experiment. The table includes the ratio of the experimental-to-analytical lateral load corresponding to the occurrence of these milestones. As shown in Table 4.3, the ratio for event A, is equal to 0.86, and for events B, C, and D, the ratios are equal to 0.97, 0.99, and 1.03, respectively.

4.3 Design approach for PSW

The analytical and experimental results provided key insights into the lateral load response of the PSW test structure: (1) All four wall segments contribute to the lateral load resistance and (2) the peak strength is governed by the in-plane shear strength of the middle wall

segments and the end wall segments. As the lateral loading was increased, the PSW structure had a progression of steel yielding and concrete damage leading eventually to structural failure.

4.3.1 Distribution of lateral load resisted to wall segments

The horizontal shear force resisted by each wall segment at the base was calculated by further post-processing the finite element analysis results (stresses in the steel and concrete elements). The proportion of the total lateral load resisted by each wall segment was estimated by dividing the corresponding horizontal shear force with the applied lateral load. Figure 4.12(a) shows the proportion of lateral load resisted by the individual wall segments as the lateral deformation increased. The line for the middle wall segment represents the shear force in one of the two middle segments divided by the total shear force. Figure 4.12(a) shows that all four segments resisted the applied lateral load almost equally (25%) up to a displacement of 0.4 in., which corresponds to lateral load of 4,300 kips (96% of the peak strength of 4,500 kips). The lateral load resistance of the middle segment reduced after this due to the degradation of the compression struts as shown earlier in Figure 4.10(c). As shear failure occurred in the middle wall segments, the lateral load proportion resisted by the end segments increased as discussed and shown earlier in Figure 4.9(c). Thus, the NIFE analysis results indicate that the proportion of the lateral load resisted by the individual wall segments was almost equal up to 96% of the peak load, and varied as the lateral displacements were increased beyond 0.4 in.

An LEFE model of the PSW test structure was developed to represent typical structural analysis design model. The model is geometrically identical to the previously described NIFE model with shell elements used for the steel plates and solid elements used for the concrete regions. The model uses linear elastic material models for the steel and concrete instead of the previously described inelastic models used in the NIFE analysis. The same modulus of elasticity for steel and for concrete are used. For simplicity, a fully-tied interaction condition is used for the steel-concrete interface instead of the previously described composite model used in the NIFE analysis. This LEFE model was analyzed for the same lateral loading as the NIFE model, but the response was linear elastic without any concrete cracking or steel yielding.

The results from the LEFE analyses were post-processed (similar to the NIFE model) to estimate the proportion of the lateral load resisted by the individual wall segments. Figure 4.12(b) shows the estimated proportions of the lateral load resisted by the individual wall segments of the LEFE model. Each of the three lines represent the horizontal shear force resisted by the wall segment divided by the lateral load applied to the structure. Figure 4.12(b) shows that the East, West, and middle wall segments resist 20%, 23%, and 28% of the applied lateral load, respectively. The proportion of the lateral load resisted by the West wall (end) segment is greater than the East segment since it has a slightly larger cross-section. Comparisons between Figure 4.12(a) and (b) indicate that the NIFE and LEFE analyses show comparable distributions of the applied lateral loads to the wall segments, especially for lateral loads up to approximately 4,300 kips, which is close to (96%) of the peak strength. This suggests that in the absence of an elaborate NIFE model and analysis

results, the LEFE model can be used to approximately estimate the proportion of the lateral load resisted by the individual wall segments. The results from the LEFE analysis will be limited by its own assumption, but still useful for design.

4.3.2 Lateral load capacity based on ACI 34-06

Since the lateral load is distributed relatively equally between the four wall segments (each segment resists 25% according to the NIFE model, and 20-30% according to the LEFE model), the design shear strength of the PSW structure can be calculated as the summation of the individual shear strength of the four segments. The structural behavior of all of the SC wall segments was comparable and similar to reinforced concrete squat shear wall behavior (i.e., diagonal cracking and compression struts in the concrete, and steel yielding). Therefore, careful application of the ACI 349-06 [2] code shear strength equations is proposed for the calculation of the shear strengths of the wall segments. The seismic provisions in Chapter 21 of ACI 349-06 provide the following equations for calculating the shear strength of reinforced concrete shear walls:

$$V_n = A_{cv} \cdot \left(\alpha_c \sqrt{f'_c} + \rho_t \cdot f_y \right) \qquad \text{Equation 4.1}$$

$$\alpha_c = 3.0 \text{ for } \frac{h}{l_w} \leq 1.5 \qquad \text{Equation 4.2}$$

$$\alpha_c = 2.0 \text{ for } \frac{h}{l_w} \geq 2.0 \qquad \text{Equation 4.3}$$

In Equation 4.1, A_{cv} is the concrete shear area of the critical section, f'_c is the concrete compressive strength (with psi units), ρ_t is the reinforcement ratio of the horizontal reinforcement, and f_y is the steel yield strength. Equation 4.1 defines the total shear strength

as the sum of individual steel and concrete contributions. The concrete contribution is modified with a coefficient that depends on the overall aspect ratio (h/l_w) of the wall segment. The coefficient α_c, is defined in Equation 4.2 and Equation 4.3. Equation 4.1 was used to calculate the shear strength of the four individual wall segments with A_{cv} defined as the cross-sectional area of each segment. The steel area was defined as the projection of the cross-sectional area of the steel plates (in the wall segments) in the lateral loading direction. The steel plates that were parallel or almost parallel to the lateral load direction were considered effective in resisting shear and included in the calculation of steel area. Figure 4.13(a) shows (in red) the effective lengths of the steel plates that were projected in the direction of lateral loading, and used for the calculation of the reinforcement ratio, ρ_t. Additionally, the thicker steel plates lining the four openings were also included in the calculation of the steel area. Figure 4.13(b) from the NIFE analysis shows that all these effective lengths were fully yielded at the peak strength as assumed in this calculation.

Table 4.4 lists the shear strengths calculated using Equation 4.1 for all of the wall segments. The measured yield strength (f_y = 67.3 ksi) and measured concrete strength (4,728 psi) were used in this calculation. The lateral load capacity ($V_{n\text{-}psw}$) of the PSW structure was calculated as the sum of the shear strengths of the four individual SC wall segments and equal to 4,647 kips. The calculated shear strength of the end wall segments is approximately equal to 50% of the total shear strength and the middle wall segments resist approximately 50%. Figure 4.14 shows a graphical comparison of the calculated lateral load capacity ($V_{n\text{-}psw}$) with the analytical and the experimental lateral load-displacement responses. It also identifies the steel (V_s) and concrete (V_c) contributions to $V_{n\text{-}psw}$. As shown,

the calculated lateral load capacity ($V_{n\text{-}psw}$) is slightly conservative with respect to the experimental strength and marginally higher (1.03) than the analytical strength. The calculated steel shear strength contribution (V_s) is much greater than the calculated concrete shear strength contribution (V_c). This is due to the very large quantity of steel plates in the PSW structure.

ACI 349-06 also specifies an upper bound on the shear strength equal to $8 \cdot A_{cv} \cdot \sqrt{f'_c}$. Where A_{cv} is taken as the sum of the concrete areas of the four wall segments. This upper bound is placed to account for failure modes such as sliding shear or diagonal compression failure, which were not observed for the PSW test structure. As shown in Figure 4.14, this limit is not applicable, and therefore very conservative for the PSW test structure with the multiple steel plates and web plates resulting in the multi-cellular layout shown in Figure 4.2(a).

4.3.3 Design overturning moment

The lateral load capacity of the PSW structure is governed by the shear failure and strength of the wall segments. However, the overturning moment (at the base) caused by the applied lateral load must also be checked. The overturning moment at the base (M_{OTM}) is equal to the lateral load capacity ($V_{n\text{-}psw}$) multiplied by h, the distance from the critical section at the base which is the elevation of the applied lateral load. As shown in Figure 4.15, this total overturning moment is resisted by two primary mechanisms: (i) individual frame-action bending of the wall segments, and (ii) the force couple developed by the vertical axial forces in the two end segments.

The results from both the NIFE analysis and the LEFE analysis were post-processed to determine the portion of the total overturning moment resisted by the individual wall segments, and by the axial force couple between the two end segments. Figure 4.16 shows the results of this evaluation. It includes in Figure 4.16(a) the proportion of the total overturning moment resisted by the wall segments and the axial force couple from the NIFE analysis. Similarly, Figure 4.16(b) shows these proportions from the LEFE analysis. Despite of the inherent limitations, the results from the LEFE analysis are comparable to those from the NIFE analysis. Both analyses indicate that approximately 60% of the overturning moment is resisted by the axial force couple in the end wall segments. Approximately 10% of the overturning moment is resisted by each middle segment, and approximately 10% of the overturning moment is rested by the end wall segments.

The overturning moment at the base corresponding to the lateral load capacity ($V_{n\text{-}psw}$) of the wall, and the proportions from the LEFE analysis (Figure 4.16(b)) were used to estimate the axial force and bending moment demands (P_r, M_r) for each of the wall segments. Additionally, the axial force-bending moment (P-M) capacity interaction curves for each SC wall segment were calculated using the plastic stress distribution method in AISC 360-10 Chapter I2.2a [65], which was implemented using a section fiber analysis approach due to the complexity of the segment cross-sections. The approach assumes that all of the steel on the cross-section has reached a state of yield and that the concrete on the compression side of the neutral axis (over a length of defined as the distance from the extreme compressions fiber to the neutral axis multiplied by β_1) has reached the concrete stress limit of $0.85f'_c$. The concrete section stress on the tension side of the neutral axis is equal to zero

and therefore considered fully cracked. Figure 4.17 shows the full P-M interaction curve developed for the middle segment. The fiber model was generated in a spreadsheet program with fiber layers assigned to rows in the spreadsheet program. In the figure the interaction curve is plotted with a series of points each representing a different value for the neutral axis depth. Three data points are also shown in Figure 4.17 that represent three different combinations of axial force, *P*, and moment, *M*. The fiber model results for these three points are shown in Figure 4.18, Figure 4.19, and Figure 4.20, respectively. In the three figures, the section bending stresses are plotted (shown in (a) and (b) in each figure). The concrete stresses are all limited to 0.85(4,728 psi) = 4,019 psi, and the steel stresses are limited to the yield, 67.3 ksi. In the three figures, (c) shows the fiber model concrete cross-section were the cells that are filled in with ones represent the compression region and the blank cells represent the tension side of the neutral axis. The area for each cell is defined as the total gross uncracked area of the segment divided by the number of cells. Therefore, the concrete fiber force for each cell can be calculated by multiplying the fiber stress by the area of the given fiber. A similar process is implemented for the steel on the cross section and the forces from the steel and concrete fibers are summed to get the total force for each fiber. The axial force, *P*, for the whole section is then equal to the summation of all of the individual fiber forces. Each fiber force is then multiplied by the distance from the respective fiber to the centroid of the gross cross-section. These values are then summed up for all fibers to determine the total section moment, *M*. The fiber forces for the concrete are plotted for the three sections in Figure 4.18(d), Figure 4.19(d), and Figure 4.20(d).

The resulting *P-M* capacity interaction curves for each of the wall segments are shown in Figure 4.21 along with the corresponding axial force and bending moment demands (*Pr, Mr*). As shown, the axial force and bending moment demands for all of the segments are within their *P-M* interaction curves.

As expected, the individual wall segments of the PSW structure did not fail due to the axial forces and bending moments induced by the overturning moment. The lateral load capacity of the test structure was governed by the shear strength of the wall segments. However, the evaluation presented is useful for design, where the lateral load capacity of a PSW structure should be checked for all internal forces including the axial force, bending moment, and shear force in the individual wall segments.

4.4 Summary and conclusions

This chapter presented the development and benchmarking of a 3-D NIFE model for predicting the lateral load behavior and strength of a complex PSW test structure consisting of very thick SC walls with three (exterior, middle, and interior) steel plates. The PSW structure had large openings, which divided the structure into four walls segments: two end segments (East and West) and two middle segments. A $1/6^{th}$ scale physical model of the PSW structure was tested in Japan and the experimental results were used to benchmark the model and analysis results. The 3-D NIFE model accounted for various complexities of behavior including steel plate yielding and buckling, concrete cracking and the composite interaction between the steel plates, concrete infill, and shear studs. The models were developed and analyzed using Abaqus/Explicit with quasi-static cyclic and

monotonic loadings. The 3-D NIFE model was analyzed for monotonically increasing lateral loading (under deformation control), and also analyzed for the first three cycles from the cyclic loading protocol for the test. The results from the monotonic analysis compared favorably with the envelope of the lateral load deformation response from the experiment. The results from the cyclic analysis also compared reasonably with the cyclic hysteresis load-deformation responses from the experiment. The NIFE model results were post-processed to establish the occurrence of major milestones or events along the load-deformation response such as flexural cracking of concrete, flexural yielding of the steel plates, shear yielding of the steel plates, peak strength, and deformation capacity before failure. The lateral loads corresponding to the occurrence of these major milestones were compared with those observed during the test and reported by Shodo et al. [5]. These comparisons benchmarked the 3-D NIFE model and established its accuracy for predicting the lateral load-deformation response of the tested $1/6^{th}$ scale PSW structure.

The analytical results provided significant insight into the behavior of the PSW structure. All three (exterior, middle, and interior) steel plates yielded extensively just before the peak strength was reached. The concrete infill of the wall segments developed diagonal cracks and inclined compression struts as the lateral load was increased. The peak strength was reached due to the yielding of the plates and the degradation of the compression struts in the concrete infill. The compression struts in the middle segments started degrading earlier than those in the end segments. Overall, the behavior of the wall segments of the PSW structure was similar to that of reinforced concrete squat shear walls.

The NIFE model results were post-processed further to estimate the proportion of the lateral load resisted by the individual well segments. This evaluation indicated that the proportion of the lateral load resisted by the individual wall segments in shear was almost (approximately 25% for each wall segment) equal up to 96% of the peak load, and varied as the lateral displacements were increased beyond 0.4 in. Since the lateral load was distributed relatively equally between the four segments, the lateral load capacity of the PSW structure was calculated as the sum of the shear strengths of the individual wall segments. Since the behavior of the individual wall segment was similar to that of reinforced concrete squat shear walls, the ACI 349-06 code equations (from Chapter 21) for calculating the shear strength of shear walls were used to estimate the shear strength of the individual wall segments. These equations included the contributions from both the steel reinforcement (plates) and concrete infill. The calculated lateral load capacity ($V_{n\text{-}psw}$) compared favorably with the experimental and analytical peak strengths.

The NIFE model results were post-processed further to estimate the proportion of the total overturning moment at the base resisted by the individual wall segments and the axial force couple in the end wall segments. This evaluation indicated that 60% of the overturning moment was resisted by the axial force couple in the end segments, approximately 10% was resisted by each of the middle segments, and 10% by the end wall segments. These proportions and the lateral load capacity, $V_{n\text{-}psw}$, were used to estimate axial force and bending moment demands (P_r, M_r) at the base of the individual wall segments. These demands were compared with the *P-M* interaction curves developed for the individual wall segments using the plastic stress distribution method. As expected, the individual wall

segments of the PSW structure did not fail due to the axial forces and bending moment induced by the overturning moment at the base. The lateral load capacity of the test structure was governed by the shear strength of the wall segments.

3-D LEFE models were also developed for the PSW test structure. These models were geometrically identical to the NIFE models including the steel plates and concrete infill. However, there was no concrete cracking, steel inelasticity, or slip between the steel and concrete in this LEFE model. The model was analyzed for the same lateral loading, and the results were post-processed and compared with those from the NIFE model. These comparisons indicate that in spite of the limitations, the LEFE model can reasonable estimate: (i) the proportion of the lateral load resisted by the individual wall segments in shear and (ii) the axial forces and bending moments at the base of the individual wall segments. This is particularly useful for design because in the absence of an elaborate NIFE model and analysis results, the LEFE model can be used to estimate the force demands (axial force, bending moment, and shear force) for the individual wall segments for various load combinations. These design force demands can then be compared with the calculated shear strength and the P-M interaction curve for the individual wall segments.

Table 4.1 Summary of 1/6th scale PSW test behavior milestones (Shodo et al. [5])

Number	Description	Force level (kips)
1a	Concrete cracking at corner formed by opening	290
2a	Flexural tension concrete cracking at base of East wall segment	560
2b	Flexural tension concrete cracking at base of East end segment	726
3a	Concrete shear cracking in middle segments	565
4b	Shear yielding at corner formed by opening (interior steel plate)	2,067
5a	Flexural yielding at end segment	2,165
5b	Flexural yielding at end segment (exterior steel faceplate)	2,700
6a	Shear yielding on tension side (exterior steel faceplate)	2,454
7a	Shear yielding in middle segment (exterior steel faceplate)	3,060
7b	Shear yielding in middle segment (exterior steel faceplate)	2,859
8a	Steel local buckling at corner of opening (exterior steel faceplate)	4,383
9a	Steel local buckling at corner of opening (exterior steel faceplate)	4,612
10a	Peak strength	4,676
11a	Weld fracture at corner formed by the opening	4,636

Table 4.2 1/6th scale PSW analytical model properties

Steel typical element size	3 in.
Concrete infill typical element size	3 in.
Element sizes for base and loading block	Variable
Concrete material properties	f'_c = 4,728 psi E_c = 3,920 ksi w_c = 0.01 in. f_{ctm} = 0.37 ksi G_F = 0.78 lb./in. d_{max} = 0.2 in.
Steel material properties	σ_y = 67.3 ksi σ_u = 80.0 ksi ε_u = 0.20 n = 6
Stud anchor properties	Stud dia. = 0.15 in. Stud spacing = 1.3 in. Q_u = 1.15 kips (per stud)

Table 4.3 Experimental and analytical milestones

Events	Exp. force level (a-dir.), kips	Exp. force level (b-dir.), kips	Average exp. force, kips	Analytical force level, kips	$\frac{\text{Exp.}}{\text{Analysis}}$
A	560	726	643	750	0.86
B	2,165	2,700	2,433	2,500	0.97
C	3,060	2,859	2,960	3,000	0.99
D	4,676	NA	4,676	4,500	1.03

Descriptions of events:

(A) Flexural tension concrete cracking in end segments
(B) Flexural tension yield of the exterior steel plate in the end wall segment
(C) Shear yield of the steel plate in the middle wall segment
(D) Peak PSW strength

Table 4.4 Calculated segment shear strengths

Segment location	Proj. steel area, A_s, in.^{2}	Conc. area, A_{cv}, in.^{2}	$V_s = \rho_t \cdot fy \cdot A_{cv}$, kips	$V_c = \alpha_c \cdot (f'_c{}^{0.5}) \cdot A_{cv}$, kips	$V_n = V_s + V_c$, kips
East	14.1	1,132	950	156	1,106
Middle	15.1	719	1,013	148	1,162
West	15.5	1,250	1,045	172	1,217
Total, $V_{n\text{-}psw}$					4,647

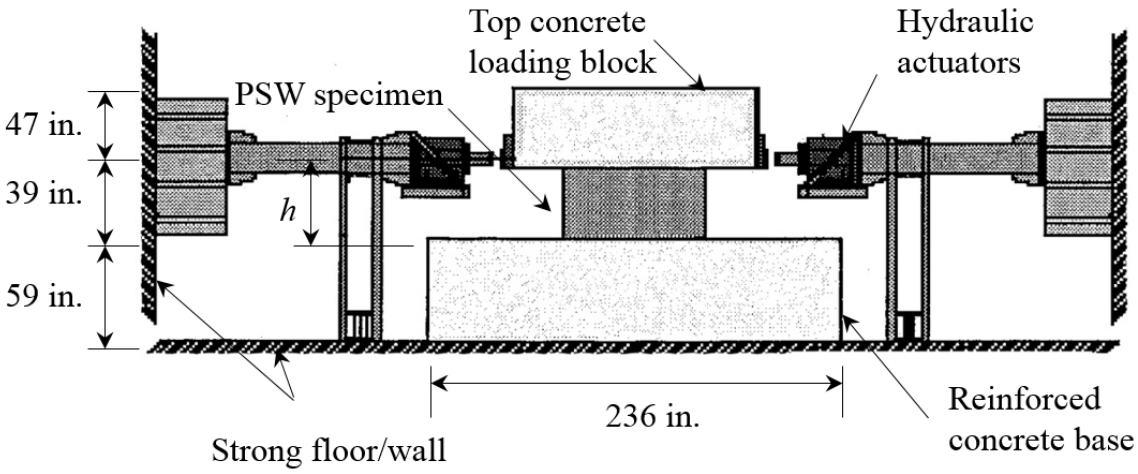

Figure 4.1 Test setup for 1/6th scale PSW test (Shodo et al.[5])

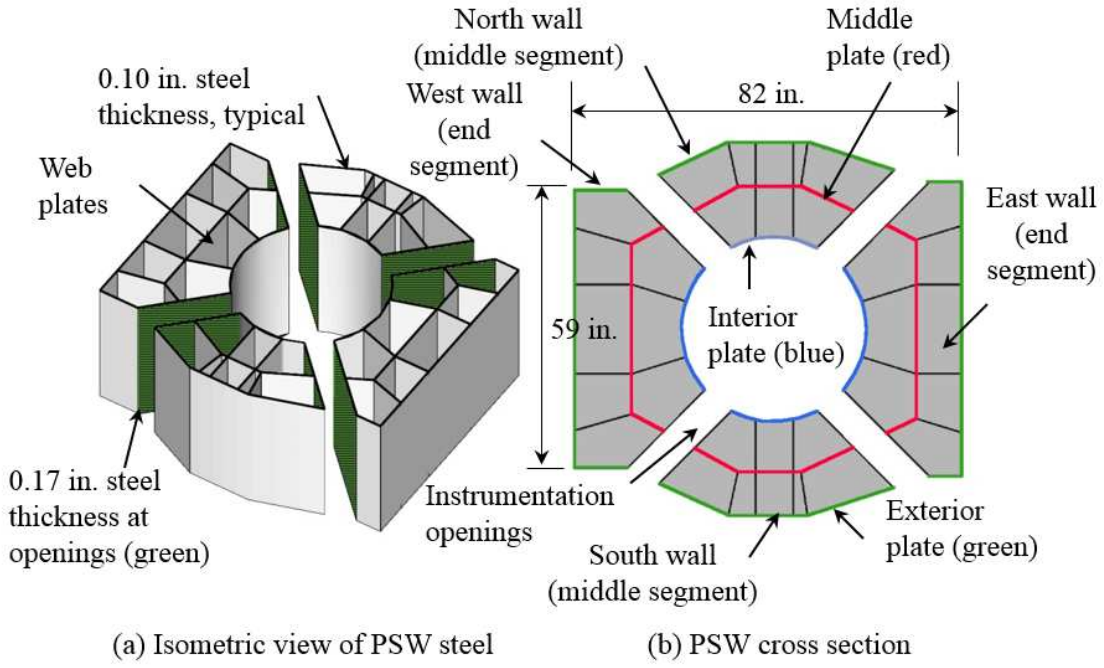

Figure 4.2 PSW details and dimensions

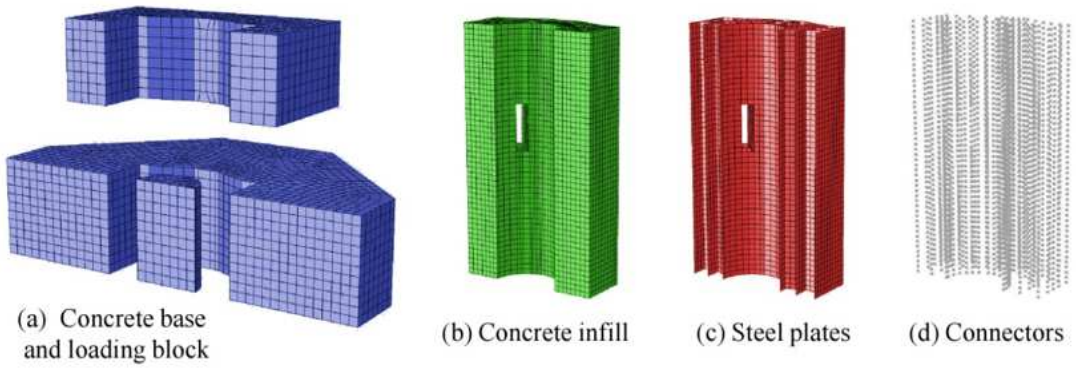

Figure 4.3 Meshing and part instances for PSW model

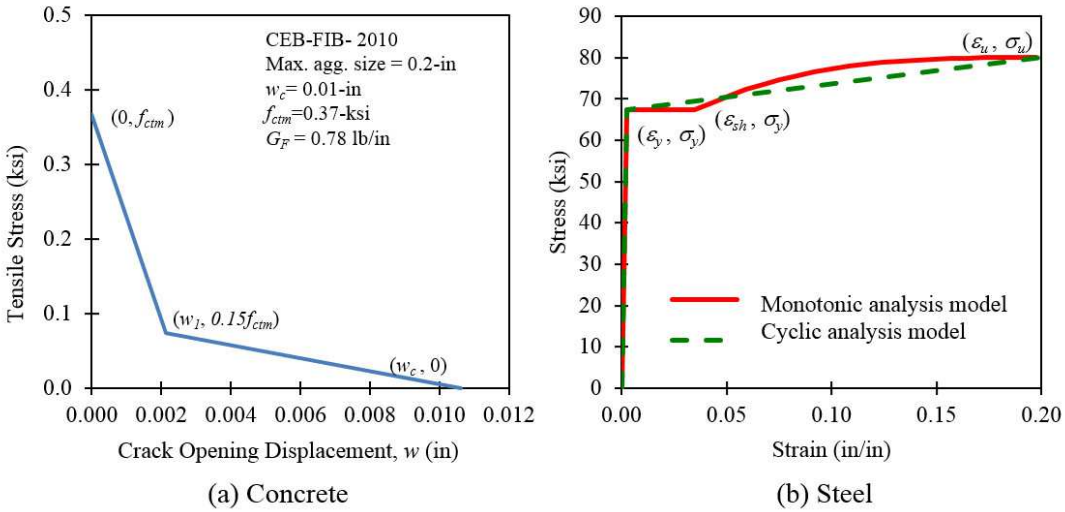

(a) Concrete (b) Steel

Figure 4.4 Concrete and steel uniaxial stress-strain models

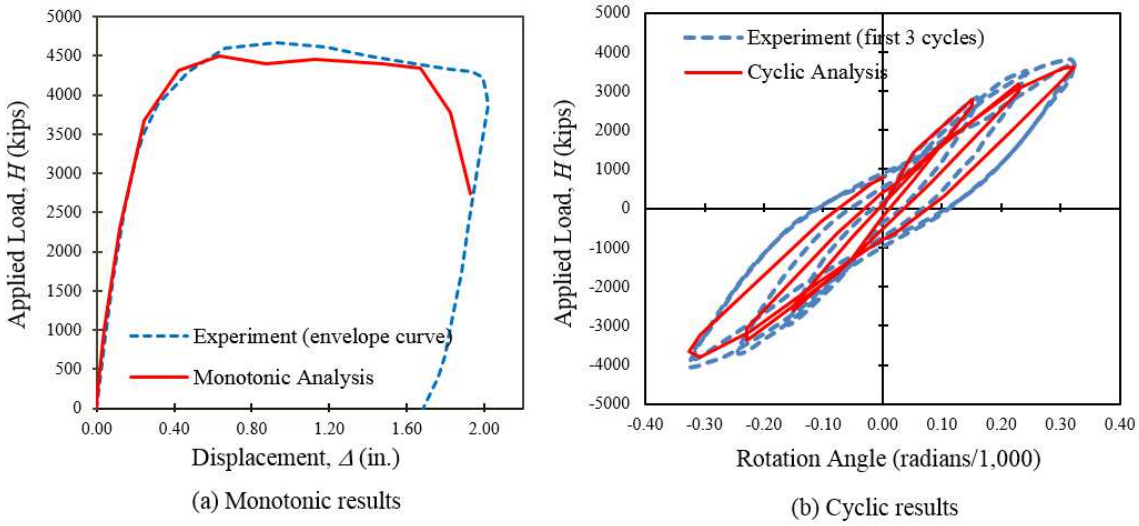

Figure 4.5 PSW experimental and analytical force-displacement plots

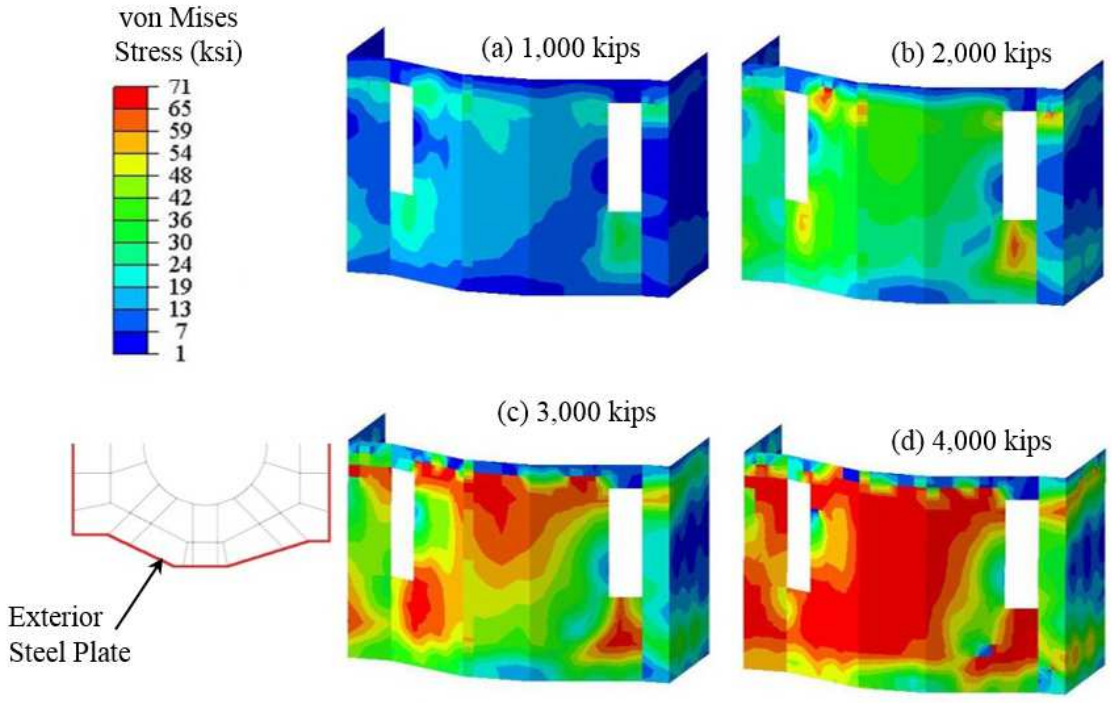

Figure 4.6 Mises stress, exterior faceplate

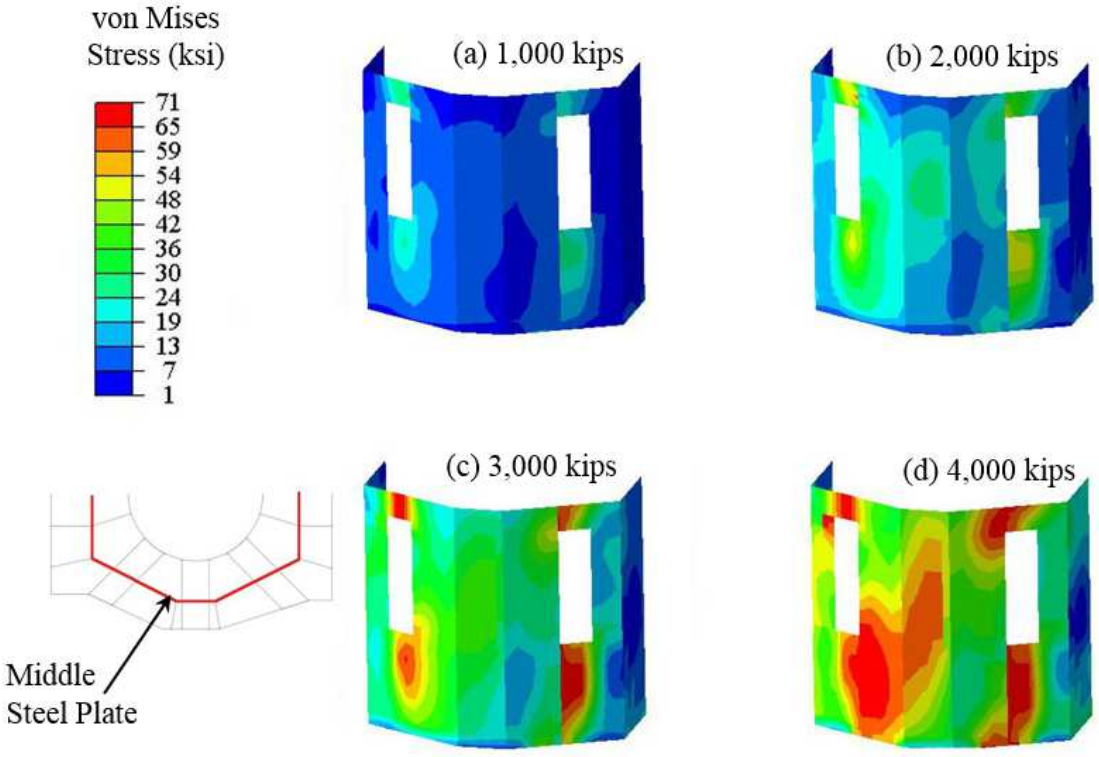

Figure 4.7 Mises stress, middle plates

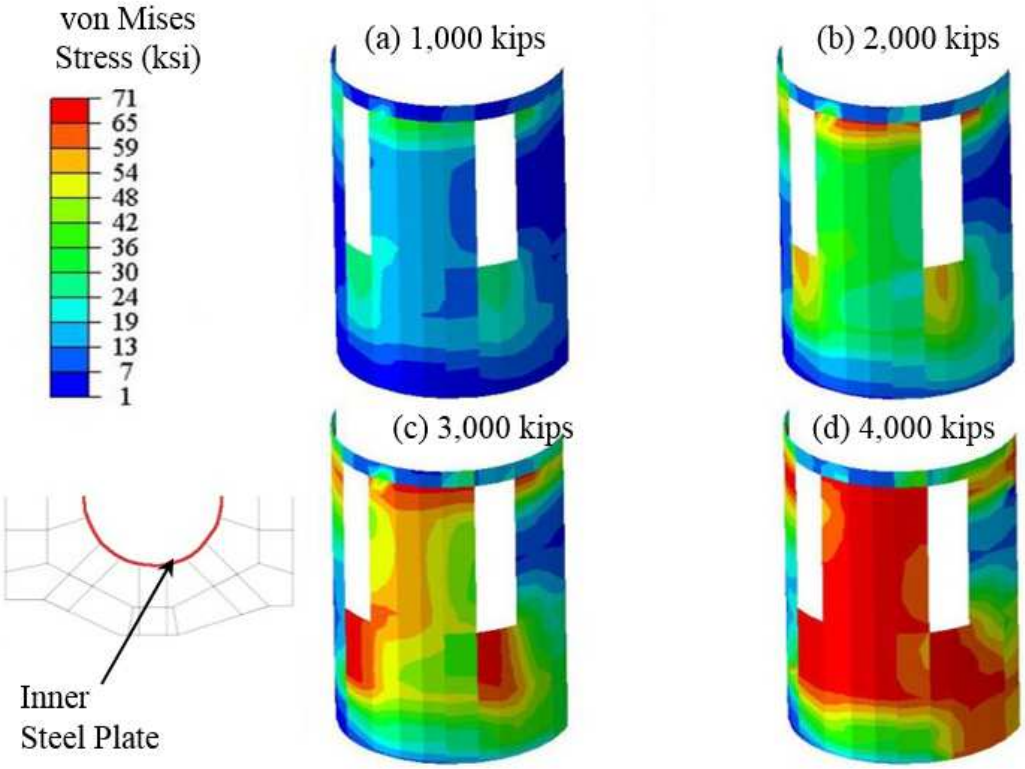

Figure 4.8 Mises stress, interior plates

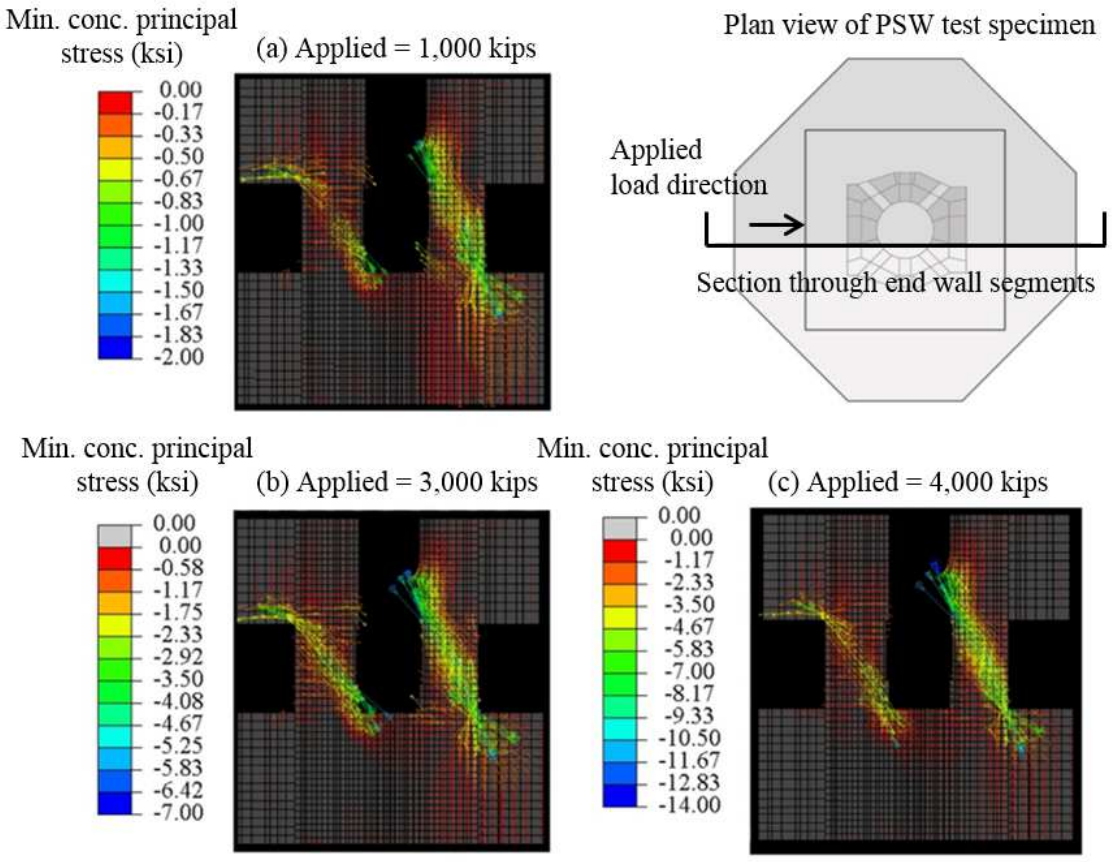

Figure 4.9 Min. princ. conc. stresses in end wall segments

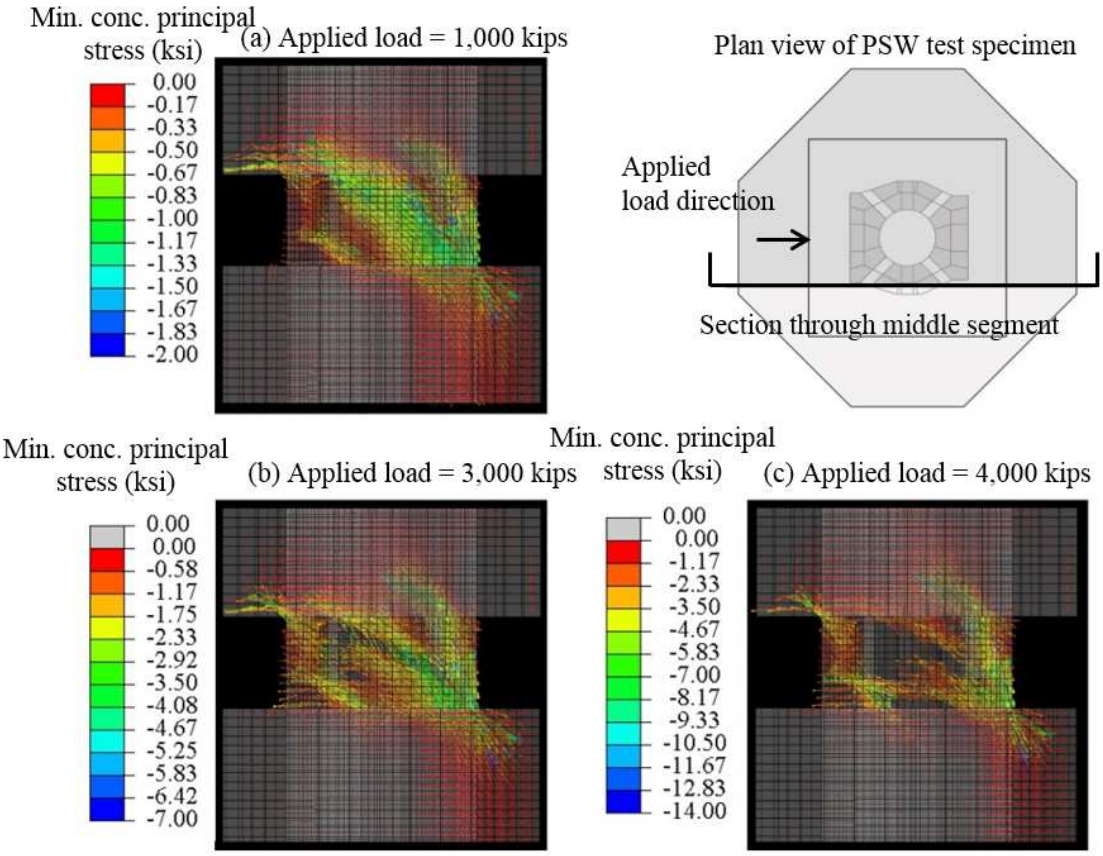

Figure 4.10 Min. princ. conc. stresses in middle wall segments

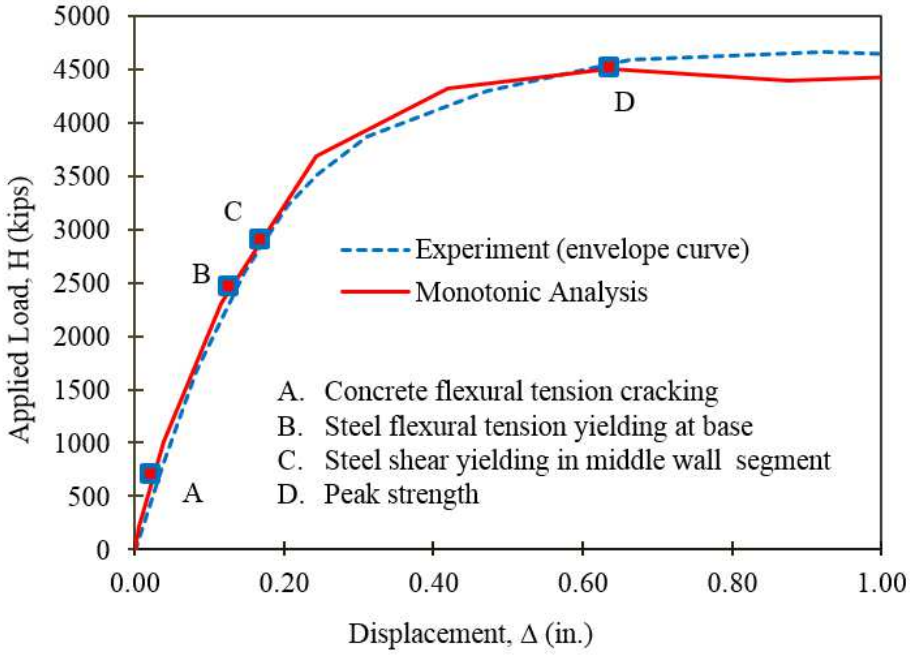

Figure 4.11 PSW experimental and analytical behavior milestones

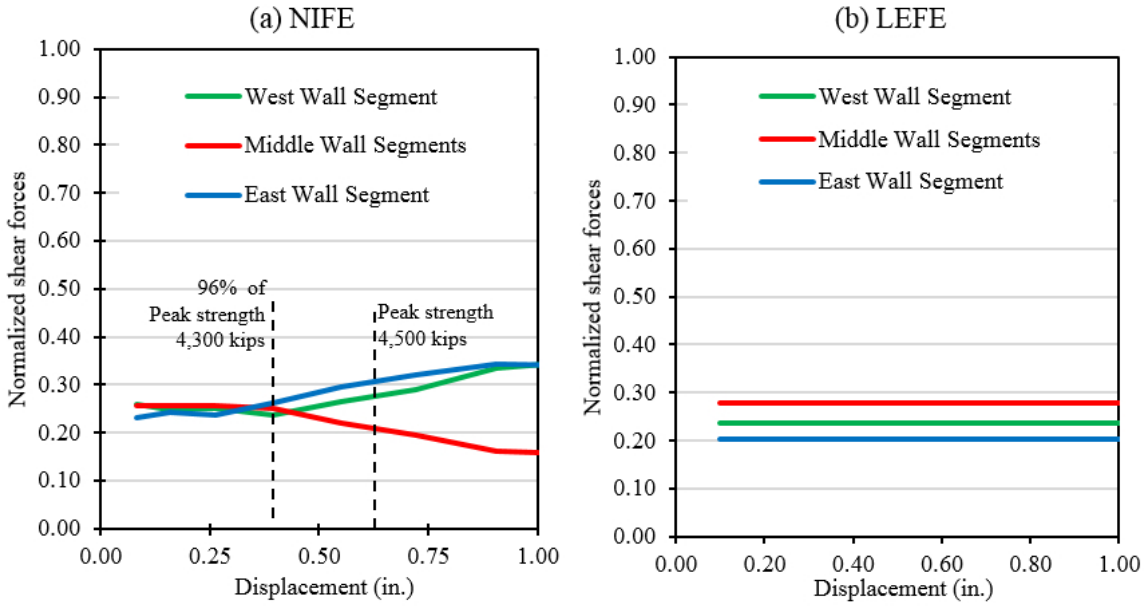

Figure 4.12 Proportion of applied load resisted by wall segments

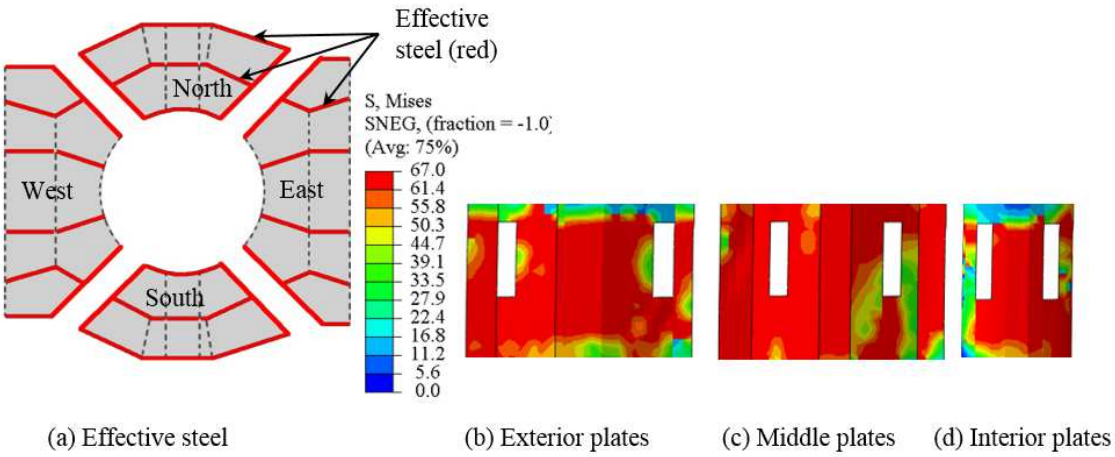

Figure 4.13 Eff. lengths of steel plates and the Mises stresses

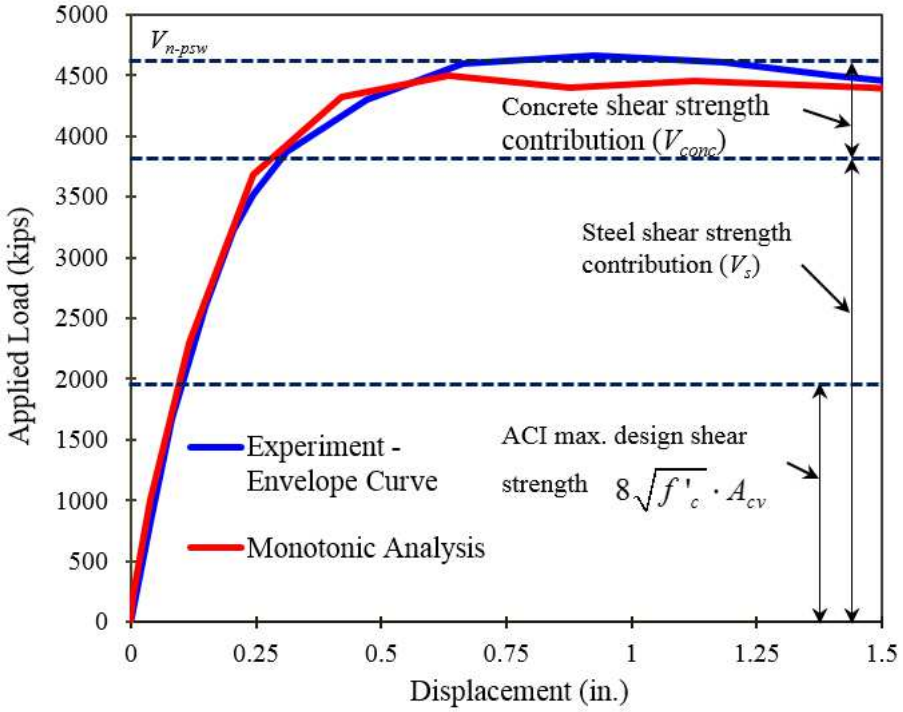

Figure 4.14 Calculated lateral capacity

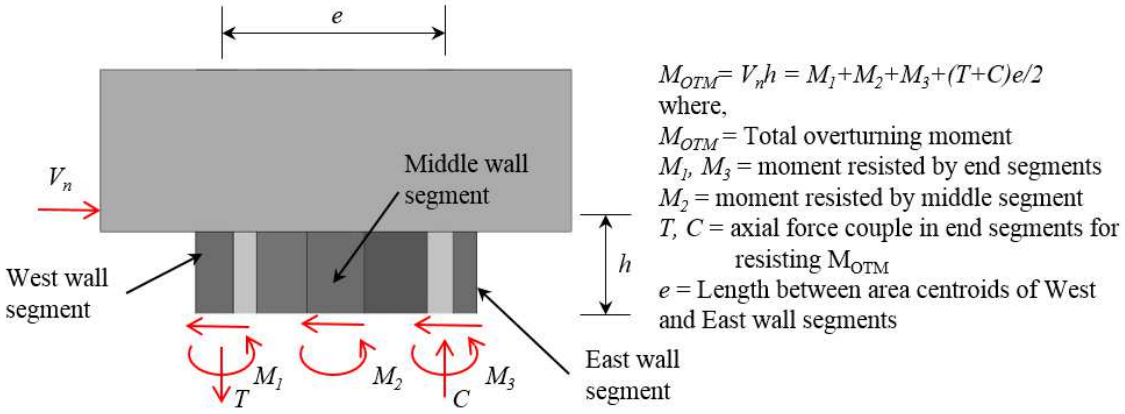

Figure 4.15 Free-body of PSW

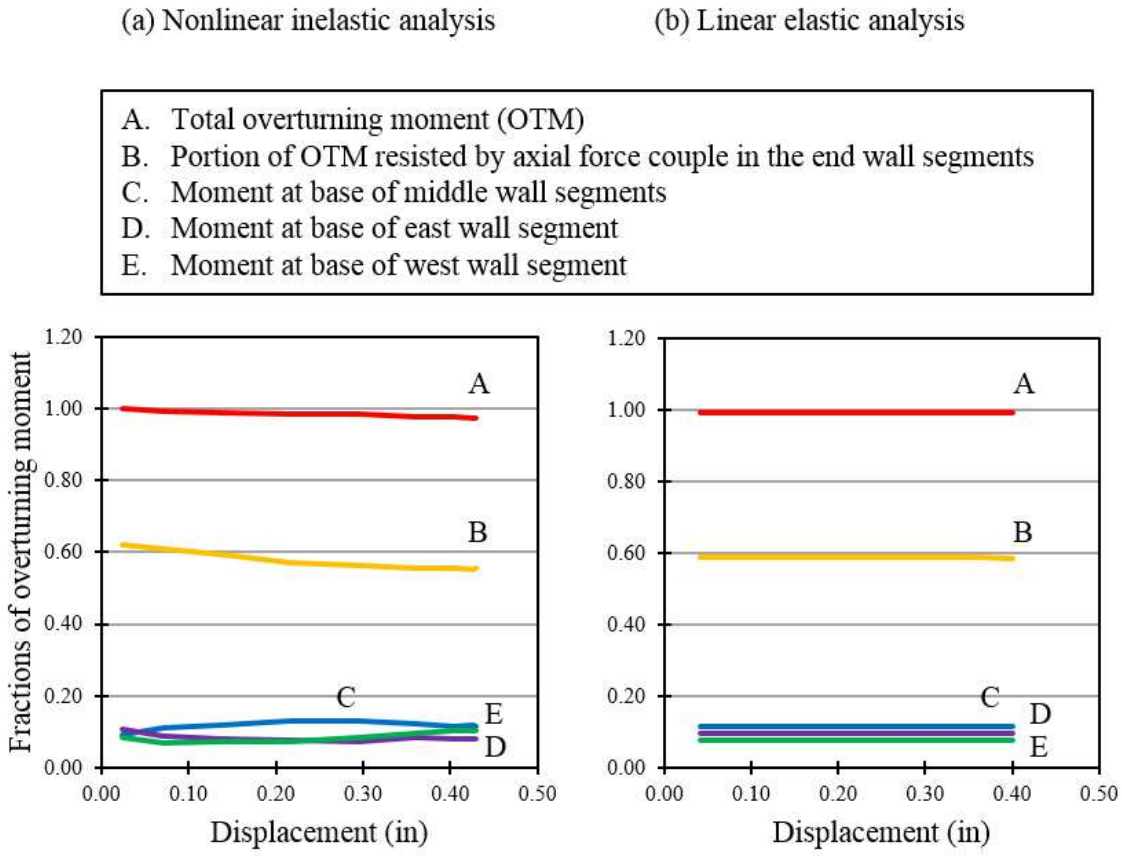

Figure 4.16 Proportion of overturning moment resisted by the PSW wall segments

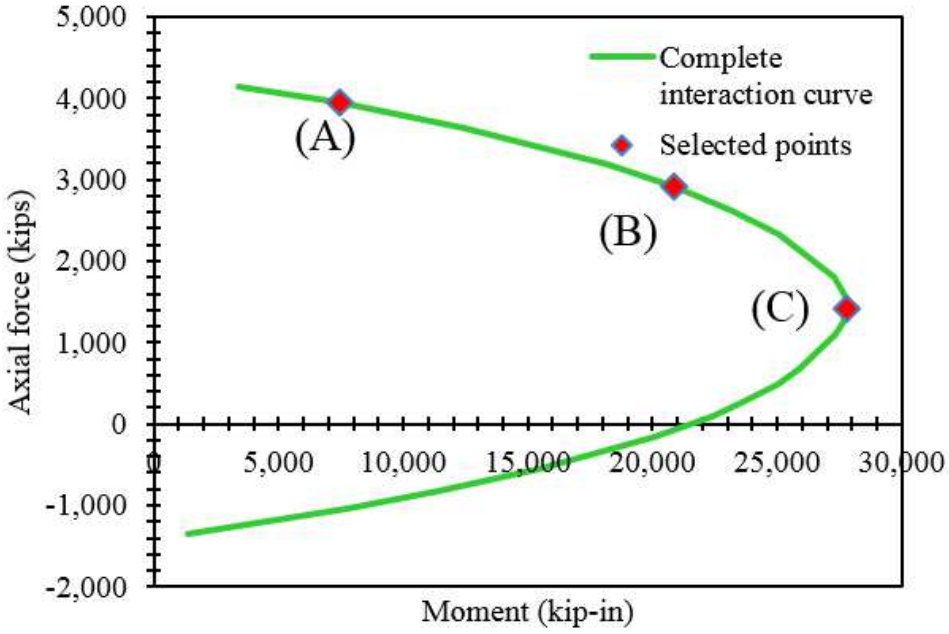

Figure 4.17 P-M Interaction curve for middle wall segment

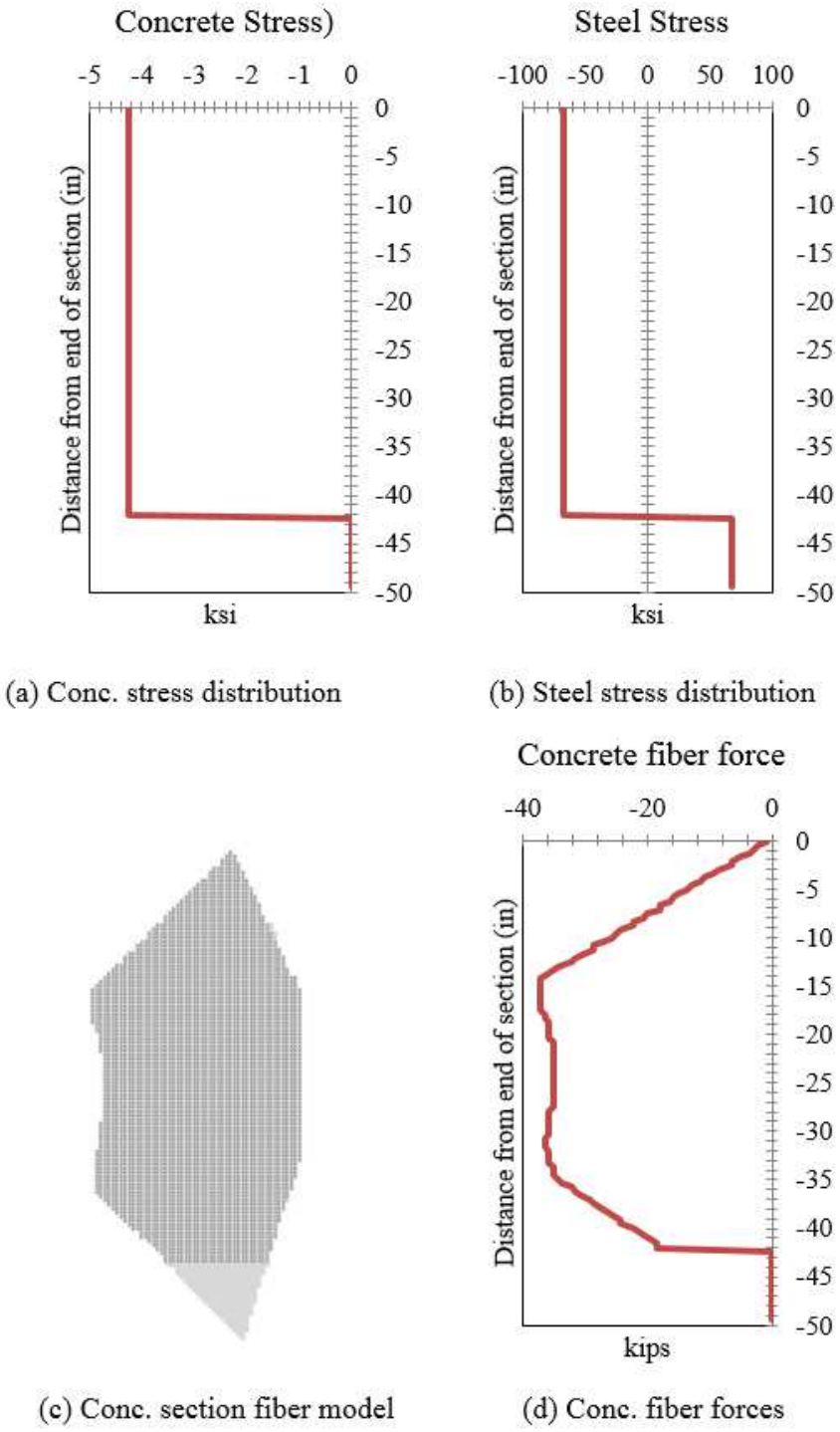

(a) Conc. stress distribution

(b) Steel stress distribution

(c) Conc. section fiber model

(d) Conc. fiber forces

Figure 4.18 Fiber model results for middle segment (point A shown in Figure 4.17)

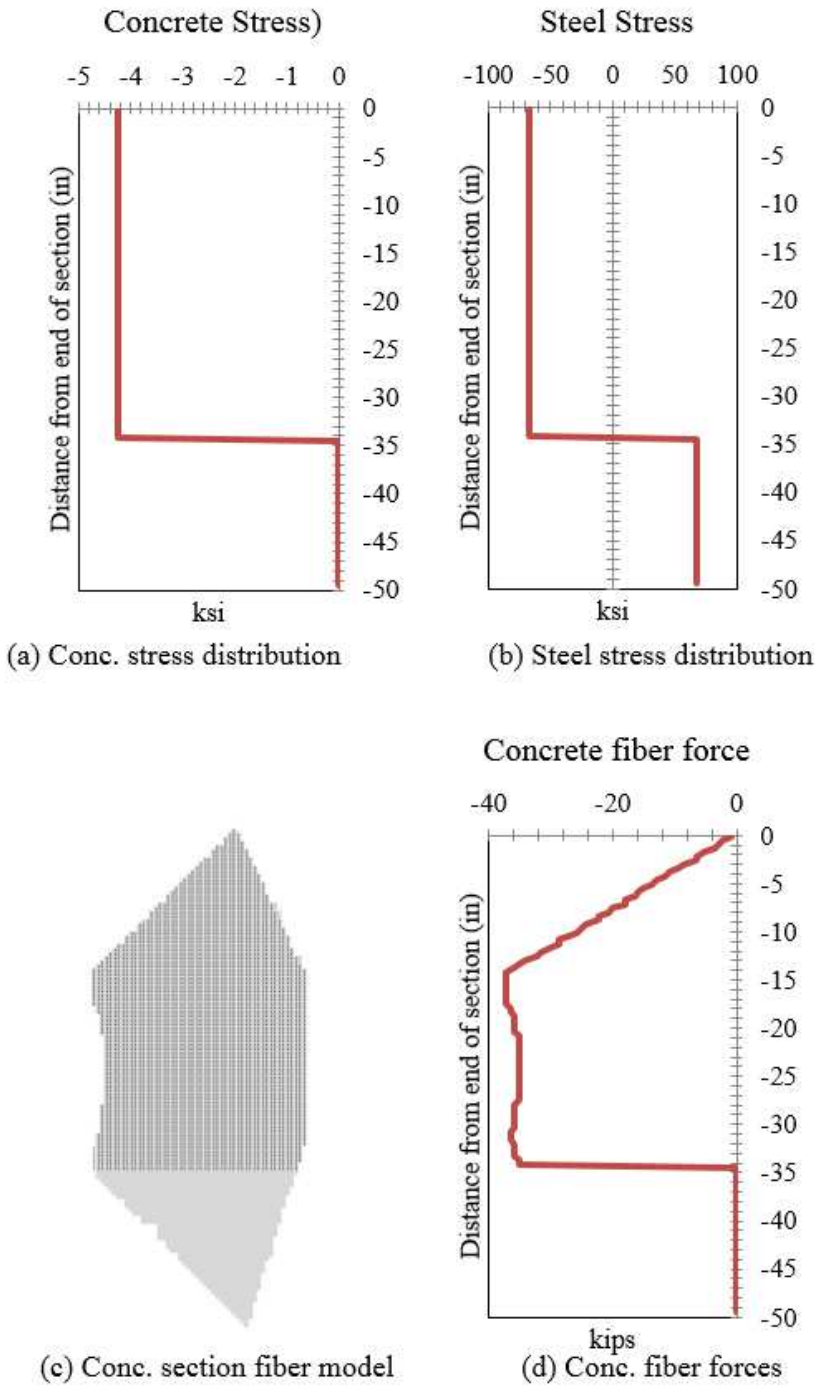

Figure 4.19 Fiber model results for middle segment (point B shown in Figure 4.17)

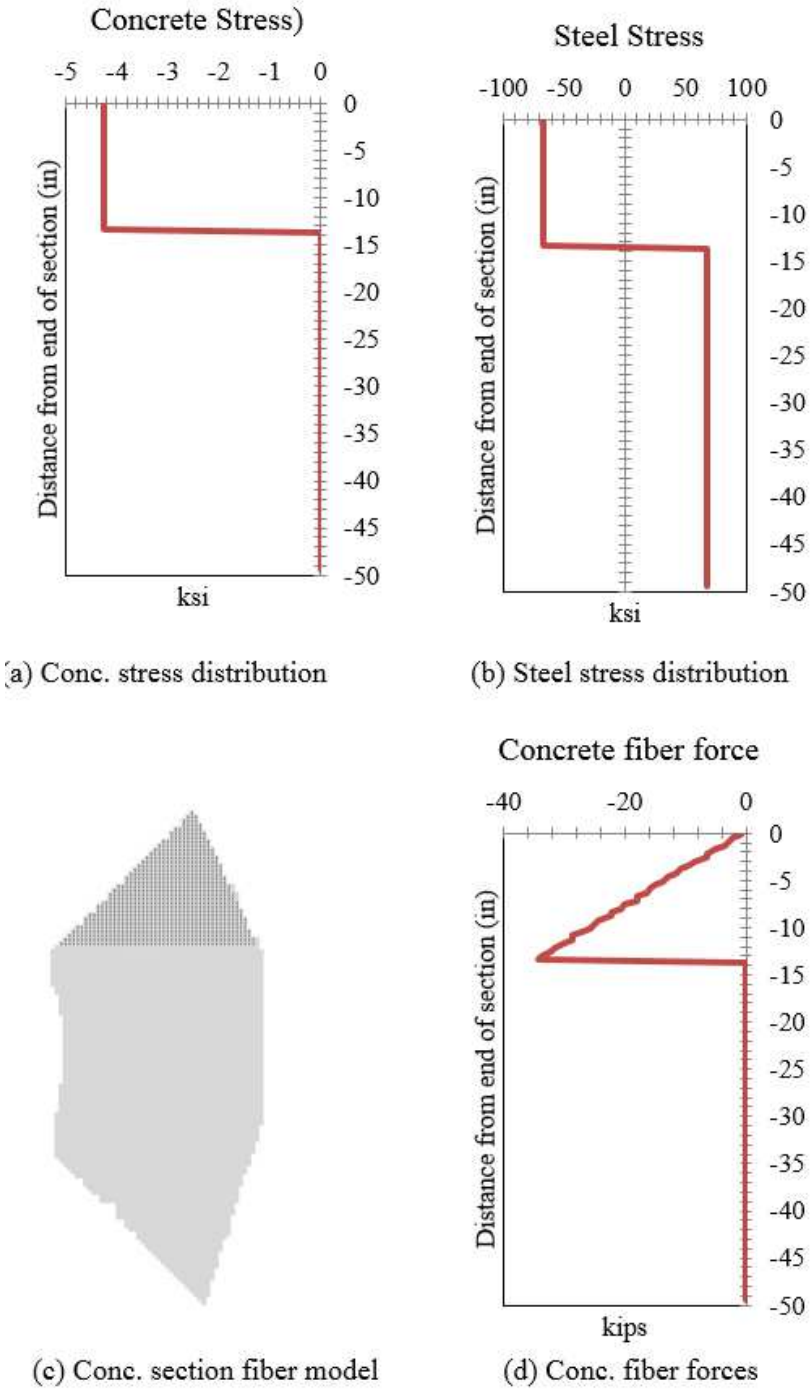

Figure 4.20 Fiber model results for middle segment (point B shown in Figure 4.17)

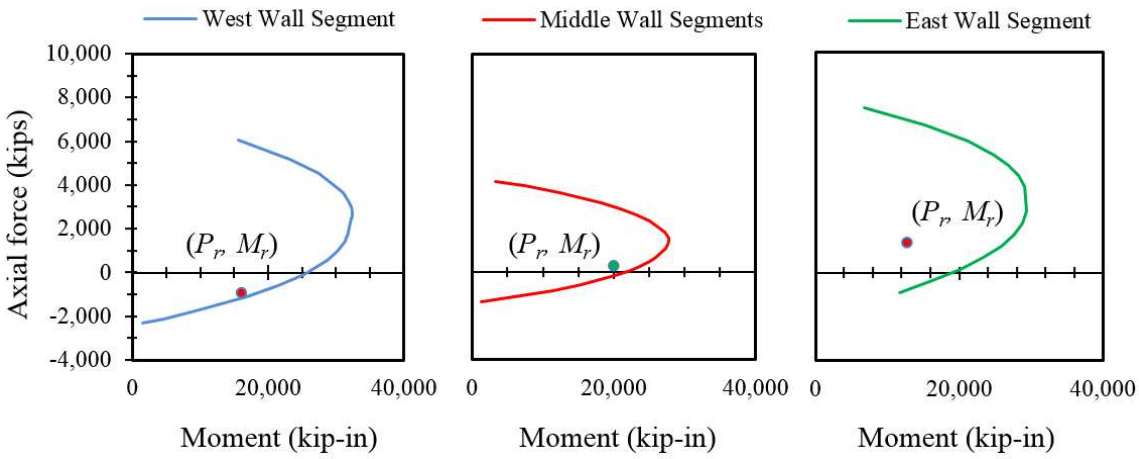

Figure 4.21 P-M int. curves for wall segments

CHAPTER 5. IN-PLANE SHEAR STRENGTH OF SC WALLS

The lateral force resisting systems in a number of recent nuclear power plant designs such as the Westinghouse AP1000 [69] and the Mitsubishi Nuclear Energy Systems US-APWR [71] are constructed with steel-plate composite (SC) walls. In these structures, many of the walls in the containment internal structure, the outer shield building (in the case of the AP1000), and auxiliary buildings are constructed with prefabricated structural modules primarily to expedite construction and improve quality. In the United States, the design, analysis and detailing of safety-related SC structures is governed by AISC N690s1-15 [4]. The SC walls are constructed with steel faceplates on both surfaces of the wall with allowable thicknesses (t_p) between 0.25 in. to 1.50 in. Wall thicknesses (t_{sc}) range between 12 in. and 60 in. and composite action is developed between the concrete infill and the steel faceplates with combinations of welded headed stud anchors and transverse steel tie-bars. The tie-bars (most commonly channels, angles or rods) attach the two steel faceplates together and provide multiple functions including bracing for construction loads (during erection and concrete placement) and also act as transverse shear reinforcement in the completed wall. A cut-away view of an SC wall assembly is shown in Figure 5.1(a) with representative detailing and the cross-section of an SC wall is shown in Figure 5.1(b) with typical welded headed stud anchors and transverse reinforcement.

Power plant structures are typically constructed with numerous intersecting and connected structural walls that are located and oriented in complex geometric layouts. Unlike commercial multi-story buildings that often use slender (high aspect ratio) shear walls or core wall structures that are primarily governed by flexure, power plant shear wall structures are often proportioned with low aspect ratios resulting in higher levels of base shear. This, in combination with monolithic like construction results in complex combined loadings of flexure, shear, and axial forces that must be taken into account in the design of these systems.

SC shear walls are generally either configured as pier walls without boundary elements, or shear walls that are connected on multiple sides to boundary elements, adjacent perpendicular walls, or flanges. SC walls in both configurations show composite behavior and resist lateral loads with a combination of biaxial stresses in the steel faceplates and diagonal compression in the concrete infill. As lateral loads are increased beyond the concrete cracking threshold, diagonal compression action occurs with crack orientations primarily occurring in directions approximately parallel to the direction of principal compression. In pier walls, the compression (diagonal and vertical flexural compression) in the concrete infill resulting from the flexure and shear demands is held in equilibrium with the steel faceplates, and for flanged shear walls the concrete compression is resisted by a combination of the steel faceplates and the surrounding boundary elements. This results in additional lateral load resisting capacity in flanged wall configurations or walls with boundary elements since the concrete can develop higher compression stresses beyond the point of yielding of the faceplates by reacting directly with the boundary elements.

5.1 Research significance

Safety-related SC shear walls are designed with overstrength connections (in the case of wall-to-wall connections the required strength is 125% of the lesser of the nominal strengths of the connected walls) so that the response of the overall lateral force resisting system is not influenced by failures at connections and is rather governed by the ductile response of the shear wall panels. The current in-plane shear strength design equations in AISC N690s1-15 [4] are conservative and represent a lower bound prediction of in-plane shear strength governed by the limit of yielding of the steel faceplates. This is considered a conservative estimate of the shear strength specifically for SC walls that adhere to the detailing, material, and dimensioning limits permitted in AISC N690s1-15. For SC wall reinforcement ratios ($2t_p/t_{sc}$) between 1.5% and 5.0%, yielding of the steel faceplates occurs prior to compression or shear failure of the concrete infill when subjected to pure shear. The purpose of this study is to provide insight into the post-yield response of SC walls subjected to pure shear, and to develop a simple method based on composite shell theory for prediction of the ultimate shear strength and deformation of SC shear walls. An ultimate shear strength prediction is necessary in order to correctly calculate the required overstrength of wall connections as part of an overall structural system.

5.2 Mechanics model

The complete in-plane shear force-shear strain response of an SC panel can be developed with composite shell theory. The approach only considers membrane stresses (since the cross-sectional geometric and material properties are assumed symmetric about the wall centerline) and takes into account concrete cracking, yielding of the steel faceplates,

compression softening of cracked concrete, and the ultimate strength of the shear panel governed by concrete compression failure. This approach has been used previously in a number of studies for prediction of the lateral load-deformation response of SC panels by Ozaki et al. [36], Varma et al. (2011) [44], and Varma et al. (2014) [72]. The load-deformation response is divided into a series of piecewise linear loading phases with calculated shear stiffnesses and strengths defined for the following mechanical states: (1) uncracked stiffness response followed by initial cracking of the concrete infill, (2) cracked concrete stiffness followed by steel faceplate yielding, and (3) (in the Ozaki et al. formulation) prediction of the ultimate strength governed by concrete compression failure and steel faceplate tension field action. The analytical work in this study builds on these prior studies and presents an alternative formulation for prediction of the ultimate ultimate shear strength that takes into account concrete compression softening and proposes an approach for prediction of the strain state at ultimate.

A pure shear loading condition is assumed in the analytical model. The pure shear assumption is a simplification that must be verified on a case-by-case basis depending on the boundary conditions applied to an actual shear wall panel. In general, shear wall panels that are connected to perpendicular flange walls or boundary elements at the ends are primarily subjected to in-plane shear so this assumption is applicable in many cases. In contrast, SC pier walls are subjected to substantial in-plane flexure in addition to in-plane shear and therefore require a more detailed approach that takes into account the combined loading state. With the pure shear assumption, a given composite membrane element is subjected to a resultant unit shear force S_{xy}, and the in-plane resultant unit normal forces S_x

and S_y are equal to zero, as shown in Figure 5.2 (a). Equilibrium requires that the resultant unit forces (S_x, S_y, and S_{xy}) are equal to the summation of the respective components of concrete and steel stresses multiplied by the respective concrete and steel thicknesses, $2t_p$ and t_{sc} (shown in Figure 5.2). The concrete and steel stress components in x-y coordinates are shown in Figure 5.2 (b) and (c). The concrete element (Figure 5.2(b)) is subjected to concrete normal and shear stresses ($\sigma_x^c, \sigma_y^c, \tau_{xy}^c$) and the steel element (representing the two faceplates) is subjected to the steel normal and shear stresses ($\sigma_x^s, \sigma_y^s, \tau_{xy}^s$). The model assumes that the steel and concrete layers are fully-bonded, therefore strain states in the concrete infill and steel faceplates are equal to the composite element strain state and also identical at every point on the composite element.

5.3 Uncracked concrete in-plane shear response

Ozaki et al. [36] and Varma et al. [72] developed identical approaches for calculating the initial uncracked concrete state of the SC shear element with plane stress elastic isotropic constitutive models for the concrete infill and the steel faceplates. For the loading condition of pure shear and with isotropic constitutive models, the composite shear stiffness is equal to the summation of the steel ($G_s \cdot 2t_p$) and concrete ($G_c \cdot t_{sc}$) shear stiffnesses since the normal and shear components of the stiffness matrix are uncoupled. G_s and G_c are the elastic shear moduli of steel and concrete respectively (equal to $\frac{E_s}{2(1+\nu_s)}$ and $\frac{E_c}{2(1+\nu_c)}$). The unit shear force-shear strain relationship is based on these assumptions and defined in AISC N690s1-15 (Eq. A-N9-9) as shown in Equation 5.1.

$$S_{xy} = K_{xy}^{uncr}\gamma_{xy} = \left(G_s 2t_p + G_c t_{sc}\right)\cdot\gamma_{xy} \qquad \text{Equation 5.1}$$

Where γ_{xy} is the shear strain in *x-y* coordinates (shown in Figure 5.2(b)). As shear forces are increased, the tensile strength of the concrete infill is eventually reached resulting in cracking. For the isotropic model and pure shear, maximum and minimum principal stresses occur with an orientation rotated 45 degrees from the x-y reference coordinates. The resulting principal stresses (and strain directions) are shown in Figure 5.3 and denoted 1-2. The formulation for the concrete cracking threshold derived by Varma et al. [72] has subsequently been codified in AISC N690s1-15 (Eq. A-N9-10). This approach assumes that the concrete infill transitions to a cracked state when the maximum principal stress (the 1-direction for the pure shear case shown in Figure 5.3) reaches the cracking tensile strength. The resultant unit cracking shear force is then derived by transforming from principal coordinates to x-y coordinates and can be written as shown in Equation 5.2 in terms of the concrete and steel shear moduli, G_c and G_s.

$$S_{xy}^{cr} = \frac{0.063\sqrt{f'_c}}{G_c}\cdot\left(G_s 2t_p + G_c t_{sc}\right) \qquad \text{Equation 5.2}$$

Where f'_c is the concrete compressive strength and $0.063\sqrt{f'_c}$ (ksi) is the reduced concrete tensile strength that accounts for shrinkage cracking that commonly occurs in SC walls. The shear strain at the point of concrete cracking is calculated by substituting Equation 5.2 into Equation 5.1 and solving for shear strain (Equation 5.3).

$$\gamma_{xy}^{cr} = \frac{S_{xy}^{cr}}{K_{xy}^{uncr}}$$ Equation 5.3

5.4 Cracked concrete in-plane response

When the applied shear increases above the concrete cracking threshold, the uncracked isotropic concrete constitutive model described previously is replaced with a cracked concrete model and the plane stress isotropic steel model is maintained since the steel is still in the elastic range. The stress state is assumed to be identical at every point on the panel with cracking occurring parallel to the direction of minimum principal concrete stress. A plane stress orthotropic constitutive concrete model is substituted for the previous (uncracked) isotropic model with zero stiffness assumed in the maximum principal direction (1-direction) to account for the cracking and an effective compression elastic modulus equal to E'_c is assumed in the minimum principal direction, and Poisson's effect is neglected. The concrete constitutive relationship takes the form shown in Equation 5.4 in principal directions (1-2) with the 1-direction parallel to the assumed crack orientations and the 2-direction parallel to the direction of diagonal compression. In this formulation, the effective concrete elastic compression modulus E'_c, takes into account the reduction of stiffness due to cracked concrete and nonlinear compression response and is equal to $0.7E_c$, where E_c is the concrete secant stiffness defined in ACI 349-06 [2]. After the initiation of concrete cracking, the shear force shear strain response is then assumed to be linear until the steel faceplates reach von Mises yield. This is a reasonable assumption as long as

concrete stresses are sufficiently low and remain in the approximate linear range of response.

$$\begin{pmatrix} \sigma_1^c \\ \sigma_2^c \\ \tau_{12}^c \end{pmatrix} = \begin{bmatrix} 0 & 0 & 0 \\ 0 & E'_c & 0 \\ 0 & 0 & 0 \end{bmatrix} \cdot \begin{pmatrix} \varepsilon_1 \\ \varepsilon_2 \\ \gamma_{12} \end{pmatrix} \qquad \text{Equation 5.4}$$

AISC N690s1-15 provides a simplified, approximate design equation with the shear force shear strain relationship written as shown in Equation 5.5, where the composite cracked concrete shear stiffness K_{xy}^{cr}, is decomposed into steel and composite terms (Equation 5.6 and Equation 5.7) in order to expedite design calculations and ν_s and E_s are steel Poisson's ratio and elastic modulus, respectively.

$$S_{xy} = K_{xy}^{cr}\gamma_{xy} = \left(K_s + K_{sc}\right)\gamma_{xy} \qquad \text{Equation 5.5}$$

$$K_s = G_s \cdot 2t_p \qquad \text{Equation 5.6}$$

$$K_{sc} = \frac{1}{\frac{4}{0.7E_c \cdot t_{sc}} + \frac{2(1-\nu_s)}{2 \cdot t_p \cdot E_s}} \qquad \text{Equation 5.7}$$

An approximate equation for calculation of the yield strength (Equation 5.8) was developed by Seo et al. [73] and is used conservatively as the nominal in-plane shear strength in AISC N690s1-15 (Eq. A-N9-19). The shear strength accounts for the strength contributions from the yielded steel faceplates and also the resistance provided by the cracked concrete infill. Material properties (f'_c and f_y) and variations in reinforcement ratio slightly affect the yield shear strength, S_{xy}^y. Therefore, the code equation (Equation 5.8) is multiplied by a coefficient κ that corrects for these effects.

$$S_{xy}^{y} \cdot l_w = V_y = \kappa \cdot f_y \cdot 2 \cdot t_p \cdot l_w = \kappa \cdot f_y \cdot A_s \qquad \text{Equation 5.8}$$

Equation 5.9 defines κ in terms of the normalized reinforcement ratio $\bar{\rho}$ (Equation 5.10):

$$\kappa = 1.11 - 5.16 \cdot \bar{\rho} \leq 1.0 \qquad \text{Equation 5.9}$$

$$\bar{\rho} = \frac{1}{31.6} \cdot \frac{f_y \cdot 2t_p}{t_{sc}\sqrt{f'_c}} \qquad \text{Equation 5.10}$$

When the shear wall has reached the yield strength, V_y, the cracked concrete infill is in a state of uniaxial stress (in the 2-direction shown in Figure 5.3(a)). The minimum principal strain is equal to ε_2^y and equal to the strain at cracking, ε_2^{cr} calculated with the uncracked concrete constitutive relationship, plus the strain increment from cracking to yield calculated with the cracked concrete constitutive relationship, evaluated at S_{xy}^{cr} and S_{xy}^{y}, respectively (Equation 5.11). In the equation, the concrete compression stress corresponding with faceplate yielding (f_{cy}) is then equal to Equation 5.12 with the strain at yield multiplied by the cracked concrete effective stiffness, E'_c.

$$\varepsilon_2^y = \varepsilon_2^{cr} + \left(\varepsilon_2^{(S_{xy}^y)} - \varepsilon_2^{(S_{xy}^{cr})}\right) \qquad \text{Equation 5.11}$$

$$f_{cy} = E'_c \left(\frac{-S_{xy}^{cr}(1+\nu_c)(1+\nu_s)}{2 \cdot E_s \cdot t_p (1+\nu_c) + E_c \cdot t_{sc}(1+\nu_s)} - \frac{(S_{xy}^{y} - S_{xy}^{cr})(1+\nu_s)}{2 \cdot E_s \cdot t_p + E'_c \cdot t_{sc}} \right) \qquad \text{Equation 5.12}$$

The principal stresses in the steel faceplates, σ_1^s and σ_2^s, are shown in Figure 5.3(b). At the yield point, the stress state of the steel faceplates is no longer pure shear in x-y coordinates and therefore σ_1^s and σ_2^s (in principal directions) are no longer equal and opposite.

The shear strain at the point of steel yield (γ_{xy}^{y}) can be calculated by equating the ratio of change in shear force to change in shear strain equal to the cracked concrete stiffness, K_{xy}^{cr}, and then solving for the shear strain, γ_{xy}^{y}.

$$\gamma_{xy}^{y} = \frac{S_{xy}^{y} - S_{xy}^{cr}}{K_{xy}^{cr}} + \gamma_{xy}^{cr} \qquad \text{Equation 5.13}$$

5.5 Post-yield in-plane shear response

5.5.1 Incremental in-plane shear strength

As the applied shear force increases above the yield threshold of the steel faceplates, additional lateral strength can only result from increases in diagonal concrete compression as described previously. A simple model is proposed that characterizes the additional shear strength as an incremental shear force (ΔV) that when added to the yield shear V_y (Equation 5.8) is equal to the ultimate in-plane shear strength (V_u), of the wall panel:

$$V_u = V_y + \Delta V \qquad \text{Equation 5.14}$$

After the point of steel faceplate yielding, additional increases in concrete stresses can no longer be in equilibrium with the faceplates exclusively. Therefore, the only way that the shear wall panel can develop additional resistance is with diagonal compression stresses in the infill that are resisted directly with the boundary elements connected around the perimeter of the wall panel. Therefore, it is assumed that the incremental force coming from the concrete is held in equilibrium with the connected boundary elements and the state of stress in the steel faceplates is unchanged as the shear demand is increased beyond the yield threshold. It should be noted that for the SC walls subjected to in-plane pure shear,

the maximum principal strains at the limit are generally quite low such that the effects of strain hardening in the steel faceplates can be neglected if a monotonic response is assumed (the analytical results reported in subsequent sections predict generally low maximum principal strains at ultimate of less than 1%). The incremental shear strength term (ΔV), is proportional to the increase in the principal concrete compressive stress calculated at the point of V_y, to the point of compression failure of the concrete. The change in concrete compression stress from the yield point to ultimate (Δf_c), is shown in Figure 5.3(c) and (d). The maximum principal stress (1-direction in Figure 5.3(a) is zero, and the minimum principal stress is equal to Δf_c (2-direction). Transforming principal stresses to x-y coordinates (45 deg.) yields a uniform shear parallel to the edges of the panel equal to $0.5\Delta f_c$ and a uniform compressive normal stress of $0.5\Delta f_c$ applied around the perimeter of the shear element to the edges of the concrete infill, as shown in Figure 5.3(d). The incremental shear force then becomes Equation 5.15 with the concrete edge shear $0.5\Delta f_c$, multiplied by the concrete cross section equal to the shear panel length l_w, multiplied by the SC wall thickness, t_{sc}.

$$\Delta V = 0.5\Delta f_c \cdot l_w \cdot t_{sc} \qquad \text{Equation 5.15}$$

5.5.2 Finite element modeling of SC shear panel tests

A series of finite element analyses were conducted in order to develop insight into the mechanical state of SC walls subjected to in-plane shear. Seven experimental SC shear panel membrane tests previously conducted by Ozaki et al. [36] were modeled and benchmarked. The Ozaki tests were conducted on square SC wall panels with shear loads

applied around the perimeter of the panels. Material and dimensional properties of the tests are listed in Table 5.1. All of the tests were conducted on square panels with identical outer dimensions (47.2 x 47.2 in.) and wall thicknesses of 7.87 in. The two primary control variables considered in the tests were reinforcement ratio ($2t_p/t_{sc}$) and combined shear-axial force loadings. The reinforcement ratios were 2.3% for the S2 series specimens, 3.2% for the S3 series tests, and 4.5% for the S4-00NN test.

Details of a representative test specimen are shown in Figure 5.4(a) and (b). The loading was applied around the perimeter of the panels to steel headed anchors that were embedded in the concrete infill. Steel reinforcing plates were also connected around the edges of the specimens and bolted through the panels in order to clamp the perimeters of panels and prevent concrete splitting and also to assist with distribution of the applied loading from the concrete infill to the steel faceplates.

The seven Ozaki panel tests were modeled and analyzed with Abaqus/Explicit [6]. Geometric and boundary condition symmetries allowed for the development of half models in order to reduce analysis times. Loads were applied monotonically in displacement-control on the four sides of the panels and the boundary conditions were as shown in Figure 5.5(a) and (b). The steel faceplates were modeled with 1 in. square shell elements and the concrete infill was meshed with solid 1 in. brick elements. For the steel faceplates and reinforcing plates, reduced integration (S4R) shell elements were used and for the solid concrete infill, eight-node (C3D8R) solid elements with reduced integration were used.

The modeling of composite response uses the approach described in Chapter 2 with stud anchors modeled with connector elements. The connectors tied coincident nodes of the steel faceplates to nodes on the concrete infill at stud locations and were assigned the nonlinear shear force-slip relationship for headed stud anchors by Ollgaard et al. [63].

The steel and concrete models are also based on the benchmarked modeling described in Chapter 2 with steel shell elements assigned a constitutive model with multi-axial plasticity, von Mises yield surface, kinematic hardening and associated flow rule. The concrete infill was modeled with the Abaqus brittle cracking model that is partially based on the brittle fracture model by Hillerborg et al. [55] where the fracture energy (G_f), is defined as a material property and used to define the post-cracking tensile stress-crack opening (σ - w) behavior. The concrete tensile strength is defined with a Rankine failure criterion and the post-cracking tension softening and shear retention are based on values from the CEB-FIB Model Code [60]. Table 5.1 lists concrete model properties: the mean concrete tensile strength f_{ctm}, and the crack width defined at zero concrete stress w_c. Since the concrete model assumes that the uncracked response is linear, the secant stiffness E_c, defined by ACI 349-06 was used.

The analyses were run with the explicit solver so that the concrete material discontinuities could be modeled including inelastic response due to concrete cracking, yielding of the steel plates, faceplate buckling and connector force-slip response. Shear force-average shear strain results are plotted along with the experimental results in Figure 5.6 for analyses S2-00NN, S3-00NN, and S4-00NN. The application of axial forces in the four additional

tests did not significantly alter the responses and therefore similar results were obtained for the other four specimens. The shear force-shear strain results show good agreement with the approximate bilinear loading responses from the experiments. Results from the same three analyses are also plotted in Figure 5.7 where a breakdown of contributions of the steel and the concrete shears is shown. The section forces were calculated on the cross-section passing through the middles of the analytical models shown in Figure 5.4(b) of the steel and concrete. In all three cases, an approximate bilinear shear force-shear strain response is shown with a substantial reduction of shear stiffness occurring when the faceplates reach yield. After the point of yielding, the concrete shear contribution continues to increase approximately linearly until peak strength is reached and the steel shear plateaus and diminishes slightly as local buckling of the faceplates occurs.

Figure 5.8 and Figure 5.9 show stress contours of the von Mises stresses in the steel faceplates and minimum principal concrete compression in the concrete. Both of the figures show the stress states at the (a) initial state, (b) concrete cracking, (c) faceplate yielding, and (d) peak strength. As shown in Figure 5.9, the concrete stresses are relatively uniform across the panel at low force levels, and as loads increase, a diagonal compression band forms from the upper left corner to the lower right corner. As the ultimate strength is reached (Figure 5.9(d)) a clearly defined compression strut is apparent with localized concrete failure occurring in the two corners where the struts terminate.

The maximum principal concrete strains are shown in the vector plots of Figure 5.10. Figure 5.10(c) shows that the orientations of the strain vectors remain relatively constant

and at approximately 45 degrees at the point of faceplate yield. As the loading is increased to ultimate, the maximum principal strain directions remain at 45 degrees in areas of low cracking, and appear to assume random orientations in areas of high cracking. In contrast the minimum principal strains remain oriented at approximately 45 degrees throughout the loading history as shown in Figure 5.11.

Table 5.2 summarizes the peaks strengths and average shear strains at the point of peak strength from the experiments and finite element analyses for the seven panel tests. The ratios of strains at peak load are listed in column 5 with the mean for the seven tests equal to 0.997 and a coefficient of variation of 27.5%. Similar results for peak strength are listed in column 10 with a mean of 1.010 and coefficient of variation of 8.6%.

5.5.2.1 Concrete compression softening

The compression softening behavior of cracked concrete has been widely studied in reinforced concrete members. Applied shear or combined tension-compression resulting in concrete cracking have demonstrated reduced concrete compressive strengths with respect to the reference cylinder strength, f'_c. Numerous tests of reinforced concrete shear panels have demonstrated this effect and analytical methods have been developed that correlate the extent of softening to various parameters including average principal strain ratio ($\varepsilon_1/\varepsilon_2$), orientation of cracks to reinforcement directions, proportional vs. sequential loading, etc. Experimental and analytical studies by Kollegger and Mehlhorn [74], Shirai and Noguchi [75], Belarbi and Tsu [76], Vecchio and Collins [77], and Vecchio [78] have studied the

topic of cracked concrete compression softening in depth. Analytical methods developed from a number of these studies provide a reduction factor β, that is multiplied by the uniaxial concrete stress-strain equation such as the Hognestad parabola [79] resulting in the effective stress-strain relationship.

For the SC shear panel finite element analyses, the average minimum principal concrete stresses are plotted in Figure 5.12(b) for specimens S2-00NN, S3-00NN and S4-00NN. Shown are plots of the minimum principal concrete stress ($-\sigma_2^c$) vs. average shear strain. In the plots, σ_2^c is calculated by taking the average of the minimum principal stresses from all of the finite elements of the concrete infill. The directions of the compression stresses are shown in the vector plots of Figure 5.12(a) and appear to be close to 45 degrees at the point of peak strength. For the three representative reinforcement ratios, the peak compression strengths are shown to be slightly above 50% of f'_c, and for S4-00NN, the peak strength is very close to 50%.

A number of equations have been proposed for prediction and modeling of compression softening. Vecchio and Collins [77] and Vecchio [78] developed detailed formulations for use in analytical constitutive models and simplified equations for design calculations. Since these formulations have been developed from results of studies of reinforced concrete members, the analogy to SC members is only considered approximate. For the purpose of illustration, the equation from Vecchio [78] is used for comparison to results from the SC panel analyses. The softening coefficient β, is calculated as a function of the principal strain

ratio ($-\varepsilon_1/\varepsilon_2$) and is written and plotted in Figure 5.13. Also plotted are the values of $-\sigma_2^c / f'_c$ from the seven finite element analyses (where σ_2^c is the minimum principal concrete stress at the point of ultimate strength). The results of the seven finite element analyses show approximate agreement with the curve although a trend is not apparent due to scatter and limited results.

Based on the finite element analyses, a concrete softening of 50% is proposed. Using this value, the calculated concrete compressive strength would then become 0.5*f'c*, and the incremental concrete stress described previously would be written as:

$$\Delta f_c = 0.5 \cdot f'_c - f_{cy} \qquad \text{Equation 5.16}$$

Equation 5.15 can then be combined with Equation 5.16 to calculate the ultimate shear strength:

$$V_u = V_y + 0.5 \cdot (0.5 \cdot f'_c - f_{cy}) \cdot l_w \cdot t_{sc} \qquad \text{Equation 5.17}$$

5.5.3 Peak shear strain

Results from the finite element analyses and the experimental tests both show the average shear strain at ultimate strength increases with decreasing reinforcement ratio. This is clearly shown in the experimental and finite element results in Figure 5.6 where the measured average shear strains at peak shear strength (γ_{xy}^{μ}) are 0.0098, 0.0061, 0.0053 in./in. for specimens S2-00NN, S3-00NN, and S4-00NN, respectively. Also, the calculated strain states at yield (and also the results from the finite element analyses) show that the ratio of principal strains ($\varepsilon_1/\varepsilon_2$) increases with decreasing reinforcement ratios. In Figure 5.14, the

calculated maximum and minimum principal strains (ε_1 and ε_2) are plotted against average shear strain from the post-processed finite element analyses. As shown, the relationships between the principal strains and shear strains are approximately linear. If a linear trend is assumed for loading beyond yield, then the strain state of the shear panel at ultimate can be calculated by assuming that the ratio of principal strains ($\varepsilon_1/\varepsilon_2$) remains constant from the point of yield (ε_1^y, ε_2^y) to ultimate (ε_1^u, ε_2^u). For simplicity if it is assumed that the principal concrete strain at failure is equal to -0.0016 in./in., then a prediction of the strain state at ultimate can be calculated if the strain ratio at yield (ε_1^y, ε_2^y) and the shear strain at yield γ_{xy}^y are known. The shear strain at peak strength can then be calculated using the strain transformation relationship in Equation 5.18 which is based on the condition of pure shear. This is considered an approximation since the analytical results show slightly nonlinear strain relationships especially for the principal compression strains (Figure 5.14**)**.

$$\gamma_{xy} = \varepsilon_2 \left(\frac{\varepsilon_1}{\varepsilon_2} - 1 \right) \qquad \text{Equation 5.18}$$

The principal strain ratio at yield can be calculated by solving the strain transformation equation (Equation 5.18) for $\varepsilon_1/\varepsilon_2$ as shown in Equation 5.19 in terms of the shear and minimum principal strains.

$$\frac{\varepsilon_1}{\varepsilon_2} = \frac{\gamma_{xy}}{\varepsilon_2} + 1 \qquad \text{Equation 5.19}$$

The strain ratio at yield can then be calculated by substituting Equation 5.11 and Equation 5.13 into Equation 5.19. This results in Equation 5.20 that is then substituted along with

the assumed minimum principal strain of -0.0016 in/in. back into Equation 5.18 yielding Equation 5.21.

$$\frac{\varepsilon_1^y}{\varepsilon_2^y} = \frac{\gamma_{xy}^y}{\varepsilon_2^y} + 1 \qquad \text{Equation 5.20}$$

$$\gamma_{xy}^u = -0.0016\left(\frac{\varepsilon_1^y}{\varepsilon_2^y} - 1\right) \qquad \text{Equation 5.21}$$

Using this approach, the complete tri-linear shear force-strain response of the SC shear panels can be calculated. The result is plotted in Figure 5.15 with the first leg (i) defined by the uncracked stiffness and cracking resultant unit shear S_{xy}^{cr}, the second leg (ii) defined by the cracked stiffness and resultant unit yield strength S_{xy}^{y}, and (iii) the ultimate strength equal to S_{xy}^{u} and the limit strain γ_{xy}^{u}.

The calculated shear force-shear strain relationships are plotted in Figure 5.16. In Figure 5.16(a), (c), and (e) the experimental results and calculated relationship are shown and in (b), (d), and (f) the finite element results are plotted and compared to the calculated tri-linear relationship. In the plots, the relationships are calculated with average material properties for the respective test series, i.e. for the S2 series tests the steel yield and concrete compressive strength are averaged and the same is done for the S3 series tests.

Overall, the calculated responses show close and very slightly unconservative predictions of peak strengths in comparison to the experimental results. The ratio of experimental to calculated peak strengths is equal to 0.92 (Table 5.2) with a coefficient of variation of 4.9%.

Also, the peak shear strains show reasonable agreement with an average ratio (experimental over calculated) of 1.04 and a coefficient of variation of 20.6%.

5.5.4 Comparison to experimental database

In order to determine how well the calculated shear strengths and strains compare to actual SC structures, a survey of experimental tests of flanged SC shear walls is studied. The tests considered include the series from Ozaki et al. (2001) [30] and tests conducted by Takeuchi et al. [26]. These tests (9 by Ozaki et al. and 7 by Takeuchi et al.) were conducted on flanged shear walls rigidly connected to reinforced concrete foundations. Lateral loads were applied at the tops of the walls parallel to the orientations of the web walls as shown in the elevation view of a flanged wall test setup shown in Figure 5.17(a). The loadings subjected the flanged wall systems to combinations of in-plane shear and overturning flexure in the web walls and combinations of axial tension and compression in the flanges. Aspect ratios ranged between 0.50 and 1.75. Additional geometric and measured material properties are listed in Table 5.3. All of the other specimens showed combinations of flange and web steel plate yielding, buckling, and fracture and concrete compression failure.

Since the flanged wall tests (except for No. 1) showed combinations of shear failure of the web walls and flexure failure of the flanges at peak strengths, comparison to the previously described shear strength calculation is considered relevant. To calculate the shear strengths an effective web wall area was assumed. The area (rendered with diagonal hatch marks in Figure 5.17(b) is the area considered effective in shear and defines the wall length to the centerlines of wall intersections. The in-plane shear strengths are then calculated with

Equation 5.17. The measured peak strengths are then divided by the calculated strengths and listed in the last column. The results show reasonable agreement with a mean of 1.081 and coefficient of variation of 14.7%. In Table 5.4, the shear strains are also calculated and listed. These values are compared directly with the measured drift ratios from the tests. The average of the ratios is equal to 1.06 and the coefficient of variation is equal to 26.6%, similar to the results of the shear panel tests. The calculated shear force-strain relationships are plotted in Figure 18(a), (b), and (c) for three of the seven experimental tests by Takeuchi et al. [42]. The calculated points of concrete cracking (V_{cr}, γ_{xy}^{cr}), steel yield (V_y, γ_{xy}^{y}), and ultimate strength (V_u, γ_{xy}^{u}) are plotted for comparison to experimental envelope curves. The comparison is considered approximate since the calculated values are based on the pure shear condition and additional strengths attributed to the flange walls is not included. Overall, the tri-linear relationship shows reasonable prediction of peak strength and deformation.

5.5.5 Conclusions

An analytical method is developed for calculating the in-plane shear force-deformation response of SC flanged shear walls (or walls with boundary elements) from the point of steel faceplate yield to the ultimate strength of the shear wall. This approach is combined with the results of previous analytical work in order to provide a complete model for the prediction of SC wall response from initial infill concrete cracking to ultimate strength. The approach uses composite shell theory with a pure shear assumption so that simple equations can be developed for prediction of the ultimate strength and strain. The method

assumes that the boundary elements or flange walls are sufficiently strong to develop the full strength of the concrete infill in diagonal compression.

A series of finite element analyses of SC shear panels are modeled and benchmarked with panel tests by Ozaki et al. [30]. Results from the seven analytical models show that the concrete strengths are reduced to approximately 50% of f'_c, roughly consistent with previous research studying compression softening in cracked concrete. The extent of compression softening was similar for all seven of the shear panel analyses and did not appear to depend on principal strain ratio ($\varepsilon_1/\varepsilon_2$) or reinforcement ratio. The analytical results demonstrated increasing shear deformation capacity and principal strain ratios for decreasing reinforcement ratios. The principal strain ratios were also calculated for the yield point using the composite shell theory approach and showed consistent results with the finite element results. Since the finite element results demonstrated an approximately linear principal strain-shear strain response up to ultimate strength, a simple model is proposed for prediction of ultimate shear strain that assumes that the principal strain ratio is constant and the concrete failure strain is equal to -0.0016 in./in.

The ultimate shear strengths are calculated and compared to the results of shear panel and flanged wall tests in the literature. Overall, the strengths show good agreement with a mean of 0.93 for the ratios of experimental to calculated strengths for the shear panel tests and a mean of 1.08 for the flanged wall tests. The flanged wall comparisons though showed substantially more dispersion with a standard deviation of of 0.16 compared to 0.05 for the panel tests. This can be partially explained by the high degree of variability between the

different flanged wall test series resulting in different combinations of failure modes of the flanges, web walls, and connections. Also, the shear strength calculations for the flanged wall tests did not includes the effects of combined shear-flexure loading and did not account for additional strengths from the flanges. For the calculated predictions of ultimate shear strains, the mean for the ratios of experimental to calculated strains for the panel tests was 1.04 with a standard deviation of 0.21. Similarly, comparisons to the flanged wall shear strains resulted in more dispersion with a mean of 1.06 and a standard deviation of 0.28.

Table 5.1 Properties of Ozaki et al. panel tests

Specimen ID	t_p (in)	f'_c (ksi)	f_y (ksi)	Axial load (psi)	f_{ctm} (ksi)	w_c (in)	E_c (ksi)
S2-00NN	0.091	6.1	49.4	0	0.457	0.018	4,452
S2-15NN	0.091	6.0	49.4	213	0.451	0.018	4,415
S2-30NN	0.091	6.1	49.4	426	0.457	0.018	4,452
S3-00NN	0.126	6.1	50.9	0	0.457	0.018	4,452
S3-15NN	0.126	6.0	50.9	213	0.451	0.018	4,415
S3-30NN	0.126	5.8	50.9	426	0.438	0.009	4,341
S4-00NN	0.177	6.2	50.2	0	0.463	0.009	4,488

Table 5.2 Experimental, analytical, and calculated strains at peak strength

ID	Shear strain (x1,000 in./in.)					Shear strength (kips)				
	Exp.	FEM	Calc.	$\frac{\text{Exp.}}{\text{FEM}}$	$\frac{\text{Exp.}}{\text{Calc.}}$	Exp.	FEM	Calc.	$\frac{\text{Exp.}}{\text{FEM}}$	$\frac{\text{Exp.}}{\text{Calc.}}$
S2-00NN	9.78	11.17	7.88	0.876	1.241	665	703	765	0.946	0.849
S2-15NN	6.13	7.83	7.85	0.783	0.781	699	622	758	1.124	0.901
S2-30NN	10.37	7.90	7.87	1.313	1.317	699	720	763	0.971	0.895
S3-00NN	6.10	8.93	6.65	0.683	0.917	812	901	868	0.901	0.924
S3-15NN	8.05	5.87	6.64	1.371	1.212	845	752	864	1.124	0.965
S3-30NN	5.65	6.91	6.58	0.818	0.859	839	812	845	1.033	0.981
S4-00NN	5.34	4.70	5.72	1.136	0.934	922	952	1014	0.968	0.900
1024				1.00	1.04	Mean			1.01	0.92
Standard deviation				0.274	0.21	Standard deviation			0.09	0.05
Coeff. of variation				0.275	0.21	Coeff. of variation			0.09	0.05

Table 5.3 Dimensional and material properties of SC flanged wall tests

	Specimen	t_{sc} ksi	t_p in.	t_{sc} in.	Eff. wall length, l_w in.	$f'c$ ksi	fy ksi	Aspect ratio (h/l_w)
Ozaki et al. (2001) [30]	BS70T05	9.06	0.177	9.06	70	4.7	50.1	0.70
	BS50T10	9.06	0.091	9.06	70	5.1	55.4	0.50
	BS70T10	9.06	0.091	9.06	70	4.7	55.4	0.70
	BS85T10	9.06	0.091	9.06	70	4.7	55.4	0.85
	BS70T14	9.06	0.063	9.06	70	5.1	63.8	0.70
	No. 1	9.06	0.091	9.06	70	4.9	56.9	0.85
	No. 2	9.06	0.091	9.06	70	4.9	56.9	0.70
	No. 3	9.06	0.091	9.06	70	4.9	56.9	0.70
	No. 4	9.06	0.091	9.06	70	5.8	56.9	0.70
Takeuchi et al. [10]	H07T10	9.06	0.091	9.06	65	4.3	41.5	0.99
	H10T05	4.53	0.091	4.53	65	4.7	41.5	0.99
	H10T10	9.06	0.091	9.06	65	4.7	41.5	0.99
	H10T10N	9.06	0.091	9.06	65	4.7	41.5	0.99
	H10T10V	9.06	0.091	9.06	65	4.7	41.5	0.99
	H10T15	13.58	0.091	13.58	65	4.3	41.5	0.99
	H15T10	9.06	0.091	9.06	65	4.7	41.5	1.75

Table 5.4 Results from flanged wall tests

Specimen		Shear strain (x1,000 in./in.)			Shear strength (kips)		
		γ_{xy}^{u} (exp.)	γ_{xy}^{u} (calc.)	$\frac{\text{Exp.}}{\text{Calc.}}$	V_u (exp.)	V_u (calc.)	$\frac{\text{Exp.}}{\text{Calc.}}$
Ozaki et al. (2001) [30]	BS70T05	8.06	5.75	1.401	1664	1422	1.170
	BS50T10	7.49	8.18	0.916	1484	1164	1.275
	BS70T10	7.17	8.03	0.893	1293	1112	1.162
	BS85T10	6.03	8.03	0.751	1236	1112	1.111
	BS70T14	8.40	10.21	0.823	1214	1086	1.118
	No. 1	9.53	8.08	1.180	946	1132	0.835
	No. 2	9.75	6.78	1.437	1144	1283	0.891
	No. 3	8.67	6.78	1.278	1210	1283	0.943
	No. 4	9.75	7.08	1.378	1210	1420	0.852
Takeuchi et al. [10]	H07T10	5.90	7.64	0.773	1040	893	1.165
	H10T05	5.50	5.65	0.974	583	620	0.940
	H10T10	11.40	7.83	1.456	926	956	0.968
	H10T10N	8.80	9.46	0.930	907	1207	0.751
	H10T10V	8.50	7.83	1.086	1095	956	1.145
	H10T15	8.80	7.83	1.124	1471	956	1.538
	H15T10	8.80	7.83	1.124	883	956	0.924
Mean				1.06	Mean		1.08
Standard deviation				0.28	Standard deviation		0.16
Coeff. of variation				0.27	Coeff. of variation		0.15

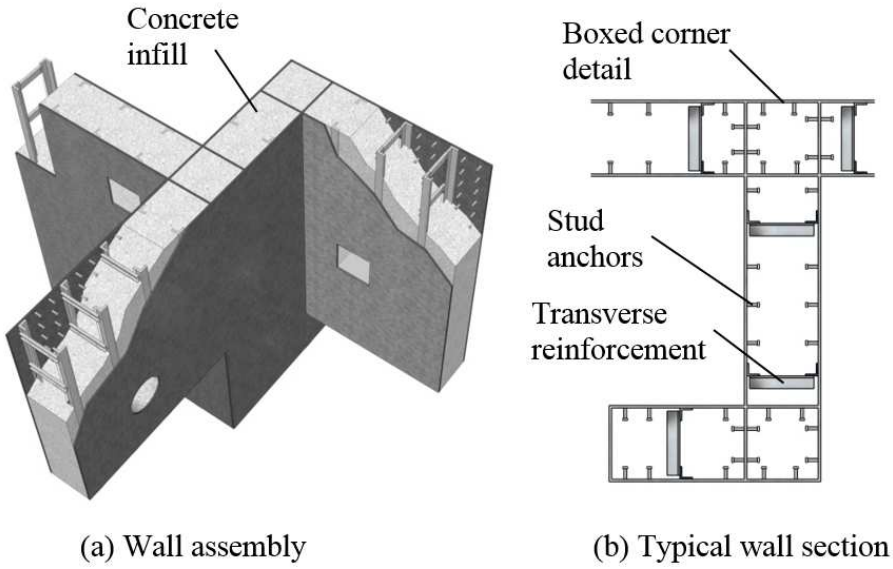

Figure 5.1 (a) Typical SC wall details, and (b) cross-section of SC wall (right)

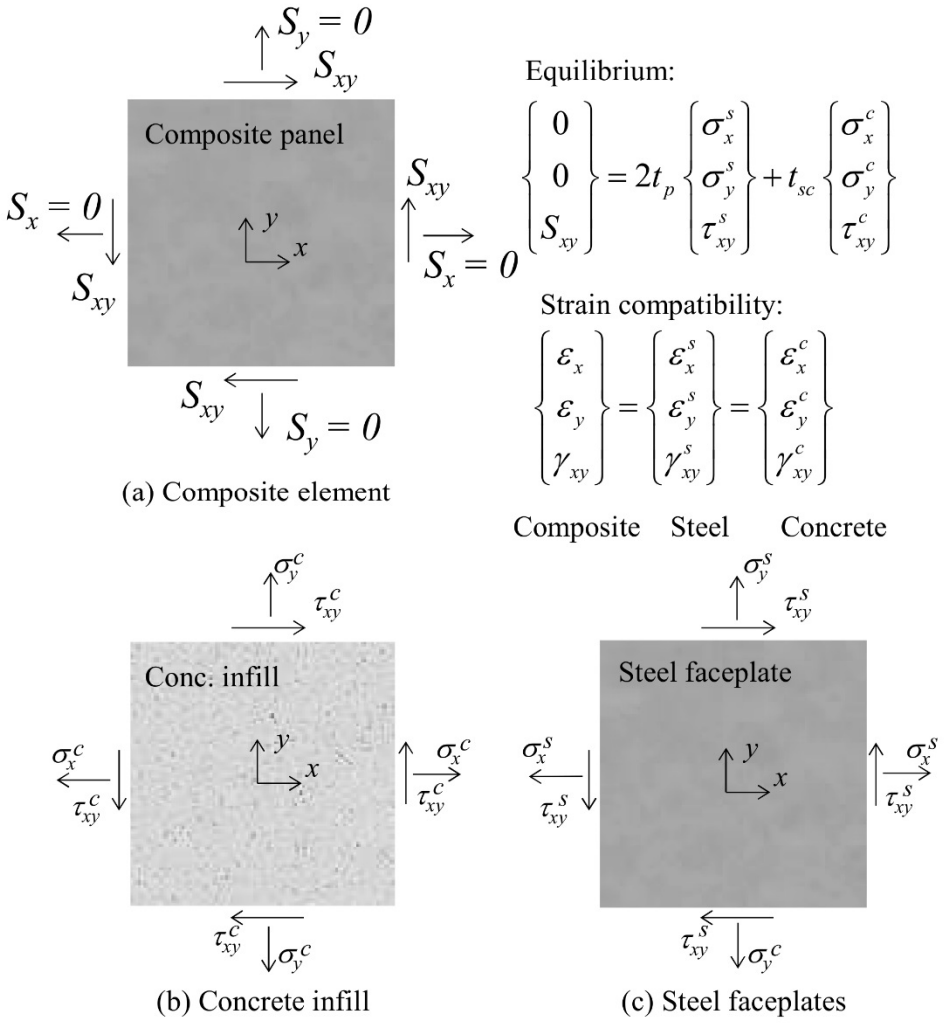

Figure 5.2 Stress states at point of steel faceplate yielding

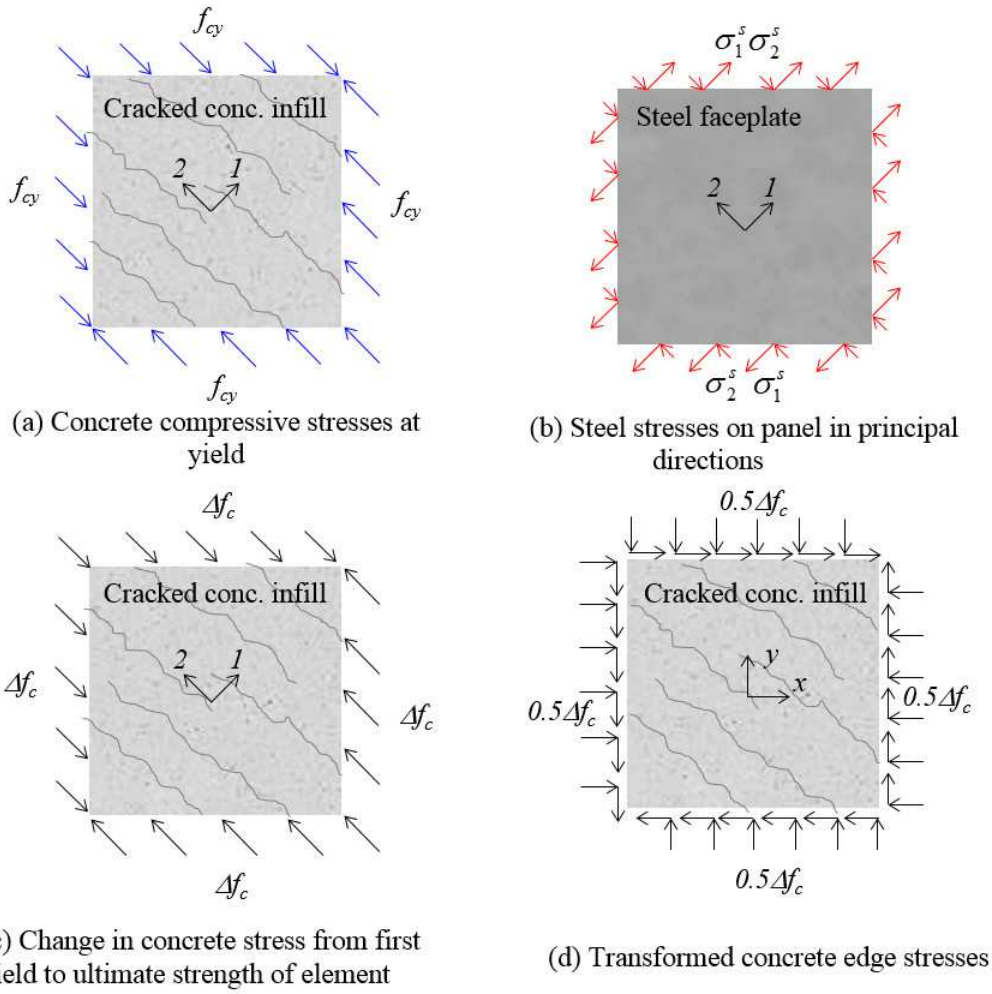

Figure 5.3 Shear element and concrete stresses at element ultimate strength

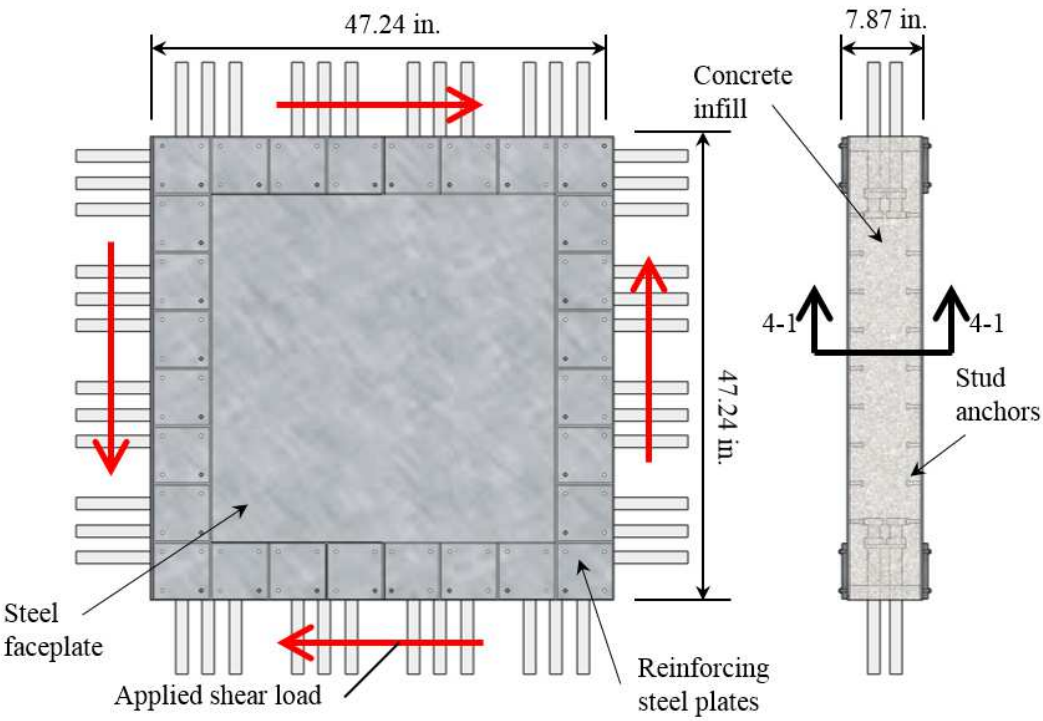

Figure 5.4 Details of Ozaki et al. SC shear panels

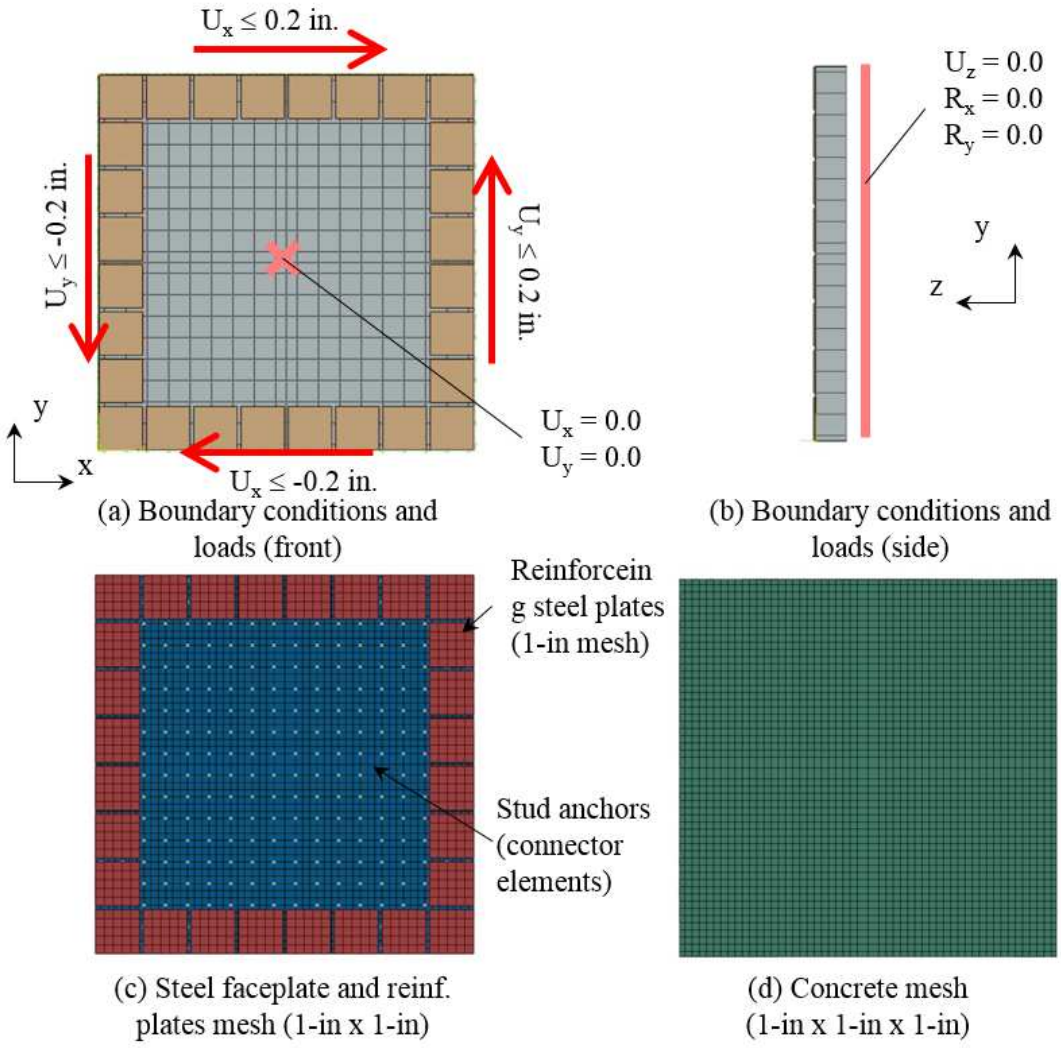

Figure 5.5 Shear panel meshing, loads, and boundary conditions

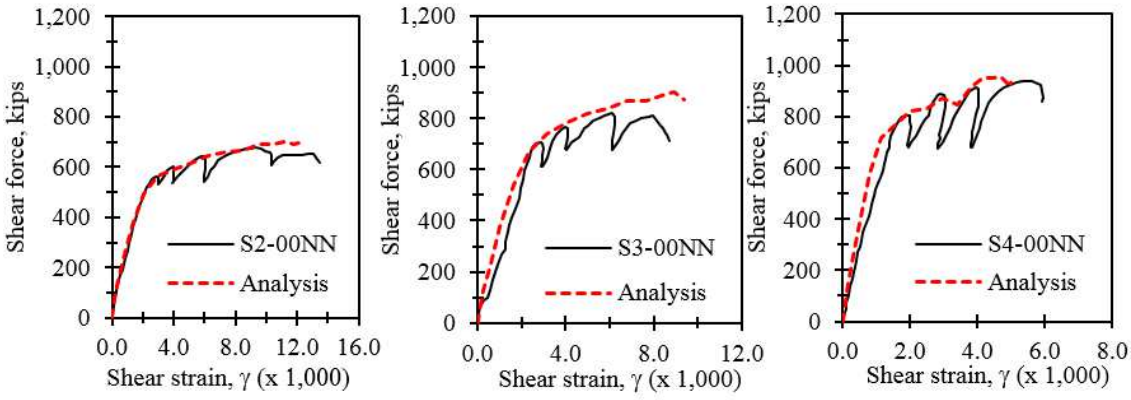

Figure 5.6 . Experimental and finite element shear force-average shear strain results

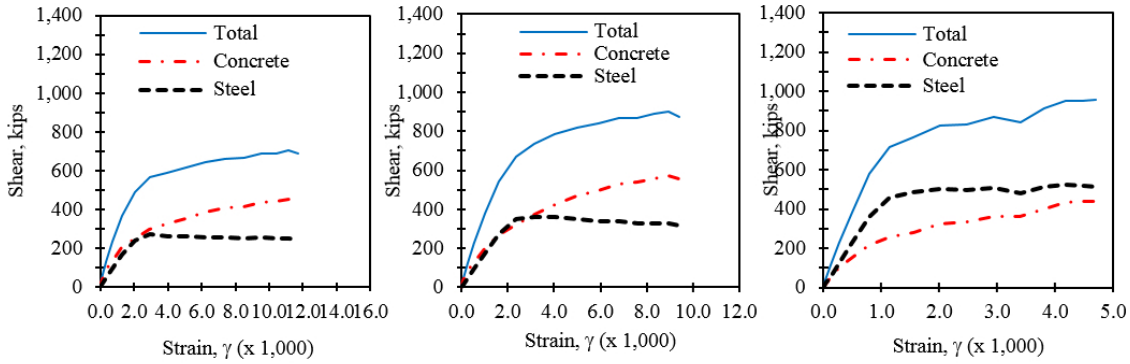

Figure 5.7 . Steel and concrete shear contributions

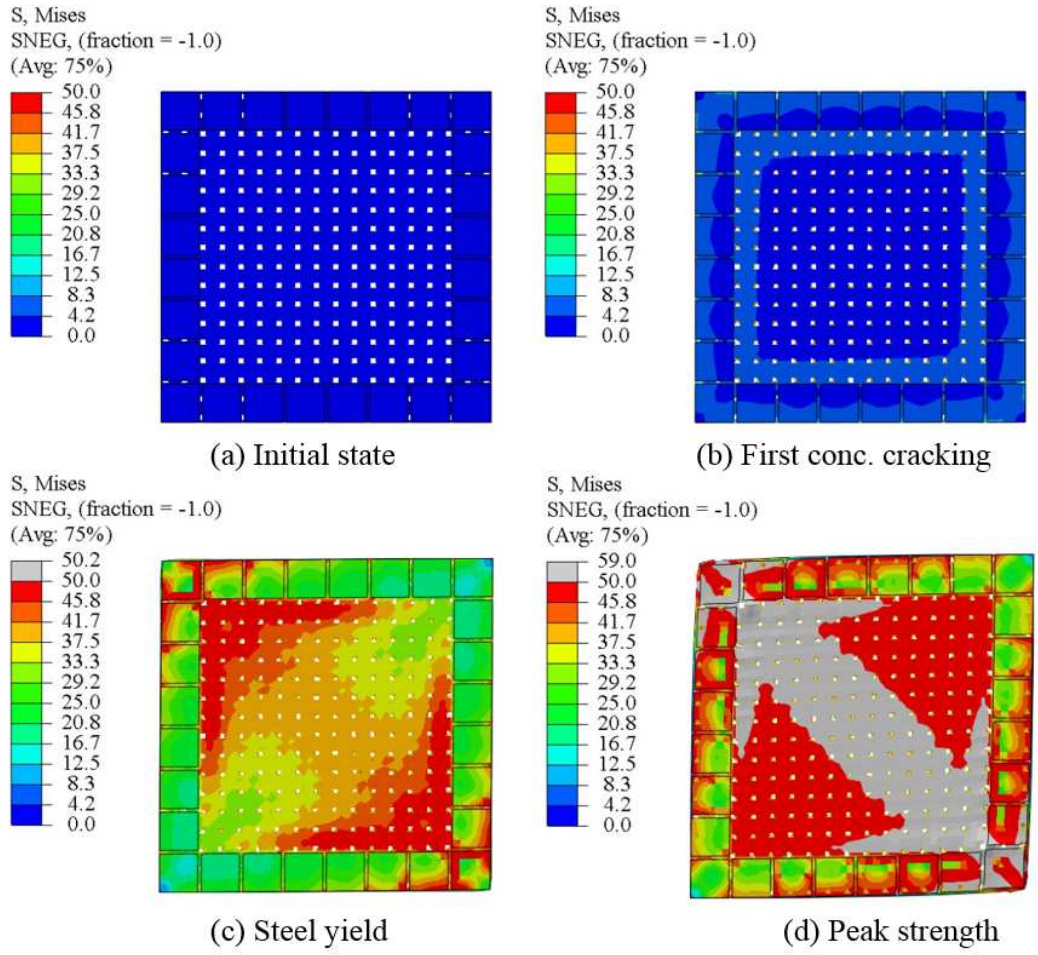

Figure 5.8 S2-00NN finite element von Mises stress contours

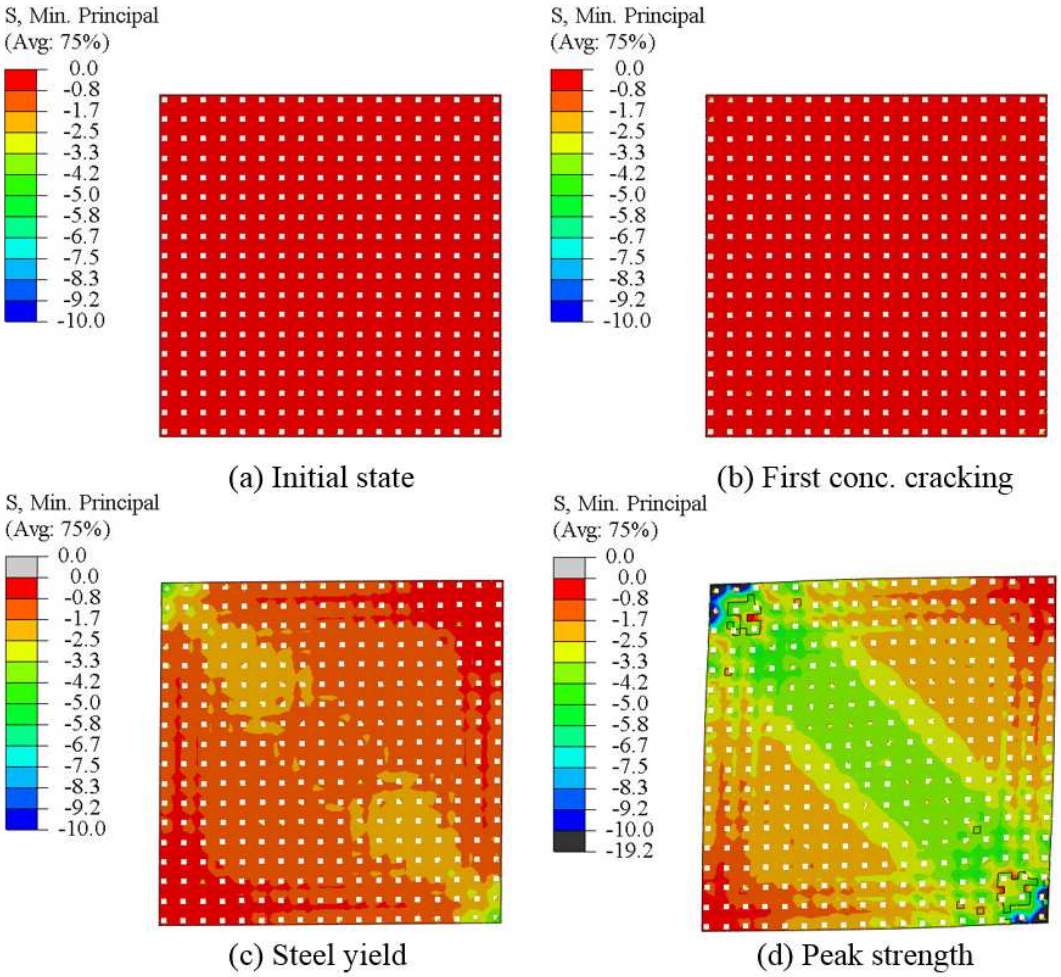

Figure 5.9 S2-00NN finite element minimum principal concrete stress contours

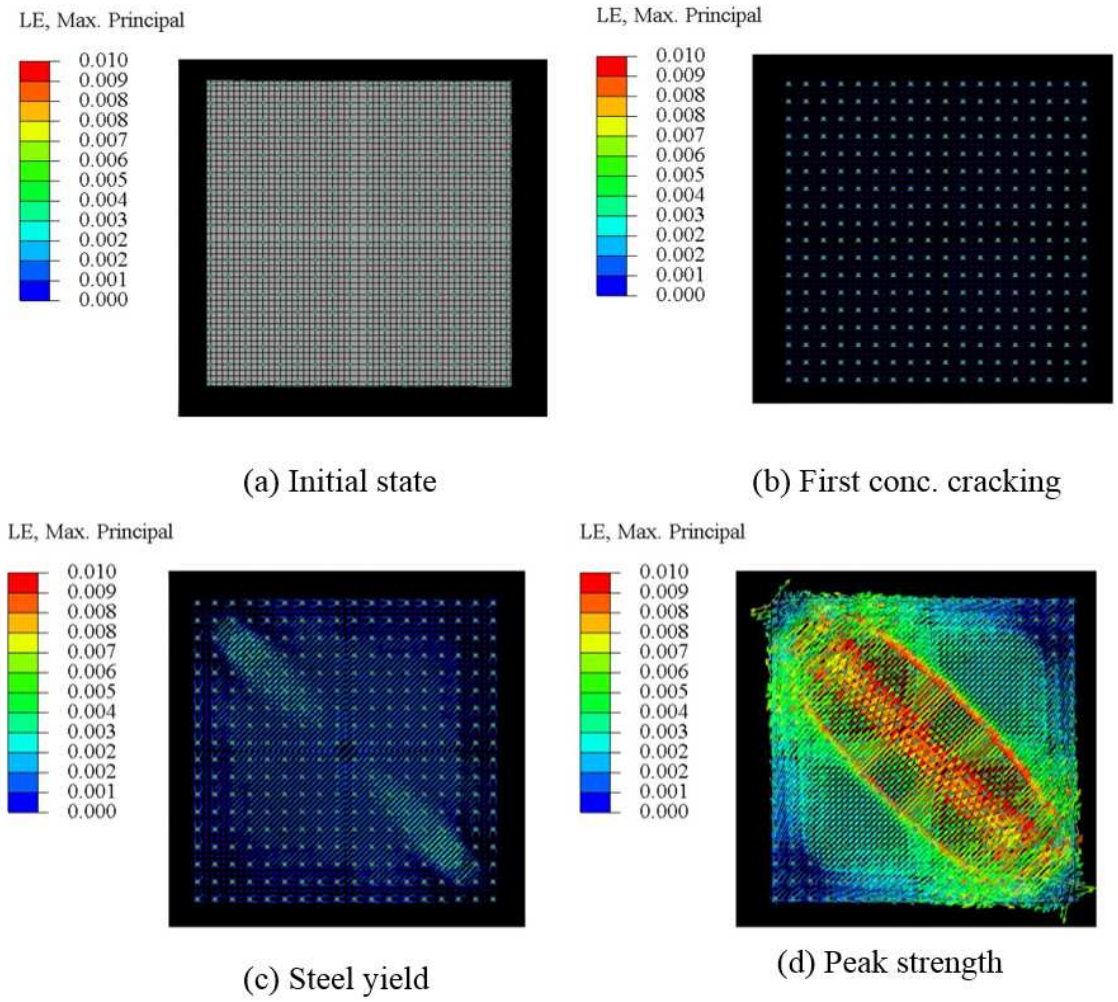

Figure 5.10 S2-00NN finite element maximum principal strain vector plots

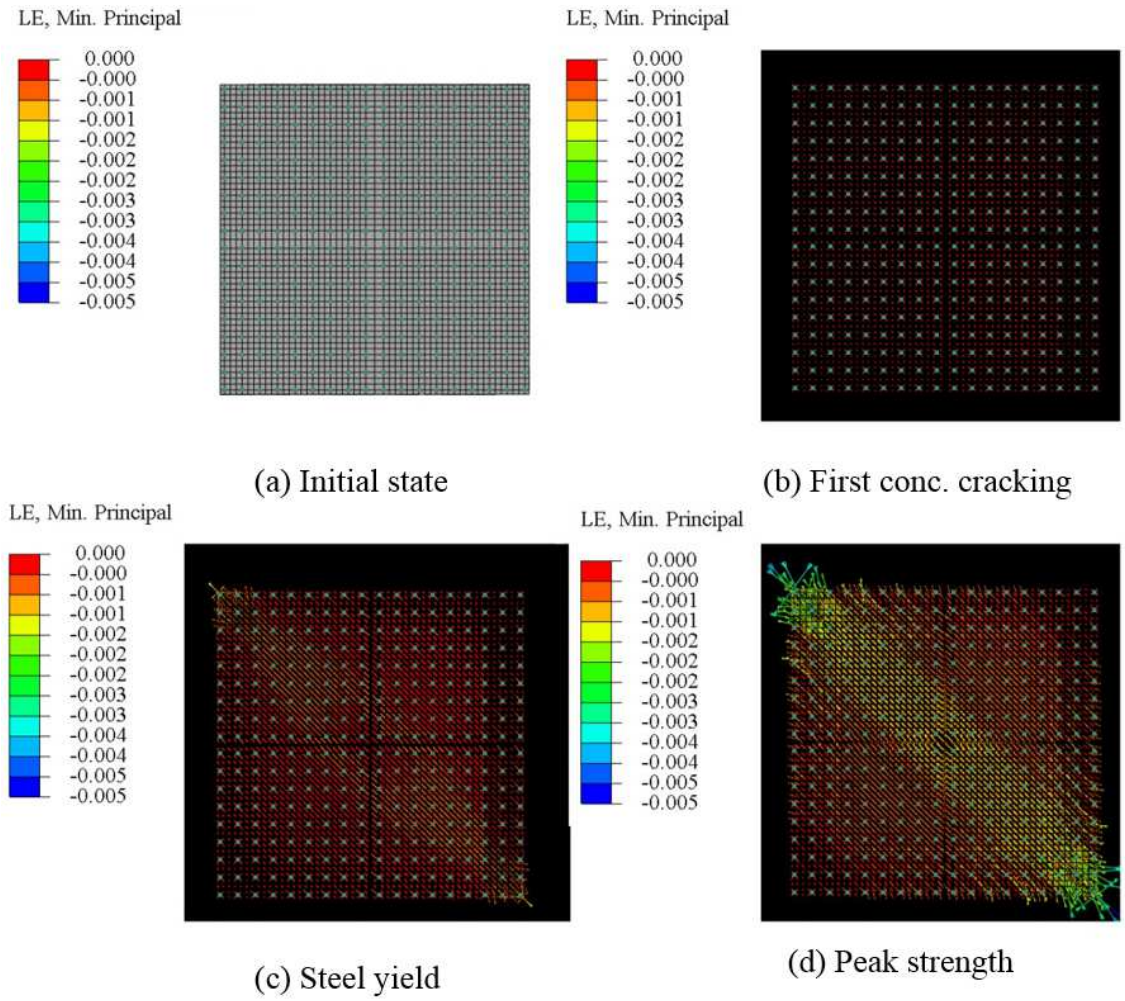

Figure 5.11 S2-00NN finite element minimum principal strain vector plots

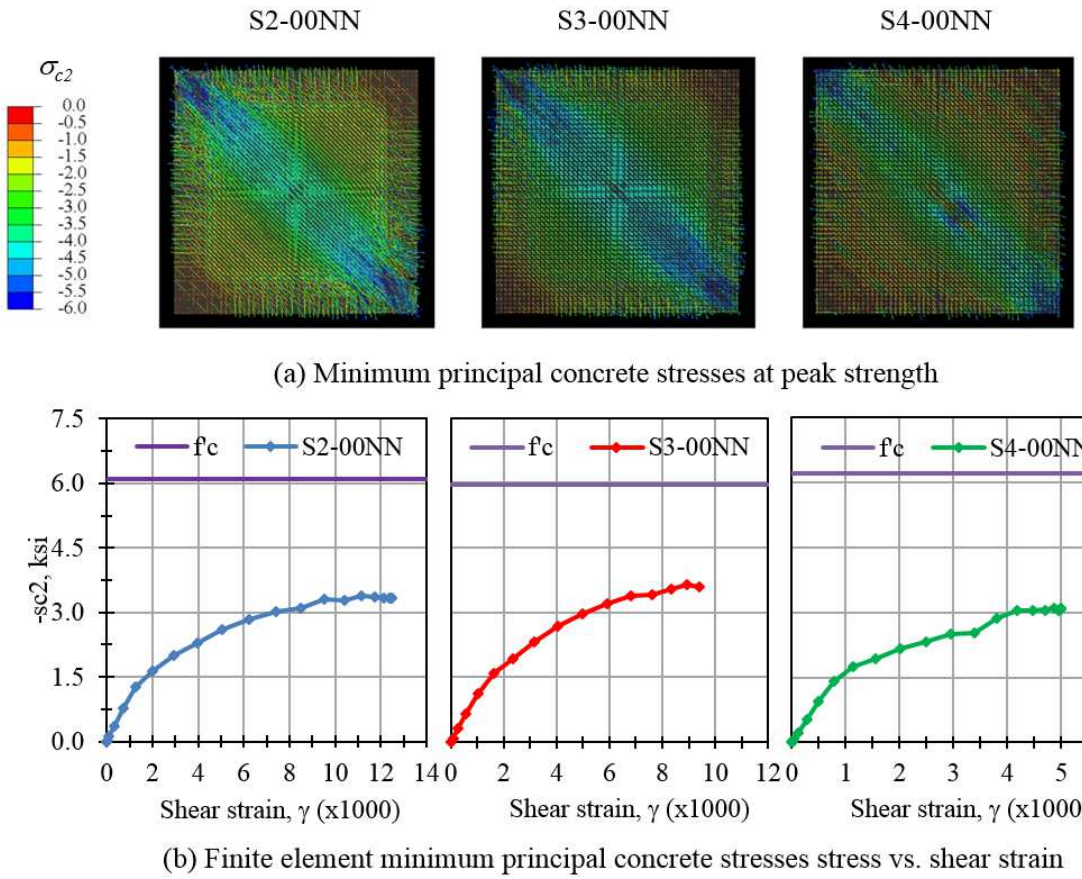

Figure 5.12 Normalized concrete compressive stresses

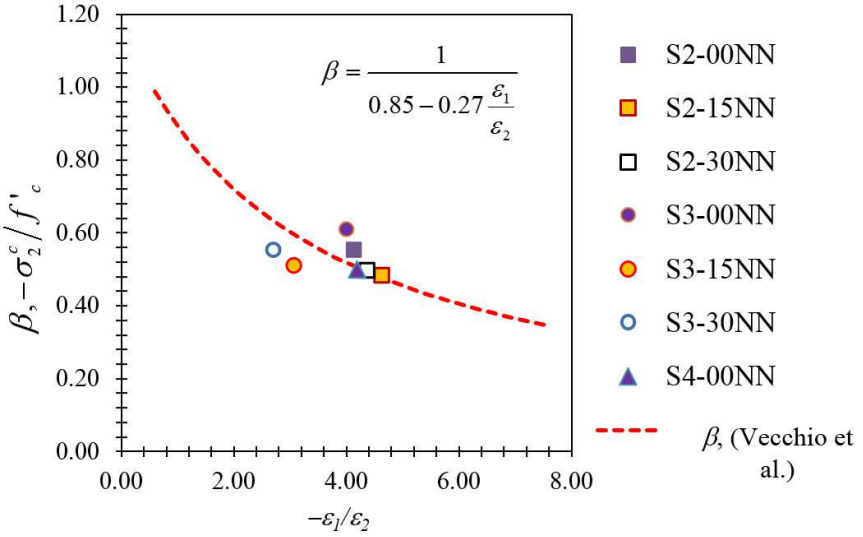

Figure 5.13 Concrete strengths for varying principal strain ratios

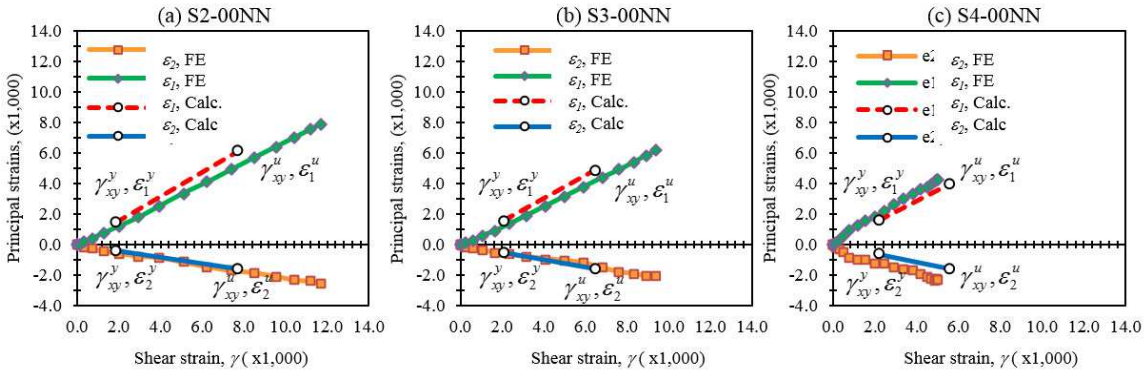

Figure 5.14 . Calculated and finite element principal stresses

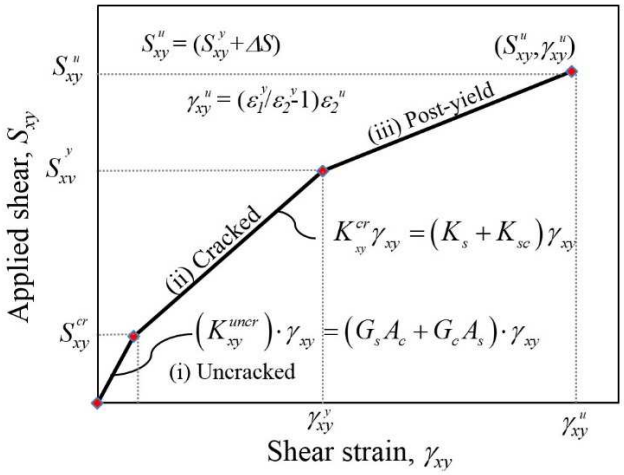

Figure 5.15 Tri-linear shear force-shear strain relationship

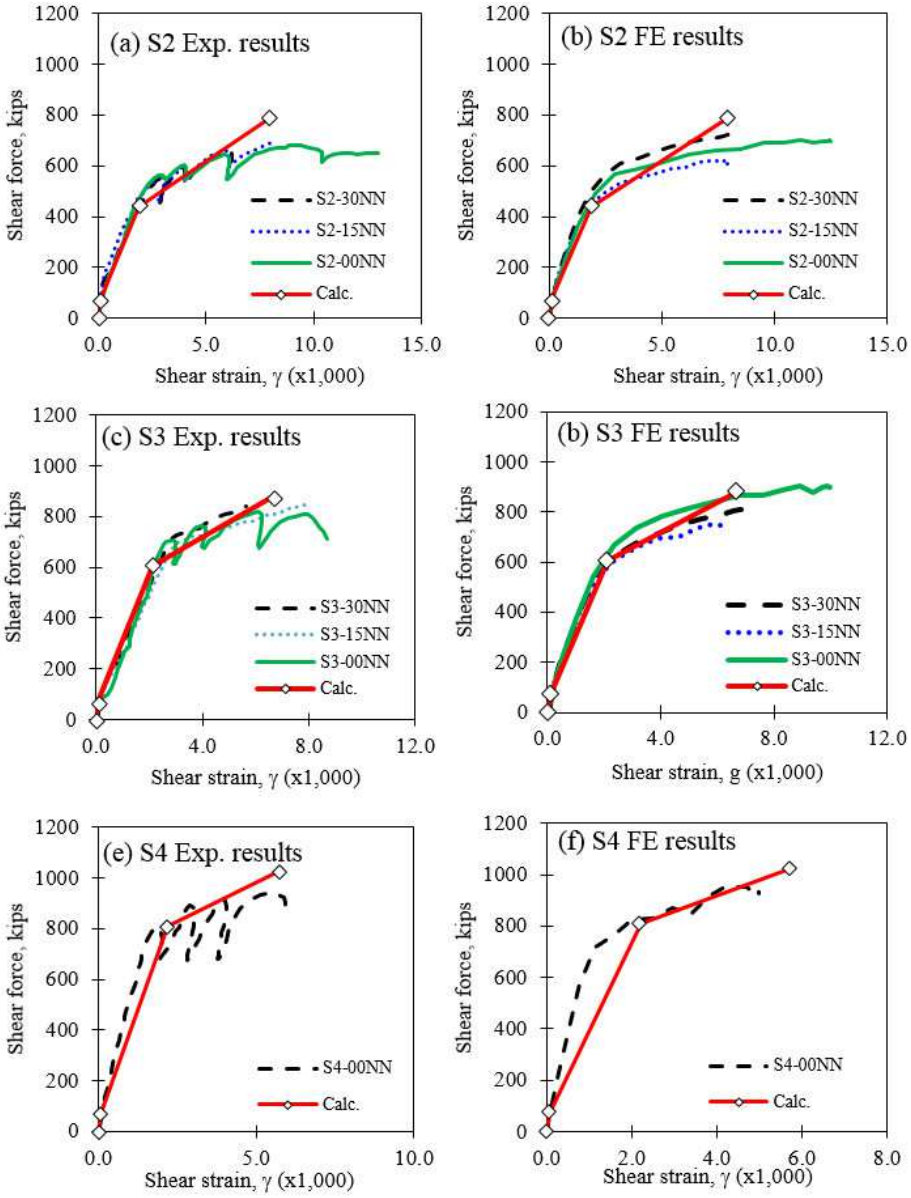

Figure 5.16 Element shear force-average shear strain results

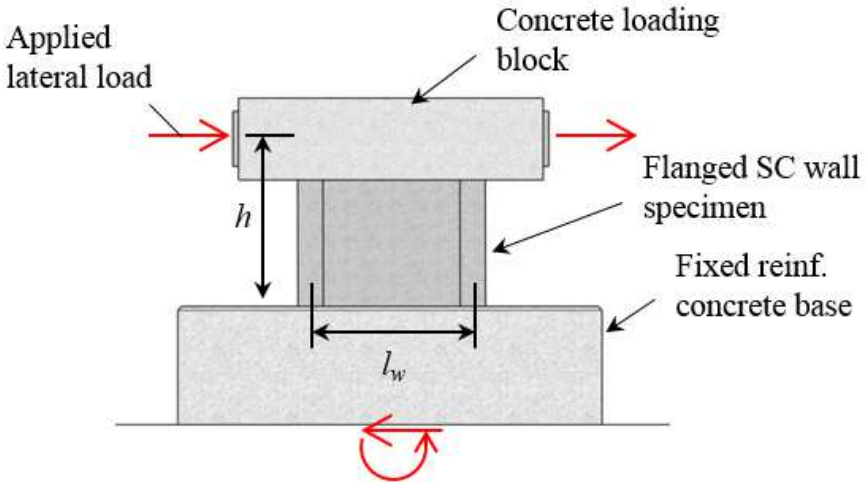

(a) Elevation view of flanged SC wall test

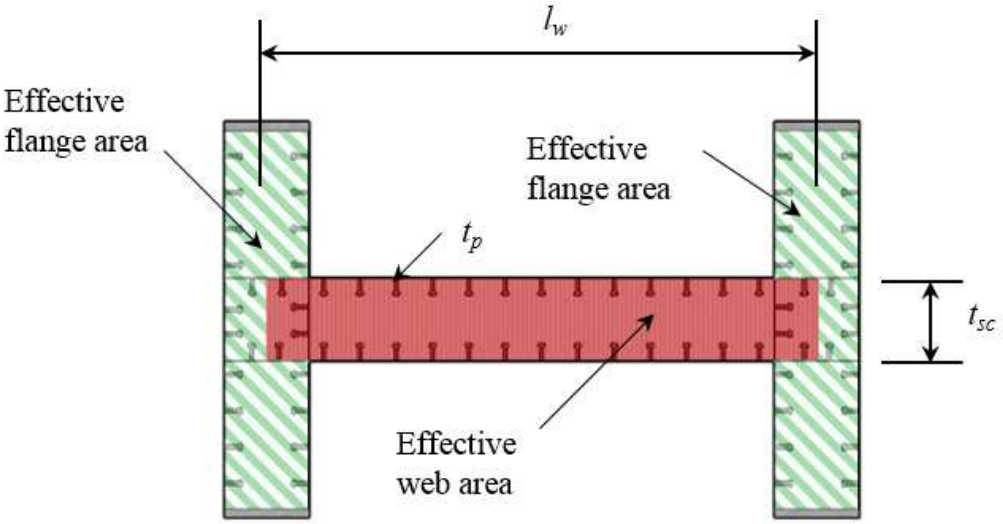

(b) Cross-section of typical flanged wall specimen with effective areas

Figure 5.17 General details of flanged SC wall tests

CHAPTER 6. FINITE ELEMENT ANALYSIS OF SC STRUCTURES

Increased use of steel-plate composite (SC) structures for nuclear power plant construction in recent years has generated the need for research studying the fundamental structural behavior of these systems. In this study, detailed finite element models of SC structures configured as lateral-load resisting core-wall structures are developed so that the global response can be studied. The effects of lateral pushover loads are studied with emphasis placed on the following three parameters: (1) geometric plan shape (square versus round), (2) wall section reinforcement ratio, and (3) structure aspect ratio. Results from the analyses are then compared to a proposed method for prediction of the ultimate lateral strength that accounts for both the flexural and shear strengths of the structure. The calculation of ultimate strength uses a methodology previously developed by the authors for prediction of the in-plane shear strength of SC walls in combination with existing code provisions for calculation of shear and flexural strengths.

6.1 Research significance

Previous research studying the lateral load-deformation behavior of SC structures has generally been limited to tests of shear walls with and without boundary elements and shear panel tests. Findings from these tests have added significantly to the current body of knowledge but have primarily focused on the mechanical behavior of SC members and not

the global behavior of whole SC structures. Two notable exceptions to this were two experimental tests conducted in Japan on reduced-scale SC containment internal structures. These tests included a $1/6^{th}$ scale primary shield wall structure composed of thick SC walls described in Shodo et al. [5] and also a test of a $1/10^{th}$ scale complete containment internal structure by Akiyama et al. [7]. Findings from these tests and subsequent supporting analytical studies provided significant insights into the behavior of this specific power plant structure based on an early pressurized water reactor power plant design by Mitsubishi Heavy Industries, Ltd. This structure had geometrically complex, thick and thin SC walls with perforations of differing shapes and sizes. Since these tests were based on a specific and unique complex power plant structure, the ability to extend the findings to general SC structures is limited. This current analytical study therefore takes the approach of using these two previous experimental tests for benchmarking of a finite element modeling approach that can then be used for development of a series of simpler SC structures for the purpose of studying fundamental lateral load-deformation behavior. To this end, core-wall structures composed of SC walls with detailing and section properties that are typically used in safety-related structures are modeled and analyzed with Abaqus/Explicit [6]. Analytical findings are then compared to strength design provisions currently in the literature and new design provisions for prediction of the strength of SC structures that have been developed by the authors.

6.2 Background

Structural building codes for safety-related SC structures have recently been adopted in a number of countries in order to regulate the design and construction of new nuclear power

plants. This has resulted in the development of the following codes: AISC N690s1-15 [4] in the US, JEAC-4618 [22] in Japan, and KEPIC-SNG [13] in Korea. The design provisions in these codes are based on findings from experimental and analytical research of SC shear walls in combination with relevant existing provisions from current structural steel and reinforced concrete codes that can be applied to SC structures. Extensive experimental testing occurred in the 1990s in Japan and was subsequently followed with additional research in North America, Korea, and the UK. Early tests primarily conducted in Japan studied fundamental structural behavior and the feasibility of SC construction as a substitute for reinforced concrete in power plant structures. Tests by Takeuchi et al. [10] on flanged SC shear walls studied the fundamental behavior of these systems and demonstrated the similarities and differences in behavior with reinforced concrete shear walls. SC shear panel tests were also conducted by Ozaki et al. (2003) [36]. This research included the development of a detailed analytical approach for the prediction of the in-plane stiffness and strength of SC walls. Additional experimental research studied the influence of specific structural detailing on behavior such as shear panel tests with partitions conducted by Takeda et al. [35] and flanged shear walls with perforations and alternative foundation connection designs conducted by Ozaki et al. (2001) [43]. More recent research in the US by Epackachi et al. (2015a) [80], Epackachi et al. (2015b) [81], and Kurt et al. [82] has studied the structural behavior of shear walls without boundary elements (pier walls) and has resulted in recommendations for analytical modeling and design of shear walls subjected to combined in-plane shear and in-plane flexure demands. The authors have recently developed a comprehensive analytical approach for prediction of the ultimate in-plane shear force-shear strain (S_{xy}-γ_{xy}) response of SC walls that is derived

with composite shell theory. This research is described in detail in Chapter 5 and is applied in this current study to SC core-wall structures. The analytical method predicts the complete in-plane shear response (assuming pure shear loading) of SC walls for all phases of applied lateral load including: (1) initial shear wall state with uncracked concrete, (2) reduction of stiffness resulting from cracking of the concrete infill, (3) prediction of the shear force associated with yielding of the steel faceplates, and (4) the post-yield shear stiffness and ultimate strength taking into account diagonal concrete compression action, concrete compression softening, and finally concrete failure. The calculation of ultimate shear strength (S_{xy}^{u}) is based on the assumption that the shear wall has sufficiently strong boundary elements and connections in order to develop the full strength of the concrete infill in diagonal compression. A mechanism is assumed where the diagonal compression in the concrete is resisted by tension in the connected boundary elements.

The design equation for in-plane shear strength of SC walls in AISC N690s1-15 defines the strength as the shear force associated with the onset of yielding of the steel faceplates. This is shown in Equation 6.1 and equal to the steel shear area A_s, multiplied by the steel yield strength f_y, and also multiplied by the coefficient κ. The in-plane yield strength of a composite section is a function of reinforcement ratio ($2t_p/t_{sc}$), relative stiffnesses of steel and concrete, and cross-sectional areas of the steel faceplates and concrete infill. A detailed derivation of this equation is developed in Seo et al. [73]. Equation 6.1 is an approximate and simplified equation for design calculations. The κ coefficient adjusts the yield strength

according to the previously described factors. κ is defined in Equation 6.2 with $\bar{\rho}$, the strength adjusted reinforcement ratio defined in Equation 6.3.

$$S_{xy}^{y} = \kappa \cdot f_y \cdot 2 \cdot t_p = \kappa \cdot f_y \cdot A_s \qquad \text{Equation 6.1}$$

$$\kappa = 1.11 - 5.16 \cdot \bar{\rho} \leq 1.0 \qquad \text{Equation 6.2}$$

$$\bar{\rho} = \frac{1}{31.6} \cdot \frac{f_y \cdot 2t_p}{t_{sc}\sqrt{f'_c}} \qquad \text{Equation 6.3}$$

The ultimate shear strength (S_{xy}^{u}) prediction developed in Chapter 5 calculates the in-plane shear strength of SC walls assuming that the strength of the concrete infill can be developed in diagonal compression. Whether a given SC shear wall is capable of developing this additional strength (above the yield limit, S_{xy}^{y}) must be considered on a case-by-case basis and depends primarily on the boundary conditions of the shear wall.

The shear stress in the concrete infill occurring when the steel faceplates reach the yield point in a given SC shear wall is defined as $0.5f_{cy}$ where f_{cy} is defined in Equation 6.4 and described in detail in Chapter 5. The 0.5 factor accounts for stress transformation from principal directions to the orientation parallel to the panel edges for the pure shear condition (a rotation of 45 degrees). In Equation 6.4, E'_c is defined as the effective concrete modulus (equal to $0.7E_c$ to account for the stiffness reduction in cracked concrete with E_c defined in ACI 349-06 [2] as the secant stiffness), E_s and ν_s are the elastic modulus and Poisson's ratio of the steel faceplates respectively, and S_{xy}^{y} is the resultant unit shear. For typical SC wall reinforcement ratios and material properties, f_{cy} ranges from approximately 20% - 30% of f'_c.

The ultimate shear strength V_u, (Equation 6.6) is equal to the yield strength S_{xy}^{y} defined in Equation 6.1 plus an incremental shear strength ΔS all multiplied by the effective shear wall length, l_w. The incremental shear strength is defined in Equation 6.5 and equal to the concrete strength $0.5 \cdot f'_c$ minus f_{cy} (Equation 6.4). The 50% reduction in concrete compressive strength ($0.5 \cdot f'_c$) takes into account the effects of concrete compression softening in cracked concrete.

$$f_{cy} = E'_c \left(\frac{-S_{xy}^{cr}(1+\nu_c)(1+\nu_s)}{2 \cdot E_s \cdot t_p (1+\nu_c) + E_c \cdot t_{sc}(1+\nu_s)} - \frac{\left(S_{xy}^{y} - S_{xy}^{cr}\right)(1+\nu_s)}{2 \cdot E_s \cdot t_p + E'_c \cdot t_{sc}} \right) \quad \text{Equation 6.4}$$

$$\Delta S = 0.5 \cdot (0.5 f'_c - f_{cy}) \cdot t_{sc} = 0.5 \Delta f_c \cdot t_{sc} \quad \text{Equation 6.5}$$

$$V_u = V_y + \Delta V = l_w \cdot S_{xy}^{y} + l_w \cdot \Delta S \quad \text{Equation 6.6}$$

6.3 FE modeling of core-wall structures

In order to study the lateral load-deformation response of SC structures, two structure shapes are modeled: (1) a structure that is square in plan, and (2) a structure that is circular in plan. The primary reason for modeling these two shapes is to determine the influence of the plan shape on global behavior. The square structure is considered since this is a common shape for core-wall structures in commercial buildings and power plants. The square structure is also the simplest geometry and therefore useful for the study of the fundamental lateral load-deformation response. The circular structure is more complex and representative of shield wall structures in power plants such as in the Westinghouse AP1000 power plant design. The geometric and detailing design of the core-wall structures were selected to be representative of actual SC structures. The detailing (steel faceplate

thickness, SC wall thickness, shear stud size, etc.) are consistent with AISC N690s1-15 and can be considered full or reduced scale depending on the type of structure they are intended to represent. For core-walls in building structures, the selected geometries are essentially full-scale and for power plant structures the dimensions could be considered full-scale or reduced scale (greater than $1/3^{rd}$ scale) depending on the structure being modeled.

The basic geometry of the circular structure is shown in Figure 6.1(a). The outer diameter (D) is equal to 227.3 in. and the wall thickness (t_{sc}) is equal to 24 in. The diameter was selected such that the cross-sectional area of the wall would be approximately equal to that of the square structure. Details of the square core-wall structure are shown in Figure 6.1(b). The outer dimensions (l) of the cross-section are 192 in. by 192 in. and the wall thicknesses are also equal to 24 in. The four corners are boxed in with web plates that partition the corner concrete from the concrete in the main walls. The cross-sectional area of the square structure is equal to 16,128 in.^{2} and the area of circular structure cross-section is equal to 15,328 in.^{2}, approximately 5% smaller. Both the square and circular structures are modeled with 24 in. thick SC walls with approximate shear connector spacing of 12 in. on center. The base of all of the structures are fixed and the tops are capped with an elastic solid that is 24 in. thick in order to distribute the applied lateral loads more uniformly to the tops of the structures.

Each finite element model is analyzed with three different steel faceplate thicknesses (t_p): 0.375 in., 0.500 in., and 0.625 in. so that the effect of varying wall section reinforcement

ratios ($2t_p/t_{sc}$) can be studied. In addition, a range of structure height divided by length aspect ratios are also modeled and analyzed with the height, *h*, defined as the height from the base of the structure to the elevation of the applied lateral load. For the square structure, aspect ratios (*h*/*l*) of 0.50, 0.75, 1.00, 1.25, 1.50, and 1.75 were considered and for the circular structure, aspect ratios (defined as structure height divided by outer diameter, *h*/*D*) of 0.53, 0.74, 1.00, 1.27, 1.48 were modeled. In summary, a total of 11 finite element models were developed, each run with three reinforcement ratios (3.1%, 4.2%, and 5.2%) for a total of 33 analyses.

Properties of the analytical models are listed in Table 6.1. The square core-wall models were each composed of 8 individual concrete parts: 4 for the corners and 4 in the SC walls. For the circular structure, a single monolithic concrete part was modeled. The top elastic blocks for both types of structures were tied at coincident surfaces at the top of the concrete and also the steel shell elements were tied to the edges of the elastic solids. A rigid body area was defined on the elastic solid with a control point defined at the point of the applied horizontal load.

6.3.1 Analytical modeling and benchmarking

As described previously, the finite element modeling approach is benchmarked using analytical results from previous work by the authors including modeling of a $1/6^{th}$ scale primary shield structure described in Booth et al. (2015) [83], and modeling of a $1/10^{th}$ scale containment internal structure experimental test described in Sener et al. [84]. The modeling properties in this current study are identical to those used in these previous

studies including: identical concrete and steel constitutive models, identical modeling of composite behavior, and explicit analysis approach.

6.3.2 Steel and concrete constitutive models

The steel faceplates are modeled with 3 in. by 3 in. 4-node reduced integration shell elements (C4R). Details of the meshing and part instances are shown in Figure 6.2 for the square structure and Figure 6.3 for the circular structure. The elements were sized such that four equal-sized elements are spaced between stud anchor locations. Multiple elements between shear connector elements allows for potential simulation of local buckling of the steel faceplates if sufficiently large slenderness ratios are present. Simpson integration rule is used with 5 integration points defined through the thickness of the shell elements. Geometric nonlinear analyses are conducted so that the post-yield and local buckling behavior of the steel faceplates can be simulated. For the steel, an elastic-plastic constitutive model is used that includes: von Mises yield surface, isotropic hardening, and associated flow rule. The uniaxial stress-strain relationship is based on a formulation by Varma and includes: (i) elastic modulus (E_s) equal to 29,000 ksi (ii) yield stress (σ_y) of 55 ksi, (iii) followed by a post-yield plateau with peak strain (ε_{sh}) equal to 15 times the yield strain (ε_y), (iv) followed by a strain hardening curve terminating with a peak strength of 75 ksi at a strain of 0.20 in./in. A nominal steel yield strength of 50 ksi is assumed for the steel faceplates, multiplied by the expected strength factor R_y = 1.1, defined in Table A3.1 of AISC 341-10 [85] (for ASTM A572 Gr. 50).

The Abaqus brittle cracking constitutive model is used to model the concrete infill with an assumed compressive strength f'_c, of 5,000 psi and secant stiffness E_c, equal to $57,000\sqrt{f'_c}$ (psi) (ACI 349-06 Chapter 8.5.1). Solid 8-node linear brick stress-displacement elements are used with reduced integration and hourglass control (C3D8R) with an average element size of 3 x 3 x 3 in. The model simulates cracking behavior with smeared cracking averaged over the element and implemented with modification of the stiffness values during subsequent analysis steps. Cracking is modeled with the fracture energy approach by Hillerborg et al. [55] and accounts Mode I and Mode II fracture, tension softening, and shear retention. Crack initiation is defined with a maximum stress criterion and crack orientations are fixed at crack initiation and limited to orthogonal planes at a given node. The post-cracking tension softening and shear retention behaviors are defined with recommended parameters from CEB-FIP Model Code for Concrete Structures [60]. For the tension softening stress-displacement response, a bilinear relationship is used with a crack width at zero tension stress of 0.0102 in. (w_c) and a concrete tensile strength (f_{ctm}) of 0.193 ksi.

6.3.3 Modeling of shear connectors and composite behavior

The composite connection between steel faceplates and concrete infill is achieved with a combination of steel tie-members oriented normal to the wall plane that connect opposing interior faces of the steel faceplates, and also headed stud anchors welded to the steel faceplates. For both the square and circular structure, ¾ in. diameter stud anchors are modeled with a vertical and horizontal spacing of 12 in. on center on all of the interior surfaces of the steel plates (including the web partitioning plates shown in Figure 6.1(b).

In the circular structure, steel tie members are also modeled with an average spacing of 31.75 in. horizontally and 24 in vertically. The tie members are modeled with truss elements embedded in the concrete infill with connector elements on both ends that tie the ends of the truss elements to nodes on the steel shell elements.

Modeling of the headed stud anchors and the overall composite response is achieved with connector elements tying coincident nodes on the surfaces of the concrete elements to shell element nodes. Calibration and modeling assumptions are based on recommendations from Zhang et al. [64] that developed benchmarked analytical models of experimental pushout tests.

The connector elements are assigned the shear force-slip relationship developed by Ollgaard et al. [63] shown in Equation 6.7 (where Q is the shear force per stud and δ is the slip occurring at the concrete-steel interface) and Equation 6.8, that defines the connection strength, Q_u, as a function of stud cross-sectional area, A_{stud}, steel tensile strength, $F_{u,stud}$, concrete compressive strength f'_c, and concrete secant stiffness, E_c. This formulation has the advantage of concisely grouping all of the force-slip response (stud bending, stud tension, concrete crushing, steel plate/concrete friction, etc.) into a single empirical equation.

$$Q = Q_u \cdot \left(1 - e^{-18\delta}\right)^{2/5} \qquad \text{Equation 6.7}$$

$$Q_u = \min\left(\phi A_{stud} \cdot F_{u,stud}, 0.5 A_{stud} \sqrt{f_c' \cdot E_c}\right) \qquad \text{Equation 6.8}$$

6.3.3.1 Lateral load-deformation response

The lateral load-displacement (V-Δ) results are plotted in Figure 6.4 and Figure 6.5 where the loading is defined as the total load applied to the top of the structure and the displacement is taken at the elevation of the applied load. Since the structures are configured as free-standing, fixed-base structures, the applied load is equal to the base shear. The four plots in Figure 6.4 each show the results for the given structure aspect ratio (0.50, 0.75, 1.00, 1.25) and also the three reinforcement ratios for each structure aspect ratio (3.1%, 4.2%, and 5.2%). Similar plots are shown in Figure 6.5 for the circular structures. As expected the taller structures show lower ultimate lateral strengths and greater displacement capacity since these structures primarily show flexural response. Similarly, the shorter structures are capable of greater base shear strengths since overturning demands are reduced.

Results from the analysis of the square structure with aspect ratio 1.25 and t_p = 0.625 in. are shown in Figure 6.6(a), (b) and (c). In the figures, stress and strain contours, and deformed shape (scaled 20x) are shown for the mechanical state at peak strength of the structures. Overall, the response shows a combination of flexural and shear behavior with vertical tension and compression occurring in the flange walls and combinations of shear and flexure in the web walls. In Figure 6.6(a), the steel von Mises stress contours are shown with yielding occurring completely at the base of the structure and also extending nearly to the top of the web walls (walls parallel to the direction of applied load). In Figure 6.6(b), minimum principal concrete stress contours are shown. A diagonal concrete compression band is apparent at peak strength with highest compression stresses occurring at the base

on the compression side of the structure and at the upper corner on the tension side of the structure. Maximum principal concrete strains are shown in Figure 6.6(c), with flexural tension concrete cracking apparent in the tension flange and combinations of flexural tension cracking and diagonal shear cracking in the web walls.

For the circular structure (shown in Figure 6.6(d), (e), and (f) similar behavior is apparent in comparison to the square structure, with vertical flexural demands largely confined to ends of the structure where the walls are oriented perpendicular to the applied load direction and shearing more prevalent in the portions of the walls oriented parallel. Unlike the square structure, shearing and flexural demands are combined to a higher degree without clearly delineated tension and compression stresses at the ends and shear behavior along the sides. The influence of structure aspect ratio on ultimate strength is illustrated in Figure 6.7. In Figure 6.7(a) and (c) peak lateral strengths are plotted versus aspect ratio for the square and circular structures respectively. For both structure shapes, the ultimate strengths of the structures converge on a maximum lateral strength since the strengths of the taller structures are controlled by flexure. Similarly, in Figure 6.7(b) and (d) the peak base shear strengths are plotted versus aspect ratio. In the plots, the base shear strengths converge to a maximum strength in all cases as the aspect ratios are decreased. For taller aspect ratios, the base shear strengths are less than the maximum since these structures are subjected to greater overturning flexure demands. In all of the plots, three trends are shown representing structures with different reinforcement ratios. Since increasing steel faceplate thicknesses are modeled, the ultimate base shear strengths increase with increasing reinforcement ratios.

6.3.4 Shear strength

The base shear strengths from each analysis are divided by the calculated shear yield strengths in Figure 6.8(a) and (b). The peak base shear strengths from the analyses, V_{base}, are divided by the total centerline wall lengths of the core-wall structures, l_{CL}, resulting in an average unit shear strength, S_{base}. This value is then divided by the unit in-plane yield strength, S_{xy}^{y} defined in Equation 6.1 and calculated for each respective reinforcement ratio. In Figure 6.8 the values of S_{xy}^{y} are listed for the three considered reinforcement ratios: 3.1%, 4.2%, and 5.2%.

In the plots, the base shear strengths are ordered from smallest to largest structure aspect ratio. As shown, for both the square and circular structures, When the strengths are normalized by the calculated shear strengths, the trends are essentially identical and therefore the strengths are proportional to the calculated yield strengths. For the square core-wall structures, the ratios (S_{base}/S_{xy}^{y}) converge to a maximum ratio of approximately 0.55 for the smallest aspect ratio. Similarly, for the circular structure, the ratio converges to approximately 0.50 for the shortest aspect ratios of 0.53 and 0.74. The effectiveness of the square shape is therefore slightly better in resisting shear than the square section although the difference is too close to draw definitive conclusions.

In Figure 6.9(a) and (b) shear stress contours are shown plotted for the circular and square structures. Concrete shear stresses are shown and oriented in the global coordinates (τ_{13}). Cross-sections are shown taken at the mid-heights of both structure shapes. The shear

stresses are highest in the wall segments parallel to the applied load direction and also in the regions of the walls that are subjected to higher vertical compression forces. Vertical compression is highest along a diagonal of the web walls in the square structure and in an approximate diagonal band of compression in the circular structure. Both structures show similar shear stress distributions with shear resistance largely confined to the web walls of the square structure and more spread out in the circular structure.

Results from previous experimental tests of SC shear walls (both flanged walls and shear panels) have demonstrated reserve in-plane shear strength after the point of yielding of the steel faceplates. As described previously, this occurs if the wall is detailed such that diagonal compression in the concrete infill is resisted directly by the boundary elements or flange walls. The extent of the reserve strength is primarily a function of the relative strengths of the shear walls and boundary elements. Many previous flanged wall tests were designed such that the governing failure mode would be shear failure of the web wall. This can be ensured by constructing flange walls that are more stout than the web walls by either adding thick steel end plates or using thicker steel faceplates. In contrast to typical flanged wall tests, core-wall structures are likely to be constructed with all of the walls having identical cross-sections. In order to determine whether web walls are capable of shear strength beyond the yield limit, results from the square core-wall analyses are post-processed. In Figure 6.10, the total base shear strengths and the shears in the web walls are plotted (Figure 6.10(a), (b) and (c)). For the three reinforcement ratios, the webs provide approximately 88% of the shear force with the remaining 12% resisted by the flange walls. The strengths of the web walls are then compared to the calculated yield and ultimate

strengths in Figure 6.10(d), (e), and (f). In the three plots, the yield strengths (V_y) calculated for the web walls are plotted (the horizontal broken line) and the ultimate (V_u) strengths using Equation 6.6 are also plotted. The yield and ultimate shears are calculated using the effective wall length, l_w, measured along the centerlines of the walls. As shown in the plots, the shear strengths of the web walls in all three cases exceed the calculated yield strengths and also slightly exceed the ultimate strengths except for the 3.1% reinforcement ratio structure where the web wall strength reaches 93% of the calculated ultimate strength. This leads to the conclusion that the web walls in the square core-wall structure are sufficiently stout to be able to develop the ultimate shear strength of the web walls.

The circular and square cross-sections are divided into individual segments so the the distribution of shear forces along the wall can be compared. In Figure 6.11(a), the circular cross-section is divided into 20 segments of equal length (31.75 in. measured along the wall centerline). In the figure, tables list the segments and associated angles with increments of 18 degrees, with the angles measured from vertical (0 deg., 18 deg., 36 deg., etc.). Wall segments 1 and 11 are oriented perpendicular to the applied load direction. A similar approach is used for segmenting the square section as shown in Figure 6.11(b).

The segment shear forces are plotted in Figure 6.12(a), (b), and (c) for three reinforcement ratios and for the structure with aspect ratio equal to 0.50. In each plot, the 20 points represent the segment unit shear force at the point of peak strength of the core-wall structure. Also, the segment shear forces are all parallel to the direction of applied load. Points 1, 2, 3, 19, and 20 represent the wall segments of the flange wall that are subjected

to compression, and points 9, 10, 11, 12, and 13 represent the flange wall segments on the tension side. As shown, the flange wall subjected to compression is much more capable of carrying out-of-plane shear. For the compression flange, the average shear force at ultimate strength (in terms of multiples of $\sqrt{f_c'}$) equals $8.6\sqrt{f_c} \cdot t_{sc}$ for the compression flanges and $1.6\sqrt{f_c} \cdot t_{sc}$ for the tension flanges. Also, in the web walls, segments towards the compression end of the walls carry very high shears and drop off towards the tension ends. The average shear forces for the webs and flange walls are also shown in the plots. Similar to Figure 6.10, the average resistance in the web walls tend to exceed the calculated shear strengths, S_{xy}^{u}, except for the ρ = 3.1% wall.

In the Figure 6.13, results from the aspect ratio 0.74 circular core-wall structure are shown for the three reinforcement ratios (3.1%, 4.2%, 5.2%). In the plots, the segment unit shear forces are plotted for the 20 segments. As shown in the plots, the segment unit shear forces in the segments near the sides (segments 7 and 15) are highest and diminish around the circle with the lowest shears occurring in the wall perpendicular to the loading direction (segments 1, 11 and 20). Also shown are slightly higher segment shear forces towards the compression side of the section (segments 9, 10, 16, and 17) since the vertical compression in the wall is higher due to overturning demands thus resulting in less concrete cracking, and therefore higher shear stiffness. The results show that when the circular structure is at peak strength, the highest shear forces along the wall (segment 7 and 15) are very close the the calculated yield unit shear strength, S_{xy}^{y}. Also shown in the three plots is the average shear strengths that are approximately equal to 42% of the calculated ultimate strengths

and 48% of the calculated yield strength. In conclusion, prediction of ultimate structure strength could be calculated by assuming an effective shear length equal to 50% of the circumferential length multiplied by the ultimate strength, S_{xy}^{y}.

6.3.5 Flexural strength

The flexural strengths of the core-wall structures are calculated using the plastic stress distribution method according to AISC 360-10 Chapter I2.2a [65] The flexural strengths M_p, are calculated using the following assumptions: (i) all of the steel on the section has reached yield, (ii) the concrete stresses on the compression side of the neutral axis are equal to $0.85f'_c$, (iii) and concrete stress on the tension side of the neutral axis are assumed equal to zero. Section fiber models are then developed of the the complete square and circular core-wall sections using a spreadsheet program with the section discretized into 1 in. elements and locations and section properties assigned to each point. The flexural strengths are then calculated and the results plotted in Figure 6.14 and Figure 6.15.

6.3.6 Core-wall lateral strength

The shear and flexural strength predictions are combined to calculate the ultimate lateral strengths of the structures. The strengths are calculated as the lesser of the shear strength multiplied by the structure height and the flexural strength of the section. The results are plotted in Figure 6.14 and Figure 6.15 and listed Table 6.2. The peak strengths from the finite element analyses are denoted M_{FE}, and the calculated strengths (M_{calc}) are defined as the lesser of M_p or either V_y or V_u multiplied by the height, h. In Table 6.2 the ratios of analytical strengths to calculated strengths are listed (M_{FE}/M_{calc}).

In Figure 6.14 each point on the plots represents the peak lateral strength of the structure for the respective aspect ratio. Figure 6.14 (a) to (c) compare the analytical results of the square structures for the three reinforcement ratios to the shear strength limit, V_y. The comparison shows very close agreement, with the structures with h/l equal to 0.50, 0.75, and 1.00 falling in the shear controlled region (to the left of the transition point), and h/l equal to 1.25 very close to the transition point and h/l greater than 1.25 in the flexure controlled region. The plots show that the strength prediction based on the in-plane yield strength is clearly conservative for h/l less than 1.25.

This is also repeated in Table 6.1 where the ratios of M_{FE}/M_{calc} are between 1.14 and 1.33. The same comparison is plotted in Figure 6.14(d) to (f) but using the ultimate shear strength, V_u, instead of V_y. As expected, using the calculated shear strength governed by the ultimate in-plane shear strength results in an improved prediction of the mean lateral strength with a coefficient of variation equal to 0.07 compared to 0.11 for the strength using V_y. The strength calculated with V_u though, results in slightly unconservative predictions near the shear-flexure transition points.

A similar comparison is shown in Figure 6.15(a) – (c) for the circular core-wall structure. The peak strengths from the 15 analyses (three reinforcement ratios for each of the five structure aspect ratios). Since the average shear was previously determined to be approximately one half of the peak shear, an effective shear area of 0.5 of the wall length (circumference measured along wall centerline) is used. Also, since the analytical results demonstrated that the peak segment shear strengths approximately reach the yield strength,

V_y, this value is reasonable for prediction of the shear strength. Therefore, the calculated shear strength is equal to $0.5 \cdot A_s \cdot \kappa \cdot f_y$, where A_s is the total cross-sectional steel area of the structure, κ is defined in Equation 6.2, and f_y is the steel yield strength. In the plots in Figure 6.15(a) – (c) the calculated shear strengths are multiplied by the structure heights (dotted blue lines).

For the circular structures, the calculated flexural strengths, M_p, are shown to be slightly conservative, with a shear-flexure transition occurring at an approximate aspect ratio (h/D) of 1.0. Overall, the ratio of analytical strengths to calculated strengths for the circular structure result in a mean of 1.14 and standard deviation of 0.19, as shown in Table 6.2.

6.4 Conclusions

Square and circular SC core-wall structures are modeled and analyzed using Abaqus/Explicit in order to study the fundamental lateral load-deformation behavior of these structures. The finite element modeling approach described in Chapter 3 was used. The analytical results demonstrate that the lateral strengths of the structures are primarily governed by flexure for h/l greater than approximately 1.25 for the square structures, and h/D greater than 1.0 for the circular core-walls. For aspect ratios less than these limits the failure mode is governed by combinations of flexure and shear.

For the square structures, higher shear strengths are capable in the web walls (reaching the ultimate in-plane shear strength S_{xy}^{u}) since reserve concrete shear strength in the web walls

is possible since the flange walls partially act as boundary elements. In contrast, the circular structures are only capable of resisting shear strengths that are approximately equal to the yield strength, S_{xy}^{y}. In terms of overall efficiency of the cross-section shapes, the square and circular shapes are very close; with the effective shear wall lengths equal to 55% of the total wall length (when using V_y as the calculated strength) compared to approximately 50% for the circular shape.

A method is presented for calculating the ultimate lateral strength of SC core-wall structures. The strength is assumed to be the lesser of the flexural strength of the structure, M_p, and the calculated shear strength (V_y or V_u) multiplied by the structure height, h.

Results from the square structure analyses demonstrate that the use of the ultimate shear strength, V_u, provides a good prediction of the mean shear strength while V_y is slightly conservative and therefore more reasonable for design calculations.

For the circular structures an effective shear wall length of 0.5 times the circumferential length of the cross-section is assumed and multiplied by the yield shear strength, S_{xy}^{y}. This results in a slightly conservative prediction of lateral strength for low aspect ratios, and a good prediction near the shear-flexure transition. For both the square and circular structures, the flexural strengths, fiber model plastic section analyses are developed using recommendations from AISC 360-10.

Table 6.1 Dimensions and properties of the square structure

Square Structure	
Outer dimensions, l	192 in. x 192 in.
Wall thickness, t_{sc}	24 in.
Faceplate thickness, t_p	0.375, 0.500, 0.625 in.
Reinf. Ratios, $2t_p/t_{sc}$	3.1, 4.2, 5.2 %
Structure height, h	8, 12, 16, 20, 24, 28 ft
Aspect ratio, h/l	0.50, 0.75, 1.00, 1.25, 1.50, 1.75
s (stud spacing)	12 in. on center
Round Structure	
Outer Diameter, d	227.3 in.
Wall thickness, t_{sc}	24 in
Faceplate thickness, t_p	0.375, 0.500, 0.625 in.
Reinf. Ratios, $2t_p/t_{sc}$	3.1, 4.2, 5.2 %
Structure height, h	10, 14, 19, 24, 28 ft
Aspect ratio, h/d	0.53, 0.74, 1.00, 1.27, 1.48
s (stud spacing)	12.8 in. (average)

Table 6.2 Dimensions and properties of the circular structure

Square structure, M_{FE}/M_{calc} (shear strength = V_y)				Square structure, M_{FE}/M_{calc} (shear strength = V_u)				Circular structure, M_{FE}/M_{calc} (shear strength = $0.5 \cdot A_s \cdot \kappa \cdot f_y$)			
h/l	ρ = 3.1%	ρ = 4.2%	ρ = 5.2%	h/l	ρ = 3.1%	ρ = 4.2%	ρ = 5.2%	h/D	ρ = 3.1%	ρ = 4.2%	ρ = 5.2%
1.75	1.04	1.01	1.00	1.75	1.04	1.01	1.00	1.48	1.44	1.43	1.53
1.50	1.04	1.01	1.00	1.50	1.04	1.01	1.00	1.27	1.19	1.20	1.25
1.25	1.03	1.01	0.98	1.25	1.03	1.01	0.98	1.00	1.05	1.01	0.97
1.00	1.12	1.14	1.17	1.00	0.95	1.01	1.10	0.74	1.05	1.02	0.99
0.75	1.24	1.27	1.27	0.75	0.99	1.13	1.20	0.53	1.05	1.00	0.99
0.50	1.33	1.31	1.27	0.50	1.07	1.17	1.20				
Standard deviation			0.13	Standard deviation			0.08	Standard deviation			0.19
Mean			1.12	Mean			1.05	Mean			1.14
Coeff. of variation			0.11	Coeff. of variation			0.07	Coeff. of variation			0.16

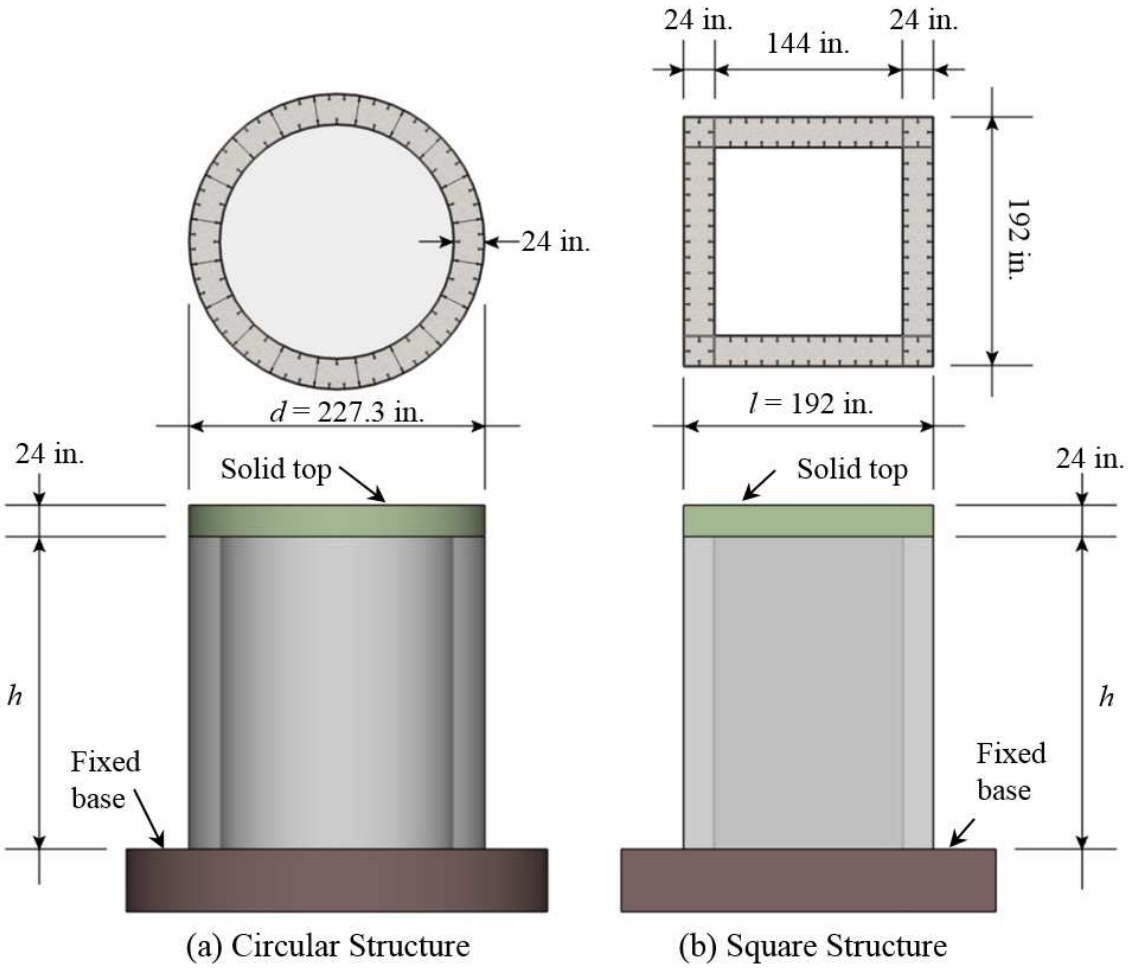

Figure 6.1 Typical modular steel-plate composite power plant structure

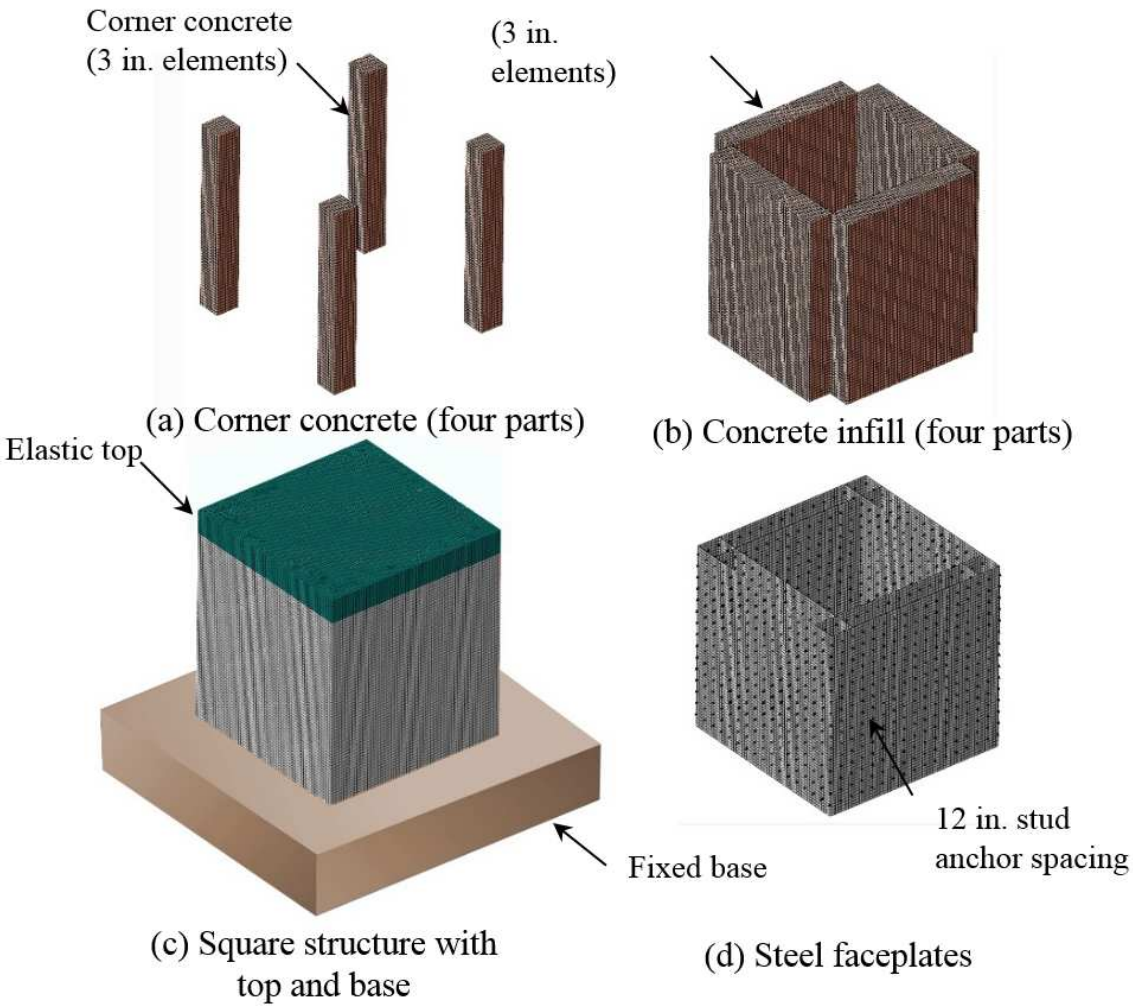

Figure 6.2 Square structure parts and meshing

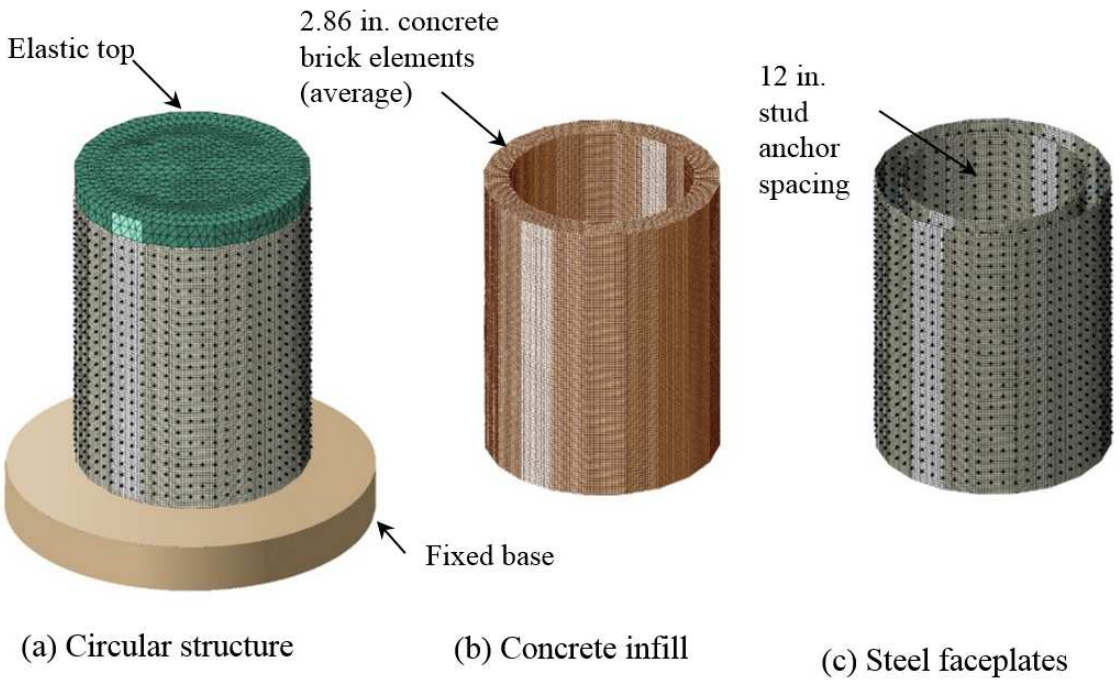

Figure 6.3 Circular structure parts and meshing

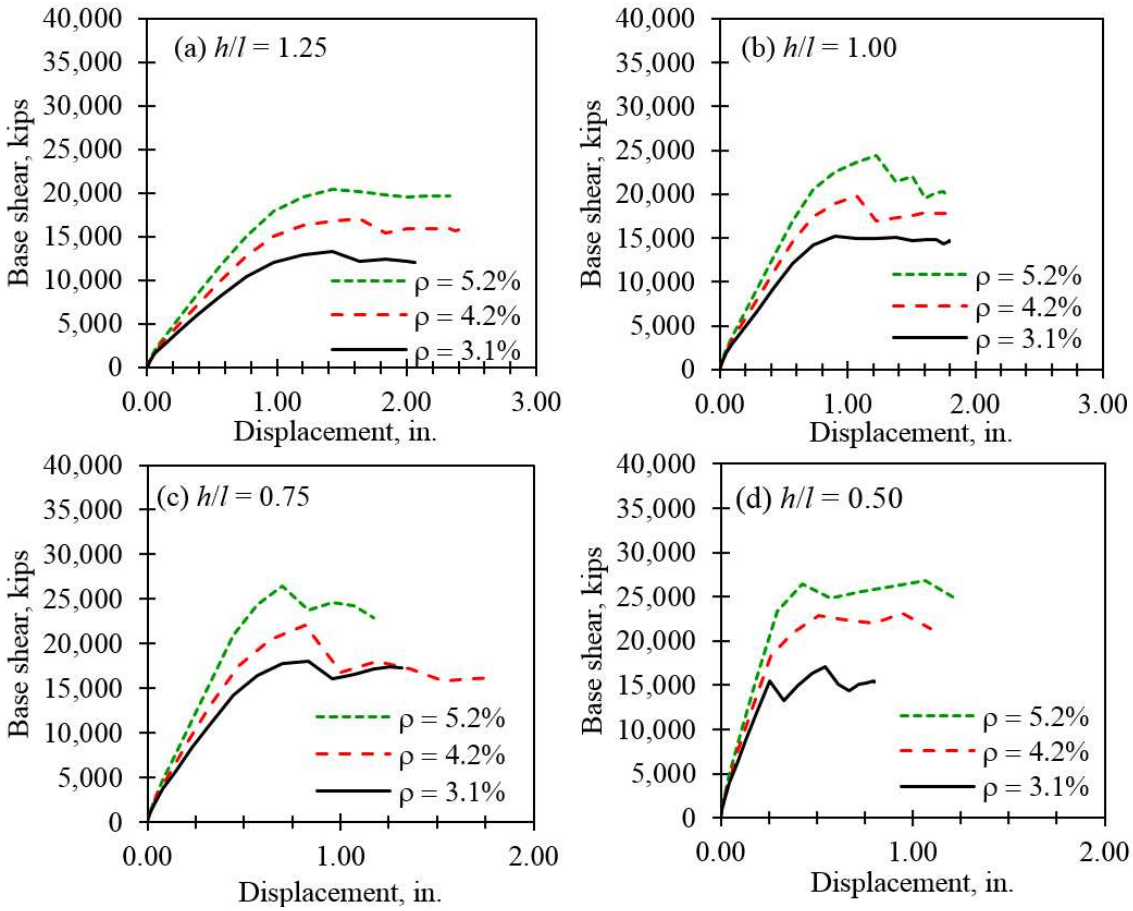

Figure 6.4 Base shear vs. drift results from square structure analyses

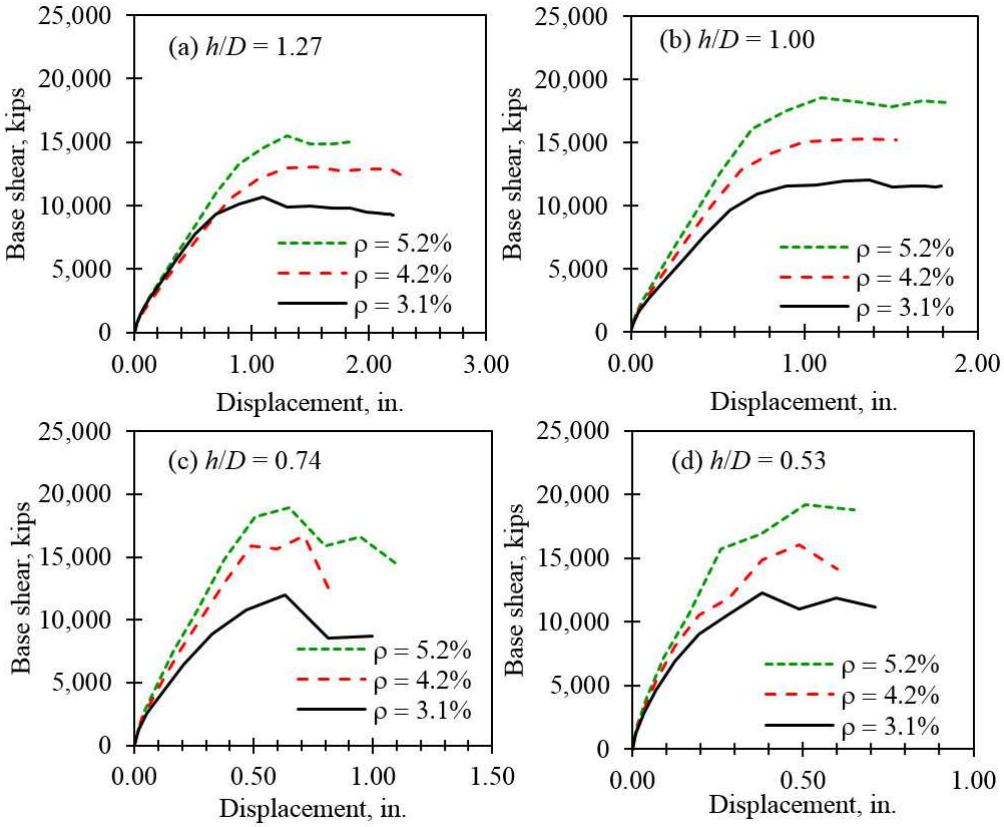

Figure 6.5 Base shear vs. drift results from circular structure analyses

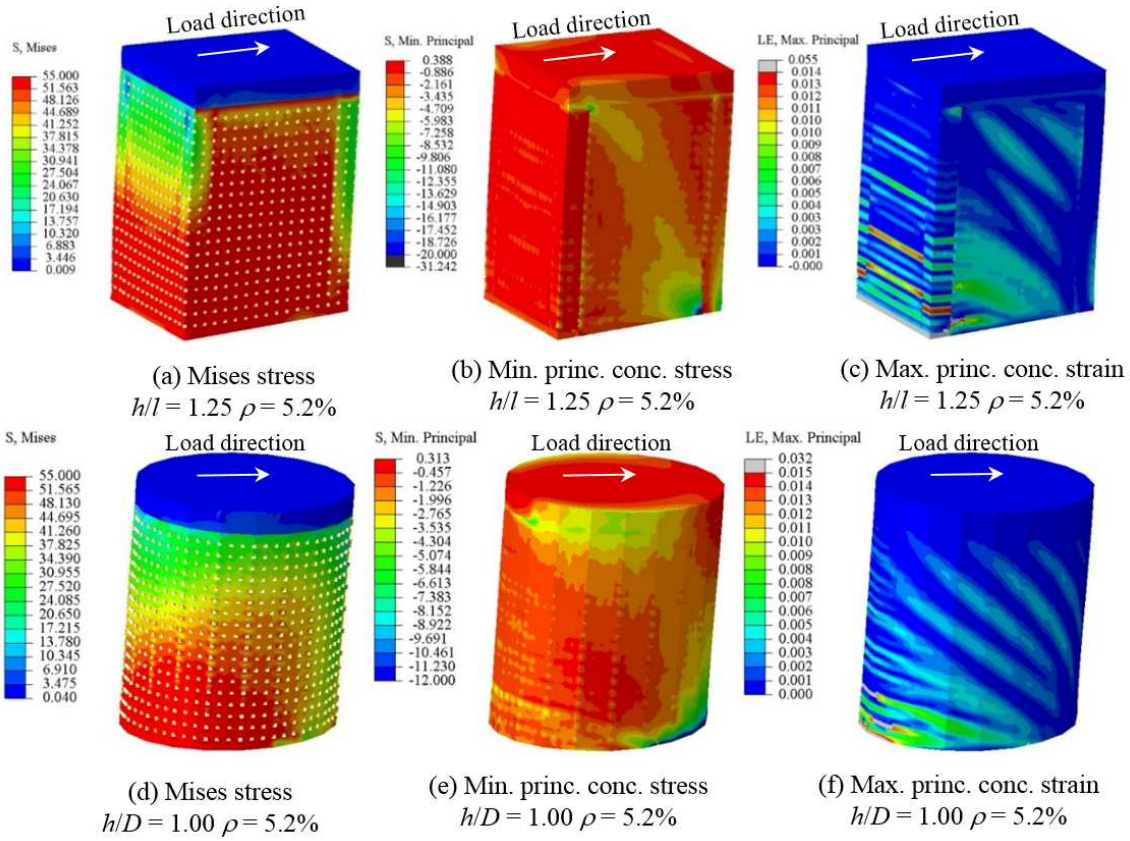

(a) Mises stress $h/l = 1.25$ $\rho = 5.2\%$

(b) Min. princ. conc. stress $h/l = 1.25$ $\rho = 5.2\%$

(c) Max. princ. conc. strain $h/l = 1.25$ $\rho = 5.2\%$

(d) Mises stress $h/D = 1.00$ $\rho = 5.2\%$

(e) Min. princ. conc. stress $h/D = 1.00$ $\rho = 5.2\%$

(f) Max. princ. conc. strain $h/D = 1.00$ $\rho = 5.2\%$

Figure 6.6 Stress and strain contours at peak strength (20x deformation scaling)

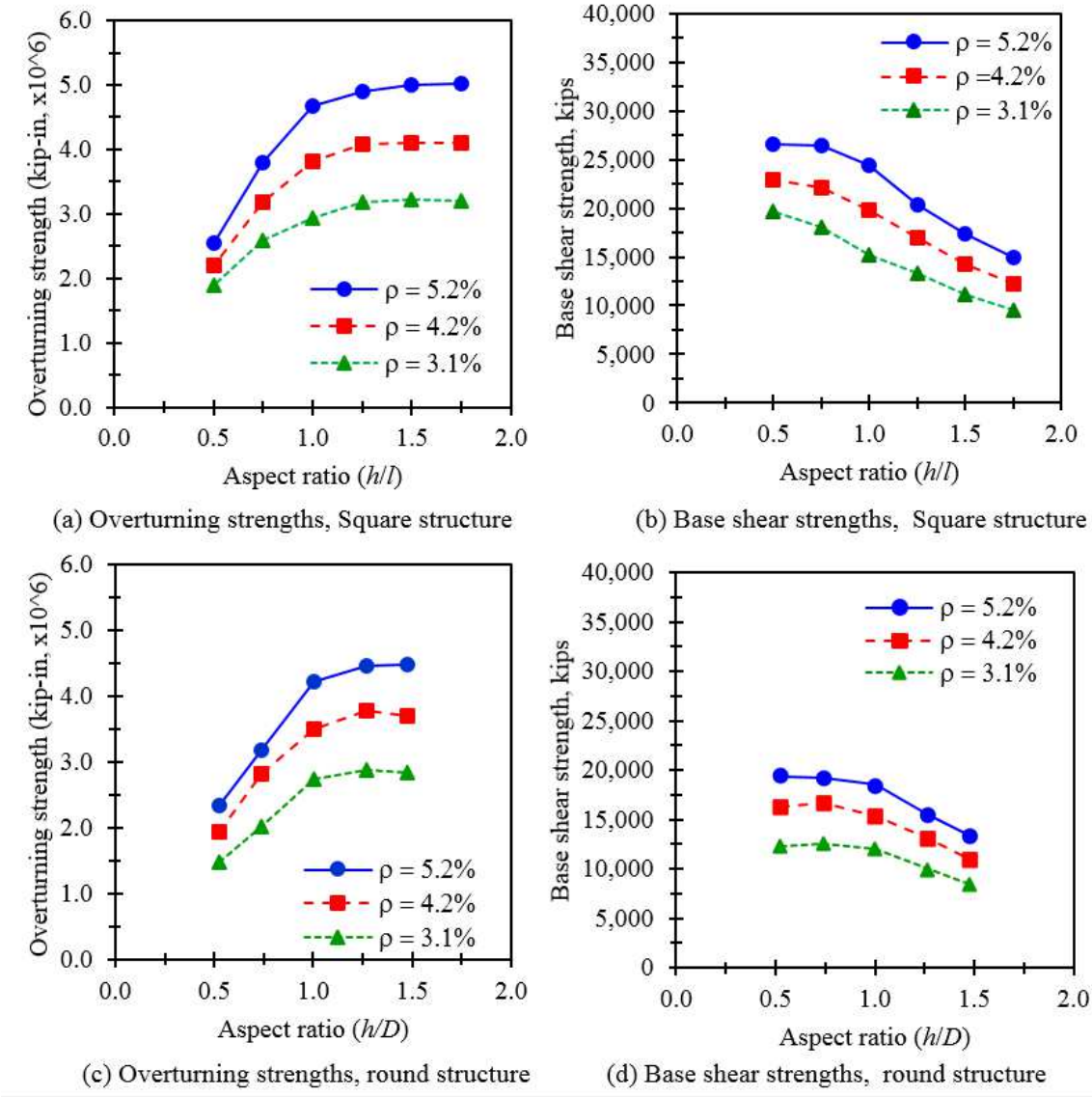

Figure 6.7 Base shear vs. drift results from Circular structure analyses

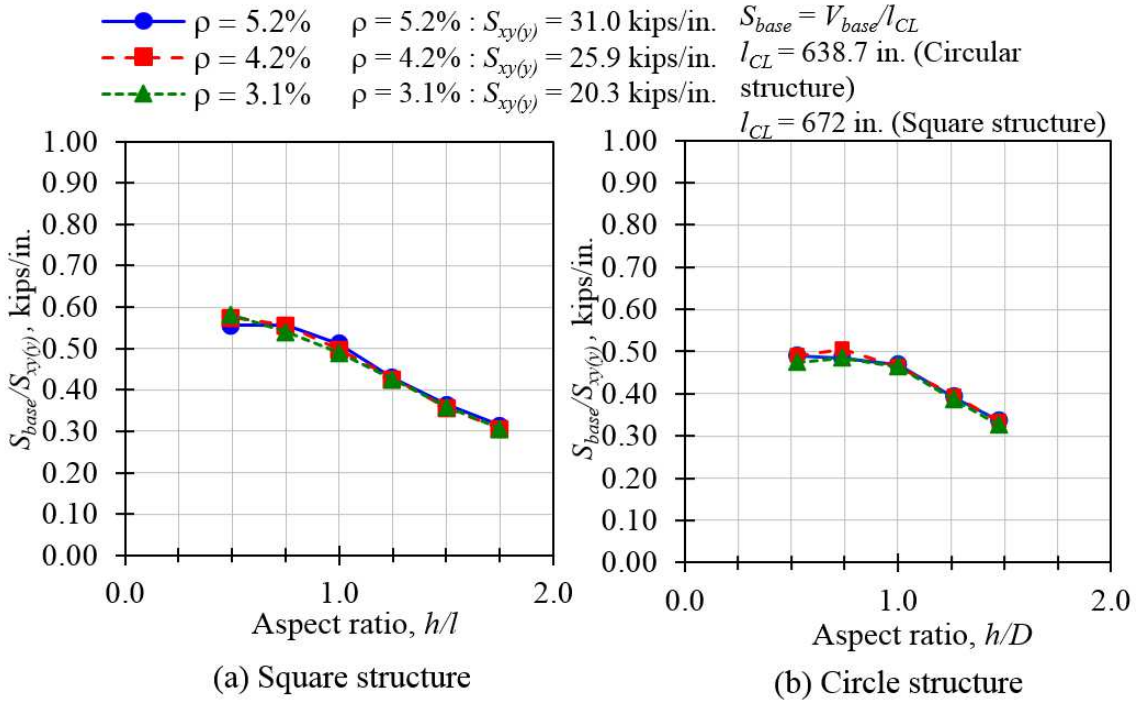

Figure 6.8 Normalized base shear strengths vs. aspect ratio

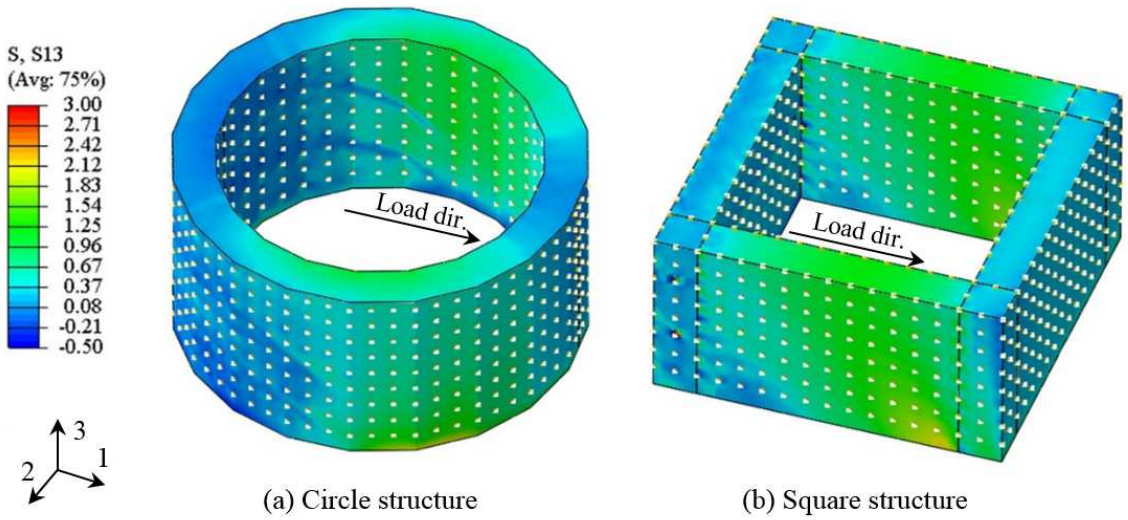

Figure 6.9 Shear stress distributions at 50% of peak load

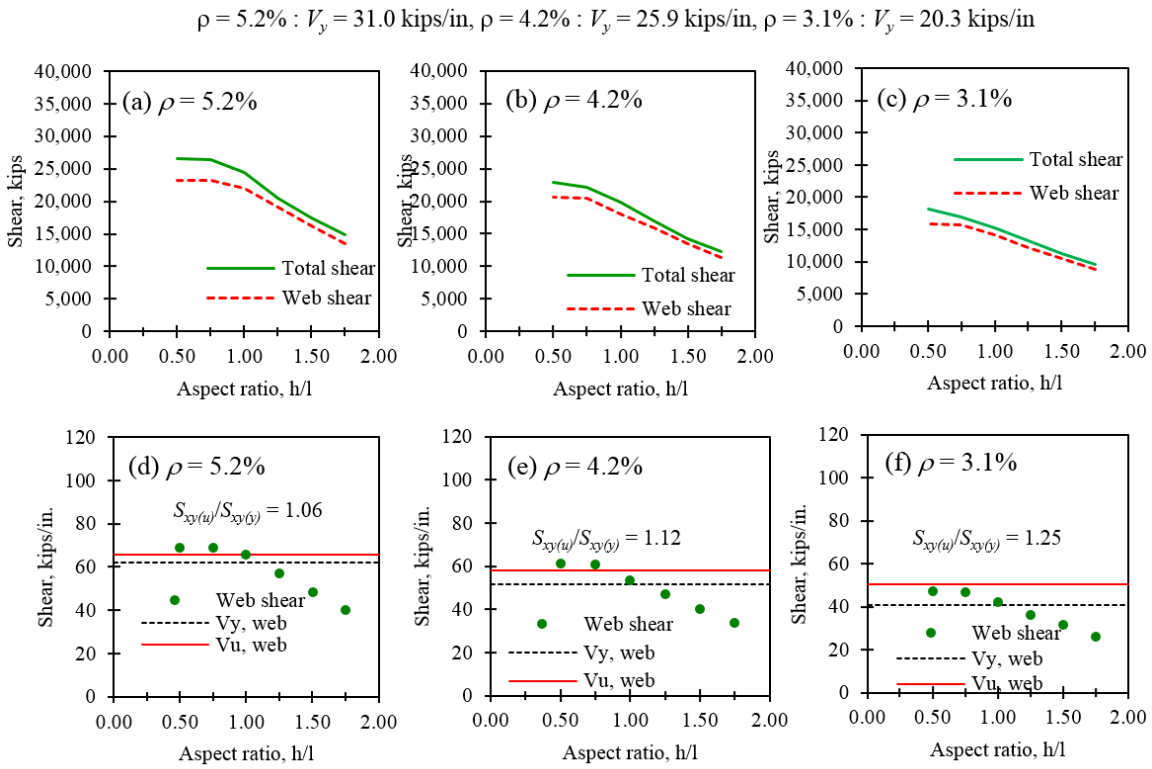

Figure 6.10 Square structure normalized base shear strengths vs. aspect ratio, *h*/*l*

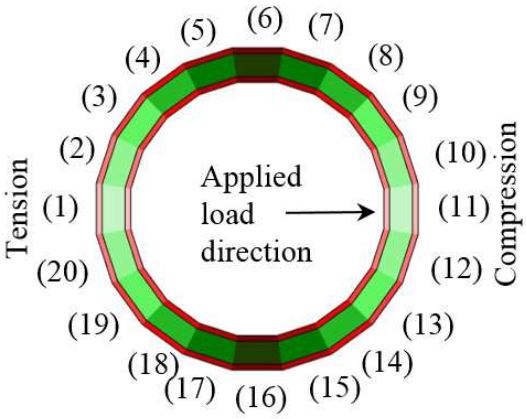

(1)	0.0 deg.	(11)	180.0 deg.
(2)	18.0 deg.	(12)	198.0 deg.
(3)	36.0 deg.	(13)	216.0 deg.
(4)	54.0 deg.	(14)	234.0 deg.
(5)	72.0 deg.	(15)	252.0 deg.
(6)	90.0 deg.	(16)	270.0 deg.
(7)	108.0 deg.	(17)	288.0 deg.
(8)	126.0 deg.	(18)	306.0 deg.
(9)	144.0 deg.	(19)	324.0 deg.
(10)	162.0 deg.	(20)	332.0 deg.

(a) Circular structure wall segments and angles

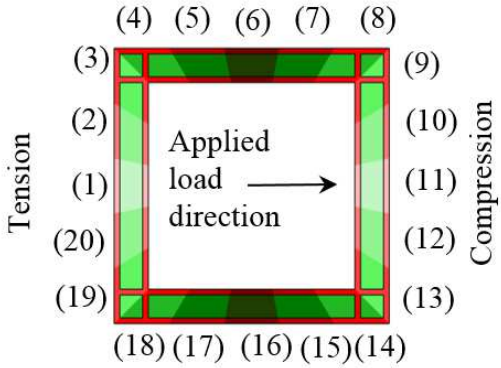

(1)	0.0 deg.	(11)	180.0 deg.
(2)	21.8 deg.	(12)	201.8 deg.
(3)	38.7 deg.	(13)	218.7 deg.
(4)	51.3 deg.	(14)	231.3 deg.
(5)	68.2 deg.	(15)	248.2 deg.
(6)	90.0 deg.	(16)	270.0 deg.
(7)	111.8 deg.	(17)	291.8 deg.
(8)	128.7 deg.	(18)	308.7 deg.
(9)	141.3 deg.	(19)	321.3 deg.
(10)	158.2 deg.	(20)	338.2 deg.

(b) Square structure wall segments

Figure 6.11 Wall segments for square and circular structures

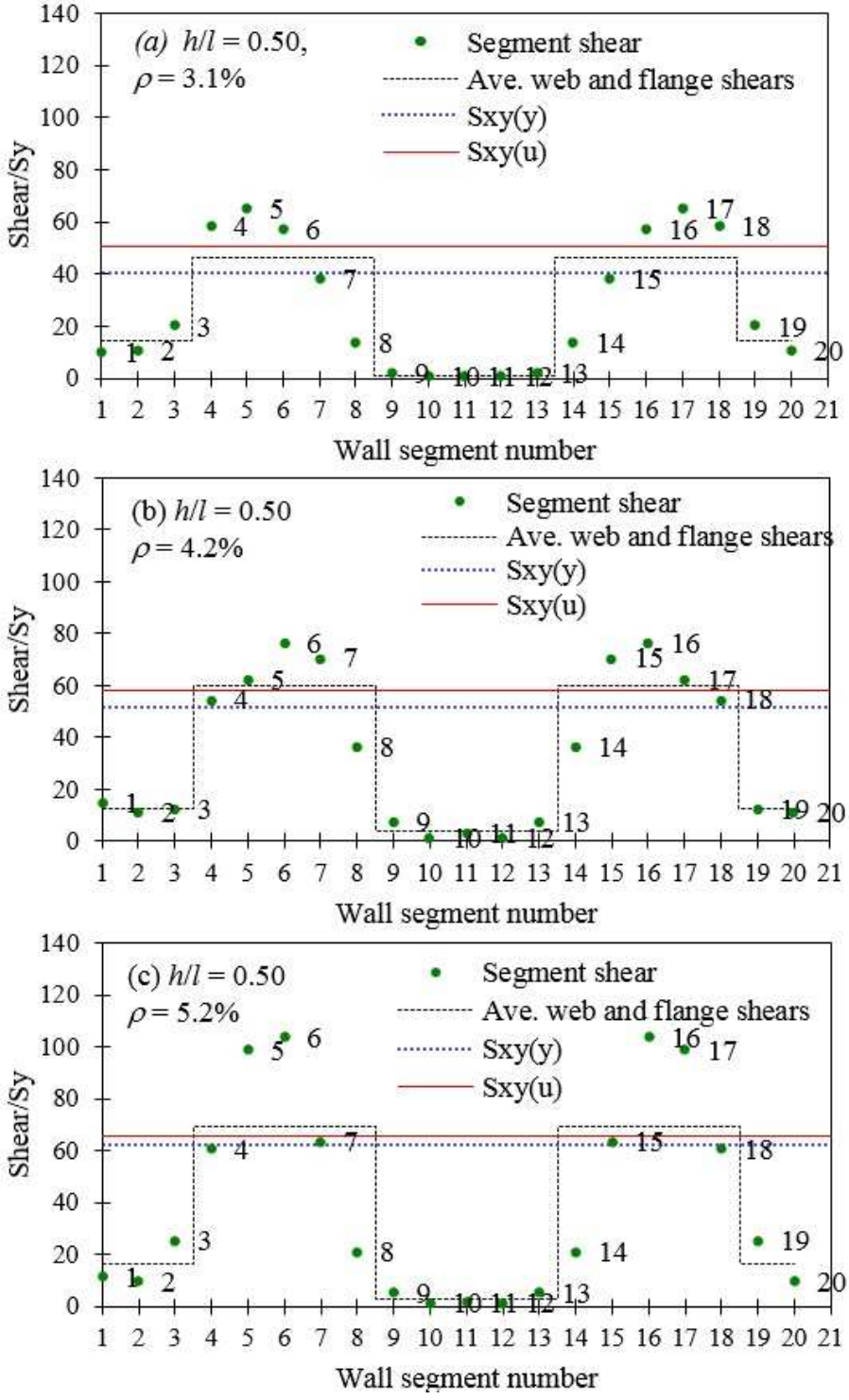

Figure 6.12 Distribution of shear around length of square structure

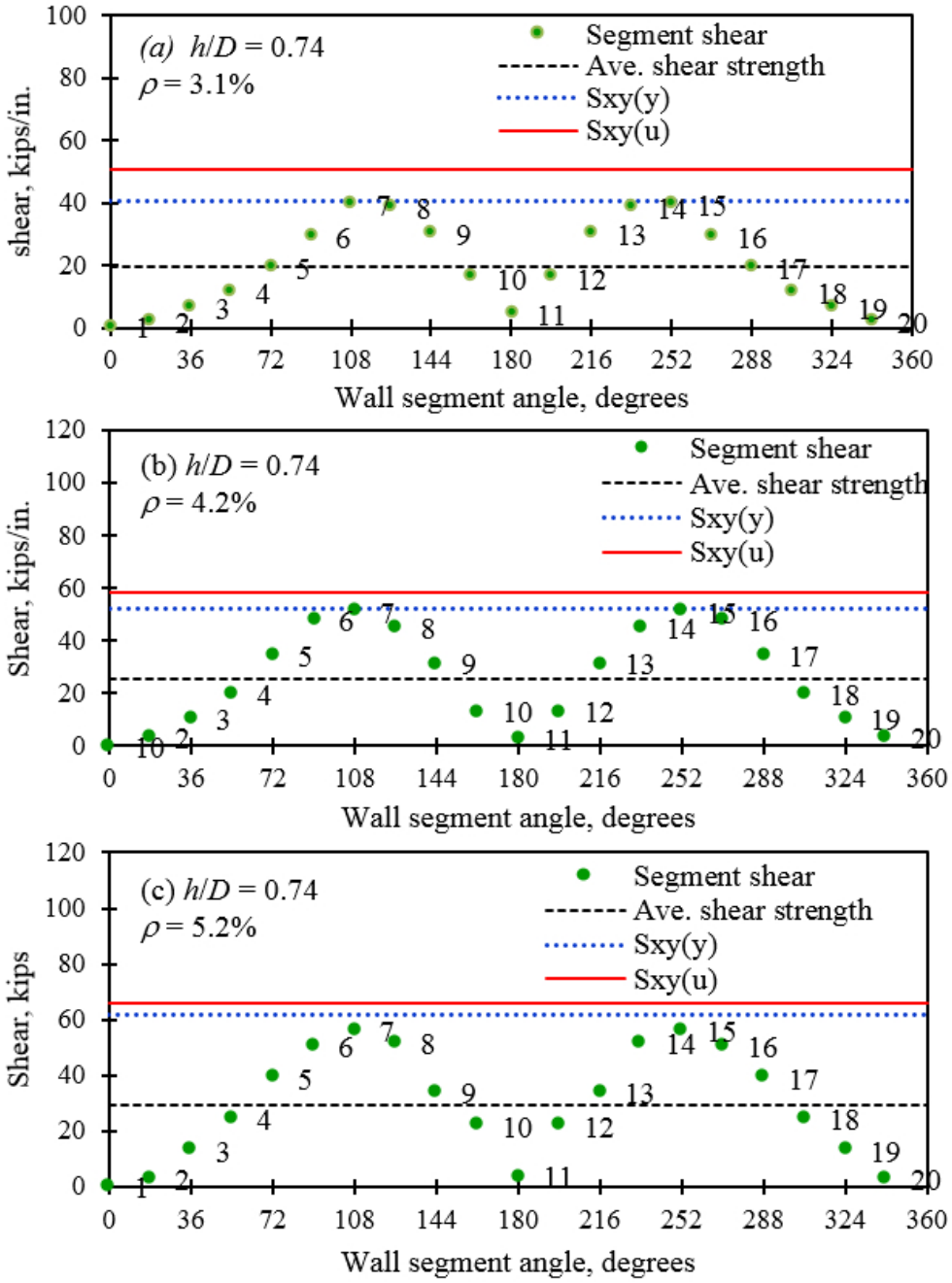

Figure 6.13 Distribution of shear around length of circular structure

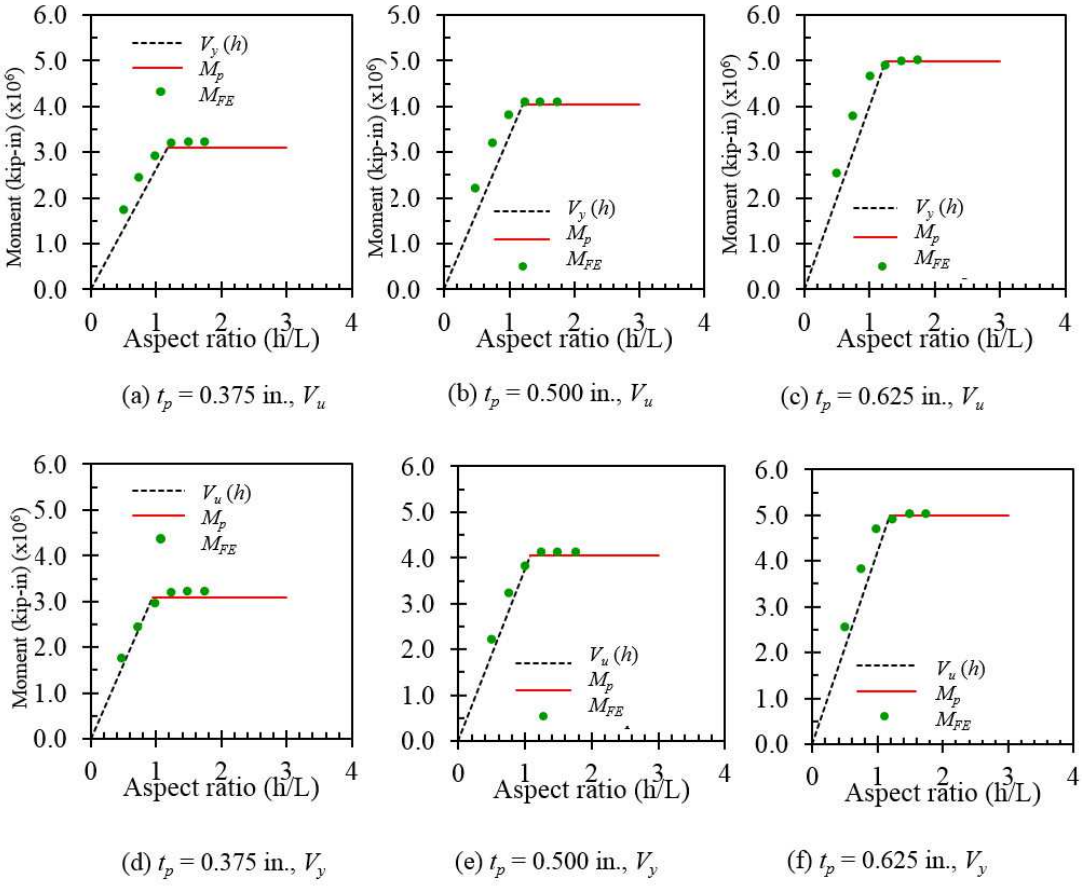

(a) t_p = 0.375 in., V_u (b) t_p = 0.500 in., V_u (c) t_p = 0.625 in., V_u

(d) t_p = 0.375 in., V_y (e) t_p = 0.500 in., V_y (f) t_p = 0.625 in., V_y

Figure 6.14 Peak strengths vs. aspect ratio - square structure

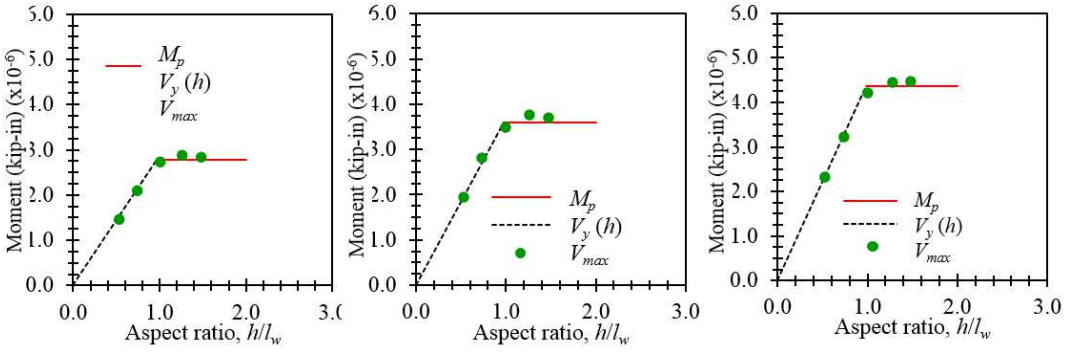

(a) t_p = 0.375 in. (b) t_p = 0.500 in. (c) t_p = 0.625 in.

Figure 6.15 Peak strengths vs. aspect ratio - round structure

CHAPTER 7. CONCLUSIONS AND RECOMMENDATIONS

The primary goal of this work is to study the global lateral load-deformation response of SC safety-related and core-wall structures. This is an important area of research since SC structures are seeing wider use in a number of new nuclear power plant designs and to date, research studying the global response has been limited. Since experimental testing of whole structures is difficult and expensive, simulation of structural behavior with detailed, benchmarked finite element modeling is considered the next best option. To that end, a modeling approach was developed with benchmarking of previous experimental tests of structural components and members in the literature. Experimental tests were selected that highlight various aspects of fundamental mechanical response including: out-of-plane flexure, in-plane shear, in-plane flexure, push-out, etc. Abaqus/Explicit was used for the finite element modeling with inelastic concrete and steel constitutive models that account for yielding of the steel faceplates, concrete cracking, concrete tension softening, concrete shear retention, and concrete failure. Additionally, the steel-concrete composite (shear force-slip) behavior was modeled with nonlinear connector elements. The analyses were conducted with displacement-controlled quasi-static push-over loadings with the explicit solver.

7.1 Analysis of a primary shield wall structure

In Chapter 4, a detailed finite element model of a 1/6th scale PSW structure was developed and analyzed. The purpose of this analysis was to further benchmark the finite element methodology and also to develop a method based on current code equations to predict the lateral strength of the structure. The model was based on a 1/6th scale experimental test structure that was tested in Japan. The analytical model accounted for steel plate yielding, concrete cracking, shear retention, softening, and the steel-concrete composite interaction. The models were developed and analyzed using Abaqus/Explicit with quasi-static cyclic and monotonic loadings. The PSW model was analyzed with monotonically increasing lateral loading (with displacement control), and also analyzed for the first three cycles from the cyclic loading protocol for the test. The results from the monotonic analysis compared favorably with the envelope of the lateral load deformation response from the experiment. The results from the cyclic analysis also compared well with the cyclic hysteresis load-deformation responses from the experiment. The analytical model was post-processed in detail so that the results could be compared directly with reported milestones of mechanical behavior from the experimental test report. These milestones compared well and included key mechanical states such as flexural cracking of concrete, flexural yielding of the steel plates, shear yielding of the steel plates, peak strength, and deformation capacity before failure.

The ultimate strength of the PSW structure was governed by yielding of the three steel plates (exterior, middle, and interior) and failure of the concrete infill. Also, the concrete infill of the wall segments developed diagonal cracks and inclined compression struts as

the peak load was reached, similar to mechanical behavior typically observed in reinforced concrete shear walls. At a force level equal to 96% of peak lateral load, the distribution of shear force (to the four wall segments) was approximately equal (25% to each one). Since the lateral load was distributed relatively equally, the base shear strength of the PSW structure was assumed equal to the calculated sums of the shear strengths of the individual wall segments. Additionally, since the behavior of the individual wall segments were similar to that of reinforced concrete squat shear walls, the ACI 349-06 Chapter 21 code equations were used with modifications to account for the steel plates instead of rebar. The bending strengths of the four wall segments were also post-processed from the analytical results and compared to calculated flexural strengths predicted with section P-M interaction strength envelopes. In this specific case, since the overall aspect ratio of the PSW was relatively short, the calculated lateral strength of the PSW was controlled by the calculated base shear strength and not the calculated flexural strength.

Linear elastic finite element models of the PSW were also developed and the results were compared to the nonlinear analyses. The purpose of this was to determine whether simplified linear elastic modeling could be used to determine the distribution of member section forces and moments throughout the structure for the purpose of calculating demands. The comparison indicated that the proportion of the lateral load resisted by the individual wall segments (in terms of section shears, bending moments, and axial forces) were similar to the nonlinear inelastic analysis.

7.2 In-plane shear strength of SC walls

The structural walls of power plant and core-wall structures are typically designed as the primary lateral force resisting systems. The walls act as a system to resist overturning demands and also act as individual shear walls. When walls are connected together into what is effectively a monolithic system, the global response of the structure influences the demands placed on individual walls. Additionally, the overall system is primarily governed by the in-plane shear and total flexural response of the structure. An analytical method was developed for calculating the in-plane shear force-deformation response of SC walls that are part of a structural system. In this context, the walls essentially act as shear walls with boundary elements, where the the adjacent connected walls act as the boundary elements.

The mechanics based approach is combined with the results of previous analytical work in order to provide a complete model for the prediction of SC shear wall response from initial concrete infill cracking to ultimate strength. The approach uses composite shell theory with a pure shear assumption so that simple equations can be developed for prediction of the ultimate strength and strain. The method assumes that the boundary elements or flange walls are sufficiently strong to develop the full strength of the concrete infill in diagonal compression.

Finite element modeling of previous experimental SC shear panel tests by Ozaki et al. [30] provided insight into the mechanical state of an SC shear wall at and near ultimate strength. The results demonstrated that the concrete fails in diagonal compression at ultimate load. The occurrence of concrete cracking results in compression softening equal to

approximately 50% of f'_c. This finding is roughly consistent with previous research on the effect of compression softening in reinforced concrete shear walls. Although, unlike reinforced concrete shear walls, the degree of softening was relatively constant and did not appear to correlate with the measured principal normal strain ratio, $\varepsilon_1/\varepsilon_2$.

The analytical results also demonstrated increasing shear deformation capacity (γ_{xy}^{μ}) and principal strain ratios for decreasing reinforcement ratios. The principal strain ratios were also calculated for the yield point using the composite shell theory approach and showed consistent results with the finite element results. Since the finite element results demonstrated an approximately linear principal strain-shear strain response up to ultimate strength, a simple model was proposed for prediction of ultimate shear strain (γ_{xy}^{μ}) that assumes that the principal strain ratio is constant from yield to ultimate. The average of the measured peak shear strains at ultimate strength were calculated from the experimental database of shear panels and flanged wall tests. The average minimum principal strain at ultimate was then calculated (equal to -0.0016 in./in.) by coordinate transformation using the average of the observed ultimate shear strains.

Finally, the ultimate shear strengths were calculated and compared to the results of shear panel and flanged wall tests in the literature. Overall, the strengths showed good agreement with a mean of 0.92 for the ratios of experimental to calculated strengths for the shear panel tests and a mean of 1.08 for the flanged wall tests. The flanged wall comparisons though showed substantially more dispersion with a standard deviation of 0.16 compared to 0.05

for the panel tests. This can be partially explained by the high degree of variability between the different flanged wall test series resulting in different combinations of failure modes of the flanges, web walls, and connections. Also, the shear strength calculations for the flanged wall tests did not include the effects of combined shear-flexure loading and did not account for additional (out-of-plane) shear strengths from the flanges. For the calculated predictions of ultimate shear strains, the mean for the ratios of experimental to calculated strains for the panel tests was 1.04 with a standard deviation of 0.21. Similarly, comparisons to the flanged wall shear strains resulted in more dispersion with a mean of 1.06 and a standard deviation of 0.28.

The calculated shear strength and shear strain were then combined with previous analytical work in order to develop the complete shear force-shear strain relationship (S-γ_{xy}) of SC walls subjected to in-plane shear. The calculated relationship is trilinear (shown in Figure 7.1) with transition points defined by (i) initial cracking of the concrete infill ($S_{xy}^{cr}, \gamma_{xy}^{cr}$), (ii) yielding of the steel faceplates ($S_{xy}^{y}, \gamma_{xy}^{y}$), and (iii) ultimate strength of the concrete infill in diagonal compression ($S_{xy}^{u}, \gamma_{xy}^{u}$).

7.3 SC core-wall structures

Square and circular SC core-wall structures were modeled and analyzed using Abaqus/Explicit in order to study their fundamental lateral load-deformation behavior. The geometric and detailing design of the core-wall structures were selected to be representative of actual SC structures. The detailing (steel faceplate thickness, SC wall

thickness, shear stud size, etc.) are consistent with AISC N690s1-15 and can be considered full or reduced scale depending on the type of structure they are intended to represent. For core-walls in building structures, the selected geometries are essentially full-scale and for power plant structures the dimensions could be considered full-scale or reduced scale (greater than 1/3rd scale) depending on the structure being modeled. Of primary interest were the overall structure aspect ratio, the SC wall section reinforcement ratio, and the plan shape of the structure (round versus square).

The finite element modeling approach was benchmarked with analytical modeling of experimental tests of SC structures were modeled and analyzed with Abaqus/Explicit. The analytical results demonstrated that the lateral strengths of the core-wall structures are primarily governed by flexure for h/l greater than approximately 1.25 for the square structures, and h/D greater than 1.0 for the circular core-walls. For aspect ratios less than these limits the failure mode was governed by combinations of flexure and shear.

For the square structures, higher shear strengths were realized in the web walls, reaching the ultimate in-plane shear strength since reserve concrete shear strength in the web walls was possible due to the flange walls partially act as boundary elements. (In contrast, the circular structures were only capable of resisting shear strengths that were approximately equal to the yield strength, S_{xy}^{y}). In terms of overall efficiency of the cross-section shapes, the square and circular shapes were very close; with the normalized shear strengths (V_y/V_{base}) equal to 0.55 for the square structure and 0.50 for the circular structure (with Vy calculated using the total centerline length of the core wall).

A method is presented for calculating the lateral load capacity of SC core-wall structures. The strength is assumed to be the lesser of the flexural strength of the structure, M_p, and the calculated shear strength (V_y or V_u) multiplied by the structure height, h. Results from the square structure analyses demonstrate that the use of the ultimate shear strength, V_u, provides a good prediction of the mean shear strength while V_y is slightly conservative and therefore more reasonable for design calculations.

For the circular structures an effective shear wall length of 0.5 times the circumferential length of the cross-section is assumed and multiplied by the yield shear strength, S_{xy}^{y}. This results in a slightly conservative prediction of lateral strength for low aspect ratios, and a good prediction near the shear-flexure transition. For both the square and circular structures, the flexural strengths were calculated using fiber model plastic section analyses using recommendations from AISC 360-10 that assume at the flexural strength limit: zero concrete tension strength, concrete compression strength equal to $0.85f'_c$, and all of the steel section at yield. The flexural strength predictions showed good agreement with the analytical results.

7.4 Future work and recommendations

- In Chapter 4, a design methodology was developed for prediction of the lateral load strength of the geometrically complex PSW structure. The design approach drew an analogy between reinforced concrete and SC wall behavior and used reinforced concrete design equations with modifications for the SC structure. The reason for using this approach was primarily motivated by the fact that this particular structure

was exceedingly unique and complex with very thick walls, three layers of steel plates, extensive transverse steel web plates, and openings and perforations through the walls. All of this complexity in combination with SC construction required that a rational and conservative design approach be developed. The approach that was developed was confirmed to have worked for this specific PSW. Further study of this design approach applied to other structures that are similar would further confirm the methodology and design assumptions.

- For safety-related structures, accident thermal loads are of particular importance. The analysis of the PSW structure only included seismic loading and would therefore require additional study of the effects of thermal loads and combined thermal-seismic loads for completeness.

- A mechanics based approach was developed in Chapter 5 for prediction of the ultimate ultimate in-plane shear strength of SC walls subjected to pure shear. The derivation and resulting equations are lengthy and based on the exact composite shell theory solutions. Therefore, simplified design equations could be developed by identifying the most sensitive parameters (such as reinforcement ratio, relative stiffness of concrete and steel, etc.) and simplified and approximate equations could be developed for design calculations.

- The ultimate shear strength prediction described in Chapter 5 is only applicable to structure configurations that include shear wall panels connected to boundary

elements on all sides. In order to develop the full strength governed by both yielding of the steel faceplates and compression failure of the concrete infill, the connections between the boundary elements and shear panel must be sufficiently strong. Additional study is required to determine minimum connection requirements between the shear wall panels and the flange walls in order to be able to develop the full upper-bound shear strength.

- The analytical modeling of core-wall structures in Chapter 6 only considered relatively simple core-wall structure designs without openings. Actual structures would typically have openings for elevator doors or core-walls connected together with link beams. The effect of link beams or openings on local and global behavior is an important topic that would require extensive additional analytical work and study.

- For the core-wall structure analyses, only predictions of the ultimate strengths were developed. A more comprehensive study would also include predictions of the displacement responses of the core-wall structures constructed with SC walls. This would necessitate the development of a method that accounts for the flexural stiffness, shear stiffness, and the potential effects of partial composite action.

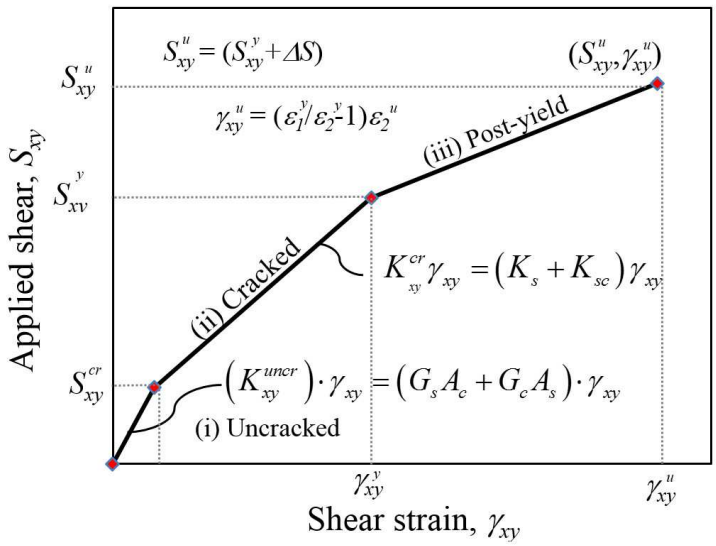

Figure 7.1 Calculated tri-linear shear force-shear strain relationship

LIST OF REFERENCES

LIST OF REFERENCES

[1] Cummins, W. E., 2001. The Advanced Passive AP1000 Nuclear Plant – Competitive and Environmentally Friendly, Transactions of the 16th International Conference on Structural Mechanics in Reactor Technology (SMiRT-16), Washington DC, USA.

[2] ACI 349-06, 2006. Code Requirements for Nuclear Safety-Related Concrete Structures and Commentary, American Concrete Institute, Farmington Hills, MI.

[3] ASCE 43-05, 2005. Seismic Design Criteria for Structures, Systems, and Components in Nuclear Facilities, American Society of Civil Engineers, Reston, USA.

[4] AISC N690s1-15 Supplement No. 1, 2015. Specification for Safety-Related Steel Structures for Nuclear Facilities, Supplement No. 1 Including Appendix N9 – Design of Steel-Plate Composite (SC) Walls, Under Preparation, AISC, Chicago, IL, USA.

[5] Shodo, K., Asao, O., Tetsuya, S., Kunihiko, T., Kazuaki, (2003). A study on the structural performance of SC thick walls: Part 1. Experiment of the SC thick wall. Summaries of Technical Papers of Annual Meeting Architectural Institute of Japan. B-2, Structures II, Structural Dynamics Nuclear Power Plans, Architectural Institute of Japan, pp. 1027–1028 http://ci.nii.ac.jp/naid/110006599717/en/

[6] SIMULIA Dassault Systems, 2013. ABAQUS Analysis User's Manual.

[7] Akiyama, H., Sekimoto, H., Tanaka, M., Inoue, K., Fukihara, M., Okuta, Y., 1989. 1/10th Scale Model Test of Inner Concrete Structure Composed of Concrete Filled Steel bearing Wall. Transactions of the 10th International Conference on Structural Mechanics in Reactor Technology (SMiRT-10), Raleigh, USA.

[8] Akiyama, H. Sekimoto, H., Fukihara, M., Nakanashi, K., Hara, K., 1991. A Compression and Shear Loading Test of Concrete Filled Steel Bearing Wall, 11th International Conference on Structural Mechanics in Reactor Technology (SMiRT-11), Tokyo, Japan.

[9] Fukumoto, T., Kato, B, 1987. Concrete Filled Steel Bearing Walls. IABSE Symposium, Paris-Versailles, France.

[10] Takeuchi, M., Akiyama, H., Narikawa, M., Hara, K., Tsubota, H., Matsuo, I., 1995. Study on a concrete filled steel structure for nuclear power plants (part 1). Outline of the structure and the mock-up test, Proceedings of 13th International Conference on Structural Mechanics in Reactor Technology (SMiRT-13), Porto Alegre, Brazil.

[11] Kato, T., Sasagawa, K., Kobayashi, M., Sakamoto, M., 1985. Experimental Study of Concrete Filled Steel Bearing Walls (Part 2: Compression Test), Abstracts of the Annual Congress of AIJ, PP. 1325-1326.

[12] Kim, W., Mun, T., Moon, I., 2009. Composite Modular Construction of Nuclear Power Plant Structures, Proceedings of Korea-China-Japan Symposium on Structural Steel Construction, Seoul, Korea.

[13] KEPIC-SNG, 2010. Specification for Safety-Related Steel Plate Concrete Structures for Nuclear Facilities, Board of KEPIC Policy Structural Committee, Korea Electric Association, Seoul, Korea.

[14] Narayan, R., Wright, H. D., Evans, H. R., Francis, R. W., 1987. Load Tests on Double Skin Composite Girders, Proceedings – Composite Structure in Steel and Concrete, ASCE.

[15] Ohno, F., Shioya, T., Nagasawa, Y., Matsumoto, G., Okada, T., Ota, T., 1987. Experimental Studies on Composite Members for Arctic Offshore Structures, Steel-Concrete Composite Structural Systems. C-FER Publication No. 1 Proceedings of special symposium held in conjunction with POAC '87, 9th International Conference on Port and Ocean Engineering under Arctic Conditions, Fairbanks, USA.

[16] Adams, P. F., Zimmerman, T. J. E., 1987. Design and Behavior of Composite Ice-resisting Walls, Steel-Concrete Composite Structural Systems. C-FER Publication No. 1 Proceedings of special symposium held in conjunction with POAC '87, 9th International Conference on Port and Ocean Engineering under Arctic Conditions, Fairbanks, USA.

[17] Matsuishi, M., Iwata, S., 1987. Strength of Composite System Ice-Resisting Structures, Steel-Concrete Composite Structural Systems. C-FER Publication No. 1 Proceedings of special symposium held in conjunction with POAC '87, 9th International Conference on Port and Ocean Engineering under Arctic Conditions, Fairbanks, USA.

[18] O'Flynn, B., MacGregor, J. G., 1987. Tests on Composite Ice-Resisting Walls, Steel-Concrete Composite Structural Systems. C-FER Publication No. 1 Proceedings of special symposium held in conjunction with POAC '87, 9th International Conference on Port and Ocean Engineering under Arctic Conditions, Fairbanks, USA.

[19] Wright, H. D., Oduyemi, T. O. S., Evans, H. R., 1991. The Design of Double Skin Composite Elements, Journal of Constructional Steel Research, UK.

[20] Bowerman, H., Chapman, J., 2002. Bi-Steel Steel-Concrete-Steel Sandwich Construction. Composite Construction in Steel and Concrete IV Proceedings, ASCE.

[21] Bi-Steel 2nd Edition, 2003, Design and Construction Guide 2nd Edition, Corus UK Ltd., North Lincolnshire, UK.

[22] JEAC-4618, 2009. Technical code for seismic design of steel plate reinforced concrete structures: buildings and structures Japanese Electric Association Nuclear Standards Committee, Tokyo, Japan.

[23] Usami, S., Akiyama, H., Narikawa, M., Hara, K., Takeuchi, M., Sasaki, N., 1995. Study on a concrete filled steel structure for nuclear plants (part 2). Compressive loading tests on wall members. Proceedings of 13th International Conference on Structural Mechanics in Reactor Technology (SMiRT-13), Porto Alegre, Brazil.

[24] Kanchi, M., 1996. Experimental Study on a Concrete Filled Structure Part 2. Compressive Tests (1), Summary of technical papers of annual meeting, architectural institute of Japan, structures, pp. 1071-1072.

[25] Varma, A. H., Zhang, K., Malushte, S. R., 2013. Local Buckling of SC Composite Walls at Ambient and Elevated Temperatures, Proceedings of 22nd International Conference on Structural Mechanics in Reactor Technology (SMiRT-22), San Francisco, CA, USA.

[26] Takeuchi, M., Fujita, F., Funakoshi, A., Shohara, R., Akira, S., Matsumoto, R. 1999. Experimental study on steel plate reinforced concrete structure, part 2: response of SC members subjected to out-of-plane load (outline of the experimental program and the results), Proceedings of the Annual Conference of Architectural Institute of Japan, pp. 1037–1038.

[27] Hong, S. G., Kim, W., Lee, K. J., Hong, N. K., Lee, D. H., 2009. Out-of-plane shear strength of steel plate concrete walls dependent on bond behavior, Proceedings of 20th International Conference on Structural Mechanics in Reactor Technology (SMiRT-20), Div-6: Paper ID# 1855, Espoo, Finland.

[28] Chu, M., Song, X., Ge, H., 2013. Structural performance of steel–concrete–steel sandwich composite beams with channel steel connectors, Proceedings of 22nd International Conference on Structural Mechanics in Reactor Technology (SMiRT-22), Div-I: Paper ID# 498, San Francisco, USA.

[29] Sener, K. C., Varma, A. H., Ayhan, D., 2015. Steel-plate composite (SC) walls: Out-of-plane flexural behavior, database, and design, Journal of Constructional Steel Research, UK.

[30] Ozaki, M., Akita, S., Niwa, N., Matsuo, I., Usami, S., 2001. Study on Steel Plate Reinforced Concrete Bearing Wall for Nuclear Power Plants Part 1: Shear and Bending Loading Tests of SC Walls, Proceedings of 16th International Conference on Structural Mechanics in Reactor Technology (SMiRT-16), Washington DC, USA.

[31] Varma, A. H., Sener, K. C., Zhang, K., Coogler, K., Malushte, S. R., 2011. Out-of-Plane Shear Behavior of SC Composite Structures, Proceedings of 21st International Conference on Structural Mechanics in Reactor Technology (SMiRT-21), New Delhi, India.

[32] Sener, K. C., Varma, A. H., 2014. Steel-plate composite walls: Experimental database and design for out-of-plane shear, Journal of Constructional Steel Research, UK.

[33] Akiyama, H., Sekimoto, H., Hara, K., 1991. A Compression and Shear Loading Test of Concrete Filled Steel Bearing Wall, Proceedings of 11th International Conference on Structural Mechanics in Reactor Technology (SMiRT-11), Tokyo, Japan.

[34] Epackachi, S., Nguyen, N., Kurt, E., Whittaker, A., Varma, A. H., 2014. In-Plane Seismic Behavior of Rectangular Steel-Plate Composite Wall Piers. Journal of Structural Engineering, Reston, VA, USA.

[35] Takeda, T., Yamaguchi, T., Nakayama, T., Akiyama, K., Kato, Y., 1995. Experimental study on shear characteristics of a concrete filled steel plate wall, Proceedings of 13th International Conference on Structural Mechanics in Reactor Technology (SMiRT-13), Porto Alegre, Brazil.

[36] Ozaki, M., Akita, S., Osuga, H., Nakayama, T., Adachi, N., 2003. Study on steel plate reinforced concrete panels subjected to cyclic in-plane shear, Nuclear Engineering and Design. doi:10.1016/j.nucengdes.2003.06.010

[37] Danay, A., 2012. Response of steel-concrete composite panels to in-plane loading, Nuclear Engineering and Design, 242 pp. 52-62.

[38] Kupfer, H., Hilsdorf, H. K., Rush, H., 1969. Behavior of Concrete under Biaxial Stresses, ACI Journal, Farmington Hills, MI, USA.

[39] Hong, S., Lee, S., Lee, M., 2014. Infrastructure Systems for Nuclear Energy, John Wiley & Sons Ltd., Chichester, West Sussex, UK.

[40] Sasaki, N., Akiyama, H., Narikawa, M., Hara, K., Takeuchi, M., Usami, S., 1995. Study on a concrete filled steel structure for nuclear power plants (part 3). Shear and bending loading tests on wall member, Proceedings of 13th International Conference on Structural Mechanics in Reactor Technology (SMiRT-13), Porto Alegre, Brazil.

[41] Suzuki, N., Akiyama, H., Narikawa, M., Hara, K., Takeuchi, M., Matsuo et al., 1995. Study on a concrete filled steel structure for nuclear power plants (part 4). Analytical method to estimate shear strength, Proceedings of 13th International Conference on Structural Mechanics in Reactor Technology (SMiRT-13), Porto Alegre, Brazil.

[42] Takeuchi, M., Narikawa, M., Matsuo, I., Hara, K., Usami, S., 1998. Study on a concrete filled structure for nuclear power plants, Nuclear Engineering and Design, 179, pp. 209-223.

[43] Ozaki, M., Akita, S., Niwa, N., Matsuo, I., Usami, S., 2001. Study on Steel Plate Reinforced Concrete Bearing Wall for Nuclear Power Plants Part 1; Shear and Bending Loading Tests of SC Walls, Transactions of the 16th International Conference on Structural Mechanics in Reactor Technology (SMiRT-16), Washington DC, USA.

[44] Varma, A. H., Zhang, K., Chi, H., Booth, P. N., Baker, T., 2011. In-Plane Shear Behavior of SC Composite Walls: Theory vs. Experiment, Transactions of the 21st International Conference on Structural Mechanics in Reactor Technology (SMiRT-21), New Delhi, India.

[45] Ramesh, S., 2013. Behavior and Design of Earthquake-Resistant Dual-Plate Composite Shear Wall Systems, Doctoral Dissertation, Purdue University, West Lafayette, IN, USA.

[46] Nie, J., Ma, X., Tao, M., Fan, J., Bu, F., 2014. Effective stiffness of composite shear wall with double plates and filled concrete, Journal of Constructional Steel Research, UK.

[47] NUREG/CR-6906 SAND2006-2274P, 2006. Containment Integrity Research at Sandia National Laboratories – An Overview, US Nuclear Regulatory Commission Office of Nuclear Regulatory Research, Washington DC, USA.

[48] NUREG/CR-6707 SAND2001/0022P, 2000. Seismic Analysis of a Reinforced Concrete Containment Vessel Model, U. S. Nuclear Regulatory Commission Office of Nuclear Regulatory Research, Washington DC, USA.

[49] Hardy, G., Soto, R., Short, S., Kassawara, R., 2015. Finite element and lumped mass structure modeling for SPRAs, Transactions of the 23rd International Conference on Structural Mechanics in Reactor Technology (SMiRT-23), Manchester, UK.

[50] Lou, M., Wang, H., Chen, X., Zhai, Y., 2011. Structure-soil-structure interaction: Literature review, Soil Dynamics and Earthquake Engineering, Volume 31, pp. 1724-1731.

[51] SAP2000, 2014. CSi Knowledge Base, Walnut Creek, CA: Computers and Structures, Inc. www.csiamerica.com/products/sap2000

[52] LS-DYNA, LSTC Livermore Software Technology Corp., Livermore, CA, USA. Retrieved August 23rd, 2015: www.lstc.com/products/ls-dyna

[53] ANSYS Structural, ANSYS, Inc., Southpointe, Canonsburg, PA, USA. Retrieved August 23rd, 2015: www.ansys.com/About+ANSYS

[54] GT STRUDL, Intergraph, Madison, AL, USA. Retrieved August 23rd, 2015: www.intergraph.com/products/ppm/gt_strudl

[55] Hillerborg, A., Modeer, M., Petersson, P. E., 1976. Analysis of Crack Formation and Crack Growth in Concrete by Means of Fracture Mechanics and Finite Elements, Cement and Concrete Research, Vol. 6, pp. 773-782.

[56] Lubliner, J., Oliver, J., Oller, S., Oñate, E., 1989. A Plastic-Damage Model for Concrete, International Journal of Solids and Structures, vol. 25, no. 3, pp. 229–326.

[57] Lee, J., Fenves, G. L., 1998. Plastic-Damage Model for Cyclic Loading of Concrete Structures, Journal of Engineering Mechanics, vol. 124, no. 8, pp. 892–900.

[58] Jirasek, M., 2011. Numerical Modeling of Concrete Cracking – Courses and Lectures – No. 532, Chapter 1: Damaged and smeared crack models, International Centre for Mechanical Sciences, Springer ISBN 978-3-7091-0896-3.

[59] Mindess, S., Young, J. F., Darwin, D., 2003. Concrete, Second Edition, Chapter 13, Prentice Hall, Pearson Education, Inc. Upper Saddle River, NJ 07458.

[60] CEB-FIP Model Code for Concrete Structures, 2010. International Federation for Structural Concrete (fib), Lausanne, Switzerland, ISBN: 978-3-433-03061-5.

[61] Rots, J. G., Blaauwendraad, J., 1989. Crack Models for Concrete: Discrete or Smeared? Fixed, Multi-directional or Rotating?, HERON, Vol. 34, No. 1, pp. 1-59.

[62] Varma, A. H., 2000. Seismic Behavior, Analysis, and Design of High Strength Square Concrete Filled Steel Tube (CFT) Columns (PhD dissertation), Lehigh University, Bethlehem, PA, USA.

[63] Ollgaard, J. G., Slutter, R. G., Fisher, J. W., 1971. Shear Strength of Stud Connectors in Lightweight and Normal-Weight Concrete, Engineering Journal of the American Institute of Steel Construction, Vol. 8, No. 2.

[64] Zhang, K., Varma, A. H., Malushte, S. R., Gallocher, S. (2014). Effect of shear connectors on local buckling and composite action in steel concrete composite walls. Nuclear Eng. and Design, Elsevier B. V. doi:10.1016/j.nucengdes.2013.08.035

[65] AISC 360-10, 2010. Specification for Structural Steel Buildings, Chicago, Illinois, USA.

[66] Booth, P. N., Varma, A. H., Sener, K. C., Malushte, S. R., 2015. Flexural behavior and design of steel-plate composite (SC) walls for accident thermal loading. Nuc. Eng. and Des., Special issue of SMiRT-22 in San Francisco: Improving Safety and Reliability of Nuclear Energy, http://dx.doi.org/10.1016/i.nucengdes.2015.07.036, Elsevier Science.

[67] Varma, A. H., Malushte, S. R., Sener, K. C., Booth, P. N., 2012. Analysis Recommendations for Steel-Composite (SC) Walls of Safety-Related Nuclear Facilities, Proceedings from ASCE Structures Congress, Chicago, IL, USA.

[68] Kurt, E. G., Varma, A. H., Booth, P., Whittaker, A. S., 2015. In-plane Behavior and Design of Rectangular SC Wall Piers without Boundary Elements, Journal of Structural Engineering, ASCE Structural Division. (in review)

[69] DCD, 2012. Design control document of the US-APWR. United States Nuclear Regulatory Commission, Washington, DC, USA. http://www.nrc.gov/reactors/new-reactors/design-cert/ap1000.html

[70] NUREG-75/087, 2007. Standard Review Plan for the Review of Safety Analysis Reports for Nuclear Power Plants: LWR Edition, United States Nuclear Regulatory Commission, Washington, DC, USA.

[71] DCD. Design Control Document for the AP1000. Washington, DC, USA: U. S. Nuclear Regulatory Commission, http://www.nrc.gov/reactors/new-reactors/designcert/ap1000.html.

[72] Varma, A. H., Malushte, S., Sener, K., Lai, Z. (2014), Steel-plate composite (SC) walls for safety related nuclear facilities: design for in-plane force and out-of-plane moments. Nuclear Engineering and Design. Vol. 269, pp: 240-249. doi.org/10.1016/j.nucengdes.2013.09.019

[73] Seo, J., Varma, A. H., Sener, K. C., Ayhan, D., (2016), Steel-plate composite (SC) walls: In-plane shear behavior, database, and design. Journal of Constructional Steel Research, Volume 119, pp: 202-215. doi:10.1016/j.jcsr.2015.12.013

[74] Kollegger, J., Mehlorn, G. (1990). “Experimentelle Untersuchungen zur Bestimung der Druckfestigkeit des gerissenen Stahlbeton, Berlin, Germany.

[75] Shirai, S., Noguchi, H. (1989). Compression deterioration of cracked concrete. Proceedings ASCE Structures Congress 1989: Design, Analysis and Testing, ASCE, New York, N. Y., 1-10.

[76] Belarbi, A., Hsu, T. T. C. (1991). Constitutive laws of reinforced concrete in biaxial tension-compression. Research Report UHCEE 91-1, University of Houston, Houston, TX, USA.

[77] Vecchio, F. J., Collins, M. P. (1993). Compression Response of Cracked Reinforced Concrete. Journal of Structural Engineering, Vol. 119, No. 12. ASCE, ISSN 0733-9445/93/0012.

[78] Vecchio, F. J. (2000). Disturbed Stress Field Model for Reinforced Concrete: Formulation. Journal of Structural Engineering, Vol. 126, No. 9, ISSN 0733-9445/00/0009-1070-1077.

[79] Hognestad, E. (1951). A study of combined bending and axial load in reinforced concrete members, University of Illinois Engineering Experiment Station, Bulletin Series No. 399, University of Illinois, Urbana, IL, USA.

[80] Epackachi, S. H., Nguyen, N., Kurt, E. G., Whittaker, A. S., Varma, A. H. (2015a). In-Plane Seismic Behavior of Rectangular Steel-Plate Composite Wall Piers. Journal of Structural Engineering, ASCE, DOI: 10.1061/(ASCE)ST.1943-541X.0001148.

[81] Epackachi, S. H., Whittaker, A. S., Huang, Y. N. (2015b). Analytical modeling of rectangular SC wall panels. Journal of Constructional Steel Research, DOI:10.1016/j.jcsr.2014.10.016

[82] Kurt, E. G., Varma, A. H., Booth, P., Whittaker, A. S. (2016). In-plane Behavior and Design of Rectangular SC Wall Piers Without Boundary Elements. Journal of Structural Engineering, ASCE.

[83] Booth, P. N., Varma, A. H., Sener, K. C., Mori, K. (2015). Seismic behavior and design of a primary shield structure consisting of steel-plate composite (SC) walls. Nuc. Eng. and Des., Elsevier. http://dx.doi.org.10.1016/j.nucengdes.2015.07.006

[84] Sener, K. C., Varma, A. H., Booth, P. N., Fujimoto, R. (2015). Seismic behavior of a containment internal structure consisting of composite SC walls. Nuc. Eng. and Design, 2015 Elsevier B. V. http://dx.doi.org.10.1016.j.nucengded.2015.07.038

[85] AISC 341-10 (2010), Seismic Provisions for Structural Steel Buildings, American Institute of Steel Construction, Chicago, IL. www.aisc.org

APPENDIX

APPENDIX

IN-PLANE SHEAR STRENGTH AND STRAIN CALCULATIONS

Composite in-plane shear stress-strain relationship

Composite shell plane stress elasticity is used for development of the complete shear stress-shear strain relationship. The following assumptions are used: strain compatibility between steel and concrete (fully bonded), only membrane stresses, and pure shear applied load.

Concrete cracking in-plane shear strength

The cracking strength is defined in AISC N690s1-15 Eq. A-N9-10 and shown below with f'_c (concrete cylinder strength) in terms of ksi units. t_{sc} is the wall thickness, t_p is the steel faceplate thickness, G_s and G_c are plane stress elastic isotropic shear moduli. This strength is defined according to the Rankine criterion when the maximum principal stress in the concrete infill reaches the cracking threshold.

$$S_{cr} = \frac{0.063\sqrt{f'_c}}{G_c} \cdot \left(G_s \cdot 2 \cdot t_p + G_c \cdot t_{sc}\right) \qquad \text{Equation A.1}$$

Uncracked concrete shear stiffness

Uncracked isotropic elastic stiffness from AISC N690s1-15 Eq. A-N9-9:

$$K_{uncr} = G_s \cdot 2 \cdot t_p + G_c \cdot t_{sc}$$ Equation A.2

Shear strain at concrete cracking

The shear strain is equal to the cracking strength divided by the uncracked composite section shear stiffness, K_{uncr}:

$$\gamma_{xy(cr)} = \frac{S_{cr}}{K_{uncr}}$$ Equation A.3

Minimum principal strain at concrete cracking

The shear strain at concrete cracking is equal to the cracking strength divided by the uncracked composite stiffness. The uncracked composite stiffness is calculated below:

Stress transformation from x-y to principal directions: 1-2 (45 degrees):

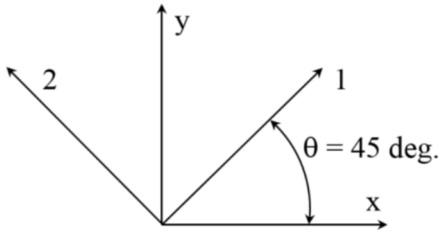

θ = 45 deg.

$$T_\sigma = \begin{pmatrix} \cos(\theta)^2 & \sin(\theta)^2 & 2\cdot\sin(\theta)\cdot\cos(\theta) \\ \sin(\theta)^2 & \cos(\theta)^2 & -2\cdot\sin(\theta)\cdot\cos(\theta) \\ -\sin(\theta)\cdot\cos(\theta) & \sin(\theta)\cdot\cos(\theta) & \cos(\theta)^2 - \sin(\theta)^2 \end{pmatrix}$$

$$T_\sigma = \begin{pmatrix} 0.5 & 0.5 & 1 \\ 0.5 & 0.5 & -1 \\ -0.5 & 0.5 & 0 \end{pmatrix}$$

In x-y coordinates, the resultant unit normal forces are equal to zero:

$$\begin{pmatrix} S_x \\ S_y \\ S_{xy} \end{pmatrix} = \begin{pmatrix} 0 \\ 0 \\ S_{xy} \end{pmatrix}$$

Resultant unit forces in 1-2 directions are then equal in magnitude to the applied shear in x-y and equal and opposite:

$$T_\sigma \cdot \begin{pmatrix} 0 \\ 0 \\ S_{xy} \end{pmatrix} = \begin{pmatrix} S_1 \\ S_2 \\ S_{12} \end{pmatrix} = \begin{pmatrix} 0.5 & 0.5 & 1 \\ 0.5 & 0.5 & -1 \\ -0.5 & 0.5 & 0 \end{pmatrix} \cdot \begin{pmatrix} 0 \\ 0 \\ S_{xy} \end{pmatrix} = \begin{pmatrix} S_{xy} \\ -S_{xy} \\ 0 \end{pmatrix}$$ Equation A.4

Steel constitutive relationship in principal coordinates:

$$\begin{pmatrix} \sigma_{s1} \\ \sigma_{s2} \\ \tau_{s12} \end{pmatrix} = \frac{E_s}{1 - \nu_s^2} \cdot \begin{pmatrix} 1 & \nu_s & 0 \\ \nu_s & 1 & 0 \\ 0 & 0 & \frac{1 - \nu_s}{2} \end{pmatrix} \cdot \begin{pmatrix} \varepsilon_1 \\ \varepsilon_2 \\ \gamma_{12} \end{pmatrix} = \begin{bmatrix} -\frac{E_s \cdot (\varepsilon_1 + \varepsilon_2 \cdot \nu_s)}{\nu_s^2 - 1} \\ -\frac{E_s \cdot (\varepsilon_2 + \varepsilon_1 \cdot \nu_s)}{\nu_s^2 - 1} \\ \frac{E_s \cdot \gamma_{12}}{2 \cdot (\nu_s + 1)} \end{bmatrix}$$

Uncracked concrete constitutive relationship in principal coordinates:

$$\begin{pmatrix} \sigma_{c1} \\ \sigma_{c2} \\ \tau_{c12} \end{pmatrix} = \frac{E_c}{1-\nu_c^{\,2}} \cdot \begin{pmatrix} 1 & \nu_c & 0 \\ \nu_c & 1 & 0 \\ 0 & 0 & \frac{1-\nu_c}{2} \end{pmatrix} \cdot \begin{pmatrix} \varepsilon_1 \\ \varepsilon_2 \\ \gamma_{12} \end{pmatrix} = \begin{bmatrix} -\frac{E_c \cdot (\varepsilon_1 + \varepsilon_2 \cdot \nu_c)}{\nu_c^{\,2}-1} \\ -\frac{E_c \cdot (\varepsilon_2 + \varepsilon_1 \cdot \nu_c)}{\nu_c^{\,2}-1} \\ \frac{E_c \cdot \gamma_{12}}{2 \cdot (\nu_c + 1)} \end{bmatrix}$$

Substitute constitutive relationships into equilibrium equation:

$$\begin{pmatrix} S_1 \\ S_2 \\ S_{12} \end{pmatrix} = \begin{pmatrix} \sigma_{c1} \\ \sigma_{c2} \\ \tau_{c12} \end{pmatrix} \cdot t_{sc} + \begin{pmatrix} \sigma_{s1} \\ \sigma_{s2} \\ \tau_{s12} \end{pmatrix} \cdot 2 \cdot t_p$$

$$\begin{pmatrix} S_1 \\ S_2 \\ S_{12} \end{pmatrix} = \begin{pmatrix} S_{xy} \\ -S_{xy} \\ 0 \end{pmatrix} = \begin{bmatrix} -\frac{E_c \cdot (\varepsilon_1 + \varepsilon_2 \cdot \nu_c)}{\nu_c^{\,2}-1} \\ -\frac{E_c \cdot (\varepsilon_2 + \varepsilon_1 \cdot \nu_c)}{\nu_c^{\,2}-1} \\ \frac{E_c \cdot \gamma_{12}}{2 \cdot (\nu_c + 1)} \end{bmatrix} \cdot t_{sc} + \begin{bmatrix} -\frac{E_s \cdot (\varepsilon_1 + \varepsilon_2 \cdot \nu_s)}{\nu_s^{\,2}-1} \\ -\frac{E_s \cdot (\varepsilon_2 + \varepsilon_1 \cdot \nu_s)}{\nu_s^{\,2}-1} \\ \frac{E_s \cdot \gamma_{12}}{2 \cdot (\nu_s + 1)} \end{bmatrix} \cdot 2 \cdot t_p$$

Three equations three unknowns, solve for ε_1, ε_2, and γ_{12}:

Given

$$\begin{pmatrix} S_{xy} \\ -S_{xy} \\ 0 \end{pmatrix} = \begin{bmatrix} -\frac{2 \cdot E_s \cdot t_p \cdot (\varepsilon_1 + \varepsilon_2 \cdot \nu_s)}{\nu_s^{\,2} - 1} - \frac{E_c \cdot t_{sc} \cdot (\varepsilon_1 + \varepsilon_2 \cdot \nu_c)}{\nu_c^{\,2} - 1} \\ -\frac{2 \cdot E_s \cdot t_p \cdot (\varepsilon_2 + \varepsilon_1 \cdot \nu_s)}{\nu_s^{\,2} - 1} - \frac{E_c \cdot t_{sc} \cdot (\varepsilon_2 + \varepsilon_1 \cdot \nu_c)}{\nu_c^{\,2} - 1} \\ \frac{2 \cdot E_s \cdot t_p \cdot \gamma_{12}}{2 \cdot \nu_s + 2} + \frac{E_c \cdot t_{sc} \cdot \gamma_{12}}{2 \cdot \nu_c + 2} \end{bmatrix}$$

$$\text{Find}(\varepsilon_1, \varepsilon_2, \gamma_{12}) \rightarrow \begin{pmatrix} \frac{S_{xy} + S_{xy} \cdot \nu_c + S_{xy} \cdot \nu_s + S_{xy} \cdot \nu_c \cdot \nu_s}{2 \cdot E_s \cdot t_p + E_c \cdot t_{sc} + 2 \cdot E_s \cdot t_p \cdot \nu_c + E_c \cdot t_{sc} \cdot \nu_s} \\ -\frac{S_{xy} + S_{xy} \cdot \nu_c + S_{xy} \cdot \nu_s + S_{xy} \cdot \nu_c \cdot \nu_s}{2 \cdot E_s \cdot t_p + E_c \cdot t_{sc} + 2 \cdot E_s \cdot t_p \cdot \nu_c + E_c \cdot t_{sc} \cdot \nu_s} \\ 0 \end{pmatrix}$$

$$\text{Find}(\varepsilon_1, \varepsilon_2, \gamma_{12}) \rightarrow \begin{pmatrix} \frac{S_{xy} + S_{xy} \cdot \nu_c + S_{xy} \cdot \nu_s + S_{xy} \cdot \nu_c \cdot \nu_s}{2 \cdot E_s \cdot t_p + E_c \cdot t_{sc} + 2 \cdot E_s \cdot t_p \cdot \nu_c + E_c \cdot t_{sc} \cdot \nu_s} \\ -\frac{S_{xy} + S_{xy} \cdot \nu_c + S_{xy} \cdot \nu_s + S_{xy} \cdot \nu_c \cdot \nu_s}{2 \cdot E_s \cdot t_p + E_c \cdot t_{sc} + 2 \cdot E_s \cdot t_p \cdot \nu_c + E_c \cdot t_{sc} \cdot \nu_s} \\ 0 \end{pmatrix}$$

$$\begin{pmatrix} \varepsilon_1 \\ \varepsilon_2 \\ \gamma_{12} \end{pmatrix} = \begin{pmatrix} \dfrac{S_{xy} + S_{xy}\cdot\nu_c + S_{xy}\cdot\nu_s + S_{xy}\cdot\nu_c\cdot\nu_s}{2\cdot E_s\cdot t_p + E_c\cdot t_{sc} + 2\cdot E_s\cdot t_p\cdot\nu_c + E_c\cdot t_{sc}\cdot\nu_s} \\ -\dfrac{S_{xy} + S_{xy}\cdot\nu_c + S_{xy}\cdot\nu_s + S_{xy}\cdot\nu_c\cdot\nu_s}{2\cdot E_s\cdot t_p + E_c\cdot t_{sc} + 2\cdot E_s\cdot t_p\cdot\nu_c + E_c\cdot t_{sc}\cdot\nu_s} \\ 0 \end{pmatrix}$$

Simplify:

$$\begin{pmatrix} \varepsilon_1 \\ \varepsilon_2 \\ \gamma_{12} \end{pmatrix} = \begin{bmatrix} \dfrac{S_{xy}\cdot(\nu_c + 1)\cdot(\nu_s + 1)}{2\cdot E_s\cdot t_p + E_c\cdot t_{sc} + 2\cdot E_s\cdot t_p\cdot\nu_c + E_c\cdot t_{sc}\cdot\nu_s} \\ -\dfrac{S_{xy}\cdot(\nu_c + 1)\cdot(\nu_s + 1)}{2\cdot E_s\cdot t_p + E_c\cdot t_{sc} + 2\cdot E_s\cdot t_p\cdot\nu_c + E_c\cdot t_{sc}\cdot\nu_s} \\ 0 \end{bmatrix}$$

Minimum principal strain at point of concrete cracking then becomes:

$$\varepsilon_{2(cr)} = -\frac{S_{xy}\cdot(\nu_c + 1)\cdot(\nu_s + 1)}{2\cdot E_s\cdot t_p + E_c\cdot t_{sc} + 2\cdot E_s\cdot t_p\cdot\nu_c + E_c\cdot t_{sc}\cdot\nu_s}$$

$$\varepsilon_{2(cr)} = \frac{-S_{xy}\cdot(\nu_c + 1)\cdot(\nu_s + 1)}{2\cdot E_s\cdot t_p\cdot(1 + \nu_c) + E_c\cdot t_{sc}\cdot(1 + \nu_s)} \qquad \text{Equation A.5}$$

with S_{cr} calculated with Equation A.1.

In-plane yield shear strength

The yield shear strength is calculated with AISC N690s1-15 Eq. A-N9-19. This equation provides an approximate solution and is calculated in terms of the normalized reinforcement ratio, ρ and κ:

$$S_y = \kappa \cdot 2 \cdot t_p \cdot f_y \qquad \text{Equation A.6}$$

With:

$$\kappa = 1.11 - 5.16 \cdot \rho < 1.0$$

$$\rho = \frac{1}{31.6} \cdot \frac{f_y \cdot 2 \cdot t_p}{t_{sc} \cdot \sqrt{f'_c}}$$

Cracked stiffness

The in-plane cracked shear stiffness is derived assuming the steel is elastic isotropic and the concrete is orthotropic with zero stiffness in the direction of maximum tension (due to cracking) and equal to E'_c in the minimum principal stress direction, where E'_c is equal to $0.7E_c$ (E_c is the concrete secant elastic stiffness). Poisson's effect is neglected for simplicity. The concrete and steel constitutive relationships are shown below, where E_S and ν_S are the steel modulus and Poisson's ratio, respectively:

Steel Concrete

$$\begin{pmatrix}\sigma_{s1}\\ \sigma_{s2}\\ \tau_{s12}\end{pmatrix} = \frac{E_s}{1-\nu^2}\cdot\begin{pmatrix}1 & \nu_s & 0\\ \nu_s & 1 & 0\\ 0 & 0 & \frac{1-\nu_s}{2}\end{pmatrix}\cdot\begin{pmatrix}\varepsilon_1\\ \varepsilon_2\\ \gamma_{12}\end{pmatrix}\begin{pmatrix}\sigma_{c1}\\ \sigma_{c2}\\ \tau_{c12}\end{pmatrix} = E'_c\cdot\begin{pmatrix}0 & 0 & 0\\ 0 & 1 & 0\\ 0 & 0 & 0\end{pmatrix}\cdot\begin{pmatrix}\varepsilon_1\\ \varepsilon_2\\ \gamma_{12}\end{pmatrix}$$

The cracked composite stiffness is defined in AISC N690s1-15 Eq. A-N9-11, in approximate form and shown in Equation A.5:

$$K_{cr} = K_s + K_{sc} = \frac{E_s\cdot 2\cdot t_p}{2\cdot(1-\nu_s)} + \frac{1}{\frac{4}{0.7\cdot E_c\cdot t_{sc}} + \frac{2\cdot(1-\nu_s)}{2\cdot t_p\cdot E_s}}$$

Equation A.7

Yield shear strain

The yield shear strain calculated by dividing the shear force increment from cracking to yield by the shear strain increment and setting equal to the cracked concrete composite stiffness.

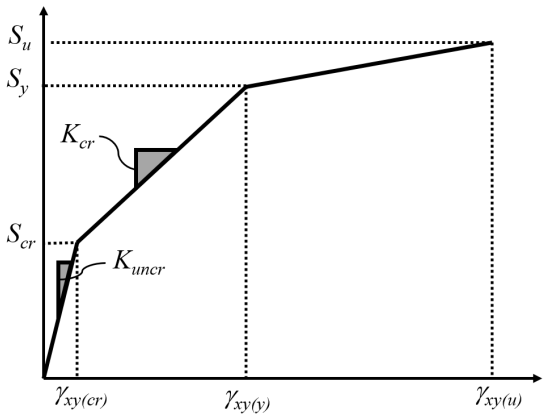

Cracked concrete composite stiffness equal to ratio of shear force to shear strain increments:

$$K_{cr} = \frac{S_y - S_{cr}}{\gamma_{xy(y)} - \gamma_{xy(cr)}}$$

Solve for yield shear strain:

$$K_{cr} \cdot \left(\gamma_{xy(y)} - \gamma_{xy(cr)}\right) = S_y - S_{cr}$$

$$K_{cr} \cdot \gamma_{xy(y)} - K_{cr} \cdot \gamma_{xy(cr)} = S_y - S_{cr}$$

$$K_{cr} \cdot \gamma_{xy(y)} = S_y - S_{cr} + K_{cr} \cdot \gamma_{xy(cr)}$$

Yield shear strain:

$$\gamma_{xy(y)} = \frac{S_y - S_{cr} + K_{cr} \cdot \gamma_{xy(cr)}}{K_{cr}} \qquad \text{Equation A.8}$$

Concrete compression stress at point of steel faceplate yield

The minimum principal concrete stress is equal to the minimum principal strain multiplied by the cracked concrete elastic modulus, E'_c. The strain is equal to $\varepsilon_{2(cr)}$ at cracking (calculated with uncracked concrete stiffness) plus increase from cracking to yield calculated with the cracked concrete stiffness $\varepsilon_{2(Sy)}$ and $\varepsilon_{2(Scr)}$:

$$\varepsilon_{2(y)} = \varepsilon_{2(cr)} + \left[\varepsilon_{2(Sy)} - \varepsilon_{2(Scr)}\right]$$

Stress and strain transformation matrices:

$\theta = 45$ deg.

$$T_\sigma = \begin{pmatrix} \cos(\theta)^2 & \sin(\theta)^2 & 2\cdot\sin(\theta)\cdot\cos(\theta) \\ \sin(\theta)^2 & \cos(\theta)^2 & -2\cdot\sin(\theta)\cdot\cos(\theta) \\ -\sin(\theta)\cdot\cos(\theta) & \sin(\theta)\cdot\cos(\theta) & \cos(\theta)^2 - \sin(\theta)^2 \end{pmatrix} \quad T_\sigma = \begin{pmatrix} 0.5 & 0.5 & 1 \\ 0.5 & 0.5 & -1 \\ -0.5 & 0.5 & 0 \end{pmatrix}$$

$$T_\varepsilon = \begin{pmatrix} \cos(\theta)^2 & \sin(\theta)^2 & \sin(\theta)\cdot\cos(\theta) \\ \sin(\theta)^2 & \cos(\theta)^2 & -\sin(\theta)\cdot\cos(\theta) \\ -2\cdot\sin(\theta)\cdot\cos(\theta) & 2\cdot\sin(\theta)\cdot\cos(\theta) & \cos(\theta)^2 - \sin(\theta)^2 \end{pmatrix} T_\varepsilon = \begin{pmatrix} 0.5 & 0.5 & 0.5 \\ 0.5 & 0.5 & -0.5 \\ -1 & 1 & 0 \end{pmatrix}$$

Equilibrium:

$$\begin{pmatrix} S_1 \\ S_2 \\ S_{12} \end{pmatrix} = \begin{pmatrix} \sigma_{c1} \\ \sigma_{c2} \\ \tau_{c12} \end{pmatrix} \cdot t_{sc} + \begin{pmatrix} \sigma_{s1} \\ \sigma_{s2} \\ \tau_{s12} \end{pmatrix} \cdot 2 \cdot t_p$$

Substitute constitutive relationships and factor out strain:

$$\begin{pmatrix} S_1 \\ S_2 \\ S_{12} \end{pmatrix} = E'_c \cdot \begin{pmatrix} 0 & 0 & 0 \\ 0 & 1 & 0 \\ 0 & 0 & 0 \end{pmatrix} \cdot \begin{pmatrix} \varepsilon_1 \\ \varepsilon_2 \\ \gamma_{12} \end{pmatrix} \cdot t_{sc} + \frac{E_s}{1 - \nu_s^2} \cdot \begin{pmatrix} 1 & \nu_s & 0 \\ \nu_s & 1 & 0 \\ 0 & 0 & \frac{1 - \nu_s}{2} \end{pmatrix} \cdot \begin{pmatrix} \varepsilon_1 \\ \varepsilon_2 \\ \gamma_{12} \end{pmatrix} \cdot 2 \cdot t_p$$

$$\begin{pmatrix} S_1 \\ S_2 \\ S_{12} \end{pmatrix} = \left[E'_c \cdot \begin{pmatrix} 0 & 0 & 0 \\ 0 & 1 & 0 \\ 0 & 0 & 0 \end{pmatrix} \cdot t_{sc} + \frac{E_s}{1 - \nu_s^2} \cdot \begin{pmatrix} 1 & \nu_s & 0 \\ \nu_s & 1 & 0 \\ 0 & 0 & \frac{1 - \nu_s}{2} \end{pmatrix} \cdot 2 \cdot t_p \right] \cdot \begin{pmatrix} \varepsilon_1 \\ \varepsilon_2 \\ \gamma_{12} \end{pmatrix}$$

The composite stiffness relationship in 1-2 directions then becomes:

$$\begin{pmatrix} S_1 \\ S_2 \\ S_{12} \end{pmatrix} = \begin{pmatrix} -\frac{2 \cdot E_s \cdot t_p}{\nu_s^{\,2} - 1} & -\frac{2 \cdot E_s \cdot t_p \cdot \nu_s}{\nu_s^{\,2} - 1} & 0 \\ -\frac{2 \cdot E_s \cdot t_p \cdot \nu_s}{\nu_s^{\,2} - 1} & E'_c \cdot t_{sc} - \frac{2E_s \cdot t_p}{\nu_s^{\,2} - 1} & 0 \\ 0 & 0 & \frac{E_s \cdot t_p}{\nu_s + 1} \end{pmatrix} \cdot \begin{pmatrix} \varepsilon_1 \\ \varepsilon_2 \\ \gamma_{12} \end{pmatrix}$$

The resultant forces for pure shear in (from Equation A.4):

$$\begin{pmatrix} S_1 \\ S_2 \\ S_{12} \end{pmatrix} = \begin{pmatrix} S_{xy} \\ -S_{xy} \\ 0 \end{pmatrix}$$

Substituting into the composite relationship yields:

$$\begin{pmatrix} S_{xy} \\ -S_{xy} \\ 0 \end{pmatrix} = \begin{pmatrix} -\frac{2 \cdot E_s \cdot t_p}{\nu_s^{\,2} - 1} & -\frac{2 \cdot E_s \cdot t_p \cdot \nu_s}{\nu_s^{\,2} - 1} & 0 \\ -\frac{2 \cdot E_s \cdot t_p \cdot \nu_s}{\nu_s^{\,2} - 1} & E'_c \cdot t_{sc} - \frac{2E_s \cdot t_p}{\nu_s^{\,2} - 1} & 0 \\ 0 & 0 & \frac{E_s \cdot t_p}{\nu_s + 1} \end{pmatrix} \cdot \begin{pmatrix} \varepsilon_1 \\ \varepsilon_2 \\ \gamma_{12} \end{pmatrix}$$

Reduce and solve for strains ε_1, ε_2, γ_{12}:

Given

$$\begin{pmatrix} S_{xy} \\ -S_{xy} \\ 0 \end{pmatrix} = \begin{bmatrix} -\dfrac{2 \cdot E_s \cdot t_p \cdot (\varepsilon_1 + \varepsilon_2 \cdot \nu_s)}{\nu_s^{\,2} - 1} \\ -\dfrac{2 \cdot E_s \cdot t_p \cdot \varepsilon_1 \cdot \nu_s - E'_c \cdot t_{sc} \cdot \varepsilon_2 \cdot \nu_s^{\,2} + 2 \cdot E_s \cdot t_p \cdot \varepsilon_2 + E'_c \cdot t_{sc} \cdot \varepsilon_2}{\nu_s^{\,2} - 1} \\ \dfrac{E_s \cdot t_p \cdot \gamma_{12}}{\nu_s + 1} \end{bmatrix}$$

$$\text{Find}(\varepsilon_1, \varepsilon_2, \gamma_{12}) \rightarrow \begin{pmatrix} \dfrac{2 \cdot E_s \cdot S_{xy} \cdot t_p \cdot \nu_s - E'_c \cdot S_{xy} \cdot t_{sc} \cdot \nu_s^{\,2} + 2 \cdot E_s \cdot S_{xy} \cdot t_p + E'_c \cdot S_{xy} \cdot t_{sc}}{4 \cdot E_s^{\,2} \cdot t_p^{\,2} + 2 \cdot E'_c \cdot t_{sc} \cdot E_s \cdot t_p} \\ -\dfrac{S_{xy} + S_{xy} \cdot \nu_s}{2 \cdot E_s \cdot t_p + E'_c \cdot t_{sc}} \\ 0 \end{pmatrix}$$

$$\begin{pmatrix} \varepsilon_1 \\ \varepsilon_2 \\ \gamma_{12} \end{pmatrix} = \begin{pmatrix} \dfrac{2 \cdot E_s \cdot S_{xy} \cdot t_p \cdot \nu_s - E'_c \cdot S_{xy} \cdot t_{sc} \cdot \nu_s^{\,2} + 2 \cdot E_s \cdot S_{xy} \cdot t_p + E'_c \cdot S_{xy} \cdot t_{sc}}{4 \cdot E_s^{\,2} \cdot t_p^{\,2} + 2 \cdot E'_c \cdot t_{sc} \cdot E_s \cdot t_p} \\ -\dfrac{S_{xy} + S_{xy} \cdot \nu_s}{2 \cdot E_s \cdot t_p + E'_c \cdot t_{sc}} \\ 0 \end{pmatrix}$$

Simplify:

$$\begin{pmatrix} \varepsilon_1 \\ \varepsilon_2 \\ \gamma_{12} \end{pmatrix} = \begin{bmatrix} \dfrac{S_{xy}\cdot(\nu_s + 1)\cdot(2\cdot E_s\cdot t_p + E'_c\cdot t_{sc} - E'_c\cdot t_{sc}\cdot\nu_s)}{4\cdot {E_s}^2\cdot {t_p}^2 + 2\cdot E'_c\cdot t_{sc}\cdot E_s\cdot t_p} \\ -\dfrac{S_{xy}\cdot(\nu_s + 1)}{2\cdot E_s\cdot t_p + E'_c\cdot t_{sc}} \\ 0 \end{bmatrix}$$

The increase in minimum principal strain from cracking to yield is equal to:

$$\varepsilon_{2(Sy)} - \varepsilon_{2(Scr)}$$

With

$$\varepsilon_{2(Sy)} = -\frac{S_y\cdot(\nu_s + 1)}{2\cdot E_s\cdot t_p + E'_c\cdot t_{sc}}$$

$$\varepsilon_{2(cr)} = -\frac{S_{cr}\cdot(\nu_s + 1)}{2\cdot E_s\cdot t_p + E'_c\cdot t_{sc}}$$

And cracking strain from Equation A.5:

$$\varepsilon_{2(cr)} = \frac{-S_{cr}\cdot(\nu_c + 1)\cdot(\nu_s + 1)}{2\cdot E_s\cdot t_p + E_c\cdot t_{sc} + 2\cdot E_s\cdot t_p\cdot\nu_c + E_c\cdot t_{sc}\cdot\nu_s}$$

The strain at yield then becomes:

$$\varepsilon_{2(y)} = \varepsilon_{2(cr)} + \left[\varepsilon_{2(Sy)} - \varepsilon_{2(Scr)}\right]$$

$$\varepsilon_{2(y)} = \frac{-S_{cr}\cdot(\nu_c + 1)\cdot(\nu_s + 1)}{2\cdot E_s\cdot t_p\cdot(1 + \nu_c) + E_c\cdot t_{sc}\cdot(1 + \nu_s)} + \left[\frac{-S_y\cdot(\nu_s + 1)}{2\cdot E_s\cdot t_p + E'_c\cdot t_{sc}} - \frac{-S_{cr}\cdot(\nu_s + 1)}{2\cdot E_s\cdot t_p + E'_c\cdot t_{sc}}\right]$$

$$\varepsilon_{2(y)} = \frac{-S_{cr}\cdot(\nu_c + 1)\cdot(\nu_s + 1)}{2\cdot E_s\cdot t_p\cdot(1 + \nu_c) + E_c\cdot t_{sc}\cdot(1 + \nu_s)} - \frac{(S_y - S_{cr})\cdot(\nu_s + 1)}{2\cdot E_s\cdot t_p + E'_c\cdot t_{sc}}$$

Equation A.9

Ultimate in-plane shear strength calculation

The ultimate in-plane shear strength assumed equal to the yield strength plus an incremental strength, ΔS. This incremental strength is equal to the increase in concrete stress from yield to ultimate and assumes the ultimate compression strength of cracked concrete is equal to $0.5f'_c$.

Concrete compression stress increment:

$$\Delta f_c = 0.5 \cdot f'_c - f_{cy}$$

with fcy equal to Equation multiplied by E'c:

$$f_{cy} = \left[\frac{-S_{cr} \cdot (\nu_c + 1) \cdot (\nu_s + 1)}{2 \cdot E_s \cdot t_p + E_c \cdot t_{sc} + 2 \cdot E_s \cdot t_p \cdot \nu_c + E_c \cdot t_{sc} \cdot \nu_s} - \frac{(S_y - S_{cr}) \cdot (\nu_s + 1)}{2 \cdot E_s \cdot t_p + E'_c \cdot t_{sc}} \right] \cdot E'_c \qquad \text{Eq.A.10}$$

The unit shear is transformed to x-y with the 0.5 factor and multiplied by the wall thickness:

$$\Delta S = 0.5 \cdot \Delta f_c \cdot t_{sc}$$

The ultimate in-plane shear strength is then (kips/in.):

$$S_u = S_y + \Delta S$$

Shear strain at ultimate

Assume that the strain state at ultimate is equal to that at yield but proportionally scaled up such that the compression concrete strain is equal to -0.0016 in./in. Using this approach, the ratio of principal strains at yield ($\varepsilon_{x(y)}/\varepsilon_{y(y)}$) are equal to the ratio of principal strains at ultimate ($\varepsilon_{x(u)}/\varepsilon_{y(u)}$).

Transform strain state from x-y to 1-2:

$\theta = 45$ deg.

$$T_\varepsilon = \begin{pmatrix} \cos(\theta)^2 & \sin(\theta)^2 & \sin(\theta)\cdot\cos(\theta) \\ \sin(\theta)^2 & \cos(\theta)^2 & -\sin(\theta)\cdot\cos(\theta) \\ -2\cdot\sin(\theta)\cdot\cos(\theta) & 2\cdot\sin(\theta)\cdot\cos(\theta) & \cos(\theta)^2 - \sin(\theta)^2 \end{pmatrix}$$

$$T_\varepsilon = \begin{pmatrix} 0.5 & 0.5 & 0.5 \\ 0.5 & 0.5 & -0.5 \\ -1 & 1 & 0 \end{pmatrix}$$

$$\begin{pmatrix} \varepsilon_1 \\ \varepsilon_2 \\ 0 \end{pmatrix} = \begin{pmatrix} 0.5 & 0.5 & 0.5 \\ 0.5 & 0.5 & -0.5 \\ -1 & 1 & 0 \end{pmatrix} \cdot \begin{pmatrix} \varepsilon_x \\ \varepsilon_y \\ \gamma_{xy} \end{pmatrix}$$

$$\begin{pmatrix} \varepsilon_1 \\ \varepsilon_2 \\ 0 \end{pmatrix} = \begin{pmatrix} 0.5\cdot\varepsilon_x + 0.5\cdot\varepsilon_y + 0.5\cdot\gamma_{xy} \\ 0.5\cdot\varepsilon_x + 0.5\cdot\varepsilon_y - 0.5\cdot\gamma_{xy} \\ \varepsilon_y - \varepsilon_x \end{pmatrix}$$

Solve in terms of strain ratio $\varepsilon_1/\varepsilon_2$:

$$\varepsilon_1 = 0.5\cdot\varepsilon_x + 0.5\cdot\varepsilon_y + 0.5\cdot\gamma_{xy}$$

$$\varepsilon_2 = 0.5\cdot\varepsilon_x + 0.5\cdot\varepsilon_y - 0.5\cdot\gamma_{xy}$$

$$0 = \varepsilon_y - \varepsilon_x$$

$$\varepsilon_x = \varepsilon_y$$

$$\varepsilon_1 = \varepsilon_y + 0.5\cdot\gamma_{xy}$$

$$\varepsilon_y = \varepsilon_1 - 0.5 \cdot \gamma_{xy}$$

$$\varepsilon_2 = \varepsilon_1 - 0.5 \cdot \gamma_{xy} - 0.5 \cdot \gamma_{xy}$$

$$\varepsilon_2 = \varepsilon_1 - \gamma_{xy}$$

$$\frac{\varepsilon_2}{\varepsilon_2} = \frac{\varepsilon_1}{\varepsilon_2} - \frac{\gamma_{xy}}{\varepsilon_2}$$

$$1 = \frac{\varepsilon_1}{\varepsilon_2} - \frac{\gamma_{xy}}{\varepsilon_2} \qquad \text{Equation A.11}$$

The shear strain at ultimate then becomes:

$$\frac{\varepsilon_1}{\varepsilon_2} = 1 + \frac{\gamma_{xy}}{\varepsilon_2}$$

The strain ratio can be calculated since $\gamma_{xy(y)}$ and $\varepsilon_{2(y)}$ are already known:

$$\frac{\varepsilon_{1(y)}}{\varepsilon_{2(y)}} = 1 + \frac{\gamma_{xy(y)}}{\varepsilon_{2(y)}}$$

This is then substituted back into Equation A.11:

$$\gamma_{xy(u)} = \left[\frac{\varepsilon_{1(y)}}{\varepsilon_{2(y)}} - 1\right] \cdot \varepsilon_{2(u)}$$

With:

$$\varepsilon_{2(u)} = -0.0016$$

$$\gamma_{xy(u)} = \left[\frac{\varepsilon_{1(y)}}{\varepsilon_{2(y)}} - 1\right] \cdot -0.0016 \qquad \text{Equation A.12}$$

Summary

Cracking strength:

$$S_{cr} = \frac{0.063\sqrt{f'_c}}{G_c} \cdot \left(G_s \cdot 2 \cdot t_p + G_c \cdot t_{sc}\right)$$

Cracking strain:

$$\gamma_{xy(cr)} = \frac{S_{cr}}{K_{uncr}}$$

Yield strength:

$$S_y = \kappa \cdot 2 \cdot t_p \cdot f_y$$

Yield strain:

$$\gamma_{xy(y)} = \frac{S_y - S_{cr} + K_{cr} \cdot \gamma_{xy(cr)}}{K_{cr}}$$

Ultimate strength:

$$S_u = S_y + \Delta S \text{ with } \Delta S = 0.5 \cdot \Delta f_c \cdot t_{sc}$$

Ultimate Strain:

$$\gamma_{xy(u)} = \left[\frac{\varepsilon_{1(y)}}{\varepsilon_{2(y)}} - 1\right] \cdot -0.0016$$

VITA

VITA

Peter Booth was born in New Mexico and grew up in New York. He attended The University of Texas at Austin and received a Bachelor of Science in Civil Engineering degree in 2004. He subsequently matriculated at Purdue University, West Lafayette where he received a Master in Science in Civil Engineering in 2008. After gaining experience working in a structural consulting office for a number of years, Peter enrolled in the structural engineering Ph.D. program at Purdue University, West Lafayette and received a Ph.D. degree in 2016.